Forschungszentrum Karlsruhe

Technik und Umwelt

Wissenschaftliche Berichte

FZKA 6412

Investigation of an Overheated PWR-Type Fuel Rod Simulator Bundle Cooled Down by Steam

Part I: Experimental and Calculational Results of the QUENCH-04 Test

L. Sepold, P. Hofmann, C. Homann, W. Leiling, A. Miassoedov, D. Piel, G. Schanz, L. Schmidt, U. Stegmaier, M. Steinbrück, H. Steiner

Institut für Materialforschung
Institut für Reaktorsicherheit
Programm Nukleare Sicherheitsforschung

Part II: Application of the SVECHA/QUENCH Code to the Analysis of the QUENCH-01 and QUENCH-04 Bundle Tests

A.V. Palagin, A.V. Boldyrev, A.V. Berdyshev, V.E. Shestak, M.S. Veshchunov

Nuclear Safety Institute,
Russian Academy of Sciences, Moscow

Forschungszentrum Karlsruhe GmbH, Karlsruhe

2002

Impressum der Print-Ausgabe:

Als Manuskript gedruckt

Forschungszentrum Karlsruhe GmbH
Postfach 3640, 76021 Karlsruhe

Mitglied der Hermann von Helmholtz-Gemeinschaft
Deutscher Forschungszentren (HGF)

ISSN 0947-8620

Zusammenfassung

Untersuchung eines überhitzten DWR-Brennnstabsimulator-Bündels unter Abkühlung mit Dampf

Teil I: Experimentelle und analytische Ergebnisse des Versuchs QUENCH-04

Teil II: Anwendung des SVECHA/QUENCH-Rechenprogramms auf die Analyse der Bündelversuche QUENCH-01 und QUENCH-04

In den QUENCH-Versuchen soll der Wasserstoffquellterm bei der Einspeisung von Notkühlwasser in einen trockenen, überhitzten Reaktorkern eines Leichtwasserreaktors (LWR) ermittelt werden.

Das QUENCH-Testbündel ist mit 21 Brennstabsimulatoren bestückt und hat eine Gesamtlänge von ca. 2,50 m. 20 Brennstabsimulatoren sind auf einer Länge von 1024 mm beheizt, der Zentralstab ist unbeheizt. Als Heizer werden Wolfram-Stäbe von 6 mm Durchmesser verwendet, die im Zentrum der Brennstabsimulatoren angeordnet und von ZrO_2-Ringtabletten umgeben sind. Die Stabhüllen sind identisch mit LWR-Hüllrohren: Zircaloy-4, 10,75 mm Außendurchmesser und 0,725 mm Wanddicke. Testbündel und Shroud sind mit Thermoelementen instrumentiert. Sie sind auf 17 Messebenen im Abstand von 100 mm angeordnet.

Während des gesamten Tests bis zur Abkühlphase wird überhitzter Dampf zusammen mit Argon als Trägergas am unteren Ende in die Teststrecke eingespeist und verlässt diese zusammen mit dem Wasserstoff, der sich durch die Zirkonium-Dampf-Reaktion gebildet hat, am oberen Ende. Der Wasserstoff wird mit Hilfe von drei Messgeräten analysiert: zwei Massenspektrometer und ein „Caldos-7G“-Analysegerät (Wärmeleitfähigkeits-Messprinzip).

In Teil I dieses Berichts sind die Ergebnisse des Experiments QUENCH-04, das am 30. Juni 1999 in der QUENCH-Versuchsanlage des Forschungszentrums Karlsruhe durchgeführt wurde, beschrieben. Ziel des Versuchs QUENCH-04 war die Untersuchung des Verhaltens von nicht voroxidierten LWR-Brennstäben während der Kühlung eines Brennstabbündels mit Dampf anstelle von Wasser.

Das Experiment lief mit folgenden Versuchsphasen ab: einer Anfahr- oder Aufheizphase, um das Gesamtsystem bei ca. 900 K Bündeltemperatur ins thermische Gleichgewicht zu bringen, einer transienten (Aufheiz-) Phase und einer Abschreck- bzw. Quench-Phase. In der transienten Phase wurde das Versuchsbündel mit einer Aufheizrate von 0,35 K/s (900 – 1400 K) bzw. 1,0 K/s (1400 K bis zur Temperatureskalation) auf die maximale Stab-Hüllrohrtemperatur von ~2340 K gebracht. Zur Abschreckung des Versuchsbündels wurde Dampf mit einer mittleren Rate von 50 g/s von unten in die Teststrecke eingeleitet (Dampfgeschwindigkeit: 15 - 20 m/s). Die Dampfkühlung war unter diesen Bedingungen so effektiv, dass das Versuchsbündel in ca. 20 Sekunden um etwa 1000 K abgekühlt wurde.

Die gesamte freigesetzte Wasserstoffmenge während des Versuchs QUENCH-04 wurde zu 12 g ermittelt. Davon wurde der Hauptanteil während der Transiente und nur ein kleiner Anteil während der Flutphase gebildet.

Nach dem Experiment zeigte sich am Shroud eine lokale Schmelzzone zwischen 930 und 1000 mm Bündelhöhe, die durch den Kontakt einiger Stäbe mit dem Shroud hervorgerufen worden war. In diesem Bereich waren die Teststäbe stark verformt. Im Testbündel kam es nur im Innern von Teststäben zur Bildung und Verlagerung von Schmelzphasen.

Am Hüllrohr des Stabs Nr. 19 wurde eine maximale Oxidschichtdicke von 170 μm bei Bündelkote 950 mm gemessen. Vor der Temperatureskalation und dem Abkühlen mit Dampf betrug der Wert 85 μm (auf der Grundlage des bei ~1780 K gezogenen Zirkaloy-Eckstabs B).

Nachrechnungen mit dem CALUMO-Rechenprogramm wurden durchgeführt, um das Oxidationsverhalten der Brennstabsimulatoren und des Shrouds sowie die Wasserstoffproduktion zu untersuchen.

Teil II dieses Berichts behandelt die Ergebnisse der Anwendung des SVECHA/QUENCH (S/Q)-Rechenprogramms auf die Ergebnisse der FZK-QUENCH-Experimente. Die Angleichung des S/Q-Rechenprogramms an diese Art von Rechnungen wird beschrieben. Die numerische Behandlung der Nachrechnung der Temperatur-Versuchsdaten und die Anfertigung der S/Q-Programm-Eingabe werden präsentiert. Insbesondere werden die Ergebnisse bezüglich der Versuche QUENCH-01 and QUENCH-04 diskutiert.

Das Hauptgewicht der Arbeiten wurde auf den zeitlichen Verlauf der Zentralstab-Temperatur gelegt. Sie wurde für jede Versuchsphase, d. h. von der Voroxidation bis hin zur Flutphase, modelliert; denn ihr Verlauf beeinflusst deutlich den Ablauf anderer Prozesse.

Obgleich die wesentlichen Ergebnisse der Arbeiten die des Zentralstabs sind, werden doch einige Ergebnisse, wie die Wasserstoff-Erzeugungsrate und die Gesamtmenge des erzeugten Wasserstoffs, auf das gesamte Stabbündel extrapoliert, um die Rechnungen mit den Messwerten des Massenspektrometers zu vergleichen.

Abstract

The QUENCH experiments are to investigate the hydrogen source term that results from the water injection into an uncovered core of a Light-Water Reactor (LWR).

The test bundle is made up of 21 fuel rod simulators with a length of approximately 2.5 m. 20 fuel rod simulators are heated over a length of 1024 mm, the one unheated fuel rod simulator is located in the center of the test bundle. Heating is carried out electrically using 6-mm-diameter tungsten heating elements installed in the center of the rods and surrounded by annular ZrO_2 pellets. The rod cladding is identical to that used in LWRs: Zircaloy-4, 10.75 mm outside diameter, 0.725 mm wall thickness. The test bundle is instrumented with thermocouples attached to the cladding and the shroud at 17 different elevations with an axial distance between the thermocouples of 100 mm.

During the entire test up to the cooldown phase, superheated steam together with the argon as carrier gas enters the test bundle at the bottom end and leaves the test section at the top together with the hydrogen that is produced in the zirconium-steam reaction. The hydrogen is analyzed by three different instruments: two mass spectrometers and a ”Caldos 7 G” hydrogen measuring device (based on the principle of heat conductivity).

Part I of this report describes the results of test QUENCH-04 performed in the QUENCH test facility at the Forschungszentrum Karlsruhe on June 30, 1999. The objective of the experiment QUENCH-04 was to investigate the reaction of the non-preoxidized rod cladding on cooldown by steam rather than quenching by water.

The experiment consisted of a heatup phase to temperature plateau of around 900 K, a transient phase, and a cooldown phase. All phases were conducted in an argon/steam atmosphere. At the beginning of the transient phase the test bundle was ramped at around 0.35 K/s in the temperature range 900 – 1400 K and 1.0 K/s from 1400 K to the temperature excursion which led to a maximum rod cladding temperature of 2340 K. For cooling the test bundle, steam was injected at the bottom of the test section at a mean rate of 50 g/s (steam velocity: 15 - 20 m/s). This steam rate was so effective that the test bundle was cooled down for about 1000 K within around 20 s.

The total amount of hydrogen released during the QUENCH-04 experiment was 12 g. Most of it has been produced during the transient and only a small portion during the cooldown.

After the test the shroud showed a localized molten zone between 930 mm and 1000 mm probably caused by close contact of test rods with the shroud. In this region the rods were severely displaced. Melt formation was only observed within rods but not in the test bundle.

The maximum oxide layer thickness measured at the rod cladding # 19 amounted to 170 μm at around 950 mm elevation. Prior to the temperature escalation and cooldown by steam, i.e. in the middle of the transient, the ZrO_2 layer thickness had a maximum of ~85 μm at the same level. The latter data were obtained from corner rod B which was withdrawn from the test bundle at ~1780 K.

Posttest calculations were performed with the CALUMO computer code to investigate the oxidation behavior of the fuel rod claddings and the shroud as well as the hydrogen production.

Part II of the present report deals with the results of the SVECHA/QUENCH (S/Q) code application to the FZK QUENCH bundle tests. The adaptation of the S/Q code to such kind of calculations is described. The numerical procedure of the recalculation of the temperature test data, and the preparation for the S/Q code input is presented. In particular, the results of the QUENCH-01 and QUENCH-04 test simulations are discussed.

The main attention was paid to the central rod temperature history modeled for every phase of the tests, i.e. from the pre-oxidation up to the flooding, since it strongly influences progression of other processes.

The main results were obtained for the central rod. However, some results such as the hydrogen generation rate and the total hydrogen production were extrapolated to the whole bundle in order to compare the calculations with integral values measured by the mass spectrometer.

Part I:

Experimental and Calculational Results of the QUENCH-04 Test

Contents

List of Tables

List of Figures

Introduction

The most important accident management measure to terminate a severe accident transient in a Light Water Reactor (LWR) is the injection of water to cool the uncovered degraded core. Analysis of the TMI-2 [1] accident and the results of integral out-of-pile (CORA [2, 3]) and in-pile experiments (LOFT [4], PHEBUS, PBF) have shown that before the water succeeds in cooling the fuel pins there could be an enhanced oxidation of the Zircaloy cladding that in turn causes a sharp increase in temperature, hydrogen production and fission product release.

Besides, quenching is considered a worst-case accident scenario regarding hydrogen release to the containment. For in- and ex-vessel safety analyses one has to prove that the hydrogen release rate and total amount do not exceed limits for the considered power plant. The hydrogen generation rate must be known to design appropriately accident mitigation measures for the following reasons.

- Passive autocatalytic recombiners require a minimum hydrogen concentration to start. Moreover, they work slowly, and their surface area and their position in the containment have to be quantified carefully.

- The air-steam-hydrogen mixture in the containment may be combustible for only a short time before detonation limits are reached. This limits the time period during which ignitors can be used.

The physical and chemical phenomena of the hydrogen release are, however, not sufficiently well understood. Presently it is assumed that new metallic surfaces are formed by cracking and fragmentation of the oxygen-embrittled cladding tubes as a result of the thermal shock during flooding leading to enhanced oxidation and hydrogen generation. Consequently, in most of the code systems describing severe fuel damage, the quench phenomena are either not considered or only modeled in a simplified empirical manner.

No models are yet available to predict correctly the thermal-hydraulic or the clad behavior of the quenching processes in the CORA and LOFT LP-FP-2 tests. No experiments have been conducted that are suitable for calibrating the existing models. The increased hydrogen production during quenching cannot be determined on the basis of the available Zircaloy/steam oxidation correlations. An extensive experimental database is needed as a basis for model development and code improvement.

The Forschungszentrum Karlsruhe has therefore started the QUENCH program on the determination of the hydrogen source term. The main objectives of this program are:

- The provision of an extensive experimental database for the development of detailed mechanistic fragmentation models,

- The examination of the physico-chemical behavior of overheated fuel elements under different flooding conditions,

- The provision of an improved understanding of the effects of water injection at different stages of a degraded core,

- The determination of cladding failure criteria, cracking of oxide layers, exposure of new metallic surfaces to steam which are currently supposed to result in renewed temperature escalation and hydrogen production, and

- The determination of the hydrogen source term.

The experimental part of QUENCH program began with small-scale experiments with short Zircaloy fuel rod segments [5, 6]. On the basis of these results well-instrumented large-scale bundle experiments with fuel rod simulators under nearly adiabatic conditions are performed in the QUENCH facility at the Forschungszentrum Karlsruhe. The large-scale bundle experiments are more representative of prototypic reactor accident conditions than are the single-rod experiments. Important parameters of the bundle test program are (see Table I-1): quench medium, i.e. water or steam, fluid injection rate, cladding oxide layer thickness, and the temperature at onset of flooding. The results of the first experiments QUENCH-01, QUENCH-02, and QUENCH-03 are documented in references [7], [8], and [9].

This report consists of two independent parts. Part I describes the test facility together with the test bundle, and the main results of the QUENCH-04 experiment. In addition, one section is dedicated to the calculational support performed with the CALUMO (oxidation) computer code. Part II of the report deals with the results of the SVECHA/QUENCH (S/Q) code application to the QUENCH-01 and QUENCH-04 bundle tests. The adaptation of the S/Q code to such kind of calculations is described.

1 Description of the Test Facility

The QUENCH test facility consists of the following component systems:

- the test section with 21 fuel rod simulators
- the electric power supply for the test bundle heating
- the water and steam supply system
- the argon gas supply system
- the hydrogen measurement devices
- the process control system
- the data acquisition system.

A simplified flow diagram of the QUENCH test facility is given in Fig. I-1, a three-dimensional schematic of the components in Fig. I-2. The main component of the facility is the test section with the test bundle (Figs. I-3 and 4). The superheated steam from the steam generator and superheater together with argon as the carrier gas for the hydrogen detection systems enter the test bundle at the bottom end. The steam that is not consumed, the argon, and the hydrogen produced in the zirconium-steam reaction flow from the bundle outlet through a water-cooled off-gas pipe to the condenser (Figs. I-1 and 2). Here the steam is separated from the non-condensable gases argon and hydrogen. The cooldown phase with steam is initiated by turning off the superheated steam of 3 g/s whereas the argon gas remains unchanged. At the same time saturated steam of 50 g/s is injected at the bottom of the test bundle through the same line.

The design characteristics of the test bundle are given in Table I-2. The test bundle is made up of 21 fuel rod simulators, each with a length of approximately 2.5 m, and of four corner rods (see cross section in Fig. I-5). The fuel rod simulators are held in their positions by five grid spacers, four of Zircaloy, and one of Inconel in the lower bundle zone (Fig. I-6). The cladding of the fuel rod simulators is identical to that used in PWRs with respect to material and dimensions, i.e. Zircaloy-4, 10.75 mm outside diameter, 0.725 mm wall thickness. The rods are filled with a mixture of 95 % argon and 5 % krypton to approx. 0.22 MPa, i.e. a pressure slightly above the system pressure. The gas filling of all rods is realized by a channel-like connection system inside the lower sealing plate. The krypton additive allows to detect fuel rod failure during the experiment with help of the mass spectrometer.

Twenty fuel rod simulators are heated electrically over a length of 1024 mm, the one unheated fuel rod simulator is located in the center of the test bundle. The unheated fuel rod simulator (Fig. I-7) is filled with ZrO_2 pellets (bore size 2.5 mm ID). For the heated rods (Fig. I-6) 6 mm diameter tungsten heating elements are installed in the center of the rods and are surrounded by annular ZrO_2 pellets. The tungsten heaters are connected to electrodes made of molybdenum and copper at each end of the heater. The molybdenum and copper electrodes are joined by high-

frequency/high-temperature brazing performed under vacuum. For electrical insulation the surfaces of both types of electrodes are plasma-coated with 0.2 mm ZrO_2. To protect the copper electrodes and the O-ring-sealed wall penetrations against excessive heat they are water-cooled (lower and upper cooling chamber). The copper electrodes are connected to the DC electric power supply by means of special sliding contacts at the top and bottom. The total heating power available is 70 kW, distributed among the two groups of heated rods with 35 kW each. The first group consists of the inner eight rods (rod numbers 2 – 9), the second group consists of the outer twelve rods (rod numbers 10 – 21). The rod designation can be taken from Fig. I-8.

The four corner positions of the bundle are occupied either by solid zircaloy rods with a diameter of 6 mm or by solid rods (upper part) and Zry tubes (lower part) of ∅ 6 x 0.5 mm for thermocouple instrumentation at the inside (Fig. I-8). The positioning of the four corner rods avoids an atypically large flow cross section at the outer positions and hence helps to obtain a rather uniform radial temperature profile. A solid Zry rod can be pulled out to determine the axial oxide layer thickness at that time.

The lower boundary for the lower cooling chamber is a sealing plate made of stainless steel with plastic inlays for electrical insulation, sealed to the system by O-shaped rings. The upper boundary of the lower cooling chamber is a sealing plate of stainless steel. An insulation plate made of plastic (PEEK) forms the top of the upper cooling chamber, and a sealing plate of Al_2O_3, functioning as a heat-protection shield, is the lower boundary of the upper cooling chamber (see Fig. I-6).

In the region below the upper Al_2O_3 plate the copper electrode is connected firmly to the cladding. This is done by hammering the cladding onto the electrode with a sleeve of boron nitride put between electrode and cladding for electrical insulation. The axial position of the fuel rod simulator in the test bundle is fixed by a groove and a locking ring in the top Cu electrodes. Referred to the test bundle the fixing of the fuel rod simulators is located directly above the upper edge of the upper insulation plate. So, during operation the fuel rod simulators are allowed to expand downwards. Clearance for expansion of the test rods is provided in the region of the lower sealing plate. Also in this region relative movement between cladding and internal heater/electrode can take place.

The test bundle is surrounded by a 2.38 mm thick shroud (80 mm ID) made of Zircaloy with a 37 mm thick ZrO_2 fiber insulation and an annular cooling jacket made of stainless steel (Figs. I-4 and 5). The 6.7 mm annulus of the cooling jacket is cooled by an argon flow. Above the heated zone, i.e. above the 1024 mm elevation there is no ZrO_2 fiber insulation to allow for higher radial heat losses. This region of the cooling jacket is cooled by a water flow (Figs. I-3 and 4). Both the lack of ZrO_2 insulation above the heated region and the water cooling force the axial temperature maximum downward.

2 Test Bundle Assembly

The test section consists of three subassemblies pre-assembled separately. One subassembly comprises the cooling jacket with the bundle head casing; the second subassembly includes the instrumented shroud with the bundle foot; and the third subassembly is composed of the instrumented test bundle with the bundle head. The test bundle and the shroud, including the

respective thermocouples, must be replaced for each experiment. The instrumentation of the bundle head and the foot as well as the cooling jacket, however, remains unchanged.

3 Test Bundle Instrumentation

The test bundle was instrumented with sheathed thermocouples attached to the rod claddings at 17 different elevations between -250 mm and 1350 mm and at different orientations (Figs. I-9 through 11). The elevations of the surface-mounted shroud thermocouples are from -250 mm to 1250 mm. In the lower bundle region, i.e. up to the 550 mm elevation, NiCr/Ni thermocouples (1 mm diameter) are used for temperature measurement of rod cladding and shroud as is illustrated in Fig. I-9. The thermocouples of the hot zone are high-temperature thermocouples with W-5Re/W-26Re wires, HfO_2 insulation, and a duplex sheath of tantalum (internal)/Zircaloy with an outside diameter of 2.1 mm (Fig. I-10). The leads of the thermocouples from -250 mm to 650 mm leave the test section at the bottom whereas the TCs above 650 mm penetrate the test section at the top.

The thermocouple attachment technique for the surface-mounted high-temperature TCs is illustrated in Fig. I-11. The TC tip is held in place by two clamps of zirconium. As these clamps are prone to oxidation and embrittlement in a steam environment an Ir-Rh wire of 0.25 mm diameter is additionally used in the experiments with pre-oxidation. In test bundle QUENCH-04 (without pre-oxidation) there was no wire used for the additional fixing of the TCs.

The designations of the surface-mounted cladding and shroud thermocouples are “TFS” and “TSH”, respectively. The unheated fuel rod simulator of the QUENCH-04 bundle was especially instrumented to provide information on the accuracy of the temperature measurement with externally mounted thermocouples, particularly during cooldown. Therefore, two thermocouples were inserted in the center of the central rod (designation “TCRC”), two thermocouples at the rod cladding inner surface (designation “TCRI”, ∅ 0.5 mm), and two thermocouples at the rod cladding outer surface (designation “TCR”, ∅ 1 mm). These three thermocouple positions were realized at the 350 and 550 mm elevation (see Figs. I-12 and 13).

The wall of the inner tube of the cooling jacket is instrumented between -250 mm and 1150 mm with 22 NiCr/Ni thermocouples (designation “TCI”). Five NiCr/Ni thermocouples are fixed at the outer surface of the outer tube of the cooling jacket (“TCO”). The designation of the thermocouples inside the Zircaloy instrumentation rods (corner positions) is “TIT” (Fig. I-14). Three of the four corner rods of the QUENCH-04 test bundle were instrumented as follows:

- Rod A: W/Re, 2.1 mm diam., Zr/Ta duplex sheath, 950 mm elevation (TIT A/13)
- Rod C: NiCr/Ni, 1 mm diam., stainless steel sheath, 550 mm elevation (TIT C/9)
- Rod D: W/Re, 2.1 mm diam., Zr/Ta duplex sheath, 850 mm elevation (TIT D/12).

A list of the instruments for experiment QUENCH-04 installed in the test section and at the test loop are given in Table I-3.

4 Hydrogen Measurement Devices

The hydrogen is analyzed by three different measurement systems: (1) a Balzers mass spectrometer (MS) “GAM 300” (Fig. I-15) located at the off-gas pipe, approx. 2.7 m downstream from the test section outlet, (2) a hydrogen detection system ”Caldos 7 G” (Fig. I-17), (3) a second MS, both located in a bypass to the off-gas line behind the condenser. The second, simpler mass spectrometer “Prisma” made by Balzers was used for the first time. It was installed close to the Caldos device in a way that the off-gas, i.e. the argon/hydrogen mixture, downstream the condenser passed at first the mass spectrometer “Prisma” and then the Caldos analyzer before it exited to the outside (Figs. I-1 and I-2). Due to their different locations in the facility the mass spectrometer “GAM 300” responds almost immediately (less than 5 s) to a change in the gas composition in the bundle whereas the mass spectrometer “Prisma” and the Caldos device have a delay time of about 20 – 30 s.

Fig. I-16 presents the upgrade of the Caldos system with respect to its delay time. After test QUENCH-03 the void volume of the inlet line of the Caldos system was reduced and an additional pump was added in a bypass to the existing pump. With these modifications the delay time was decreased from 100 s to approx. 20 s.

The mass spectrometer “BALZERS GAM 300“ used is a completely computer-controlled quadrupole MS with an 8 mm rod system which allows quantitative measurement of gas concentrations down to less than 10 ppm. For the MS measurement a sampling tube is inserted in the off-gas pipe (Fig. I-16). It has several holes at different elevations to guarantee that the sampling of the gas to be analyzed is representative. To avoid steam condensation in the gas pipes between the sampling position and the MS the temperature of the gas at the MS inlet is controlled by a heat exchanger to be between 110 °C and 150 °C (the upper operating temperature of the MS inlet valves). This allows the MS to analyze the steam production rate. Besides, the concentrations of the following species were continuously measured by the mass spectrometer during all test phases: argon, hydrogen, steam, nitrogen, oxygen, and krypton. As the fuel rod simulators are filled with krypton as a tracer gas in addition to the argon, i.e. a mixture of argon and 5% krypton, the measurement of krypton can be used as an indicator for a cladding failure. Additionally, the MS is used to control the atmosphere in the facility, e.g., to monitor the gas composition at the beginning of the test.

The temperature and pressure of the analyzed gas are measured near the inlet valve of the MS. The MS is calibrated for hydrogen with well-defined argon/hydrogen mixtures and for steam with mixtures of argon and steam supplied by the steam generator of the QUENCH facility. The MS off-gas is released into the atmosphere because the amount of hydrogen taken out of the system is negligible.

The principle of measurement of the Caldos system is based on the different heat conductivities of different gases. The Caldos device is calibrated for the hydrogen-argon gas mixture. To avoid any moisture in the analyzed gas a gas cooler, which is controlled at 296 K, is connected to the gas analyzer (Fig. I-17). The response time of the gas analyzer is documented by the manufacturer to be 2 s, i.e. a time in which 90 % of the final value should be reached. In contrast to the mass spectrometer the Caldos device only measures the hydrogen content. Gases other than H_2 cannot be analyzed by this system.

For the Caldos device as well as for the MS the hydrogen mass flow rate is calculated by referring the measured H_2 concentration to the known argon mass flow rate according to equation (1):

$$\dot{m}_{H_2} = \frac{M_{H_2}}{M_{Ar}} \cdot \frac{C_{H_2}}{C_{Ar}} \cdot \dot{m}_{Ar} \tag{1}$$

with M representing the molecular masses, C the concentrations in vol-% and $\dot{m}$ the mass flow rates of the corresponding gases.

With an argon-hydrogen (two-component) mixture that in fact exists at the location of the Caldos analyzer equation (1) can be written as follows

$$\dot{m}_{H_2} = \frac{M_{H_2}}{M_{Ar}} \cdot \frac{C_{H_2}}{100 - C_{H_2}} \cdot \dot{m}_{Ar} \tag{2}$$

5 Data Acquisition and Process Control

A computer-based control and data acquisition system is used in the QUENCH facility. Data acquisition, data storage, online visualization as well as process control, control engineering and system protection are accomplished by three computer systems that are linked in a network.

The data acquisition system allows recording of about 200 measurement channels at a maximum frequency of 25 Hz per channel. The experimental data and the date and time of the data acquisition are stored as raw data in binary format. After the experiment the raw data are converted into SI units and stored as ASCII data.

For process control, a system flow chart with the most important actual measurement values is displayed on the computer screen. Furthermore, the operating mode of the active components (pumps, steam generator, superheater, DC power system, valves) is indicated. Blocking systems and limit switches ensure safe plant operation. Operating test phases, e.g. heatup or quenching phases, are pre-programmed and can be started on demand during the experiment. The parameter settings of the control circuits and devices can be modified online.

Online visualization allows to observe and to document the current values of selected measurement positions in the form of tables or plots. Eight diagrams with six curves each can be displayed as graphs. This means that altogether 48 measurement channels can be selected and displayed online during the course of the experiment.

The data of the main data acquisition system and of the mass spectrometers were stored on different computers. Both computers were synchronized by radio-controlled clocks.

The data of the main acquisition system were stored at frequencies of 1 Hz (until 2046 s, i.e. up to approx. 2000 K), and 5 Hz (from 2046 s on), respectively. The mass spectrometer data were recorded at a frequency of 1 Hz during the entire test.

6 Test Conduct and General Results

In the QUENCH-04 experiment the bundle was heated from room temperature to ~900 K in an atmosphere of flowing argon (3 g/s) and steam (3 g/s). The bundle was stabilized at this temperature for about 2 hours, the electrical power being 4.3 kW (see Fig. I-18). The sequence of events is summarized in Table I-4.

At the end of the stabilization period the electrical power was increased from 4.3 kW to a maximum of 16.2 kW (Fig. I-19, top) so that the bundle was ramped at 0.31 W/s per rod giving an average temperature increase of about 0.35 K/s between 900 K and 1400 K and 1.0 K/s between 1400 K and 1750 K (Fig. I-19, bottom).

The coolant temperature at the lower end of the heated zone was ~600 K according to thermocouple TFS 2/1 at -250 mm as can be taken from Fig. I-20. An oxidation excursion started at 750 mm when the temperature there reached 1560 K (Figs. I-24 and I-30). At the 950 mm elevation (Fig. I-32) the heatup rate during the temperature excursion amounted to approx. 6 K/s and at the 850 mm level to above 20 K/s (Figs. I-24, I-25, and I-31). Corner rod B was withdrawn from the bundle at about 2012 s and ~1780 K to check the oxide layer thickness accumulated up to that time ($\leq$ 90 μm with the maximum at ~950 mm). The pre-planned steam cooling sequence was initiated when three rod thermocouples showed a clear temperature excursion. Then the steam flow of 3 g/s was turned off at around 2064 s whereas the argon gas remained unchanged. For cooling the test bundle, steam was injected at the bottom of the test section at a mean rate of 50 g/s for 242 s (F 204 in Fig. I-21, top). During the steam injection the steam temperature at the inlet of the test section changes continuously (T 511: 405 - 580 K) because of initial condensation in cold pipes (Fig. I-20), not used before the cooldown phase, and because of heating up in hot pipes that were used during all previous phases of the test. The injected steam rate resulted in a steam velocity of 15 - 20 m/s (based on a coolant flow channel area of 30 cm^2) and thus a time for flowing through the 1.6 m long test section of around 0.1 s.

In Fig. I-21 the cooldown steam injection (F 204 total input = 11631 g) is compared with the flow measurement F 601 (standard orifice plate, total of 10856 g) and the condensed water level L 701 in the condensate collector both representing the steam output. The L 701 data meet the input data when a delay of 30 s for the onset of cooling, i.e. 2095 s instead of 2065 s, is assumed. The original F 601 data, not shown here, give a zero signal up to the onset of cooling so that one can assume that the sudden increase in the signal is a result of the steam injection. So, with a known density the data can be converted to a mass flow rate. The spike at the onset of steam injection that also shows in Fig. I-21, top, is not real, however. This is because the F 601 instrument is a standard orifice plate in the off-gas pipe and is designed for steady-state flow conditions. The total numbers, however, could be compared to learn if the F 601 data can be used for a steam balance which is of importance in the water injection tests to get information on the steaming rate and water/steam balance, respectively. The steam rate can also be measured with help of the mass spectrometer. The original MS data, however, overestimate the steam flow rate. This is true particularly during the cooldown phase due to the fact that the MS was

calibrated during the stabilization period by applying 3 g/s of steam plus 3 g/s argon. In separate calibration tests with a dummy test section it was realized that a portion of the steam condensed in the off-gas pipe at conditions which generally exist during the stabilization period, i.e. at ~900 K. The steam condensation leads to a wrong calibration factor for the MS steam data. With the test facility at temperature and the steam flow rate elevated during cooldown, the condensation is negligible. Therefore, the MS steam data had to be corrected. They are presented as flow rates and as integral values in Fig. I-22, top and bottom, respectively.

At 2088 s the electrical power was reduced to 4 kW within 15 s, and was shut off at 2302 s (about the time when the cooldown steam was turned off) terminating the experiment.

Different from the quenching experiments with water the steam injection led to immediate cooling of the rods at all levels within one second (Fig. I-25). As is illustrated in Fig. I-26 the cooldown by steam did not result in a precursory cooling phase (observed in the experiments with flooding by water) but led directly to the rapid cooling phase which is comparable to the behavior beyond the onset of quenching after flooding the bundle with water.

The cooling of the shroud occurred at the same time with the exception of the upmost shroud region, i.e. 1050 mm and above, following about 3 - 5 s later. At 1050 mm elevation and above the shroud data in Fig. I-33 show the delay mentioned above but also stronger temperature excursions than those of the test rods which are also presented in Table I-5. At the elevations 1150 mm and 1250 mm the maximum temperatures were measured at the shroud (Table I-6). The development in the heated zone and above can be seen in the axial temperature distribution plots provided for 500 s and 2050 s (transient), 2065 s (onset of cooldown), and 2075 s (cooldown phase, see times selected in Fig. I-35) in Figs. I-36 to I-42. Particularly at 2075 s the shroud temperatures TSH are above the rod temperatures of types TFS 2 and TFS 5 (Fig. I-42). Furthermore, as was observed in the other QUENCH experiments the axial temperature profiles of test rod type 5 (outer coolant channel), i.e. TFS 5, exhibit pronounced temperature fluctuations from one thermocouple level to the next one (Fig. I-37). The temperatures of the inner coolant channel, TFS 2, do not show such strong local effects [8].

According to some TC data of the region 750 - 950 mm the rate of temperature increase slowed down prior to the steam injection (at about 2057 s), but then accelerated again with the beginning of the steam injection. The peak temperature reached 2340 K at the 850 mm elevation (TFS 5/12) before the rapid cooling commenced. The signals of the surface-mounted TCs demonstrated reheating of the rod cladding about 1 s after the peak temperature and the following sharp temperature drop were reached. For the elevations between 750 mm and 1050 mm reheating amounted to 50 - 150 K. In the region from 1150 to 1350 mm up to 600 K could be observed. (It should be noted that this temperature behavior does not present the behavior of the rod but that of the cladding thermocouples which are mounted at the rod outer surface.) After this short reheating smooth cooling resumed. A short pause in the cooling was also observed later, at different times at the 750 mm to 1050 mm elevations. The upper shroud region, i.e. from 1050 mm upwards, experienced a temperature excursion with pronounced local temperature differences in the azimuthal direction (Fig. I-33). The maximum azimuthal temperature difference observed in the 1150 mm elevation was around 500 K for thermocouples TSH 15/0 and TSH 15/180. The maximum temperature rise rate was about 35 K/s at the 1250 mm elevation (TSH 16/0).

A first local rod failure can be indicated by a slow drop in the rod internal pressure P 411 as well as in the sudden increase in the krypton concentration of the off-gas which can be measured by the mass spectrometer. The krypton is an additive of the rod filling gas to be detected at the offgas measurement location upon rod failure. In Fig. I-34, top the P 411 history is given together with the system pressure at the inlet (P 511) and outlet of the test section (P 512), and the krypton concentration in the off-gas. P 411 drops at 2269 s even to a pressure below the system pressure (which is not possible), and the krypton concentration increases rapidly at 2307 s so that a first rod failure could lie between 2269 and 2307 s.

In contast to previous tests, all thermocouples survived the experiment. The main reason for this is certainly that in this experiment without pre-oxidation the thermocouples were not as long exposed to the steam atmosphere at a high temperature as the experiments with pre-oxidation. Thermocouple TFS 5/14 failed prior to the test.

Shroud failure occurred at 2065 s, i.e. at the onset of cooling as is demonstrated in Fig. I-34, bottom. At this time the pressure P 406 measured in the volume between inner cooling jacket and shroud increases for 0.1 bar within 3 s and drops afterwards to the bundle pressure level within around 20 s. The pressure increase could indicate a decrease of the volume by a local ballooning of the shroud as was found to have taken place. The subsequent pressure decrease presents the time of failure, i.e. rupture of the shroud. In addition to the pressure trace the nitrogen concentration measured in the off-gas by the mass spectrometer reflects shroud failure by a first spike that coincides with the pressure drop. Prior to the test the nitrogen as part of the air is still entrained in the void volume of the shroud insulation (ZrO_2 fiber). During heatup the air is released from the insulation into the volume between inner cooling jacket and shroud and enters the test section upon shroud failure. The second spike in the N_2 concentration could indicate a delayed release of air from the pores of the fiber insulation.

The total hydrogen production was determined to be 12 g (11.5 - 12.2 g), with reasonable agreement between the Caldos analyzer and the two mass spectrometers (Fig. I-23). The mass spectrometer “GAM300” data show a very short peak of 0.31 g/s whereas the maximum H_2 rate of the Caldos device and the mass spectrometer “Prisma” resulted in about 0.06 g/s. Less than 1 g of the total H_2 is associated with the cooldown phase. A significant increase in the hydrogen release rate can be observed from 2040 s on, i.e. when temperatures at the 750 and 850 mm elevation escalate (increase more rapidly). So, there seems to exist a correlation between hydrogen release and the temperature of the hot region.

A comparison of the chemical power poduced by the exothermal Zircaloy-steam reaction and the electric bundle power in Fig. I-24, bottom shows that most of the heat generated is due to electrical heating almost during the entire test except for a period of around ten seconds at the end of the transient phase and the beginning of the cooldown phase.

In Fig. I-27 the hydrogen generation as measured by the “GAM300” MS is related to the electric power input, rod temperature at 850 mm (thermocouple TFS 5/12), and cooldown steam injection rate. At the time when the cooldown steam is injected (at 2065 s) the temperature increases to its maximum (2339 K as absolute maximum, TFS 5/12) and hydrogen generation increases significantly as well. The injected steam (single-phase flow) is so effective in cooling the test bundle that the temperature decreases drastically within one second and the hydrogen buildup as well as the temperature excursion is stopped immediately.

7 Temperature Differences across the Rod Cladding

As the cladding thermocouples are externally mounted they do not measure the “real” wall temperature. To account for the deviation of external surface TCs the central rod was equipped at levels 350 mm and 550 mm with TCs on the cladding inner surface and in the rod center in addition to the TCs on the cladding outer surface. The differences of internal and external rod cladding temperatures turned out to be relatively small during the transient in the steam-argon atmosphere (3 g/s + 3 g/s), i.e. at about 2000 s and a temperature of 1100 – 1200 K. The internal TCs “TCRI” and “TCRC” and the pertinent external cladding TCs “TCR” of the central rod resulted in temperature differences of 8 - 30 K during the transient of test QUENCH-04. Figs. I-28 and I-29 give the temperature history of the 350 mm and 550 mm elevation, respectively.

The “onset of cooling” is represented well by external and internal cladding TCs, shroud TCs, and internal corner rod TCs “TIT”. The temperature response of all internal TCs is, however, delayed during cooldown but represents the rod behavior better than the TCs on the cladding outer surface do. Table I-7 provides the onset of cooling for all thermocouples. Differences between external cladding, shroud, and corner rod internal TCs in the times and quenching temperatures as were observed in the water injection experiments [6, 7, 8] do not show up in test QUENCH-04.

8 Posttest Examination

8.1 Sectioning of the Test Bundle

The mould for filling the bundle with epoxy resin was set up vertically. For the encapsulation of the bundle the epoxy system Rütapox 0273 with the hardener designated LC (Epoxy resin and hardener manufactured by Bakelite GmbH, Iserlohn) was used. The epoxy generally shows some heating during the curing stage due to the exothermal reaction. After epoxying the bundle the resin is allowed to harden for a minimum of one week. To obtain the cross sections a saw with a 2.0 mm-thick diamond blade (mean diamond size 138 µm) of 350 mm OD is used to cut the slabs at 1300 rpm. As an overview the sectioning map is given for test bundle QUENCH-04 in Fig. I-46. The exact elevations are listed in Table I-8. During withdrawal of rod No. 19 a downward displacement of the bundle relatively to the shroud occurred. The estimated amount of 70 mm was the basis to compensate the displacement by cutting the test section at pairs of elevations. The designation of the cuts refers to the shroud as e.g. cut No. 3 or to the bundle as e.g. cut No. 3a. From the evaluation of the cross sections the displacement was finally determined to be 50 mm instead of 70 mm. For this reason the elevations available for shroud and bundle differ by 20 mm.

The cross sections that were selected for metallographic examination (see also Table I-8) were polished. For this purpose, the samples were infiltrated by "Araldit" resin to close up residual voids, then ground and polished. The work is performed using a semi-automatic machine with a closed water circuit for grinding and an automatic lubricant feeder for the polishing steps.

8.2 Visual Observation

After the experiment the shroud showed a localized molten zone between ~930 mm and 1000 mm, between 270° and 0° orientation (Figs. I-43 to I-45). The large azimuthal temperature differences at the 1150 mm and 1250 mm elevations with the maximum at the 0° orientation that were observed during the temperature excursion of the upper shroud are not related to the molten zone since the axial levels are different. At the elevation of the once-molten region, ~70 – 80° apart from it, the shroud had deformed with a dent at around 250° orientation. There were generally no signs of significant oxidation on the shroud outer surface. All shroud thermocouples and their clips were intact and still in good contact with the shroud wall.

As was mentioned above the test bundle was found to be positioned approx. 50 mm lower than the shroud. This difference between shroud and bundle is indicated in the photographs of the cross sections (Figs. I-47 through I-55) and in the list of sectioning (Table I-8).

The cross sections (unpolished condition) in Figs. I-47 through I-55 reveal an oval shape of the shroud from ~750 mm upwards. In this region the test rods are considerably bent, lacking sufficient support by the spacer grids which are located at 550 mm and 1050 mm elevation. The ovality of the shroud increases in the upward direction. At around 950 mm two heated rods (Nos. 13 and 14) and corner rod A are found in close contact with the shroud certainly having caused the local burnout of the shroud. Above the grid spacer at the 1050 mm elevation there is no such derangement of the fuel rod simulators. The central rod is missing between ~670 and 895 mm elevation. No melt is observed within the test bundle, however, as to be described below, rod-internal melt formation and relocation occurred. The physico-chemical state of the Zircaloy cladding material was investigated and evaluated by light-optical microscope.

8.3 Microstructural Analysis of Polished Cross Sections

8.3.1 Introductory remarks

Since the lower half of the bundle did not follow the escalation the series of cross sections selected for the detailed microstructural post-test evaluation was restricted to the upper bundle half. The observations gained are presented and discussed in the sequence of elevations from bottom to top.

Of special interest was the determination of the oxide layer thickness on the Zircaloy cladding tubes and the shroud, the formation of through-wall cracks in the cladding tubes and the oxidation of the crack surfaces. Oxidation of the metallic part of the crack surfaces and the steam exposed area of the inner cladding surface could result in an additional generation of hydrogen during flooding, and are thus considered as an item of primary interest.

It is mentioned again that corner rod B, pulled during the test before the final bundle escalation and the quench phase, as well as fuel rod simulator No. 19, removed from the bundle after the test, before embedding into epoxy resin, in order to allow separate analysis of oxidation status and hydrogen uptake, are missing in the prepared cross section slabs.

8.3.2 Bundle elevation 730 mm

The overview (Fig. I-56) shows the fuel rod simulators and the three remaining corner rods at various distances from each other and from the slightly oval shroud with the externally attached thermocouples. The status of the rods with respect to oxidation is demonstrated by Fig. I-57. The indicated regular growth of ZrO_2 scale and α-Zr(O) layer on the β-Zr matrix corresponds to usual observations. The embrittlement of the α-Zr(O) layer gave rise to some mechanical failure, cracking and loss of fragments, which occurred during cool-down or during metallographic preparation procedures. Those features can be easily distinguished from damage, arising during the hot test phase, which have not been observed at that elevation. The only slightly thicker scale of the central rod compared to a rod of the second row is the consequence of the rather flat lateral temperature distribution across the bundle that existed throughout the experiment.

8.3.3 Bundle elevation 830 mm

The overview illustrates the shroud ovality and the increased rod displacements at that elevation, which, however, did not result in rod contacts (Fig. I-58). Detectable temperature variations from rod to rod can be deduced from their oxide scale morphology (Fig. I-59): Since mainly the peak temperatures influence the microstructure, observed after cool-down, it is possible for the compared two rods to deduce the stated temperature indications, being related to the allotropic oxide phase transformation from tetragonal to cubic ZrO_2 at 1800 K. (Above this lower boundary for the stability of cubic ZrO_2 this phase co-exists as internal sub-layer together with the tetragonal external one up to the - not well known - stability limit of the latter modification (2400 - 2600 K). Decomposition of the cubic phase during cool-down results in the α-Zr(O) precipitation at grain boundaries of the previously homogeneous sub-scale.) The peak temperature variation corresponds to a minor scale thickness variation for the compared positions of the two rods.

Fig. I-60 illustrates the reliable performance of the thermocouples. The TC duplex sheath, consisting of an external, now partly oxidised zircaloy (Zry) layer and an internal tantalum layer has survived in its function. Moreover, the TC fixing procedure, to use Zr strips and to spot-weld them as clamps to the rod, is shown as a reliable method. When the clamp itself is already consumed by oxidation the spot welds are still intact. Up to then a TC detachment from the contact position has been prevented.

8.3.4 Bundle elevation 930 mm

The overview of this cross section (Fig. I-61) shows the loss of the central rod due to fragmentation and relocation of the fragments. Approaching the hot zone, this damage and the fractures of most of the other rods were expected for that elevation. The annular pellet of rod No. 3 was lost during preparation. The corner rods are massive at the given elevation. The still protective character of the oxide scale of the rods is illustrated by Fig. I-62. Both rods and the shroud have seen peak temperatures above 1800 K at the given positions, according to the indications described above. The scale microstructure of the two rods shows a comparable self-healing of a scale crack during enhanced thickening at the “weak” position. So the obviously less sub-stoichiometric and therefore brittle scale was repaired during cooling from peak temperature. This occurred in spite of the obvious embrittlement (grain cleavage and boundary de-cohesion) of the metallic matrix. In addressing the temperature measurement procedure with Fig. I-63 and

referring to elevation 830 mm the complete conversion of the clamp is noticed again. The relative protection of the cladding against oxidation below the clamp welding spots and the thermocouple itself are mentioned in addition.

Moving to the further observed rod degradation mechanism “melt formation and relocation” the description of the rod behaviour is illustrated by Fig. I-64 and Fig. I-65. In accordance with the Zr-O phase diagram (understood as modified to be representative for Zry) the temperature range to expect melting of an already heavily oxidised cladding is ca. 2100 K (Zr-type melt). In Fig. I-64 this temperature level corresponds to the top micrograph (from rod No. 5), which shows the void from relocated melt to be surrounded by the most oxygen-poor α-Zr matrix zone. Since the melting temperature increases with the oxygen content in the metal, outward spreading of the melt pool was not possible. Inward spreading towards the ZrO_2 pellet was as well prevented after the oxygen pick-up during solid state contact. The excellent simulation quality of the pellet material to replace UO_2 in this respect is stressed. The central micrograph of Fig. I-64 does not indicate a previous pellet interaction in the above mentioned sense. Alternatively it could be argued that the temperature was considerably higher. However, the range corresponding to (Zr,O)-type melt, ca. 2400 K, was clearly not reached. Correspondingly, the temperature of the third position illustrated in this figure was the highest during the observed melt relocation. (To avoid confusion it is mentioned that continued oxidation, related with additional oxygen uptake would have stabilised the status of partially non-molten cladding, even if the temperature would have increased slowly enough. This item limits to some degree the potential of temperature indications.) Coarse fragmentation at the discussed rods occurred late in the experiment, as indicated by the absence of internal steam oxidation.

In contrast, internal steam oxidation is shown in Fig. I-65. At the remaining cladding half-shell of rod No. 6 a thick steam-grown internal scale is visible. Steam ingress might have occurred quite early, since this scale acted as part of the “crucible”, which retained, and even collected melt. The left of the micrographs below seems to indicate disintegration of re-solidified metallic material by tearing under oxidation-related (scale growth related) stress, resulting in void formation. At the other position of the same melt pool, see the micrograph to the right, continued melt oxidation is related to the observed precipitation of a ceramic phase from the somewhat porous metallic matrix.

8.3.5 Bundle elevation 945 mm

Only 15 mm higher than the above reported cross section many similarities to the described behaviour show up at this elevation, presented as overview in Fig. I-66. In the further example for the thermocouple status, given in Fig. I-67 the Zry part of the duplex TC sheath is seen almost converted, the contact to the rod stabilised by formation of a scale-protected metallic neck, but somewhat impaired by internal melt relocation. Fig. I-68 documents for two rods again the retarded oxidation at azimuthal positions where thermocouples have shielded the steam supply to some extent (compare to Fig. I-63, upper left micrograph).

The further behaviour has been reported before as well. Despite the slightly higher temperature at this elevation no additional phenomena occurred. With respect to the rod-internal pellet/cladding interaction Fig. I-69 stresses the variable observations as a function of the occurrence and intensity of solid-state contact. A full range of conditions compares to the resulting range from non-detectable interaction to interaction layer formation. Accompanying

mechanisms as metal separation under tearing force (upper, left micrograph) and cladding fragmentation (rod No. 9) took place, but steam ingress did not occur at the given positions at temperatures relevant for internal steam oxidation.

In contrast, the latter case was pronounced in the example depicted in Fig. I-70. One can notice that, even if steam succeeds to penetrate into a rod, it will not necessarily reach the opposite side (or adjacent elevations), if it is locally consumed, hindered by consumption within narrow gaps, or blocked by the resulting gap closure. (The detail of a local detachment of a scale from the corresponding α-Zr(O) matrix, shown in the lower micrograph of Fig. I-70, deserves to be mentioned as rare observation.)

Due to bundle manipulation after the test a downward displacement of the bundle by ~50 mm relative to the shroud occurred, as already mentioned. This is why e.g. in Fig. I-66, showing the bundle overview, not the corresponding shroud position is visible. Dedicated additional cuts were prepared to show the shroud in elevations corresponding to the studied bundle elevations. However, due to the fact that the real displacement was determined after cutting, absolutely comparable shroud elevations are not available. Despite this fact, Fig. I-71, showing the shroud at 965 mm is discussed here in comparison with the bundle status at 945 mm elevation.

Only the damaged side of the otherwise intact shroud is depicted. The sequence of events can be identified as follows: At that orientation a hot spot must have developed, weakening the material sufficiently to respond to hoop stress by tensile yielding. The plausible influence of the heated rods Nos. 13 and 14 and the corner rod A, which came into close contact with the shroud, have been mentioned in section 8.2. This deformation must have continued after formation of some rupture opening, through which steam could escape and oxidise the external shroud surface in the neighbourhood of the crack. Fig. I-71 indicates this scenario by showing areas with thicker scale, and crack surfaces in deformation-related, finally broadened form, carrying much thinner scale, both directly connected. This oxidation behaviour during deformation has been extensively studied in the past by several working groups with respect to bundle blockage formation, which was caused by fuel rod ballooning. It results from the strong tendency of oxidising Zry to localised deformation at scale cracks. The absence of similar features at the very thick internal oxide layer of the shroud might indicate, that only the compressive growth stress in this scale was relieved, which is speculated to have contributed to the observed shroud deformation (in addition to the heating from the bundle, which is assumed to be the primary reason). The melt droplet shown in the lower micrograph of Fig. I-71, presumably shroud matrix material, demonstrates localised shroud melting at the hot spot.

8.3.6 Bundle elevation 960 mm

The bundle overview, presented in Fig. I-72 does not provide further interesting details, besides the important fact that the central rod remained at place at that elevation. Fig. I-73 documents the absence of through-wall crack oxidation for the given two positions, despite the rather high temperatures reached in the experiment. Crack surface oxidation, one major quench effect observed for the pre-oxidised QUENCH-01 bundle, can have played only a very limited role for QUENCH-04, according to the whole post-test examination.

Fig. I-74 is dedicated to clad melting and internal melt relocation, as illustrated for two rods to have occurred with distinct and common morphological features. The frequently observed interaction of pellet and cladding at positions of solid-state contact leads to oxygen transfer through an interaction layer into the cladding. This process is therefore able to retard melting of the thus stabilised cladding. In contrast, cladding at adjacent positions, separated by a gap from the pellet, melts earlier, beginning at the internal surface. After rod-internal relocation of Zr-type melt the thinned non-molten cladding shell residue stays at place, mechanically stabilised by its scale.

Fig. I-75 illustrates previously molten cladding material, which, confined between the pellet and, on the opposite side, a solid α-Zr(O) layer and the external scale, remained at place. Thus, this melt was able to pick up oxygen from the pellet to convert to the (Zr,O)-type. During a subsequent temperature decrease ZrO_2 phase precipitation began already in the still molten state, as deduced from the orientation correlation of the precipitate distribution, the dendritic growth, clearly observed in the lower micrograph of Fig. I-75. With the decreasing oxygen solubility of the α-Zr(O) phase further nucleation and growth of ZrO_2 precipitates will have taken place in the re-solidified matrix. During all this evolution the external α-Zr(O) phase layer remained solid, as deduced from the few precipitates dispersed therein.

Fig. I-76 depicts a rod position after a distinctly different history. Here, rounded voids resulting from melt relocation as above described, got exposed to steam. A massive scale on this interior surface confined the residual metallic cladding as a “melt crucible” and thus kept it during a homogenisation of the dissolved oxygen and a precipitation period for ZrO_2.

After the discussion of these features of generally observed behaviour some special items are mentioned. Fig. I-77 documents the rarely observed event of scale detachment from the cladding matrix, in this example a local effect related to bending forces, as seen in comparison with the adherent scale at the opposite side of the rod. Such phenomena cannot give rise to more than negligible contributions to potential quenching responses of the hydrogen signal as a result of quench-related exposure of non-oxidised metallic surfaces. They are thus only weak forms of the originally anticipated spalling phenomenon, which seems to be not realistic, as it was not observed in the test program up to now.

Repeatedly, the status of thermocouples is illustrated (Fig. I-78). Besides a TC from the outermost rod category with partially oxidised Zry sheath (top micrograph), void formation by melt relocation from a neck between a TC and the cladding, followed by steam oxidation of the clad via this leak is depicted (central micrograph, compare to Fig. I-67, upper pictures). Finally, the lower photo shows non-oxidised TC sheaths on the external side of the shroud, not far from the position of the shroud penetration failure to be reported next.

At the elevation of 980 mm, referred to the shroud, this local damage is identified to consist of shroud melting, melt release outward and re-solidification of porous melt (Fig. I-79). A thin shell of internal scale only remained in this region, whereas the shroud is bent but otherwise fully intact along most of its circumference. Fig. I-80 gives details on the morphology of the shroud melt at higher magnification: It shows closed porosity, variable pore fraction, crack and fragment formation from forces during re-solidification, ZrO_2 phase precipitation in relation to the variable oxygen content and scales as function of position with respect to the steam exposure.

8.3.7 Bundle elevation 1130 mm

At this elevation the bundle consists of the central pellet-filled rod and the massive molybdenum electrodes of the heated rods inside the Zry claddings, arranged in the Zry spacer grid (Fig. I-81). In closer view the regular steam-grown external ZrO_2 scale of the cladding and the ZrO_2 plasma coating layer on the Mo electrodes, serving as interaction barrier and electric insulation, are presented in Fig. I-82.

The oxidation of the spacer grid is shown in Fig. I-83 to differ from that of the rod cladding with respect to thickness and morphology. Especially splitting of the scale at the sharp edges of the spacer structure and the resulting faster inward penetration of scale, thus rounding the edges, is a clear indication of breakaway-related scale growth:

The so-called breakaway effect is well-known as a kinetic transition from regular growth of scale with diminishing rate (parabolic or cubic pre-transition kinetics) to accelerated linear rate (post-transition kinetics) occurring beyond a certain critical scale thickness. The primary reasons, still discussed in the literature with respect to details, are changes in microstructure and cohesive strength of the scale, followed by cracking and thus sudden degradation of its protective effect [10]. As the occurrence of the breakaway is only known up to ca. 1050 °C, the spacer structure is concluded to have remained at or below that level in the test, however to have gained a considerably thick scale during a period of linear-rate oxidation. In contrast, the claddings of the rods, assumed to have been hotter, were oxidised with steadily decreasing and thus finally lower rate.

As already reported in section 6, the shroud failure had been detected from pressure signals in coincidence with the detection of traces of nitrogen by the mass spectrometer. This nitrogen indicated traces of air previously entrained in the void volume of the ZrO_2 fibre material of the shroud insulation. Those observations are mentioned in the present context since air oxidation is known to give rise to quite similar microstructural features of scale growth as the steam-specific breakaway effect. Especially the observed edge splitting of the scale is characteristic for air oxidation as well. However, the pre-oxidation in steam would have protected the Zircaloy from air ingress influence where the scales remained intact. Further, a massive influence of traces of air has not yet been proved for similar conditions. It is concluded that the interference of nitrogen, though speculative, cannot be ruled out to be considered among other possible explanations for observed special oxidation phenomena and unexpected temperature excursions.

8.3.8 Lateral and axial oxidation profiles

The oxide scale thickness of each rod and of the shroud was measured in four azimuthal directions when it was possible. The results of bundle (shroud) elevations 730 (750), 830 (850), 930 (950), 945 (965), 960 (980), and 1130 (1150) mm are given in Figs. I-84 through I-89. At the 730 (750) mm elevation the scale thickness is relatively uniform. (A delayed heat-up of the massive corner rod would explain its marginally thinner scale.) The thermocouple traces, indicating escalation at this elevation are not supported by the post-test examination. Plausible is the assumption of thermocouple escalation de-coupled from the corresponding rod. At 830 (850) mm the observations are similar for a higher scale thickness level, being in accordance with TC measurement results. The following three elevations in close axial sequence can be addressed

together: Larger temperature differences must have occurred in the bundle corresponding to the determined range of scale thickness. Often the scale thickness can be traced better in the axial than in the lateral direction, i.e. relatively cooler rods can be distinguished from relatively hotter ones. The extent of oxidation as well as the microstructural observations are in agreement with the thermocouple readings.

Rod No. 19, in a condition to allow to be withdrawn from the bundle prior to the encapsulation, reveals a moderate oxidation between the ~600 and 1100 mm level with a maximum of 170 μm at ~950 mm elevation (Fig. I-90). The profile is compared to that of corner rod B, withdrawn during the test, which indicates the interim peak level of only ~80 μm at the same elevation. The axial distributions of the oxide layer thickness of heated rods, central rod, corner rods, and of rod No.19 can be taken from Fig. I-91.

8.4 Hydrogen Absorption by Zircaloy

The hydrogen absorbed in the remaining Zircaloy-4 metal was analyzed by hot extraction in the so-called LAVA facility, which is an inductively heated furnace coupled to a mass spectrometer. Two-centimeter long cladding segments taken from the rod cladding No. 19 and corner rod B were heated for 20 minutes to some 1800 K under a well-defined argon flow. The hydrogen released was measured by the mass spectrometer.

The axial profile of the hydrogen absorbed in the remaining Zircaloy-4 metal of rod cladding No. 19 and of corner rod B is plotted in Fig. I-92. The peak values are very small for both specimens, only about 0.1 at% between 700 and 1200 mm. (For comparison: 5 and 20 at% as peak values for specimens of test bundles QUENCH-01 and QUENCH-02, respectively.) Extrapolation of these data results in around 0.1 g for the entire QUENCH-04 bundle. The small amount of the hydrogen absorbed corresponds to the results obtained from the separate-effects tests with single pins. Those have shown a clear correlation between the formation and the oxidation of through-walls cracks for oxide scale thicknesses of > 200 μm and temperatures at the onset of cooldown of < 1800 K on one hand and the degree of hydrogen absorption by the remaining Zr(O) metal phases on the other hand [5, 6]. Obviously, the conditions for enhanced hydrogen pickup did not exist for the whole bundle length. Either the temperature at the onset of cooldown was too high (800 – 1050 mm) or/and the oxide scale was too thin at elevations apart from the hot region.

8.5 Summary

A lot of information could be deduced from the above documented post-test examination of the bundle and the accompanying measurements and analyses. Helpful for the description and the phenomenological interpretation or discussing argumentation was the fact that the bundle responded quickly to the fast cool-down with steam and thus retained the status at temperature as far as physico-chemically and mechanically possible.

Growth of regular, protective oxide scale with even self-healing tendencies proceeds according to the pronounced axial temperature profile along the bundle. Internal cladding interaction with the ZrO_2 pellets in dependence of contact develops with good simulation quality for UO_2 pellets. Depending on the resulting through-wall oxygen profile melting of the cladding can occur. Melt spreading or rod-internal melt relocation is determined by the further development of temperature

together with the oxidation process. Oxide scale morphology and melting indicate temperature levels above 1800 K and 2100 K, respectively.

Scale de-lamination or spalling processes play an unimportant role. Through-wall cracking of strongly oxidised cladding exposes the crack surfaces and the internal surfaces only near to the steam ingress positions, since the steam consumption limits its distribution. Strong internal steam oxidation tends to confine residual metallic melt by crucible formation and thus tends to prevent melt relocation in the flow channels. Characteristic features of melt oxidation can be studied under such conditions. As melt gets only locally exposed to steam during cooldown, no corresponding hydrogen signal is observed. Late crack formation at relatively low temperatures plays a major role in determining the final bundle status, as deduced from the typically observed absence of crack surface oxidation.

In general the thermocouple instrumentation is found in sufficiently good condition to have given reliable recordings. This holds especially for the oxidation status of the duplex sheath and the clamp fixing procedure. However, the contact between the TC and the surface of the wall is often examined as weakened. Arguments for discussion of possible improvements or erroneous readings are the oxidative consumption of the thin clamps (detachment risk) and the possibility of sheath-oxidation related excursion in de-coupled status.

The shroud failure is discussed to have resulted from overheating by close rods, tearing under oxidation-related hoop stress, leak formation and steam leakage, continued deformation during external oxidation, melt formation and oxidation. However, a clear understanding is not claimed. A further observation to be discussed is the unusual oxidation morphology of the upper spacer.

9 Calculational Support

9.1 Investigation of the oxidation behavior with the FZK code CALUMO

The code CALUMO has recently been developed as a tool for the analysis of temperature transients in FZK QUENCH tests [11]. It is based on the application of lumped parameter equations for the enthalpy of the fuel rods, the shroud, and the coolant. Its main aim is the investigation of the oxidation behavior of the fuel rod claddings and the shroud, as well as the hydrogen production.

In order to validate the code, calculations have been done for the QUENCH-03 and QUENCH-04 experiments [11].

A key parameter in calculating the bundle temperature is the kind of oxidation correlation used. In a first set of calculations the correlations of Leistikow et al. [12] were taken for temperatures below 1783 K and those of Prater/Courtright [13] were taken for temperatures above 1783 K. This was defined the base case. In scoping calculations for QUENCH-03 [12] it became evident that this choice of correlations did not provide a satisfying agreement with the experimental results. Therefore a second set of calculations was performed with the correlations of Leistikow for the whole temperature range. This was defined the low-oxidation case. Some of the results for the QUENCH-04 test concerning the low-oxidation case are to be seen in Figs. I-93 to I-98.

As QUENCH-04 is a test with steam cooldown the capabilities of the CALUMO code are sufficient to recalculate the whole test, starting at the end of the steady-state period, i.e. at 115 s. In Figs. I-93 and I-94 a comparison of measured and calculated temperature evolutions at six axial nodes is shown. The overall tendencies of the measured temperature evolutions are, in general, reproduced by the calculation.

At level 13 the agreement between measurement and calculation is rather good whereas at the other locations some discrepancies can be observed. In the second half of the transient the calculated temperature increase rates are high, especially in the central part of the test section (plane 7 to 11) whereas they are underestimated in the upper part (plane 15). The temperature escalation of some fuel rods at plane 11 is not reproduced by the code. A similar escalation was observed in QUENCH-03 [8]. There it could have been caused by bending of some test rods as became evident by the post-test examination leading to a non-uniform heat transfer. Such a displacement of test rods, however, was not found in the QUENCH-04 bundle.

Temperature escalations in the upper part of the shroud were observed in all FZK QUENCH tests conducted up to now measured by the thermocouples located in the argon-filled annulus above the 1024 mm elevation. It is known that the stability of the heat conduction regime is lost in large void volumes at a critical Grashof number [14] and that convective processes in the gas-filled volume set in. According to the critical Grashof number this natural convection in the Ar-filled volume is considered to exist at the begin of the temperature escalations at the shroud and to be responsible for transporting heat from the top of the heated zone upwards in axial direction.

The results shown in Figs. I-95 to I-96 concern the oxidation process of the rod claddings and the shroud. As a consequence of the oxidation, the absorption of oxygen leads to a reduction of the steam flow in the coolant channel (see Fig. I-95) and to a release of hydrogen (see Fig. I-96).

The maximum hydrogen production rate, as calculated by the code is nearly 0.1 g/s (see Fig. I-96) and the overall produced hydrogen of about 18 g is about 30 % higher than the experimental value of around 12 g. The calculated maximum value of the hydrogen production rate is distinctly below the maximum value measured by the mass spectrometer (0.3 – 0.4 g/s). If the difference in the maximum production rates can be attributed to a quenching effect which is not yet modeled in the code, for example crack formation in the oxide scales, is not clear at present.

A very important result of the code concerns the oxide scales thickness of the rods (Fig. I-97; dox = oxide scales of the inner cluster, doxa = oxide scale of the outer row) and the shroud (doxsh). At 2200 s into the transient the temperatures are again rather low and the calculated axial distributions are representative for the end of the test and can therefore be compared to the findings of the PTE. Fortunately, in QUENCH-04 the rods and the shroud remained fairly intact so that a comparison between measured and calculated values is possible.

The experimental values of the oxide layer thickness at different cross sections scatter considerably, due to azimuthal and radial temperature differences. The higher the temperature has become at a certain axial position the higher are the temperature differences. Thus, at 950 mm the scatter of experimental values is rather high (110 – 355 μm). Disregarding the corner rods the data band is a bit smaller (185 – 355 μm).

The overall features of the experimental values are reproduced by the code, although in details there are considerable discrepancies. The maximum calculated oxide scale thickness is distinctly lower (260 μm) than the value determined by the PTE (350 μm).

At 750 and 850 mm the calculated values are rather high compared to the rather low measured values of the oxide scale thickness. But as temperature escalations have been detected by the thermocouples at these axial positions, the discrepancy between different experimental results, i.e. temperature vs. oxide scale thickness measurements, is to be resolved as well.

Thus, for 750 mm and 850 mm elevation the measured temperature curves have been input into the code LUMPY1. This code is able to calculate the evolution of the oxide layer thickness based on a known temperature evolution, using experimental correlations for the oxidation. The calculation was performed for the base case and the low oxidation case (see Fig. I-98). The main result of this study with the LUMPY1 code is contained in Table I-9. For the base case nearly 250 μm and for the low-oxidation case about 120 μm were obtained for the oxide scale at 750 mm elevation. This is considerably higher than the experimental values (about 50 μm). Disregarding the temperature excursion a rather good agreement between measurement and calculated values of the oxide scale thickness is obtained. Nevertheless, the effect of the temperature excursion is much less important at 850 mm compared to the 750 mm level.

A general question is whether correlations obtained from steady-state conditions can be applied to transient conditions without modification. It seems that there is no such problem with slow transients but with steep transients as there is at 750 mm. It looks as if the temperature escalation has no impact on the oxidation rates. Using the low temperature increase rates one would have calculated a value of about 50 μm which is in accordance with the experimental findings.

It appears that the sensitivity of the oxidation rates on temperature escalations depends on the temperature which has been reached at the onset of the escalation. If the temperature is already sufficiently high, the temperature escalation has an impact and steady-state correlations can be applied. The question about the applicability of steady-state oxidation correlations under transient conditions is a generic issue.

References

[1] J.M. Broughton, P. Kuan, and D.A. Petti, “A Scenario of the Three Mile Island Unit 2 Accident,” Nuclear Technology, 87, 34, 1989.

[2] P. Hofmann, S. Hagen, V. Noack, G. Schanz, L. Sepold, “Chemical-Physical Behavior of Light Water Reactor Core Components Tested under Severe Reactor Accident Conditions in the CORA Facility,” Nuclear Technology, vol. 118, 1997, p. 200.

[3] S. Hagen, P. Hofmann, V. Noack, L. Sepold, G. Schanz, G. Schumacher, “Comparison of the Quench Experiments CORA-12, CORA-13, CORA-17,” FZKA 5679, Forschungszentrum Karlsruhe, 1996.

[4] R.R. Hobbins and G.D. McPherson, “A Summary of Results from the LOFT LP-FP-2 Test and Their Relationship to Other Studies at the Power Burst Facility and of the Three Mile Island Unit 2 Accident,” OECD/LOFT Final Event, ISBN 92-64-03339-4, 1991.

[5] P. Hofmann, V. Noack, M.S. Veshchunov, A.V. Berdyshev, L.V. Matweev, A.V. Palagin, V.E. Shestak: “Physico-Chemical Behavior of Zircaloy Fuel Rod Cladding Tubes During LWR Severe Accident Reflood,” FZKA 5846, Forschungszentrum Karlsruhe, 1997

[6] P. Hofmann, A. Miassoedov, L. Steinbock, M. Steinbrück, M. Veshchunov et al.: “Quench Behavior of Zircaloy Fuel Rod Cladding Tubes. Small-Scale Experiments and Modeling of the Quench Phenomena,” FZKA 6208, Forschungszentrum Karlsruhe, 1999

[7] P. Hofmann, W. Hering, C. Homann, W. Leiling, A. Miassoedov, D. Piel, L. Schmidt, L. Sepold, M. Steinbrück, “QUENCH-01, Experimental and Calculational Results,” FZKA 6100, Forschungszentrum Karlsruhe, 1998.

[8] P. Hofmann, C. Homann, W. Leiling, A. Miassoedov, D. Piel, G. Schanz, L. Schmidt, L. Sepold, M. Steinbrück, “Experimental and Calculational Results of the Experiments QUENCH-02 and QUENCH-03,” FZKA 6295, Forschungszentrum Karlsruhe, 2000.

[9] L. Sepold, P. Hofmann, W. Leiling, A. Miassoedov, D. Piel, L. Schmidt, , M. Steinbrück, “Reflooding Experiments with LWR-Type Fuel Rod Simulators in the QUENCH Facility,” Nuclear Engineering and Design 204 (2001), 205 - 220.

[10] G. Schanz, S. Leistikow, “Microstructural reasons for mechanical oxide degradation (breakaway effect) and resulting kinetical anomalies of zircaloy-4/steam high-temperature oxidation,” 8th International Congress on Metallic Corrosion (8th ICMC), Mainz, Sept. 6-11, 1981. Proc. DECHEMA, Frankfurt, FRG, 1981, Vol. 2, 1712-1717.

[11] H. Steiner, M. Heck, “The code CALUMO, a tool for the analysis of temperature transients in QUENCH tests,” FZKA 6501, 2000.

[12] S. Leistikow, et al, “Kinetik und Morphologie der isothermen Dampfoxidation von Zircaloy-4 bei 700 bis 1300 °C,” KFK 2587, 1978.

[13] J.T. Prater, E.L.Courtright, “Oxidation of Zircaloy-4 in Steam at 1300 to 2400 °C,” Zirconium in the Nuclear Industry: Seventh International Symposium, ASTM STP 939, R.B. Adamson and L.F.P. Van Swam, Eds., American Nuclear Society for Testing and Materials, Philadelphia, 1987, pp. 489-503.

[14] G. Choi and S.T. Korpela, “Stability of the Conduction Regime of Natural Convection in a Tall Vertical Annulus,” J. Fluid Mech. 99, 1980, pp. 725 – 738.

Acknowledgements

Experiment QUENCH-04 was part of the cooperation with the German nuclear industry, co-financed by Siemens/KWU and the German utilities under the leadership of EnBW and RWE.

At the Karlsruhe Research Center the broad support needed for preparation, execution, and evaluation of the experiment is gratefully acknowledged. In particular, the authors would like to thank Messrs. L. Anselment and S. Horn for the assembly of the heated test rods and for the instrumentation of the central rod, Messrs. J. Moch and R. Vouriot for assembling and instrumenting the test bundle, Mr. S. Horn for the preparation of the hydrogen measurement with the “Caldos” analyzer and the support for the test data selection. Furthermore, the authors would like to express their gratitude to Dr. W. Krauss for the hydrogen measurement with the “Prisma” mass spectrometer, to Mr. L. Anselment for sectioning the epoxied bundle and polishing the metallographic samples, to Mrs. J. Laier and Mrs. I. Werner for processing the test data, and to Mrs. M. Heck for processing the results of the metallographic examination.

Table I-1: QUENCH Test Matrix

Test	Quench medium	Flooding rate[1)]	Heat-up rate	Max. ZrO_2 layer thickness[2)]	Temp. at onset of flooding[3)]	Remarks, objectives	Date of test conduct
QUENCH-00	Water	2.8 cm/s from bottom	1.0 K/s	≈ 500 µm	≈ 1800 K	COBE Project:; commissioning tests.	Oct. 9 - 16, 97
QUENCH-01	Water	1.6 cm/s; from the bottom	0.5 K/s	≈ 300 µm	≈ 1900 K	COBE Project:; partial fragmentation of pre-oxidized cladding.	February 26, 98
QUENCH-02	Water	1.6 cm/s; from the bottom	0.5 K/s	completely oxidized	> 2400 K	COBE Project:; no additional pre-oxidation; quenching from high temperatures.	July 7, 98
QUENCH-03	Water	1.4 cm/s from the bottom	0.6 K/s	completely oxidized	> 2400 K	No additional pre-oxidation, quenching from high temperatures.	January 20, 99
QUENCH-04	Steam	≈ 50 g/s; from the bottom	0.5 K/s	≈ 170 µm	≈ 2300 K	Cool-down behavior of slightly pre-oxidized cladding by cold steam injection.	June 30, 99
QUENCH-05	Steam	≈ 50 g/s from the bottom	0.5 K/s	≈ 400 µm	≈ 2300 K	Cool-down behavior of pre-oxidized cladding by cold steam injection.	March 29, 2000
QUENCH-06	Water	1.4 cm/s from the bottom	0.5 K/s	≈ 660 µm	≈ 2300 K	OECD-ISP 45; prediction of H_2 source term by different code systems.	December, 13 2000
QUENCH-07	Steam	≈ 15 g/s from the bottom	0.5 K/s	Not yet determined	> 2300 K	COLOSS Project; impact of B_4C absorber rod failure on H_2, CO, CO_2, and CH_4 generation.	July 25, 2001

[1)] Flooding rate for water: rise of the water level at the -250 mm bundle elevation (single-phase flow).
[2)] Measured posttest at the bundle elevation of max. temperature.
[3)] Maximum measured or estimated temperature in test section

Revised: January, 2002

Table I-2: Design characteristics of the QUENCH test bundle

Bundle type		PWR
Bundle size		21 rods
Number of heated rods		20
Number of unheated rods		1
Pitch		14.3 mm
Rod outside diameter		10.75 mm
Cladding material		Zircaloy-4
Cladding thickness		0.725 mm
Rod length	heated rod (levels) unheated rod (levels)	2480 mm (-690 mm to 1790 mm) 2842 mm (-827 mm to 2015 mm, incl. extension piece)
Heater material		Tungsten (W)
Heater length		1024 mm
Heater diameter		6 mm
Annular pellet	heated rod unheated rod	ZrO_2; ∅ 9.15/6.15 mm; L=11 mm ZrO_2; ∅ 9.15/2.5 mm; L=11 mm
Pellet stack	heated rod unheated rod	0 mm to 1024 mm 0 mm to 1553 mm
Grid spacer	material length location of lower edge	Zircaloy-4, Inconel 718 Zry 42 mm, Inc 38 mm -200 mm Inconel 50 mm Zircaloy-4 550 mm Zircaloy-4 1050 mm Zircaloy-4 1410 mm Zircaloy-4
Shroud	material wall thickness outside diameter length (extension)	Zircaloy-4 2.38 mm 84.76 mm 1600 mm (-300 mm to 1300 mm)
Shroud insulation	material insulation thickness elevation	ZrO_2 fiber ~ 37 mm -300 mm to ~ 1000 mm
Molybdenum-copper electrodes: length of upper electrodes length of lower electrodes diameter of electrodes: - prior to coating - after coating with ZrO_2		 766 mm (576 Mo, 190 mm Cu) 690 mm (300 Mo, 390 mm Cu) 8.6 mm 9.0 mm
Cooling jacket	material inner tube outer tube	1.4541 stainless steel ∅ 158.3 / 168.3 mm ∅ 181.7 / 193.7 mm

12/98

Table I-3: List of instrumentation for the QUENCH-04 Test 07.07.99

Chan-nel	Designation	Instrument, location	Output in
1	TFS 2/11	TC (W/Re) fuel rod simulator 8 (type 2), 750 mm, 135°	K
2	TFS 2/13	TC (W/Re) fuel rod simulator 2 (type 2), 950 mm, 225°	K
3	TFS 2/15	TC (W/Re) fuel rod simulator 4 (type 2), 1150 mm, 315°	K
4	TFS 2/17	TC (W/Re) fuel rod simulator 6 (type 2), 1350 mm, 455°	K
5	TSH 15/180	TC (W/Re)) shroud outer surface, 1150 mm, 180°	K
6	TFS 3/10	TC (W/Re) fuel rod simulator 7 (type 3), 650 mm, 135°	K
7	TFS 3/12	TC (W/Re) fuel rod simulator 9 (type 3), 850 mm, 225°	K
8	TFS 3/13	TC (W/Re) fuel rod simulator 3 (type 3), 950 mm, 315°	K
9	TFS 3/14	TC (W/Re) fuel rod simulator 5 (type 3), 1050 mm, 45°	K
10	TFS 4/11	TC (W/Re) fuel rod simulator 14 (type 4), 750 mm, 45°	K
11	TFS 4/13	TC (W/Re) fuel rod simulator 20 (type 4), 950 mm, 135°	K
12	TFS 5/10	TC (W/Re) fuel rod simulator 12 (type 5), 650 mm, 225°	K
13	TFS 5/11	TC (W/Re) fuel rod simulator 13 (type 5), 750 mm, 45°	K
14	TFS 5/12	TC (W/Re) fuel rod simulator 15 (type 5), 850 mm, 315°	K
15	TFS 5/13	TC (W/Re) fuel rod simulator 16 (type 5), 950 mm, 135°	K
17	TSH 16/180	TC (W/Re) shroud outer surface, 1250 mm, 206°	K
18	TSH 13/90	TC (W/Re) shroud outer surface, 950 mm, 116°	K
19	TSH 14/90	TC (W/Re) shroud outer surface, 1050 mm, 116°	K
20	TSH 11/0	TC (W/Re) shroud outer surface, 750 mm, 26°	K
21	TSH 12/0	TC (W/Re) shroud outer surface, 850 mm, 26°	K
22	TFS 2/5	TC (NiCr/Ni) fuel rod simulator 2 (type 2), 150 mm, 225°	K
23	TFS 2/7	TC (NiCr/Ni) fuel rod simulator 6 (type 2), 350 mm, 45°	K
24	F 902	Off-gas flow rate before Caldos (H_2)	Nm^3/h
32	TIT A/13	TC (W/Re) corner rod A, center, 950 mm	K
33	TCRC13	TC (W/Re) central rod, center, 950 mm	K
34	TFS 2/12	TC (W/Re) fuel rod simulator 2 (type 2), 850 mm, 315°	K
35	TSH 9/90	TC (NiCr/Ni) shroud outer surface, 550 mm, 116°	K
36	TSH 9/270	TC (NiCr/Ni) shroud outer surface, 550 mm, 296°	K
37	TFS 3/16	TC (W/Re) fuel rod simulator 7 (type 3), 1250 mm, 135°	K
38	TFS 5/9	TC (NiCr/Ni) fuel rod simulator 10 (type 5), 550 mm, 315°	K
39	TFS 2/9	TC (NiCr/Ni) fuel rod simulator 8 (type 2), 550 mm, 135°	K
40	TIT D/12	TC (W/Re) corner rod D, center, 850 mm	K
41	TCR 13	TC (We/Re) central rod cladding, 950 mm	K

Chan-nel	Designation	Instrument, location	Output in
42	TFS 5/8	TC (NiCr/Ni) fuel rod simulator 21 (type 5), 450 mm, 135°	K
43	TFS 3/8	TC (NiCr/Ni) fuel rod simulator 5 (type 3), 450 mm, 45°	K
45	TCRC 7	TC (NiCr/Ni) central rod, center, 350 mm	K
46	TIT C/9	TC (NiCr/Ni) corner rod C, center, 550 mm	K
47	TFS 5/15	TC (W/Re) fuel rod simulator 19 (type 5), 1150 mm, 225°	K
48	TFS 5/16	TC (W/Re) fuel rod simulator 21 (type 5), 1250 mm, 225°	K
49	TFS 5/17	TC (W/Re) fuel rod simulator 10 (type 5), 1350 mm, 315°	K
52	TSH 13/270	TC (W/Re) shroud outer surface, 950 mm, 296°	K
53	TSH 14/270	TC (W/Re) shroud outer surface, 1050 mm, 270°	K
54	TSH 11/180	TC (W/Re) shroud outer surface, 750 mm, 206°	K
55	TSH 12/180	TC (W/Re) shroud outer surface, 850 mm, 206°	K
57	TSH 15/180	TC (W/Re) shroud outer surface, 1150 mm, 206°	K
66	TSH 15/0	TC (W/Re) shroud outer surface, 1150 mm, 26°	K
67	TSH 16/0	TC (W/Re) shroud outer surface, 1250 mm, 26°	K
68	T 512	Gas temperature bundle outlet	K
71	Ref. T 01	Reference temperature 1	K
72	TFS 2/1	TC (NiCr/Ni) fuel rod simulator 4 (type 2), -250 mm, 315°	K
73	TFS 2/2	TC (NiCr/Ni) fuel rod simulator 6 (type 2), -150 mm, 45°	K
74	TFS 2/3	TC (NiCr/Ni) fuel rod simulator 8 (type 2), -50 mm, 135°	K
75	TCRI 7	TC (NiCr/Ni), central rod, cladding inner surface, 350 mm	K
76	TFS 2/6	TC (NiCr/Ni) fuel rod simulator 4 (type 2), 250 mm, 315°	K
77	TCRI 9	TC (NiCr/Ni), central rod, cladding inner surface, 550 mm	K
78	TFS 5/4/0	TC (NiCr/Ni) fuel rod simulator 15 (type 5), 50 mm, 315°	K
79	TFS 5/4/180	TC (NiCr/Ni) fuel rod simulator 21 (type 5), 50 mm, 135°	K
80	TFS 5/5	TC (NiCr/Ni) fuel rod simulator 16 (type 5), 150 mm, 225°	K
81	TFS 5/6	TC (NiCr/Ni) fuel rod simulator 18 (type 5), 250 mm, 45°	K
82	TFS 5/7	TC (NiCr/Ni) fuel rod simulator 19 (type 5), 350 mm, 225°	K
83	TSH 4/270	TC (NiCr/Ni) shroud outer surface, 50 mm, 296°	K
84	TSH 3/180	TC (NiCr/Ni) shroud outer surface, -50 mm, 206°	K
85	TSH 4/180	TC (NiCr/Ni) shroud outer surface, 50 mm. 206°	K
86	TSH 7/180	TC (NiCr/Ni) shroud outer surface, 350 mm, 206°	K
87	TSH 4/90	TC (NiCr/Ni) shroud outer surface, 50 mm, 116°	K
88	TSH 1/0	TC (NiCr/Ni) shroud outer surface, -250 mm, 26°	K
89	TSH 4/0	TC (NiCr/Ni) shroud outer surface, 50 mm, 26°	K
90	TSH 7/0	TC (NiCr/Ni) shroud outer surface, 350 mm, 26°	K

Chan-nel	Designation	Instrument, location	Output in
91	TCI 9/270	TC (NiCr/Ni) cooling jacket inner tube wall, 550 mm, 270°	K
92	TCI 10/270	TC (NiCr/Ni) cooling jacket inner tube wall, 650 mm, 270°	K
93	TCI 11/270	TC (NiCr/Ni) cooling jacket inner tube wall, 750 mm, 270°	K
94	TCI 13/270	TC (NiCr/Ni) cooling jacket inner tube wall, 950 mm, 270°	K
95	TCR 7	TC (NiCr/Ni) central rod, cladding outer surface, 350 mm	K
96	TCI 1/180	TC (NiCr/Ni) cooling jacket inner tube wall, -250 mm, 180°	K
97	TCI 4/180	TC (NiCr/Ni) cooling jacket inner tube wall, 50 mm, 180°	K
98	TCI 7/180	TC (NiCr/Ni) cooling jacket inner tube wall, 350 mm, 180°	K
99	TCI 11/180	TC (NiCr/Ni) cooling jacket inner tube wall, 750 mm, 180°	K
100	TCI 12/180	TC (NiCr/Ni) cooling jacket inner tube wall, 850 mm, 180°	K
101	TCI 13/180	TC (NiCr/Ni) cooling jacket inner tube wall, 950 mm, 180°	K
102	TCI 15/180	TC (NiCr/Ni) cooling jacket inner tube wall, 1150 mm, 180°	K
103	TCR 9	TC (NiCr/Ni) central rod, cladding outer surface, 550 mm	K
104	TCI 9/90	TC (NiCr/Ni) cooling jacket inner tube wall, 550 mm, 90°	K
105	TCI 10/90	TC (NiCr/Ni) cooling jacket inner tube wall, 650 mm, 90°	K
106	TCI 11/90	TC (NiCr/Ni) cooling jacket inner tube wall, 750 mm, 90°	K
107	TCI 13/90	TC (NiCr/Ni) cooling jacket inner tube wall, 950 mm, 90°	K
108	TCRC 9	TC (NiCr/Ni) central rod, center, 550 mm	K
109	TCI 1/0	TC (NiCr/Ni) cooling jacket inner tube wall, -250 mm, 0°	K
110	TCI 4/0	TC (NiCr/Ni) cooling jacket inner tube wall, 50 mm, 0°	K
111	TCI 7/0	TC (NiCr/Ni) cooling jacket inner tube wall, 350 mm, 0°	K
112	TCI 11/0	TC (NiCr/Ni) cooling jacket inner tube wall, 750 mm, 0°	K
113	TCI 12/0	TC (NiCr/Ni) cooling jacket inner tube wall, 850 mm, 0°	K
114	TCI 13/0	TC (NiCr/Ni) cooling jacket inner tube wall, 950 mm, 0°	K
115	TCI 15/0	TC (NiCr/Ni) cooling jacket inner tube wall, 1150 mm, 0°	K
117	TCO 9/270	TC (NiCr/Ni) cooling jacket outer tube surface, 550 mm, 270°	K
118	TCO 4/180	TC (NiCr/Ni) cooling jacket outer tube surface, 50 mm, 180°	K
120	TCO 1/0	TC (NiCr/Ni) cooling jacket outer tube surface, -250 mm, 0°	K
121	TCO 7/0	TC (NiCr/Ni) cooling jacket outer tube surface, 350 mm, 0°	K
122	TCO 13/0	TC (NiCr/Ni) cooling jacket outer tube surface, 950 mm, 0°	K
123	T 601	Temperature before off-gas flow instrument F 601	K
124	T 513	Temperature bundle head top (wall)	K
125	T 514	Temperature bundle head, at outlet (wall)	K
128	T 104	Temperature quench water	K
129	T 201	Temperature steam generator heating pipe	K

Chan-nel	Designation	Instrument, location	Output in
130	T 204	Temperature before steam flow instrument location 50 g/s	K
131	T 205	Temperature before steam flow instrument location 10 g/s	K
132	T 301A	Temperature behind superheater	K
133	T 302	Temperature superheater heating pipe	K
134	T 303	Temperature before total flow instrument location	K
135	T 401	Temperature before gas flow instrument location	K
136	T 403	Temperature at inlet cooling gas	K
137	T 404	Temperature at outlet cooling gas	K
138	T 501	Temperature at containment	K
139	T 502	Temperature at containment	K
140	T 503	Temperature at containment	K
141	T 504	Temperature at containment	K
142	T 505	Temperature at containment	K
143	T 506	Temperature at containment	K
144	T 507	Temperature at containment	K
145	T 508	Temperature at containment	K
146	T 509	Temperature bundle head outside (wall)	K
147	T 510	Temperature at containment	K
148	T 511	Gas temperature at bundle inlet	K
149	T 901	Temperature before off-gas flow instrument F 901	K
151	Ref. T 02	Reference temperature 2	K
152	P 201	Pressure steam generator	bar
153	P 204	Pressure at steam flow instrument location 50 g/s	bar
154	P 205	Pressure at steam flow instrument location 10 g/s	bar
155	P 303	Pressure before total flow instrument location	bar
156	P 401	Pressure before gas flow instrument location	bar
157	P 511	Pressure at bundle inlet	bar
158	P 512	Pressure at bundle outlet	bar
159	P 601	Pressure before off-gas flow instrument F 601	bar
160	P 901	Pressure before off-gas flow instrument F 901	bar
161	L 201	Liquid level steam generator	mm
162	L 501	Liquid level quench water	mm
163	L 701	Liquid level main condenser	mm
164	Q 901	H_2 concentration, off-gas (Caldos)	% H_2
165	P 411	Pressure Ar-Kr supply	bar

Chan-nel	Designation	Instrument, location	Output in
166	P 403	Pressure Ar cooling of cooling jacket	bar
167	P 406	Pressure insulation shroud/cooling jacket	bar
168	F 104	Flow rate quench water	l/h
169	F 204	Flow rate steam 50 g/s	m³/h
170	F 205	Flow rate steam 10 g/s	m³/h
171	F 303	Flow rate at bundle inlet (steam + argon), orifice	mbar
172	F 401	Argon gas flow rate	Nm³/h
173	F 403	Flow rate cooling gas	Nm³/h
174	F 601	Flow rate off-gas (orifice)	mbar
175	F 901	Off-gas flow rate before Caldos (H_2)	m³/h
176	E 201	Electric current steam generator	A
177	E 301	Electric current superheater	A
178	E 501	Electric current inner ring of fuel rod simulators	A
179	E 502	Electric current outer ring of fuel rod simulators	A
180	E 503	Electric voltage inner ring of fuel rod simulators	V
181	E 504	Electric voltage outer ring of fuel rod simulators	V
182	Hub_V302	Steam supply valve lift	%
183	Ref. T 03	Reference temperature 3	K
184	Notaus	Emergency switch for test facility	-
185	Ü 24 V	Check of 24 V fuse	-
186	P 501	Containment pressure	bar
187	P 701	Condenser pressure	bar
188	F 801	Water flow, intermediate cooler	l/s
189	F 802	Water flow, intermediate cooler	l/s
190	E 101	Current feed water pump on	-
191	E 102	Current quench pump on	-
192	E 701	Current condensate pump on	-
193	GS 1 Ein	DC supply 1 on	-
194	GS 1 STÖ	DC supply 1 interruption	-
195	GS 2Ein	DC supply 2 on	-
196	GS 2 STÖ	DC supply 2 interruption	-
197	V 302 STÖ	Steam supply valve interruption	-

Note: Tip of the thermocouple TFS 2/1 is bent into flow channel to measure the fluid temperature

Table I-4: QUENCH-04; Sequence of events

Time [s]	Event
0	Start of data recording
90	Start of electric power transient
2012	Corner rod B withdrawn from the bundle (T ≈ 1780 K)
2030	Begin of temperature escalation at the 750 mm level (TFS 4/11 and TFS 5/11: ~1560 K) and at the 1050 mm level (TFS 3/14: ~1570 K)
2033	Begin of temperature escalation at the shroud (1050 mm, TSH 14/270: ~1350 K)
2040	Begin of significant H_2 production, based on the mass spectrometer data
2065	Steam flow of 3 g/s turned off and cooldown steam turned on, cooldownsteam flow at 42 g/s; strong temperature decrease at -250 mm (TFS 2/1); shroud failure
2088	16.2 kW of electric bundle power reached, start of electric power reduction from 16.2 kW to 4 kW
2103	Electric power of 4 kW reached
2269-2307	Rod failure
2302	Electric power shut off
2303	Cooldown steam flow turned off
2304	Steam flow at zero
2528	End of data recording

0 s = 14:36:00 h on June 30, 1999

Table I-5: QUENCH-04; Temperatures at the begin of excursion

Elevation [mm]	Thermocouple	Time at excursion [s]	Excursion temperature [K]
750	TFS 2/11	2034	1560
750	TFS 4/11	2030	1560
750	TFS 5/11	2030	1560
850	TFS 3/12	2043	1730
850	TFS 5/12	2043	1710
950	TFS 2/13	2050	2010
950	TFS 3/13	2050	2010
950	TFS 5/13	2053	1930
950	TCR 13	2050	2010
1050	TFS 3/14	2030	1570
1050	TSH 14/90	2048	1310
1050	TSH 14/270	2033	1350
1150	TSH 15/0	2041	1320
1150	TSH 15/180	2058	1210
1250	TSH 16/0	2047	1220
1250	TSH 16/180	2057	1200

Table I-6: QUENCH-04; Maximum measured temperature of each elevation

Elevation [mm]	Thermocouple	Time [s]	Maximum temperature [K]
- 250	TFS 2/1	2065	628
- 150	TFS 2/2	2065	696
- 50	TFS 2/3	2065	748
50	TFS 5/4/0, TFS 5/4/180	2065	809
150	TFS 2/5	2065	943
250	TFS 2/6	2065	1037
350	TFS 2/7	2065	1127
450	TFS 3/8	2065	1198
550	TFS 2/9	2065	1248
650	TFS 5/10	2065	1356
750	TFS 4/11	2065	2152
850	TFS 5/12	2065	2339
950	TCR 13	2065	2282
1050	TFS 3/14	2065	1717
1150	TSH 15/0	2068	1845
1250	TSH 16/0	2068	1811
1350	TFS 2/17	2065	1168

Table I- 7: QUENCH-04; Onset of cooling based on cladding TCs (TFS), central rod TCs (TCR, TCRC, TCRI), corner rod TCs (TIT), and shroud TCs (TSH)

Thermocouple	Elevation	Onset of cooling		Mean values	
	[mm]	Time [s]	Temp. [K]	Time [s]	Temp. [K]
TFS 2/1	- 250	2065	628	2065	628
TFS 2/2	- 150	2065	696	2065	696
TFS 2/3	- 50	2065	784	2065	784
TFS 5/4/0	50	2065	809	2065	809
TFS 5/4/180	50	2065	809		
TFS 2/5	150	2065	943	2065	931
TFS 5/5	150	2065	919		
TFS 2/6	250	2065	1037	2065	1028
TFS 5/6	250	2065	1018		
TFS 2/7	350	2065	1127	2065	1111
TFS 5/7	350	2065	1094		
TFS 3/8	450	2065	1198	2065	1181
TFS 5/8	450	2065	1163		
TFS 2/9	550	2065	1248	2065	1226
TFS 5/9	550	2065	1204		
TFS 3/10	650	2065	1341	2065	1349
TFS 5/10	650	2065	1356		
TFS 2/11	750	2065	2063	2065	2111
TFS 4/11	750	2065	2152		
TFS 5/11	750	2065	2119		
TFS 2/12	850	2065	1764	2065	2082
TFS 3/12	850	2065	2143		
TFS 5/12	850	2065	2339		

Thermocouple	Elevation	Onset of cooling		Mean values	
	[mm]	Time [s]	Temp. [K]	Time [s]	Temp. [K]
TFS 2/13	950	2065	2124	2065	2112
TFS 3/13	950	2065	2095		
TFS 5/13	950	2065	2116		
TFS 3/14	1050	2065	1717	2065	1717
TFS 2/15	1150	2065	1493	2065	1394
TFS 5/15	1150	2065	1294		
TFS 3/16	1250	2065	1287	2065	1259
TFS 5/16	1250	2065	1231		
TFS 2/17	1350	2065	1168	2065	1087
TFS 5/17	1350	2065	1005		
TCRC 7	350	*	*		
TCR 7	350	2065	1100	2065	1100
TCRI 7	350	2065	1113	2065	1113
TCRC 9	550	*	*		
TCR 9	550	2065	1224	2065	1224
TCRI 9	550	2065	1224	2065	1224
TCRC 13	950	*	*		
TCR 13	950	2065	2282	2065	2282
TIT C/9	550	2065	1179	2065	1179
TIT D/12	850	2065	1697	2065	1697
TIT A/13	950	2065	2089	2065	2089
TSH 1/0	- 250	2065	587	2065	587
TSH 3/180	- 50	2065	651	2065	651

Thermocouple	Elevation	Onset of cooling		Mean values	
	[mm]	Time [s]	Temp. [K]	Time [s]	Temp. [K]
TSH 4/0	50	2065	734	2065	721
TSH 4/90	50	2065	725		
TSH 4/180	50	2065	710		
TSH 4/270	50	2065	715		
TSH 7/0	350	2065	1058	2065	1053
TSH 7/180	350	2065	1048		
TSH 9/90	550	2065	1157	2065	1166
TSH 9/270	550	2065	1175		
TSH 11/0	750	2065	1448	2065	1448
TSH 11/180	750	2065	1448		
TSH 12/0	850	2065	1629	2065	1623
TSH 12/180	850	2065	1617		
TSH 13/90	950	2065	1927	2065	1927
TSH 13/270	950	*	*		
TSH 14/90	1050	2068	1517	2069	1614
TSH 14/270	1050	2070	1711		
TSH 15/0	1150	2068	1845	2067	1594
TSH 15/180	1150	2065	1342		
TSH 16/0	1250	2068	1811	2067	1624
TSH 16/180	1250	2066	1436		

* No clear indication

Table I-8: QUENCH-04; Cross sections for posttest examinations

23.11.2000

Sample	Sample Length (mm)	Axial position Bottom (mm)	Axial position Top (mm)	Remarks
QUE-04-a	13	-25	-12	Remnant
Cut	2	-12	-10	
QUE-04-1a	13	-10	3	3 mm = Bundle elevation 53 mm
Cut	2	3	5	
QUE-04-b	53	5	58	
Cut	2	58	60	
QUE-04-1	13	60	73	
Cut	2	73	75	
QUE-04-c	390	75	465	
Cut	2	465	467	
QUE-04-2a	13	467	480	480 mm = Bundle 530 mm
Cut	2	480	482	
QUE-04-d	53	482	535	
Cut	2	535	537	
QUE-04-2	13	537	550	
Cut	2	550	552	
QUE-04-e	113	552	665	
Cut	2	665	667	
QUE-04-3a	13	667	680	680 mm = Bundle 730 mm; polished
Cut	2	680	682	
QUE-04-f	53	682	735	
Cut	2	735	737	
QUE-04-3	13	737	750	750 mm polished
Cut	2	750	752	
QUE-04-g	13	752	765	
Cut	2	765	767	
QUE-04-4a	13	767	780	780 mm = Bundle 830 mm; polished
Cut	2	780	782	
QUE-04-h	53	782	835	
Cut	2	835	837	
QUE-04-4	13	837	850	850 mm polished
Cut	2	850	852	

Note: After the test the bundle was found to be positioned in the axial direction approx. 50 mm lower than the shroud.

Sample	Sample	Axial position		Remarks
	Length (mm)	Bottom (mm)	Top (mm)	
QUE-04-i	13	852	865	
Cut	2	865	867	
QUE-04-5a	13	867	880	880 mm = Bundle 930 mm; polished
Cut	2	880	882	
QUE-04-6a	13	882	895	895 mm = Bundle 945 mm; polished
Cut	2	895	897	
QUE-04-7a	13	897	910	910 mm = Bundle 960 mm; polished
Cut	2	910	912	
QUE-04-j	23	912	935	
Cut	2	935	937	
QUE-04-5	13	937	950	950 mm polished
Cut	2	950	952	
QUE-04-6	13	952	965	965 mm polished
Cut	2	965	967	
QUE-04-7	13	967	980	980 mm polished
Cut	2	980	982	
QUE-04-k	83	982	1065	
Cut	2	1065	1067	
QUE-04-8a	13	1067	1080	1080 mm = Bundle 1130 mm; polished
Cut	2	1080	1082	
QUE-04-l	53	1082	1135	
Cut	2	1135	1137	
QUE-04-8	13	1137	1150	1150 mm polished
Cut	2	1150	1152	
QUE-04-m	13	1152	1165	
Cut	2	1165	1167	
QUE-04-9a	13	1167	1180	1180 mm = Bundle 1230 mm
Cut	2	1180	1182	
QUE-04-n	53	1182	1235	
Cut	2	1235	1237	
QUE-04-9	13	1237	1250	
Cut	2	1250	1252	
QUE-04-o	198	1252	1450	Remnant
Cut	2	1450	1452	
QUE-04-p	378	1452	1830	Remnant

Note: After the test the bundle was found to be positioned in the axial direction approx. 50 mm lower than the shroud.

Table I-9: Comparison of measured and calculated values of oxide scale thickness for QUENCH-04

Pin No.	Axial position [mm]	Experimental value of oxide scale thickness [µm]	Calculated value [µm]	Oxide correlation bc : base case loc : low oxid. case
13 / 14	750	35 - 40	120	loc
			250	bc
			≈ 50	loc *
9 / 15	850	70 - 80	120	loc
			75	loc *
2	850	80 - 85	110	Loc

* without temperature escalation

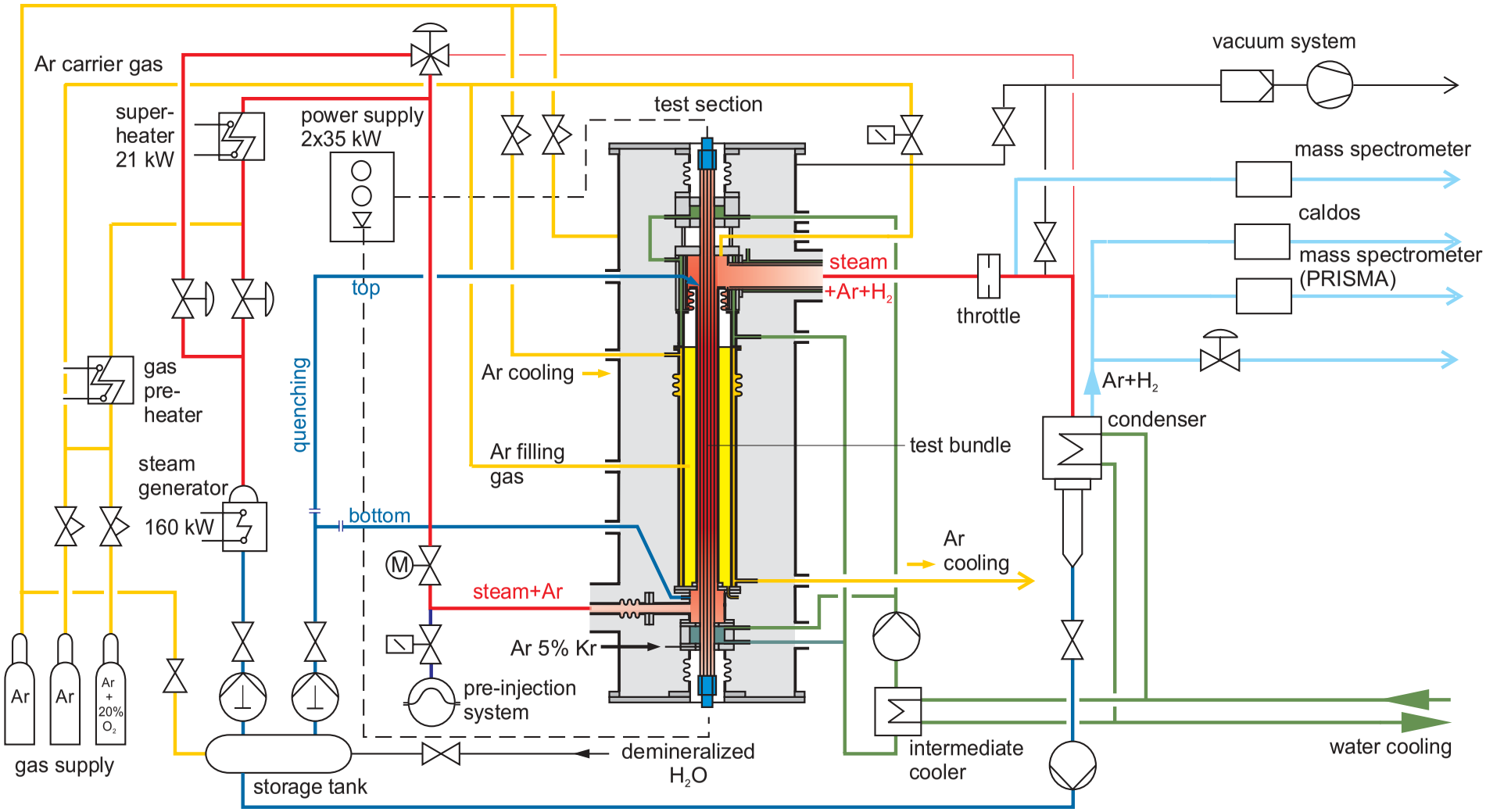

Fig. I-1: Flow diagram of the QUENCH test facility

Fig.1-QUE04-Flow diagram.cdr
21.10.01 - IMF

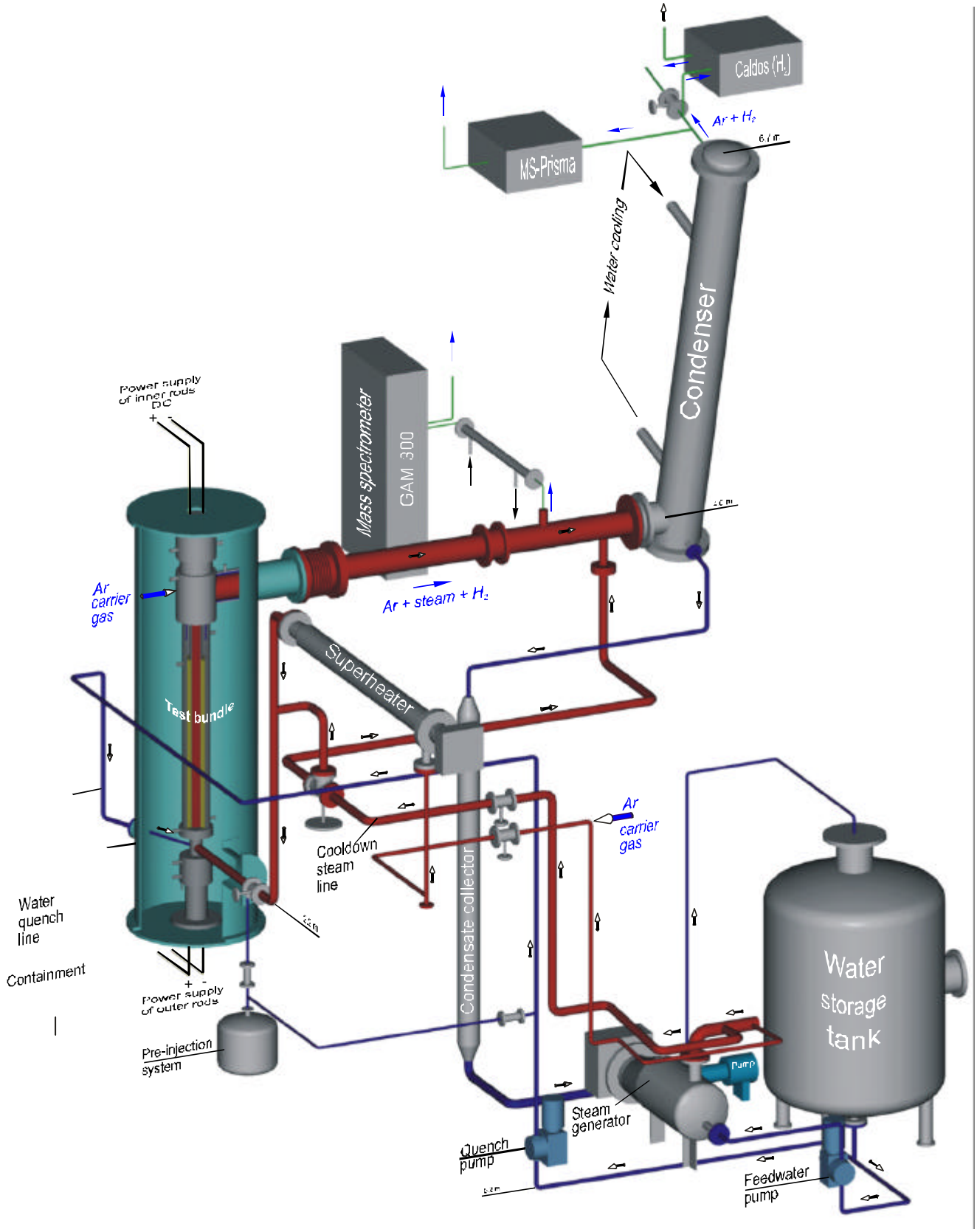

Fig. I-2: QUENCH Facility; main components

Fig.2-QUE04Gesamtanlage 3D.cdr
09.10.01-IMF

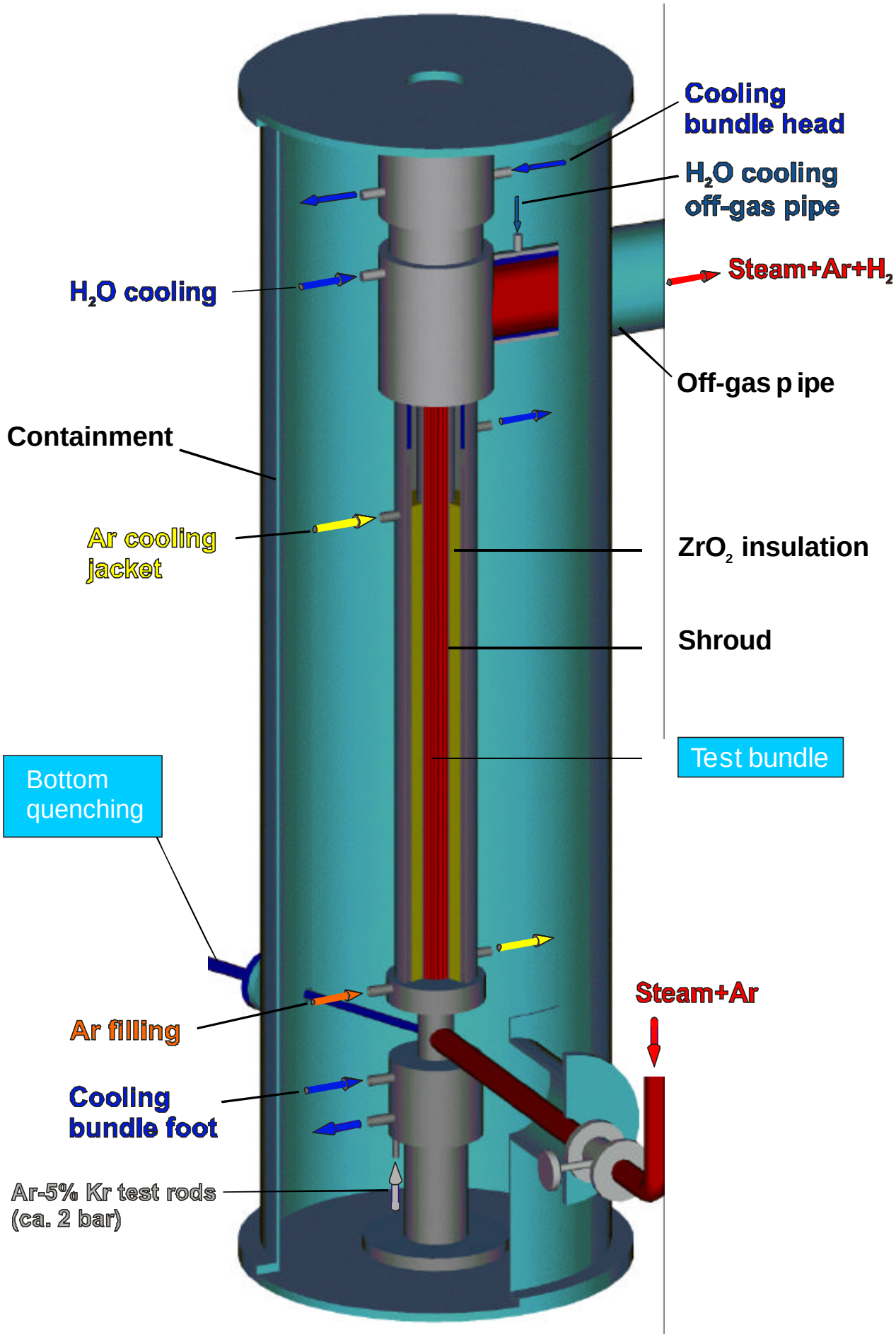

Fig. I-3: QUENCH Facility; containment and test section

Fig.3-QUE04Containment3D.cdr
10.10.01-IMF

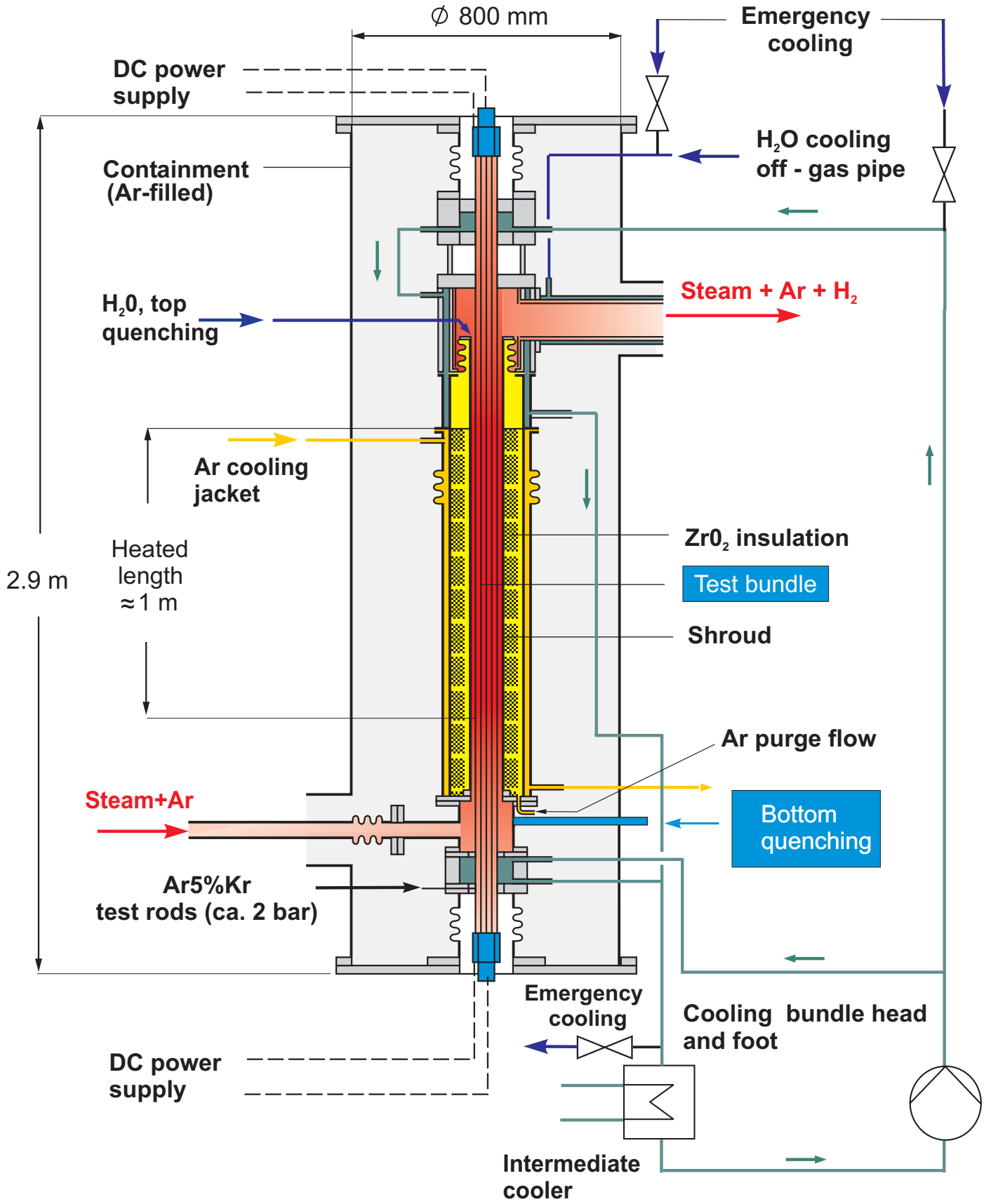

Fig. I-4: QUENCH Test section; flow lines

Fig.4-QUE04 Flow lines.cdr
10.10.01 - IMF

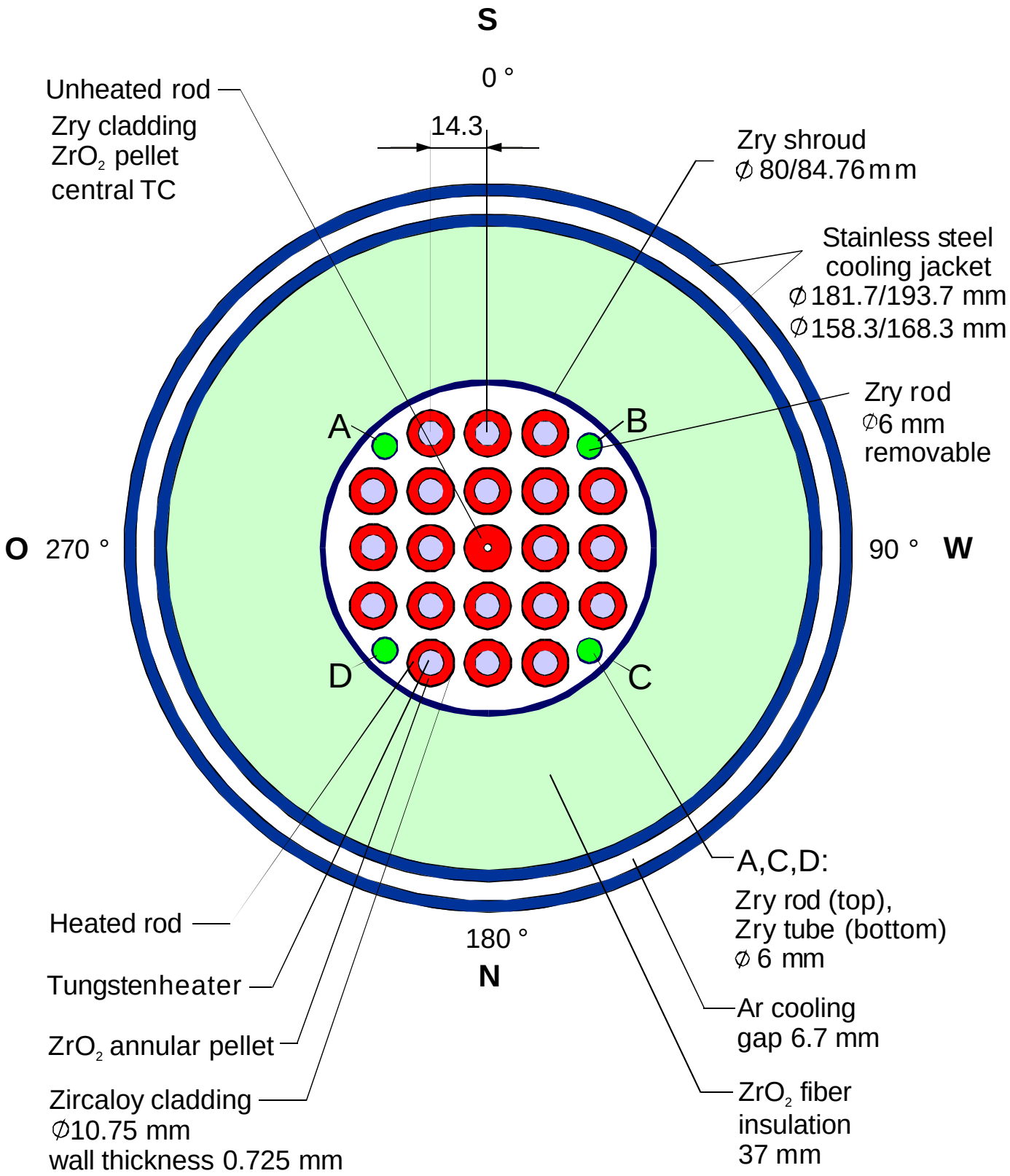

Fig. I-5: QUENCH-04; Fuel rod simulator bundle (Topview)

Fig.5-QUE04Crosssection.cdr
10.10.01-IMF

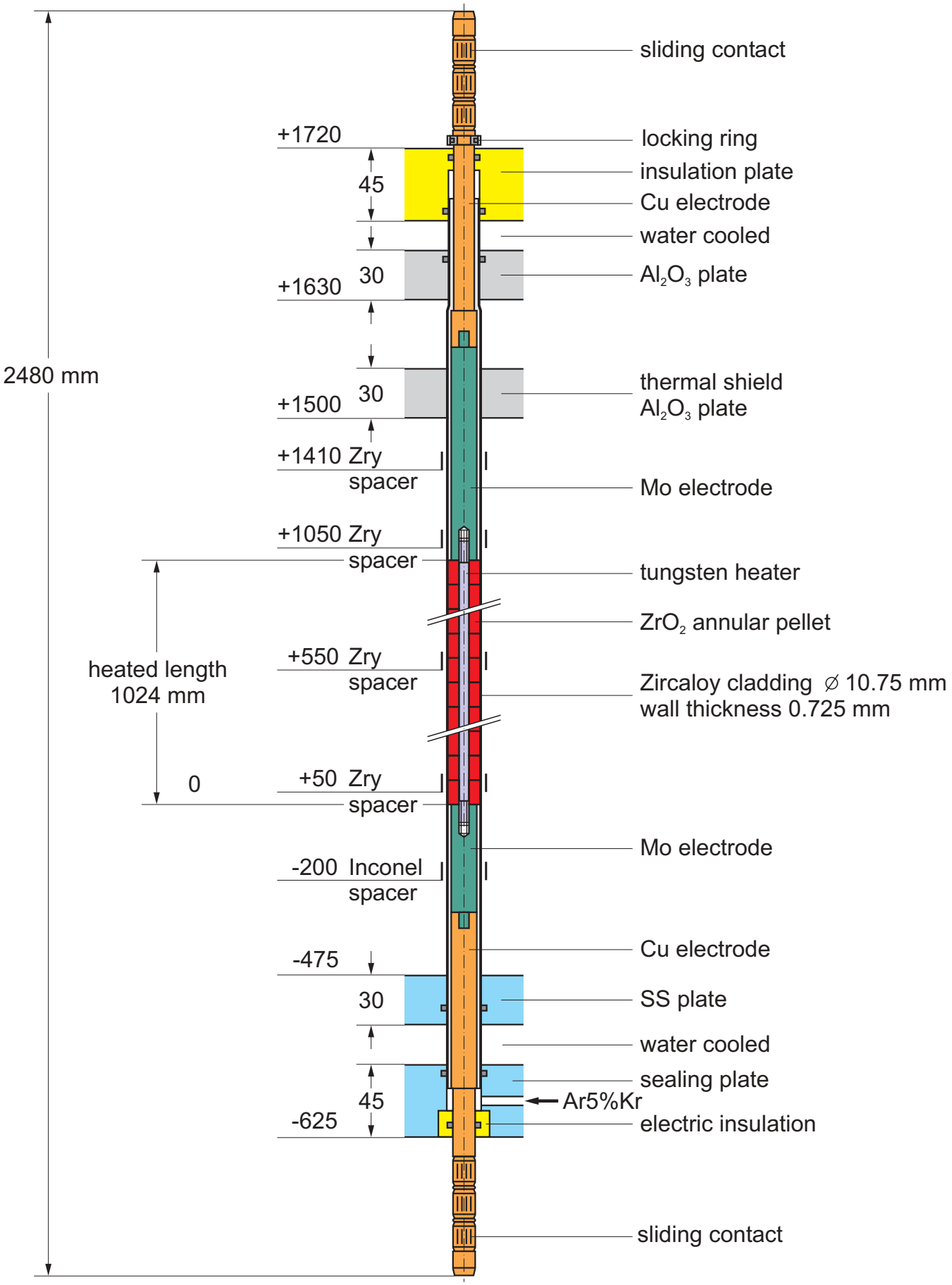

Fig. I-6: Heated fuel rod simulator

Fig.6-QUE04 Heated fuel rod sim.cdr
10.10.01 - IMF

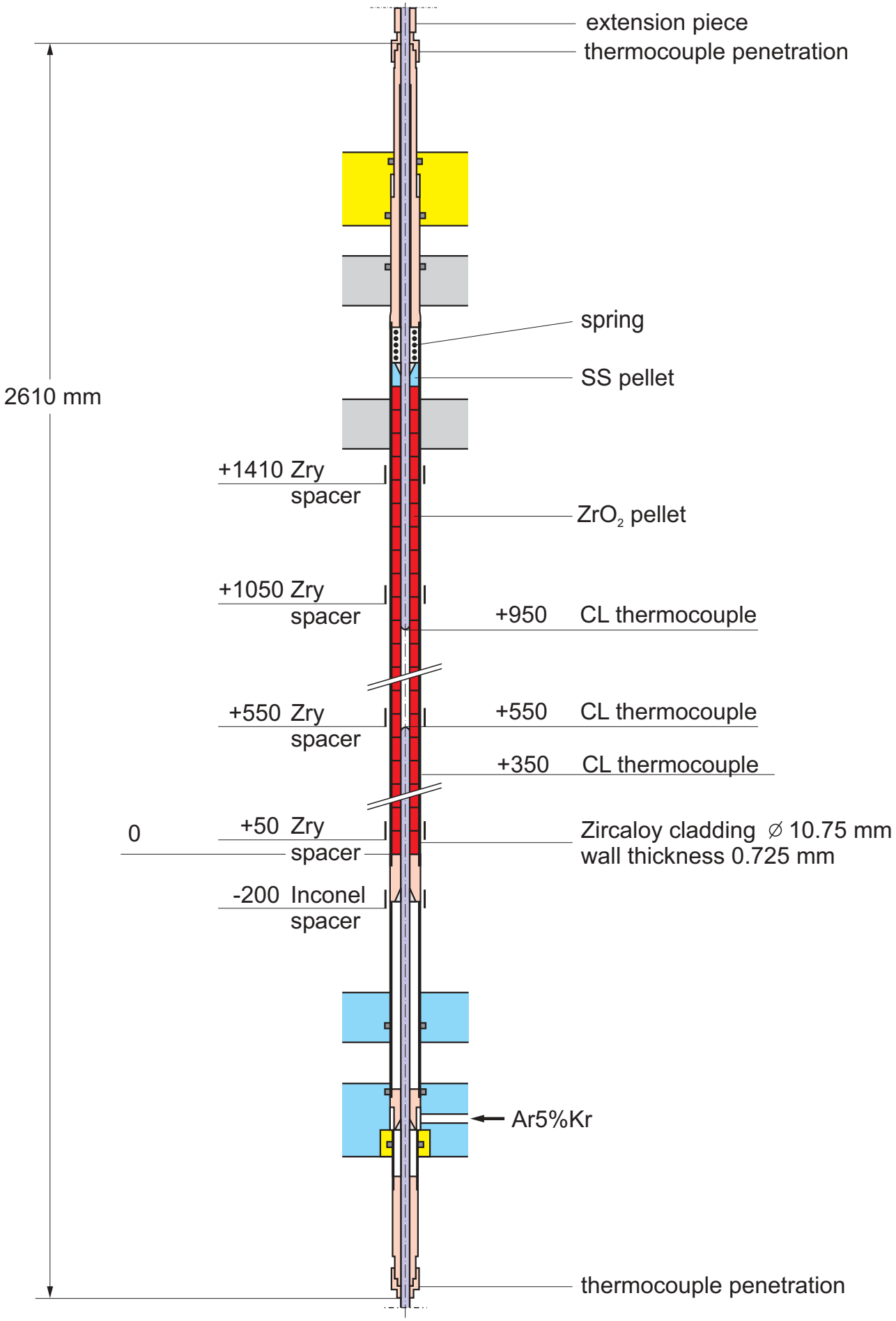

Fig. I-7: Unheated fuel rod simulator

Fig.7-QUE04 Unheated fuel rod sim.cdr
10.10.01 - IMF

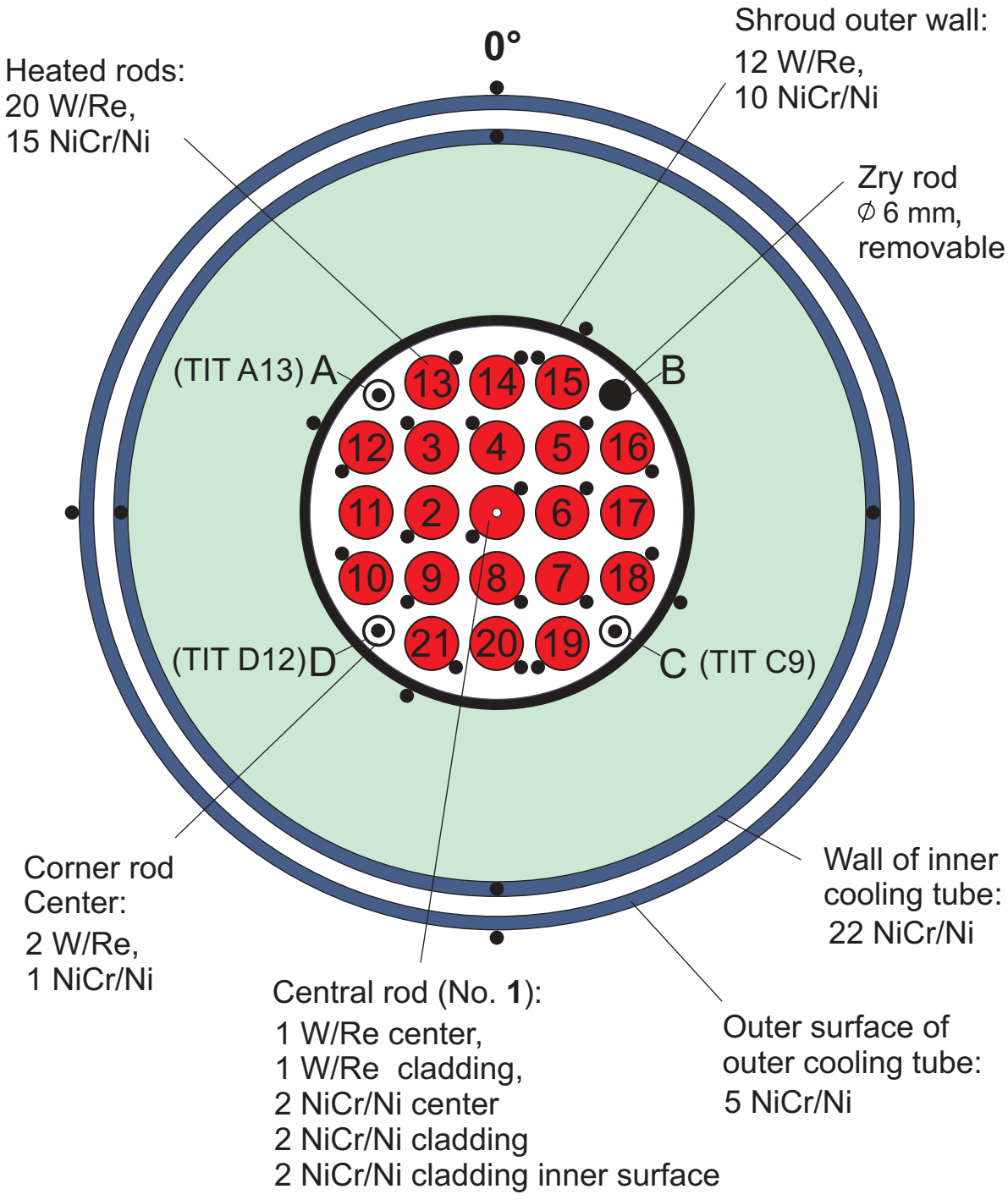

Fig. I-8: QUENCH-04; Test bundle; TC instrumentation and rod designation (top view)

Fig.8-QUE04 TC instr.cdr
11.10.01 - IMF

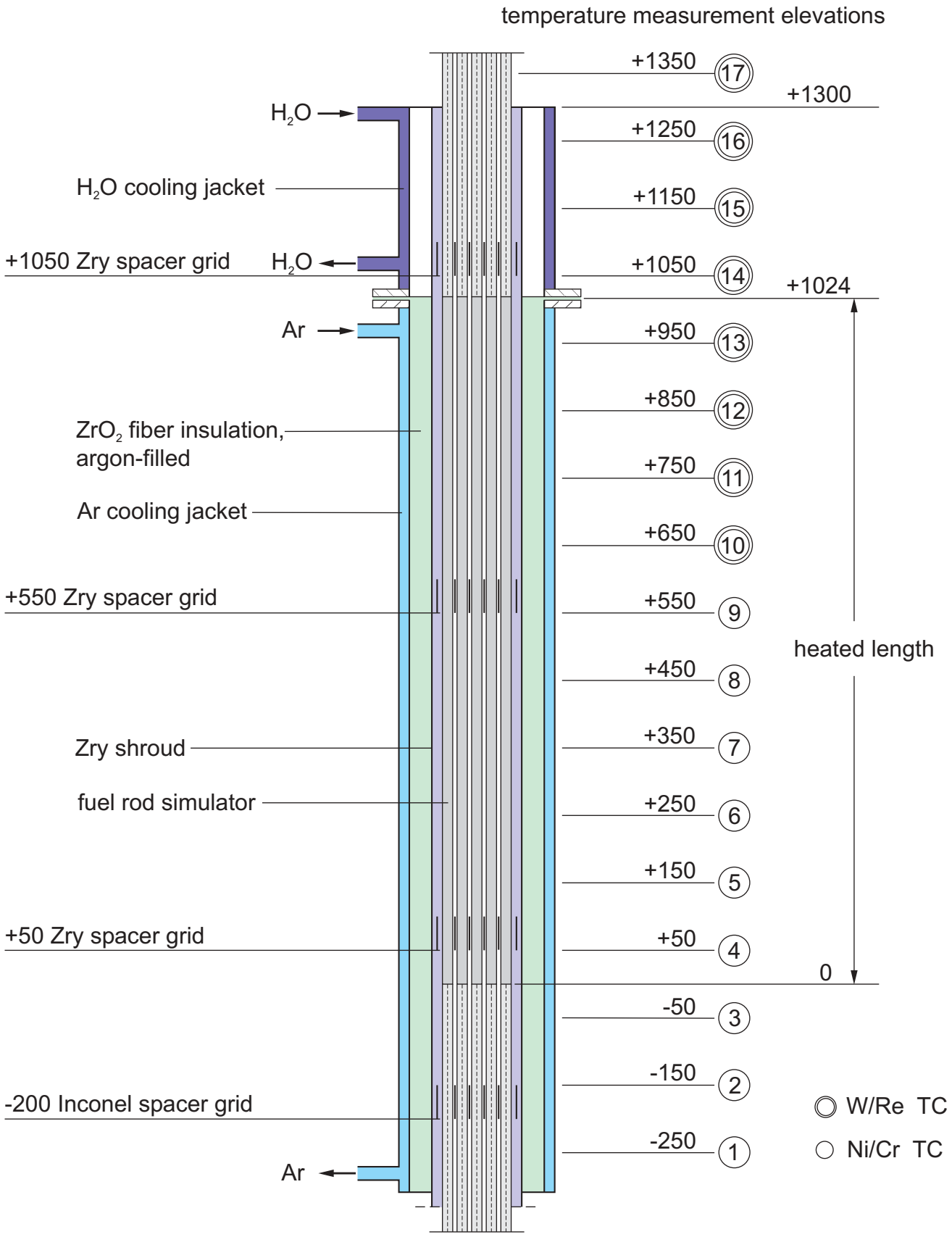

Fig. I-9: QUENCH; Test section instrumentation

Fig.9-QUE TC elevations.cdr
11.10.01 - IMF

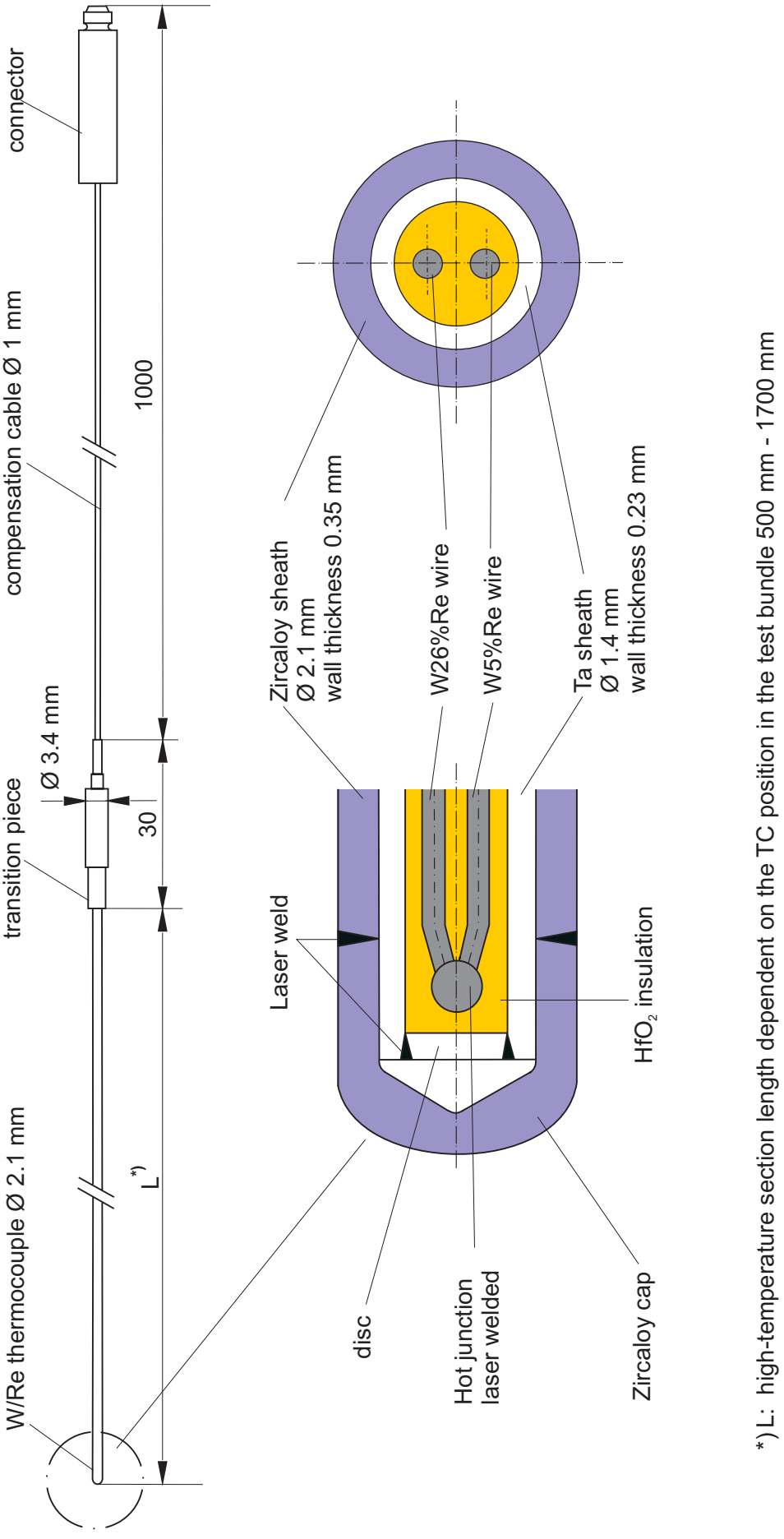

Fig. I-10: QUENCH; High-temperature thermocouple

Fig.10-QUE04 High-temp thermocouple.cdr
11.10.01 - IMF

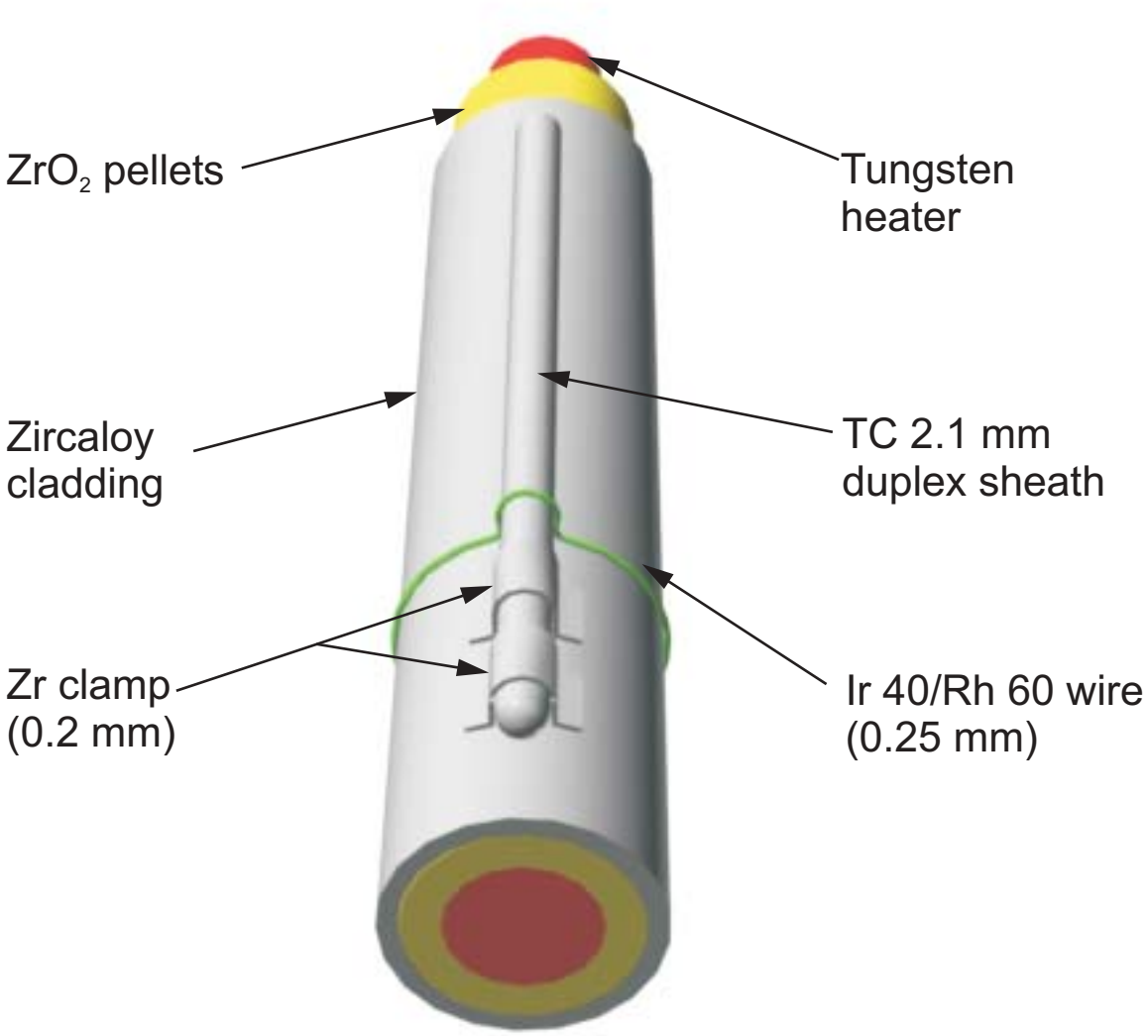

Fig. I-11: TC Fastening concept for the QUENCH test rod

Fig 11QUE04 TC Fastening3.cdr
11.10.01 - IMF

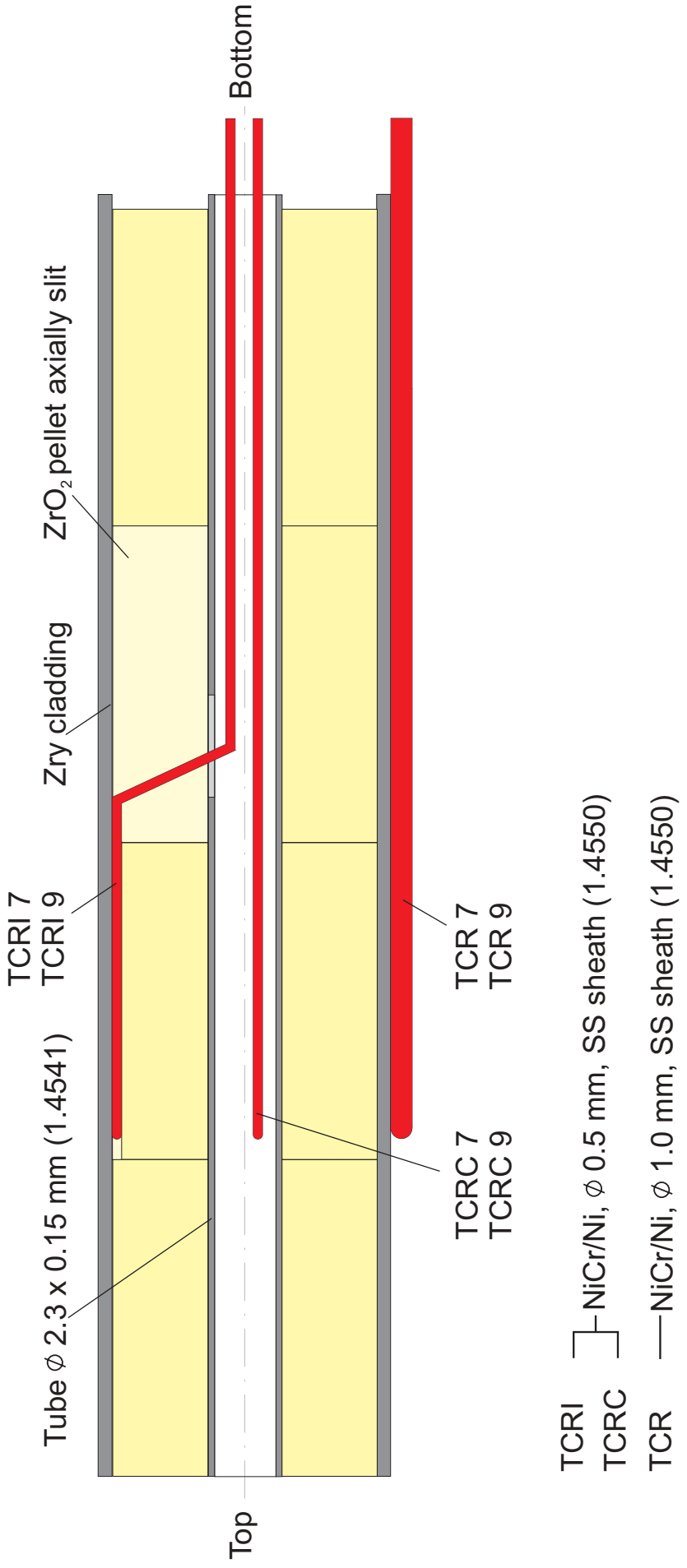

Fig. I-12: QUENCH-04; TC instrumentation of the unheated fuel rod simulator at leves 7 (350 mm) and 9 (550 mm)

Fig 12 QUE04 Zentralstab.cdr
07.11.01 - IMF

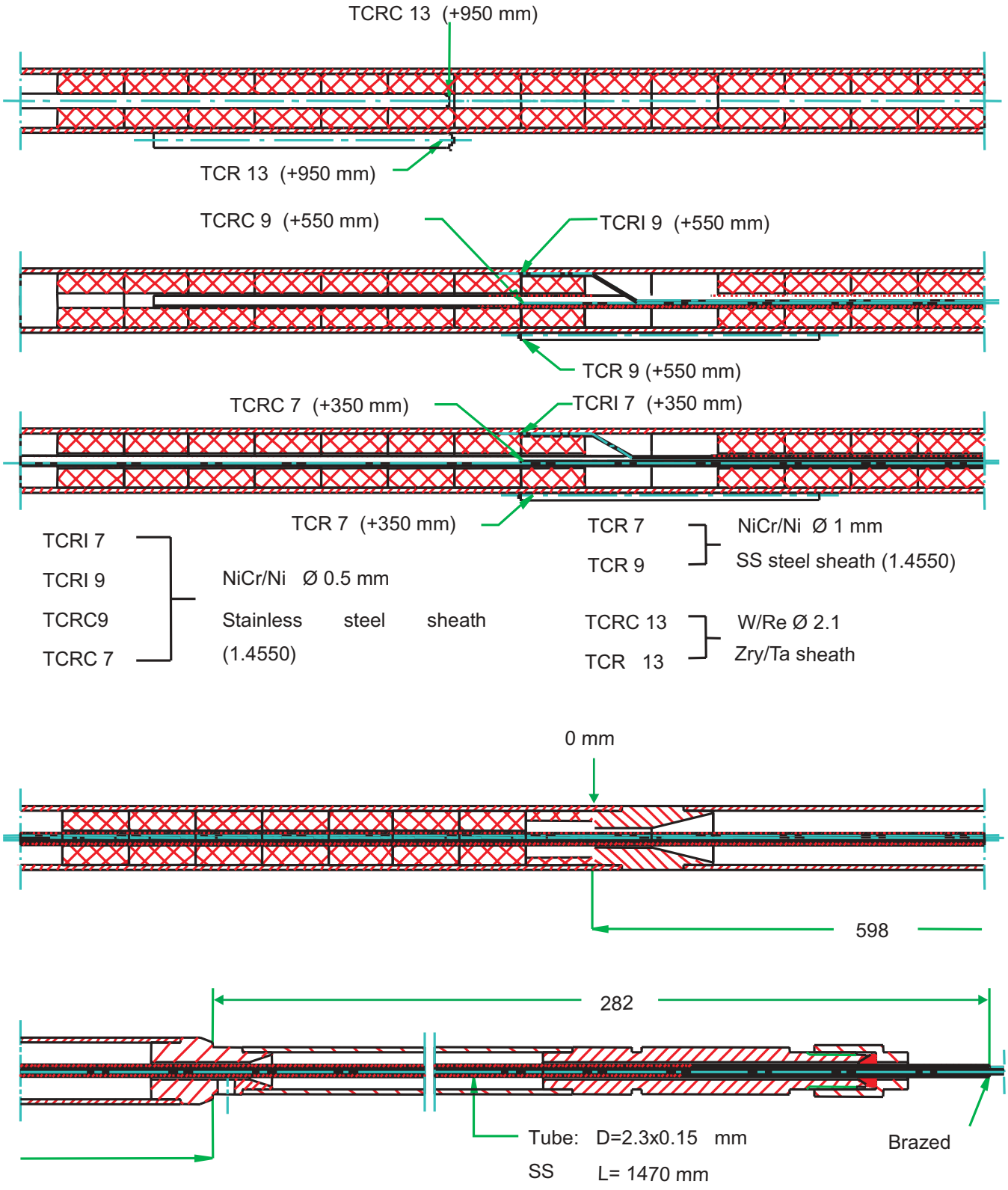

Fig. I-13: QUENCH-04; TC instrumentation of the unheated fuel rod simulator

Fig 13 QUE04-Stab unbeheizt.cdr
11.03.02 - IMF

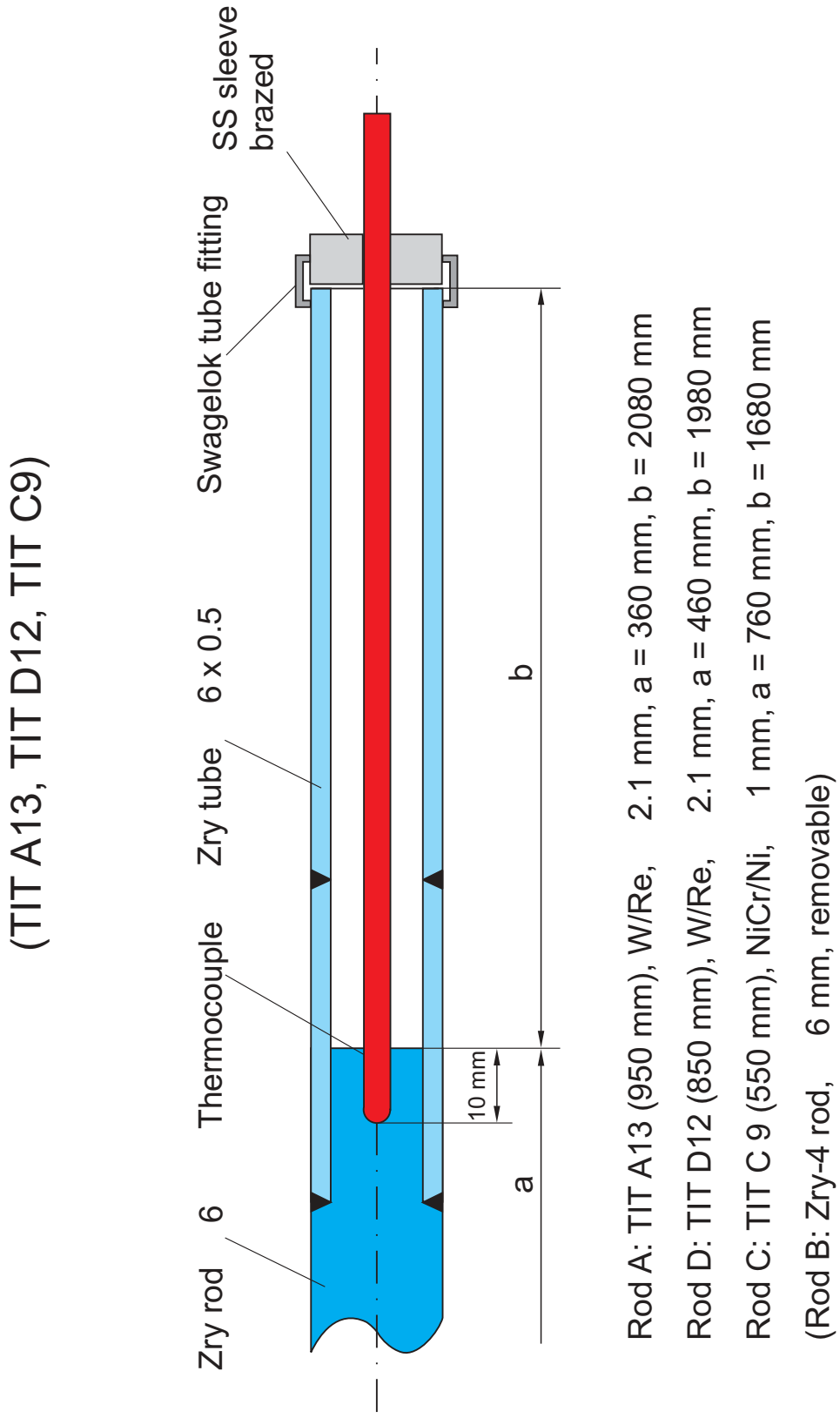

Fig. I-14: QUENCH-04; Schematic of the arrangement of the thermocouples inside the corner rods

Fig 14 QUE04 TC in Zry-rod.cdr
15.10.01 - IMF

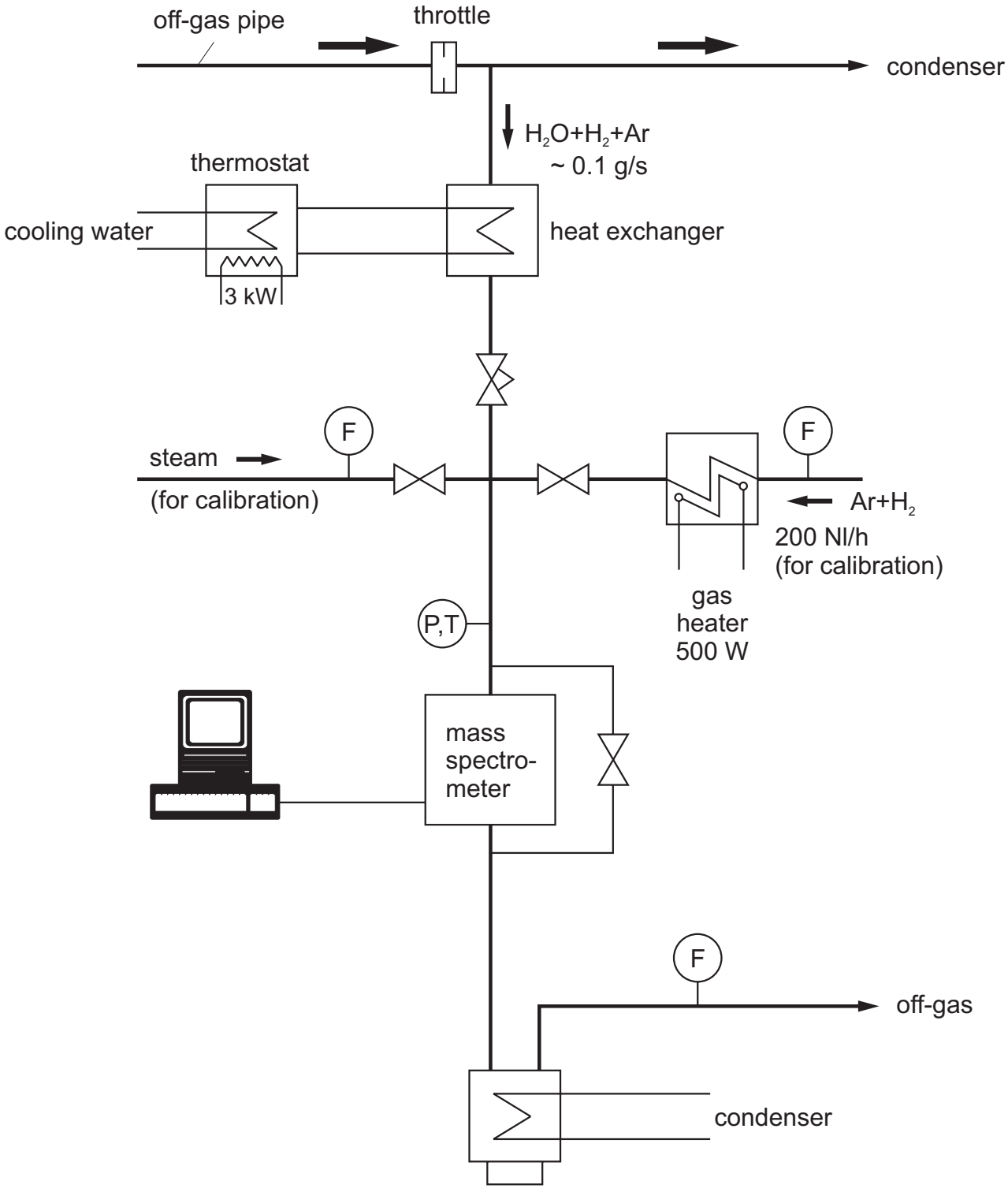

Fig. I-15: QUENCH-Facility; H_2 measurement with the mass spectrometer

Fig 15 QUE04 MS QUENCH-Facility.cdr
07.11.01 - IMF

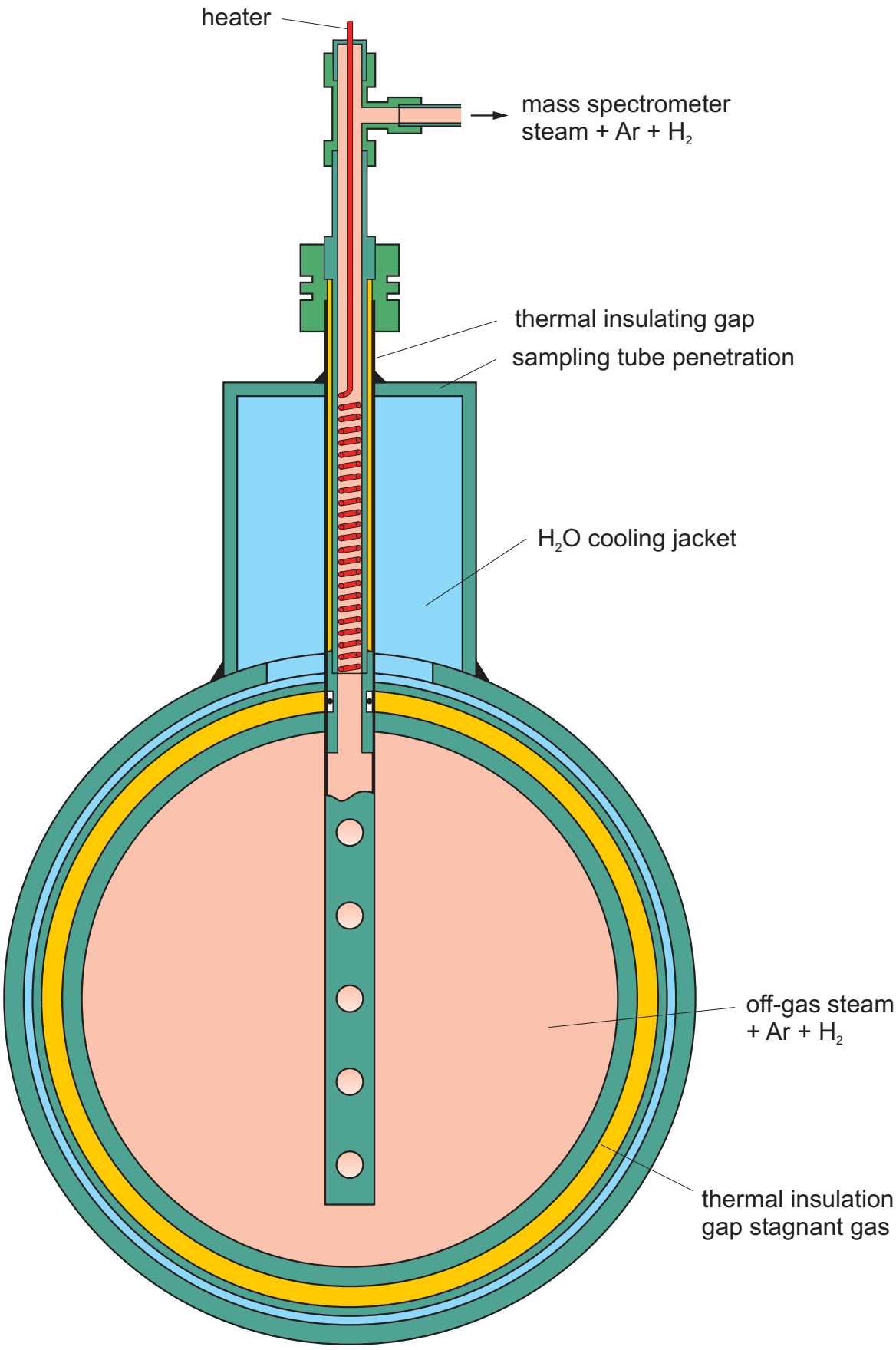

Fig. I-16: QUENCH; Mass spectrometer sampling position at the off-gas pipe

Fig 16 QUE04 MS sampling position new.cdr
15.10.01 - IMF

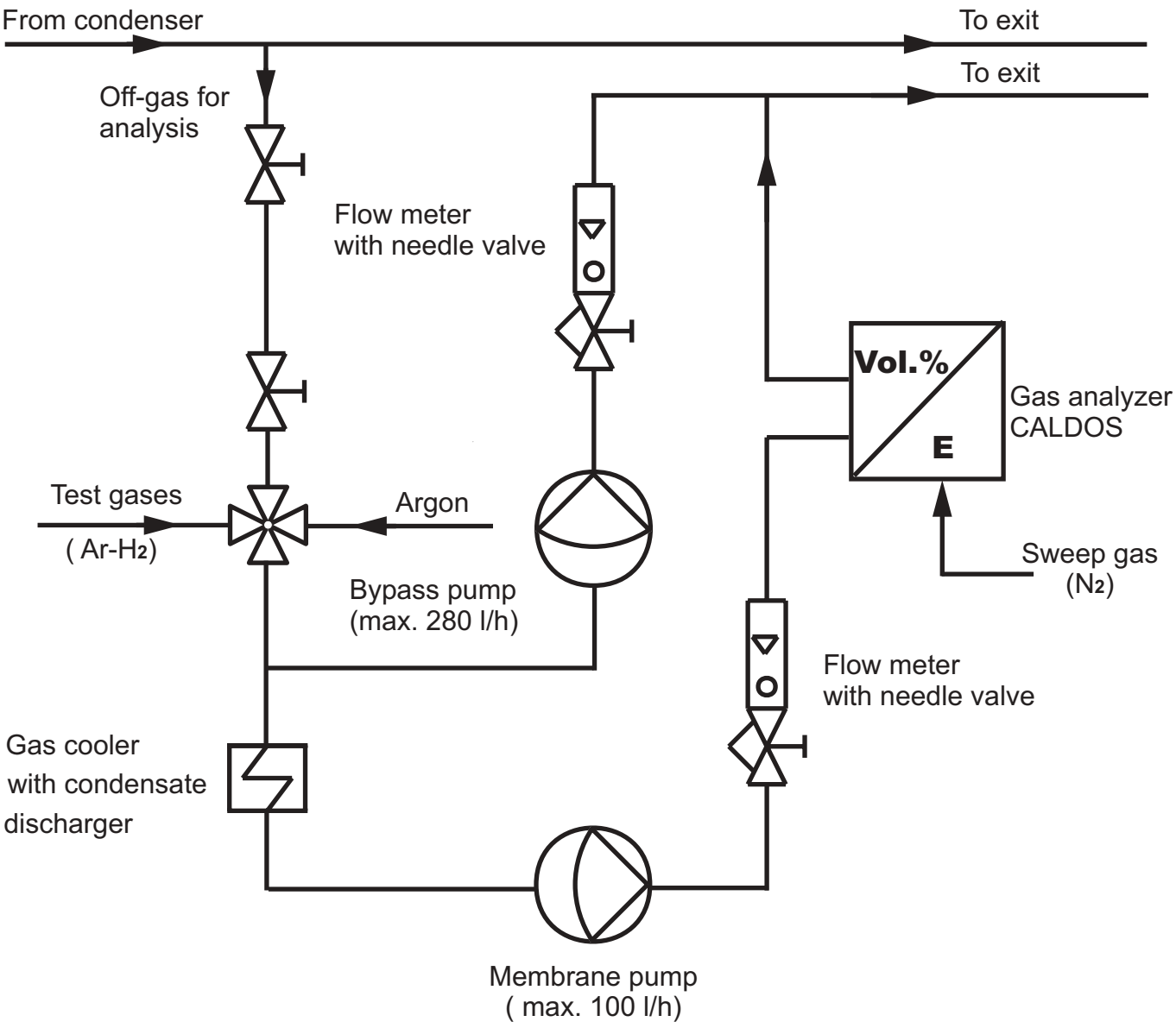

Fig. I-17: QUENCH-04; Hydrogen measurement with the CALDOS analyzer

Fig 17 QUE04 Caldos Schema (ab QUE04).cdr
07.11.01 - IMF

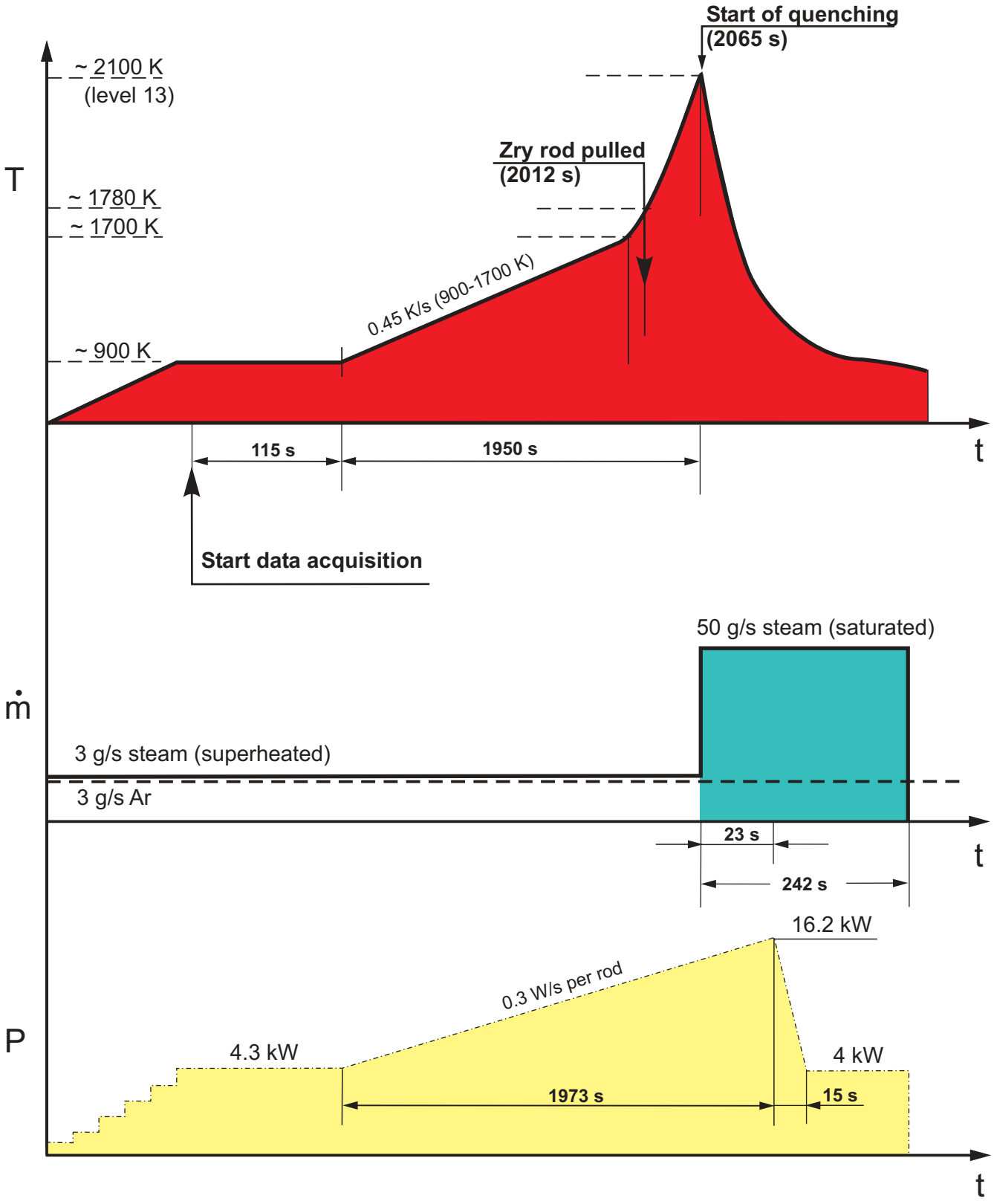

Fig. I-18: Test conduct QUENCH-04 (schematic)

Fig 18 QUE04 Test conduct.cdr
15.10.01 - IMF

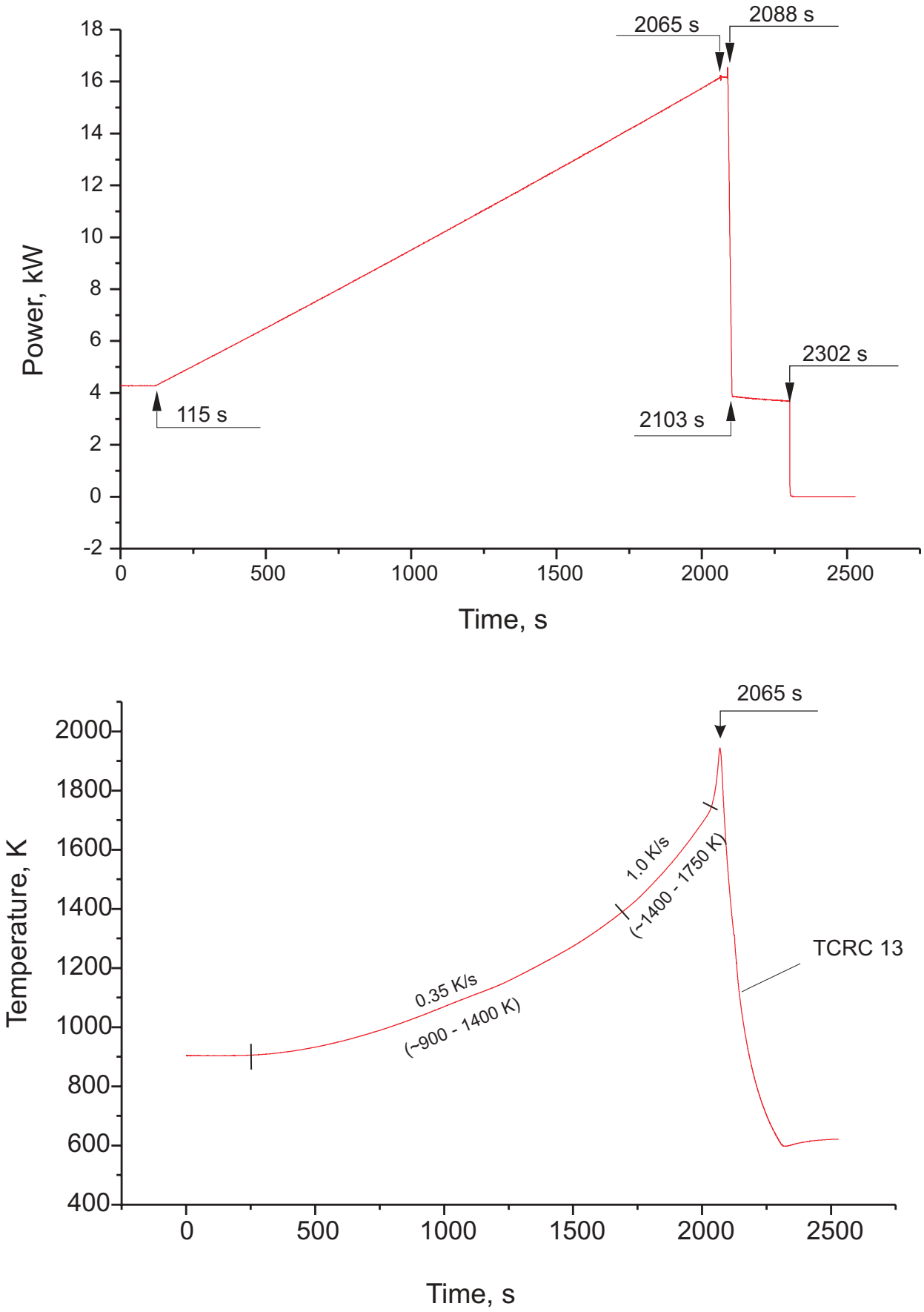

Fig. I-19: QUENCH-04; Total electric power, top, and heatup rates, bottom

Fig.19-QUE04-Leistung.cdr
01.10.01 - IMF

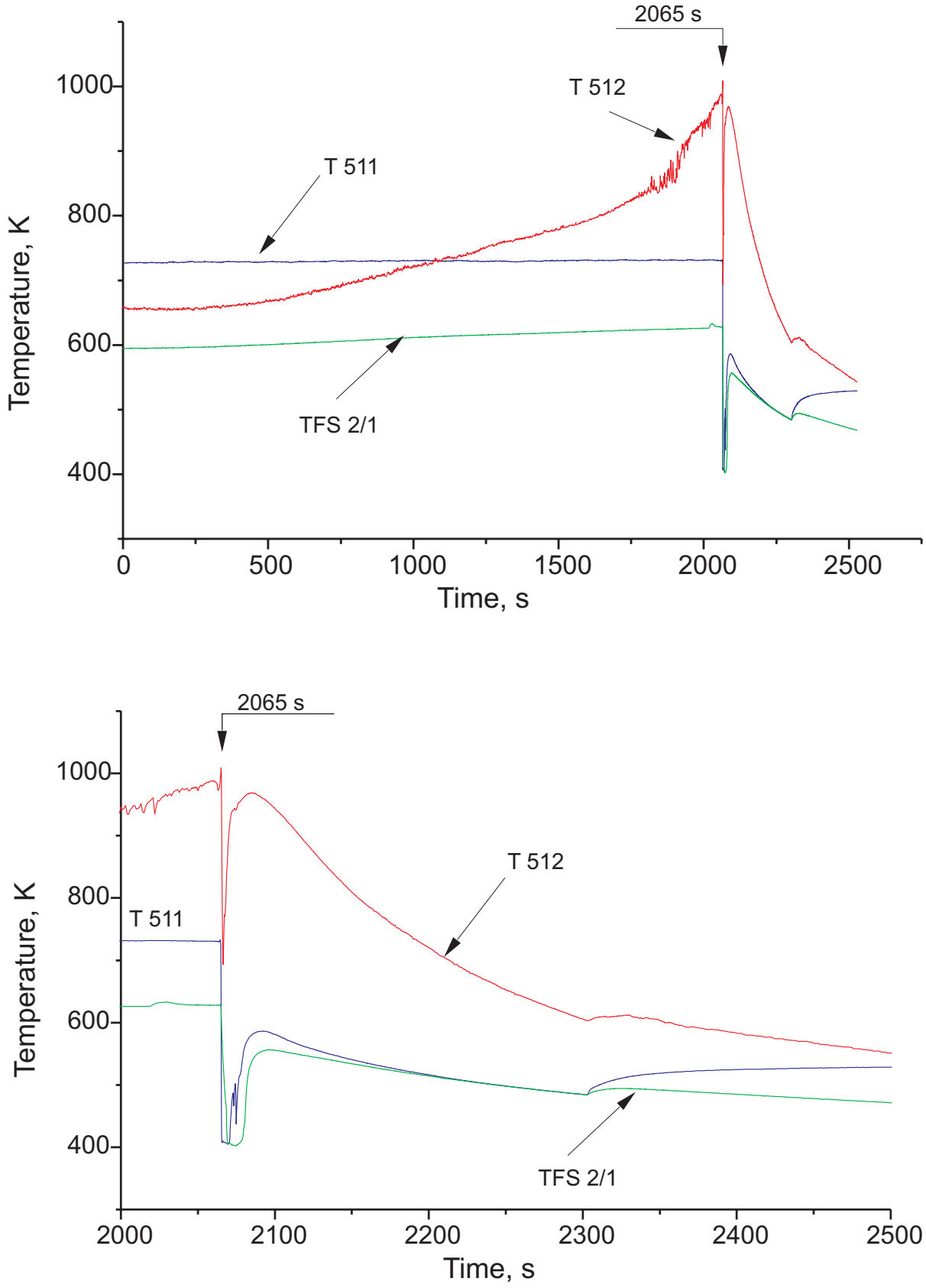

Fig. I-20: QUENCH-04; Coolant temperatures T 511 at bundle inlet, T 512 at bundle outlet, and TFS 2/1 at -250 mm

Fig.20-QUE04-Coolant temp.cdr
01.10.01 - IMF

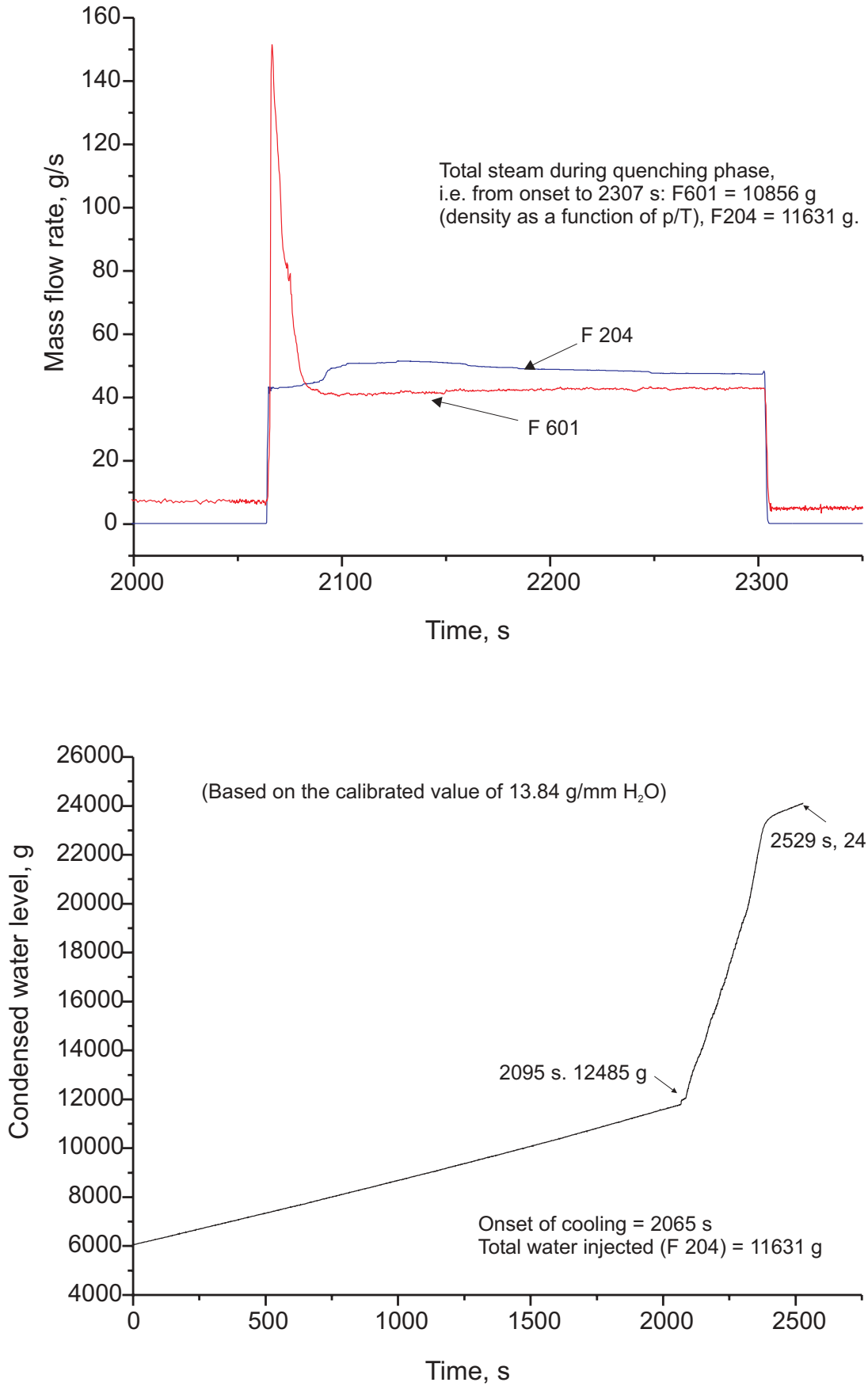

Fig. I-21: QUENCH-04; Comparison of cooldown steam input (F 204) and flow measurements F 601 in the off-gas pipe, top, and water level in the condensate collector L 701, bottom

Fig.21-QUE04-F601+L701.cdr
01.10.01 - IMF

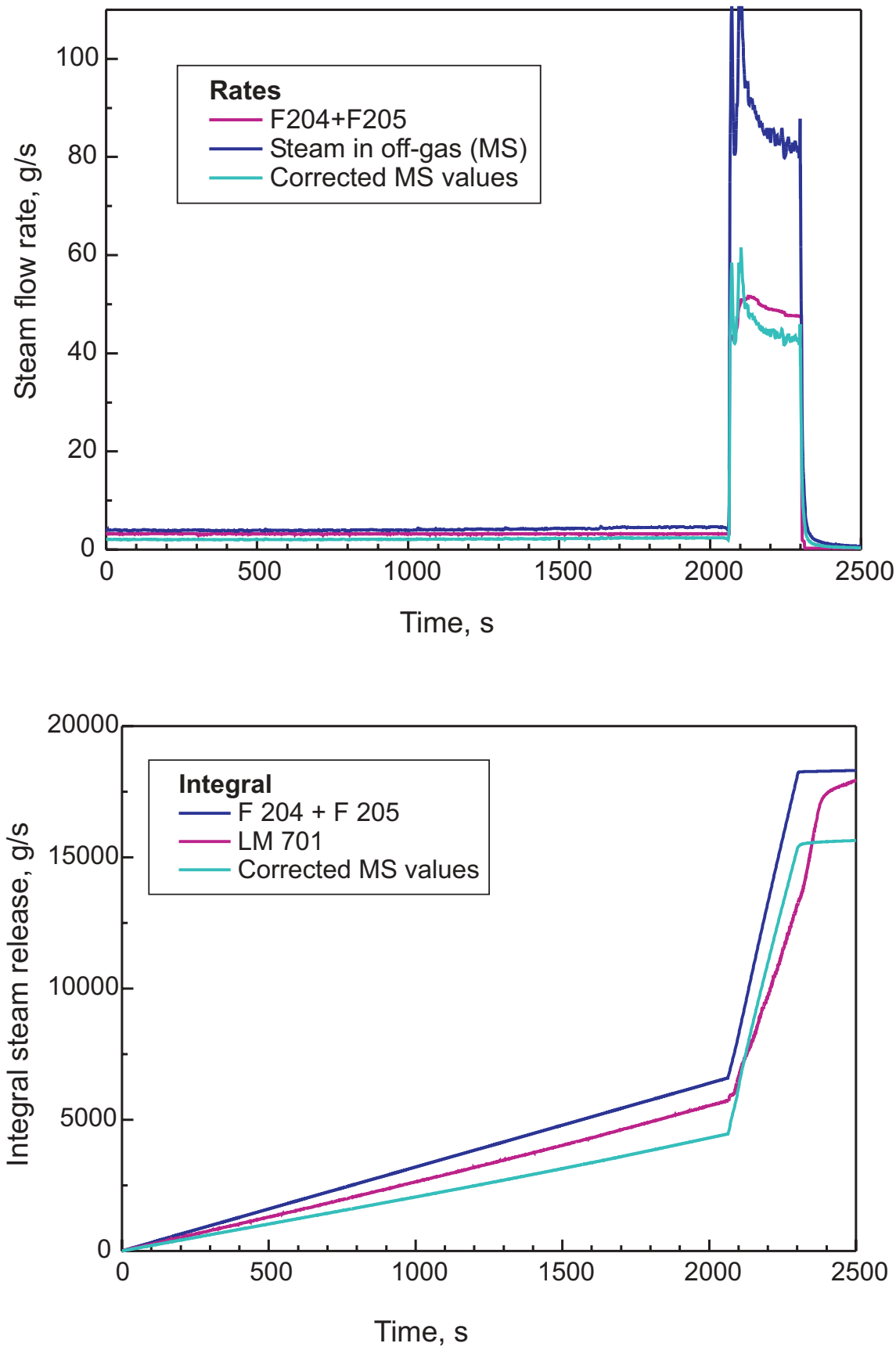

Fig. I-22: QUENCH-04; Comparison of cooldown steam input (F 204+F 205) and steam flow rates measured by the MS, top, and of integral values of F 204+F 205, MS steam, and LM 701, bottom

Fig.22-QUE04-F205+205.cdr
01.10.01 - IMF

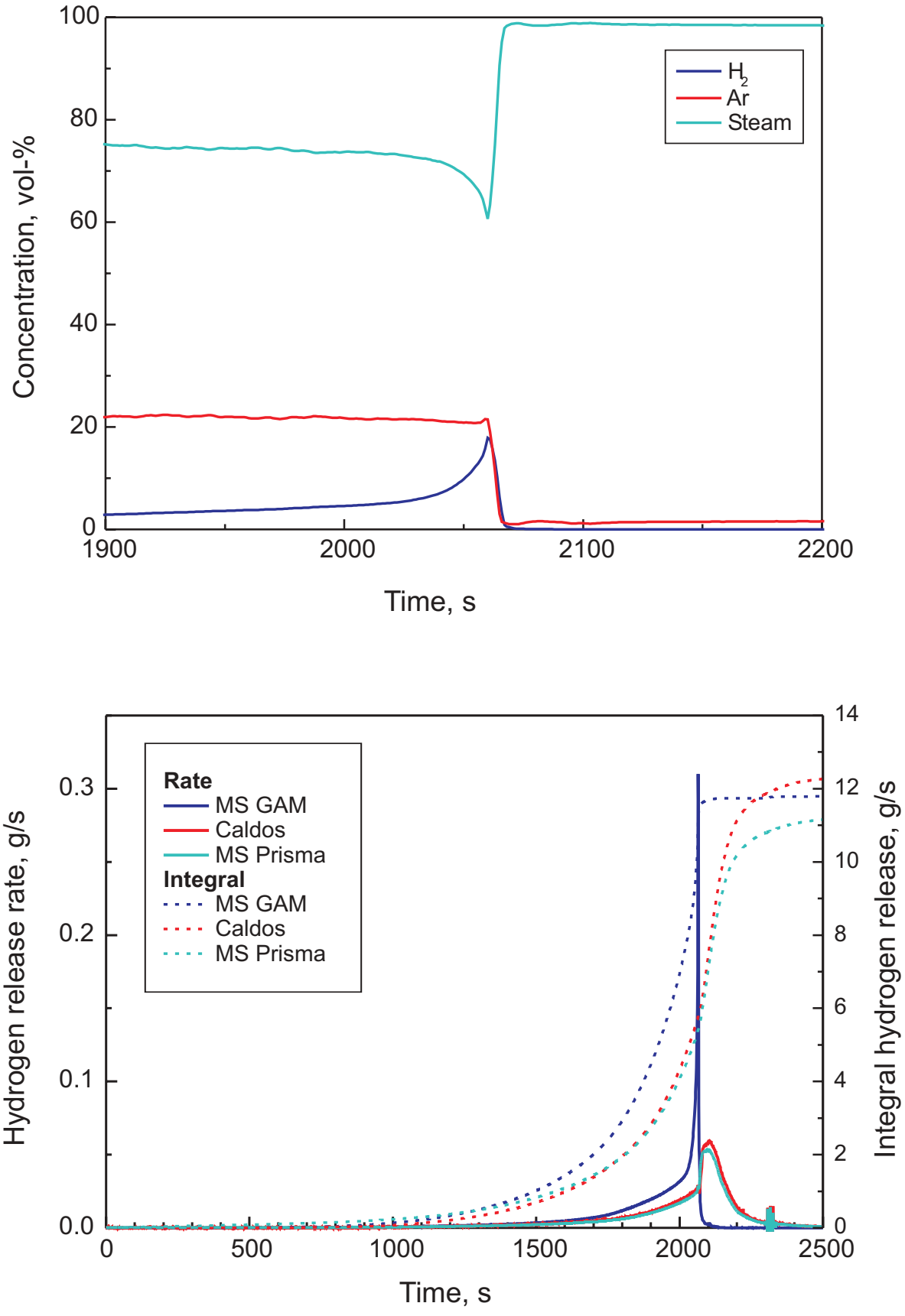

Fig. I-23: QUENCH-04; Concentrations of the main off-gas components measured by the MS, top, and hydrogen release measured by the two MS and Caldos, bottom

Fig.23-QUE04-MS&Caldos.cdr
14.11.01 - IMF

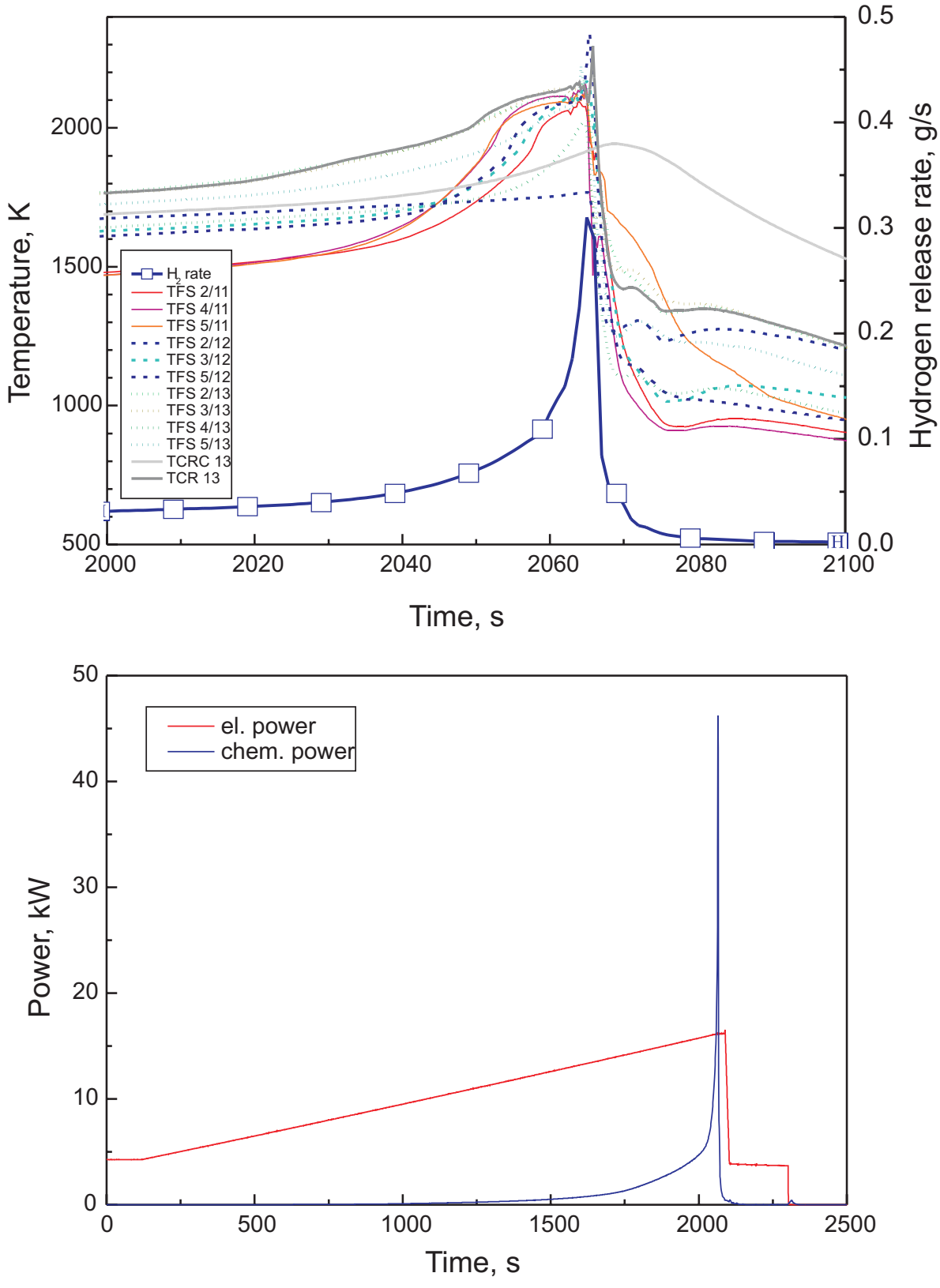

Fig. I-24: QUENCH-04; Temperature excursions at the 750 mm and 850 mm elevations together with the hydrogen release measured by the MS, top, and chemical power (produced by the exothermal Zircaloy-steam reaction) together with the electric power, bottom

Fig.24-QUE04-Temperature excursion.cdr
02.10.01 - IMF

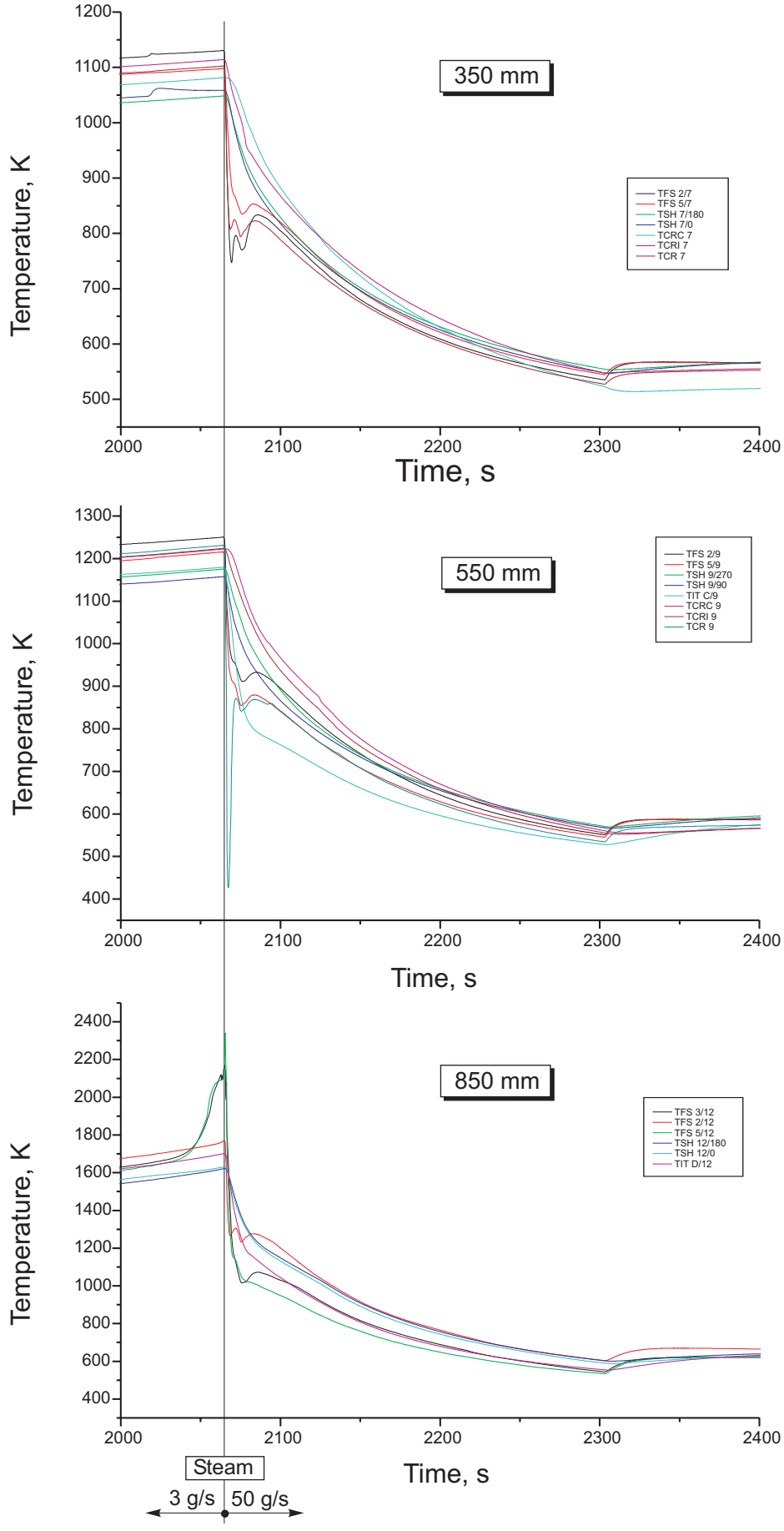

Fig. I-25: QUENCH-04; Typical temperature response during cooldown with steam at 350 mm, 550 mm, and 850 mm elevation

Fig.25-QUE04-Temperature response.cdr
21.02.02 - IMF

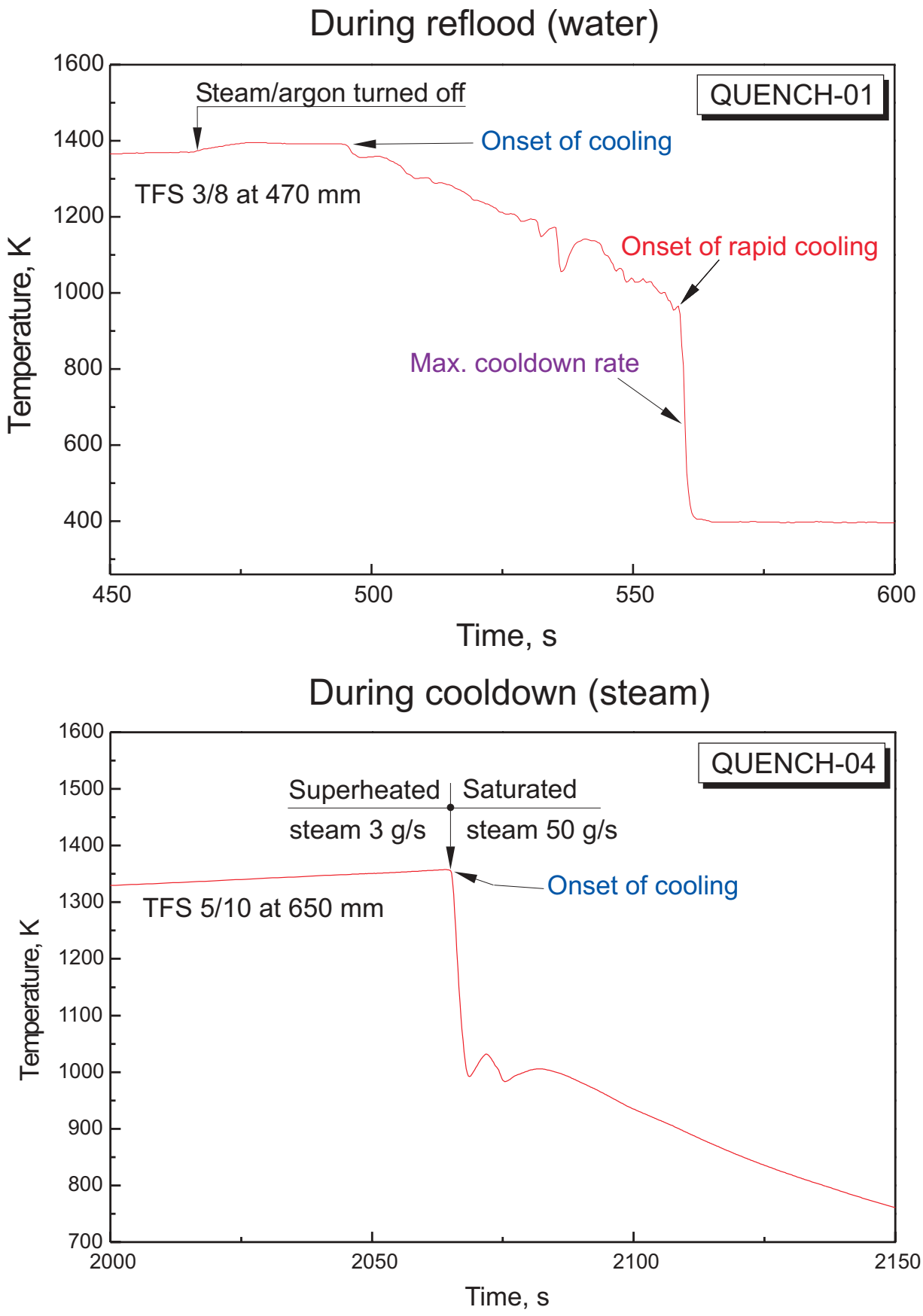

Fig. I-26: QUENCH-04; Typical temperature response during reflood with water and during cooldown with steam

Fig.26-QUE04-Typical-temp(QUE01 u. QUE04).cdr
09.10.01 - IMF

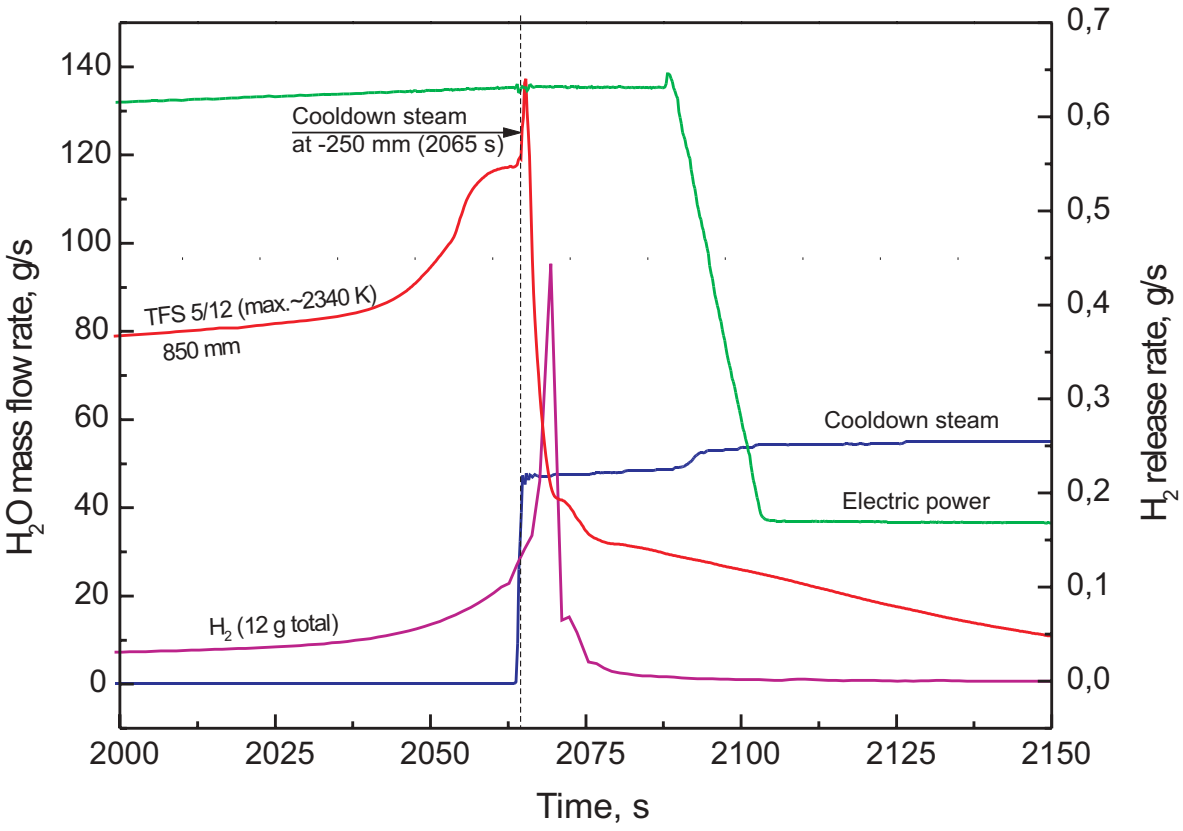

Fig. I-27: QUENCH-04; Time dependence of the electric bundle power input, characteristic rod temperature, cooldown steam flow, and of the hydrogen release rate measured by the mass spectrometer, at the initiation of the flooding phase.

Fig.27-QUE04-Zeitbezug.cdr
08.10.01 - IMF

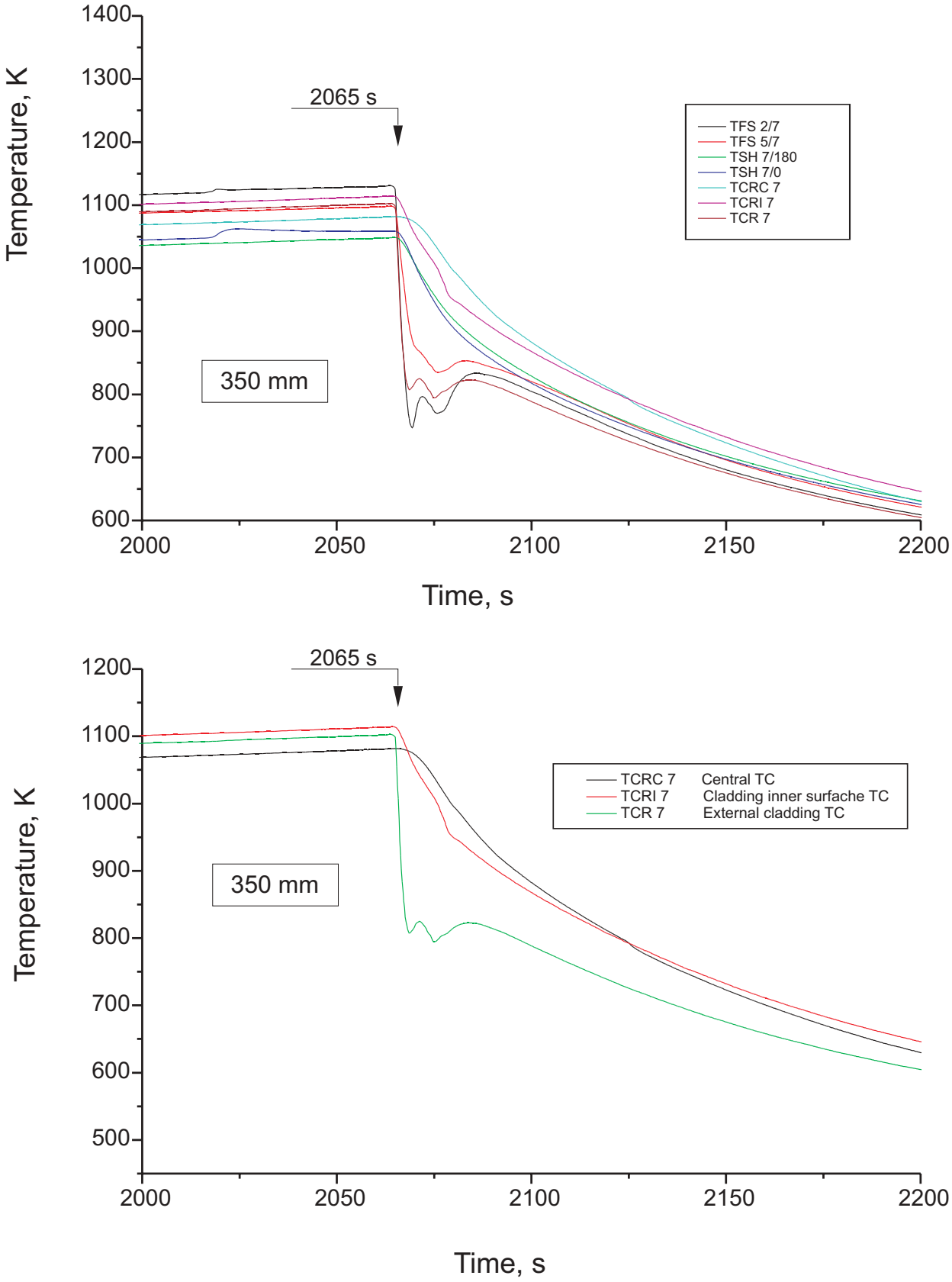

Fig. I-28: QUENCH-04; Temperatures measured by rod cladding outer surface (TFS), shroud (TSH), central rod centerline (TCRC), central rod cladding inner surface (TCRI), and central rod cladding outer surface (TRC) thermocouples at 350 mm elevation

Fig.28-QUE04-Temp-Zeit-ebe7.cdr
02.10.01 - IMF

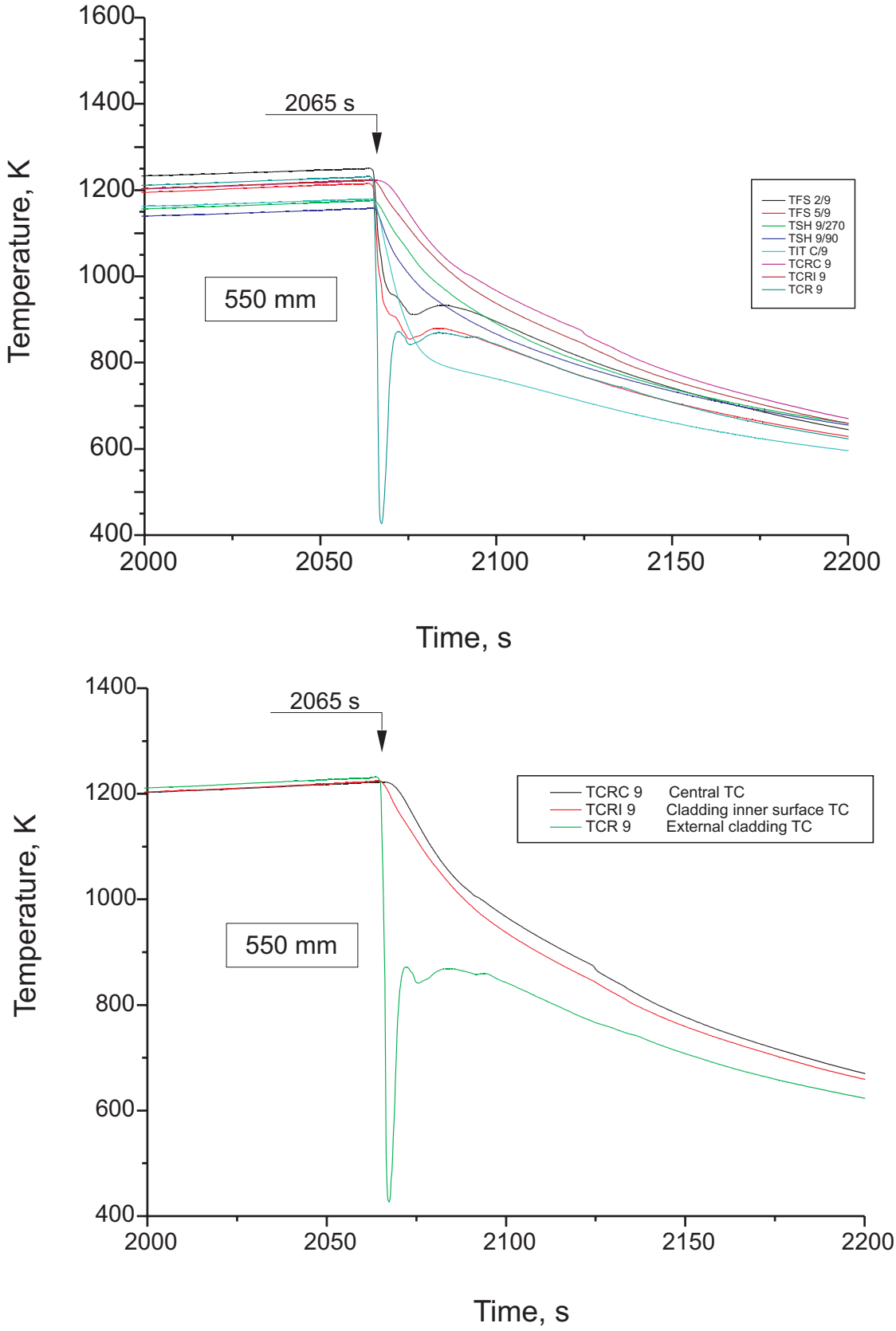

Fig. I-29: QUENCH-04; Temperatures measured by rod cladding outer surface (TFS), shroud (TSH), central rod centerline (TCRC), central rod cladding inner surface (TCRI), central rod cladding outer surface (TRC), and corner rod internal (TIT) thermocouples at 550 mm elevation

Fig.29-QUE04-Temp-Zeit-ebe9.cdr
07.11.01 - IMF

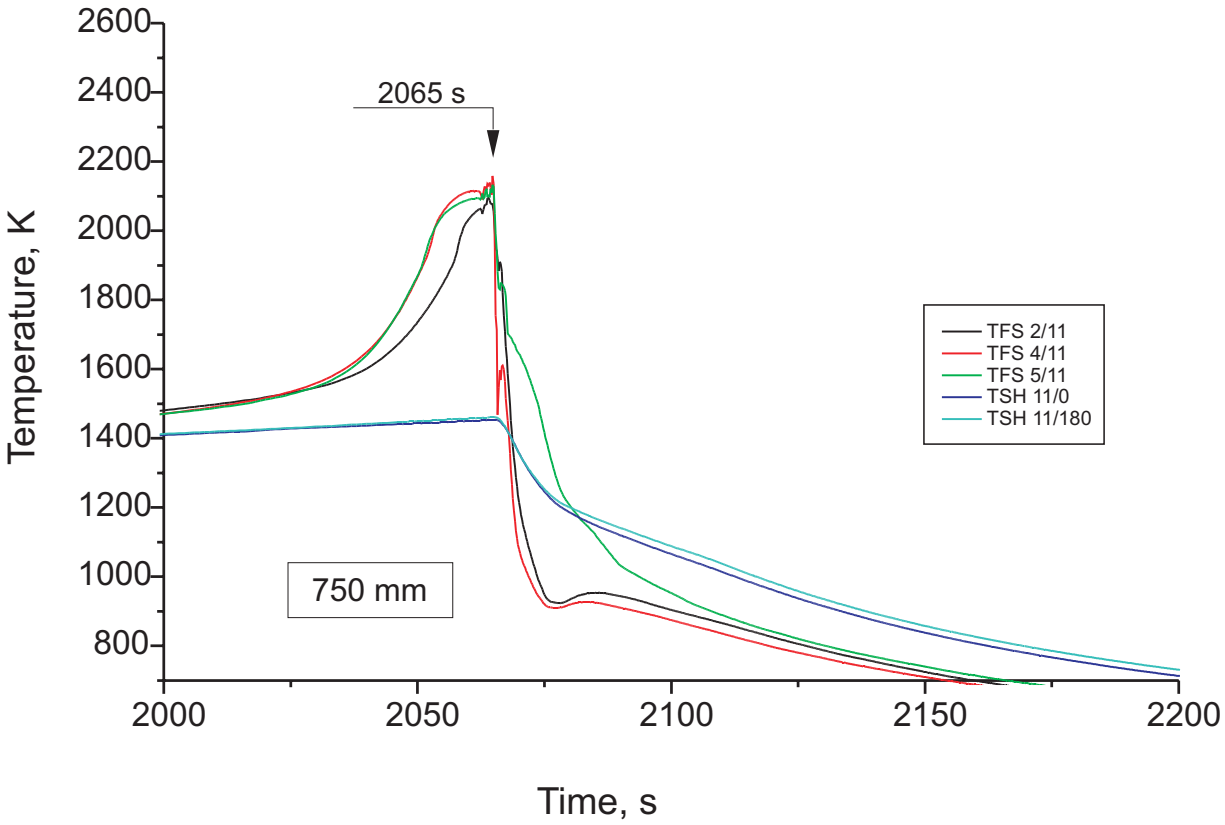

Fig. I-30: QUENCH-04; Temperatures measured by rod surface (TFS) and shroud (TSH) thermocouples at 750 mm elevation

Fig.30-QUE04-Temp-Zeit-ebe11.cdr
04.10.01 - IMF

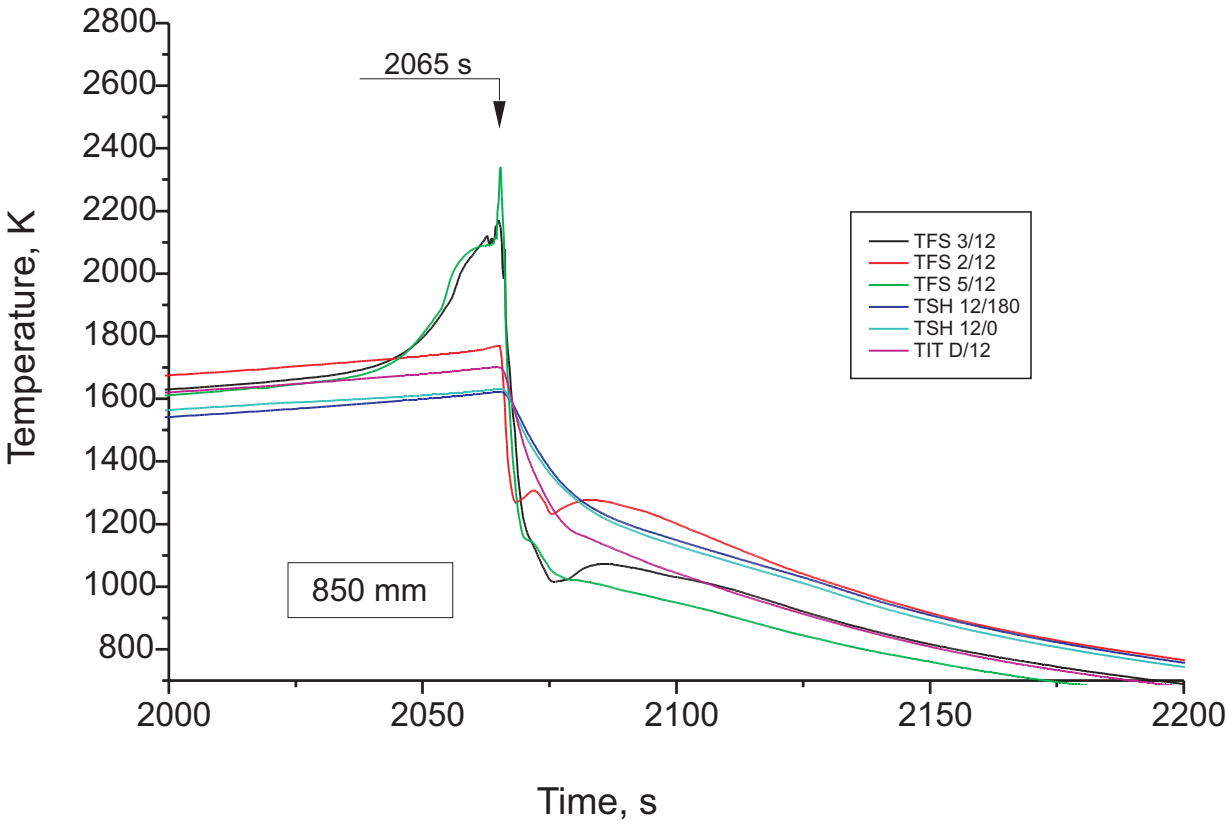

Fig. I-31: QUENCH-04; Temperatures measured by rod surface (TFS), shroud (TSH), and corner rod internal (TIT) thermocouples at 850 mm elevation

Fig.31-QUE04-Temp-Zeit-ebe12.cdr
04.10.01 - IMF

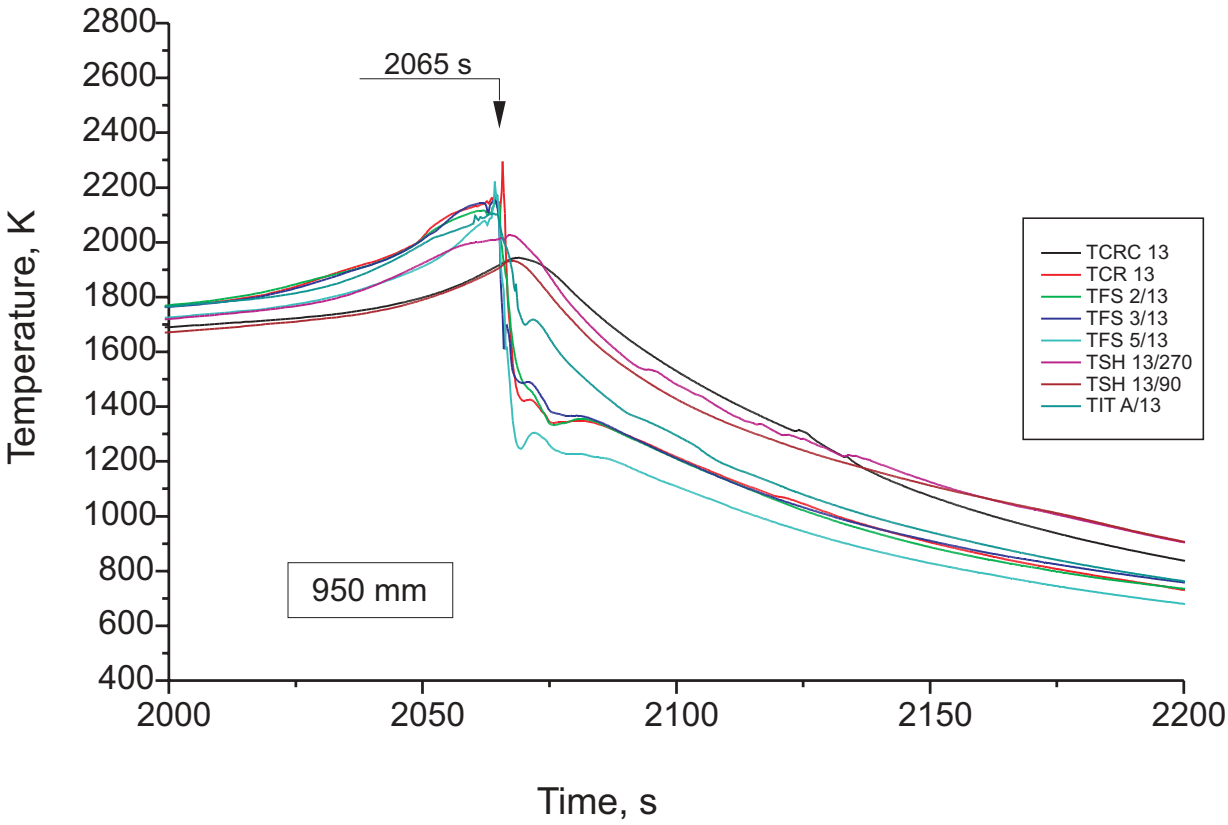

Fig. I-32: QUENCH-04; Temperatures measured by rod surface (TFS), shroud (TSH), central rod centerline (TCRC), central rod external (TRC), and corner rod internal (TIT) thermocouples at 950 mm elevation

Fig.32-QUE04-Temp-Zeit-ebe13.cdr
04.10.01 - IMF

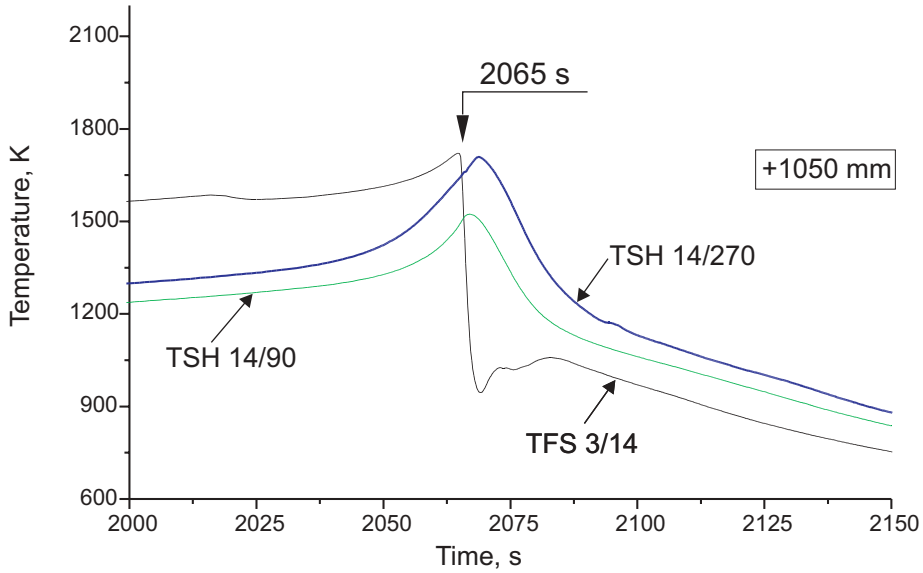

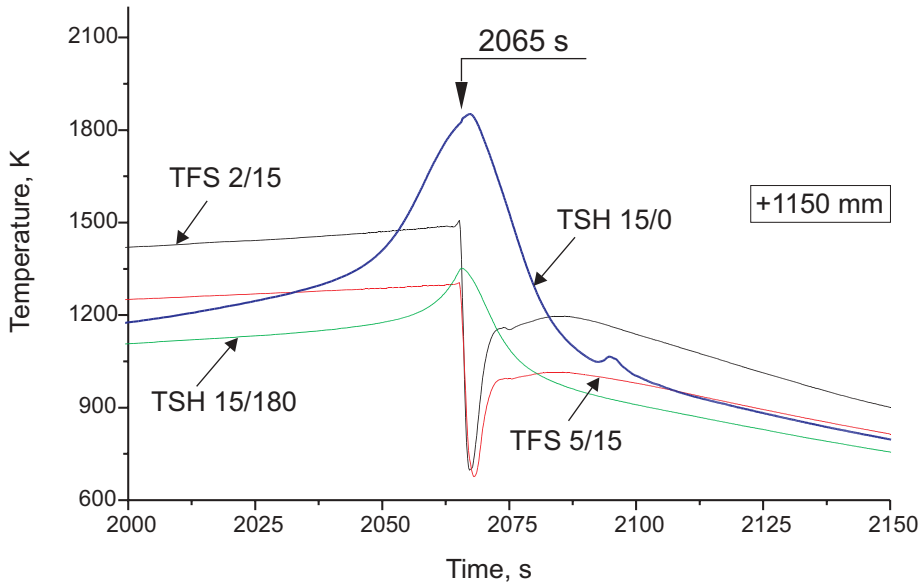

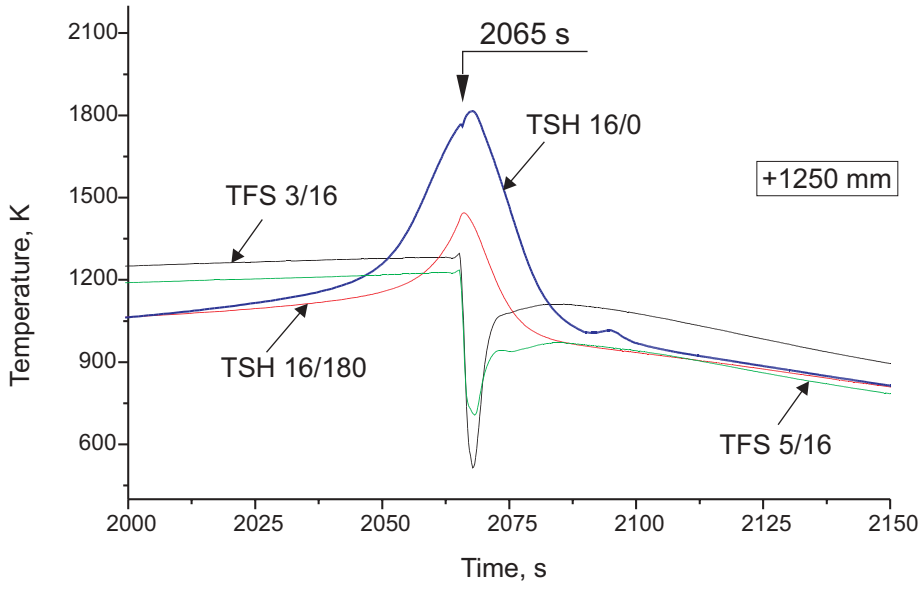

Fig. I-33: QUENCH-04; Temperature excursions at the upper shroud levels (1050 mm, 1150 mm, and 1250 mm elevation)

Fig.33-QUE04-Temperature excursion.cdr
09.10.01 - IMF

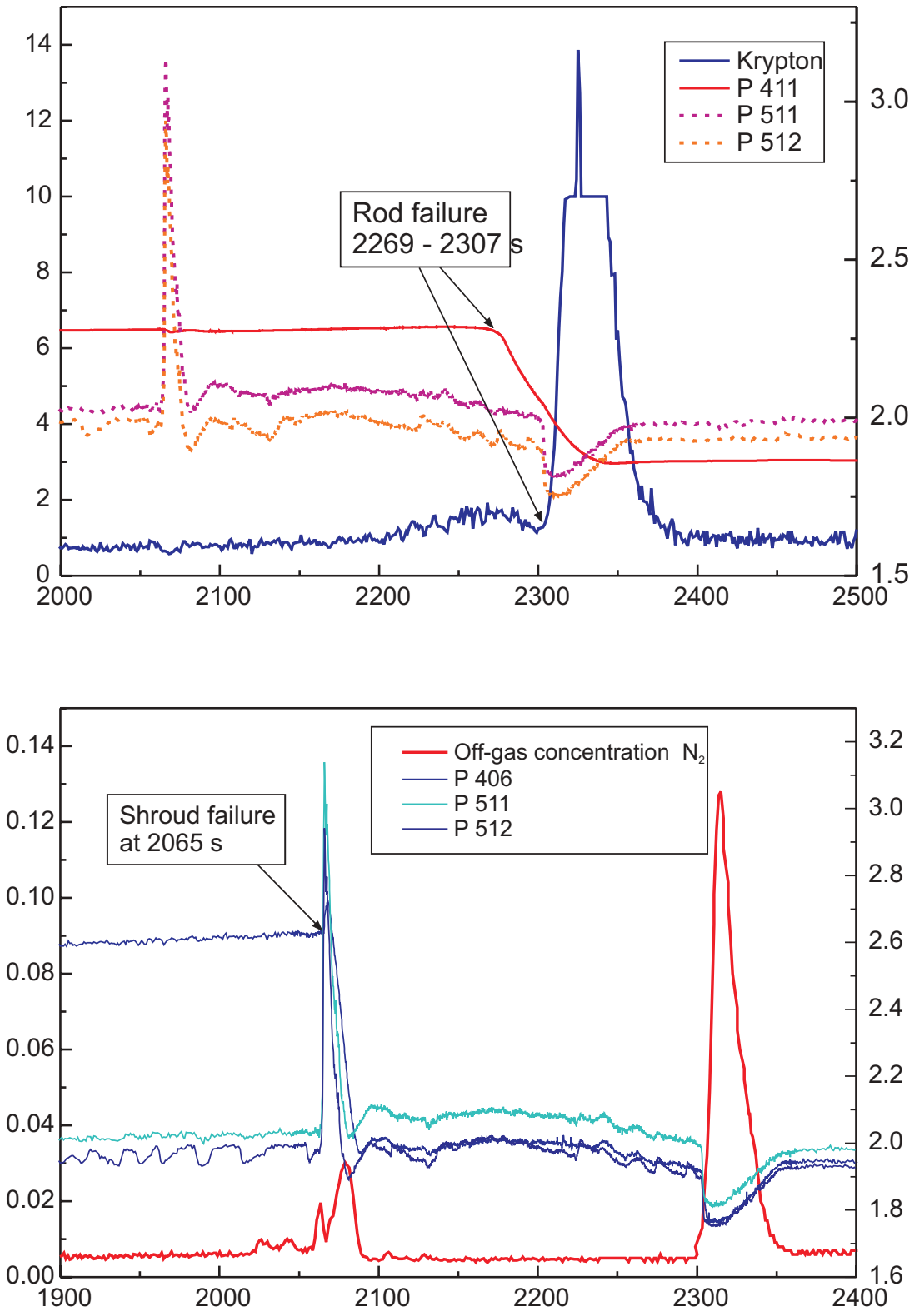

Fig. I-34: QUENCH-04; Rod internal pressure (P 411) and system pressure at test section inlet and outlet (P 511, P 512) together with the krypton concentration in the off-gas measured by the mass spectrometer, top, and shroud failure at the onset of cooling (2065 s) as indicated by the pressure P 406 measured in the space between shroud and inner cooling jacket and by the nitrogen concentration measured in the off-gas by the mass spectrometer, bottom

Fig.34-QUE04-pressure.cdr
04.10.01 - IMF

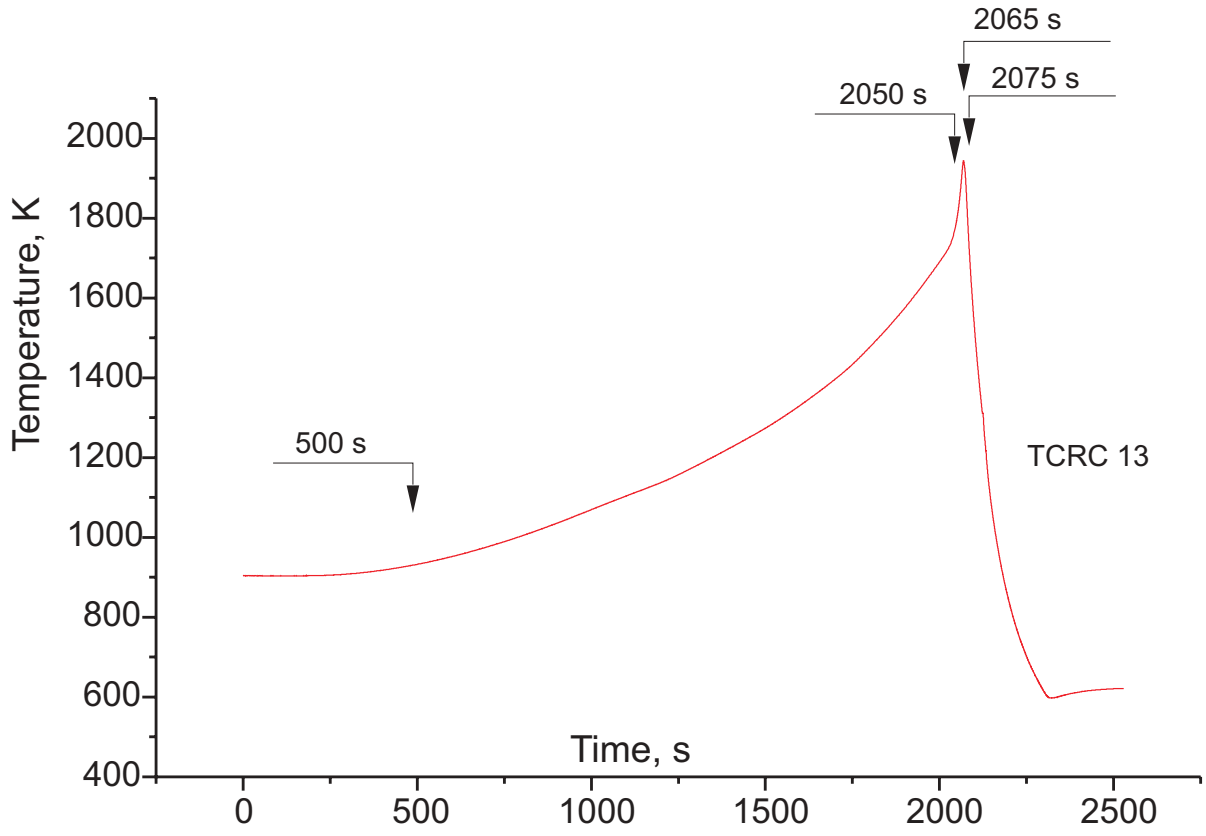

Fig. I-35: QUENCH-04; Selected times for the axial temperature profiles

Fig.35-QUE04-selected times.cdr
04.10.01 - IMF

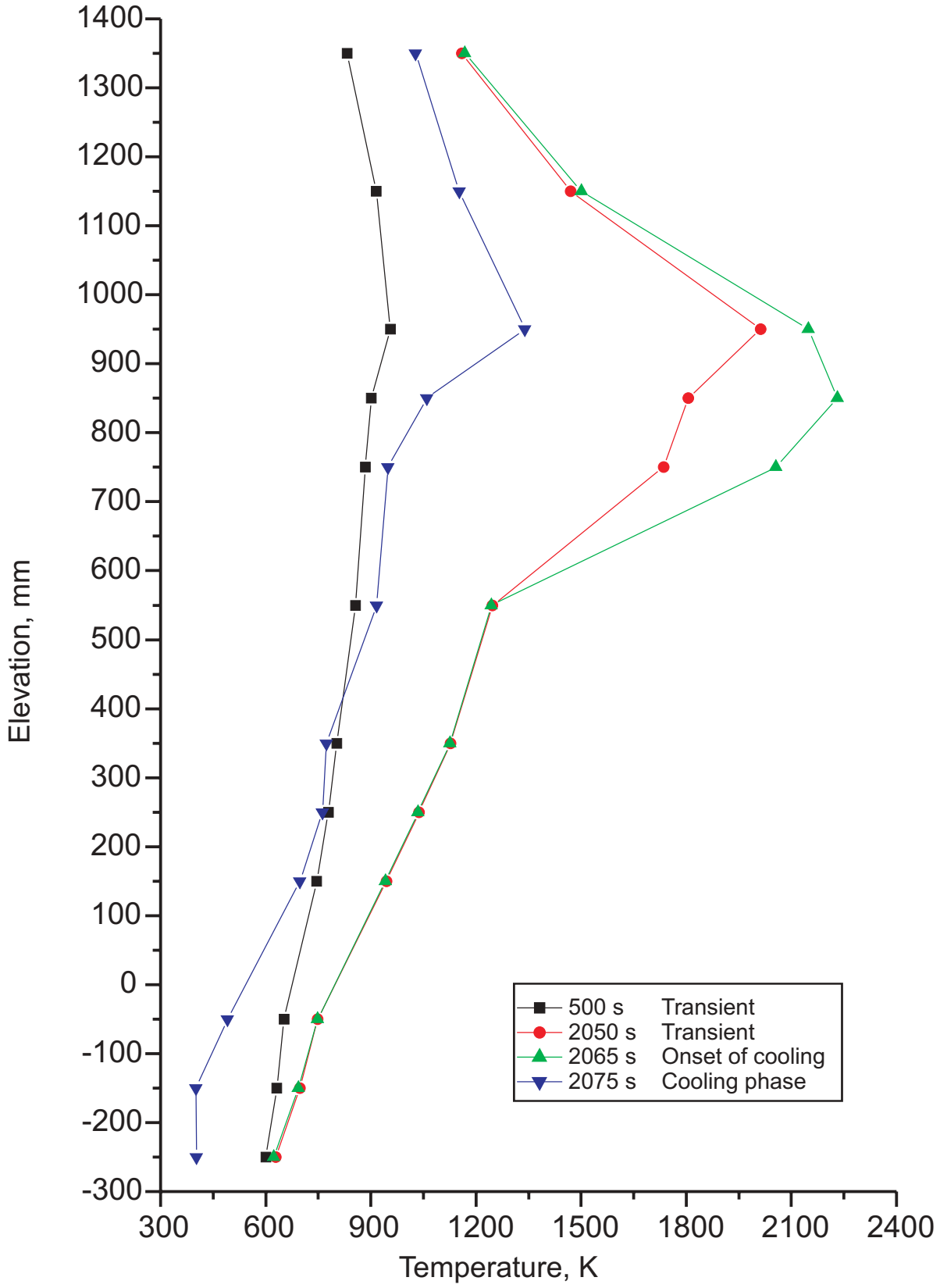

Fig. I-36: QUENCH-04; Axial temperature profile TFS 2 at 500 s, 2050 s 2065 s, 2075 s

Fig.36-QUE04-Axial TFS 2.cdr
08.10.01 - IMF

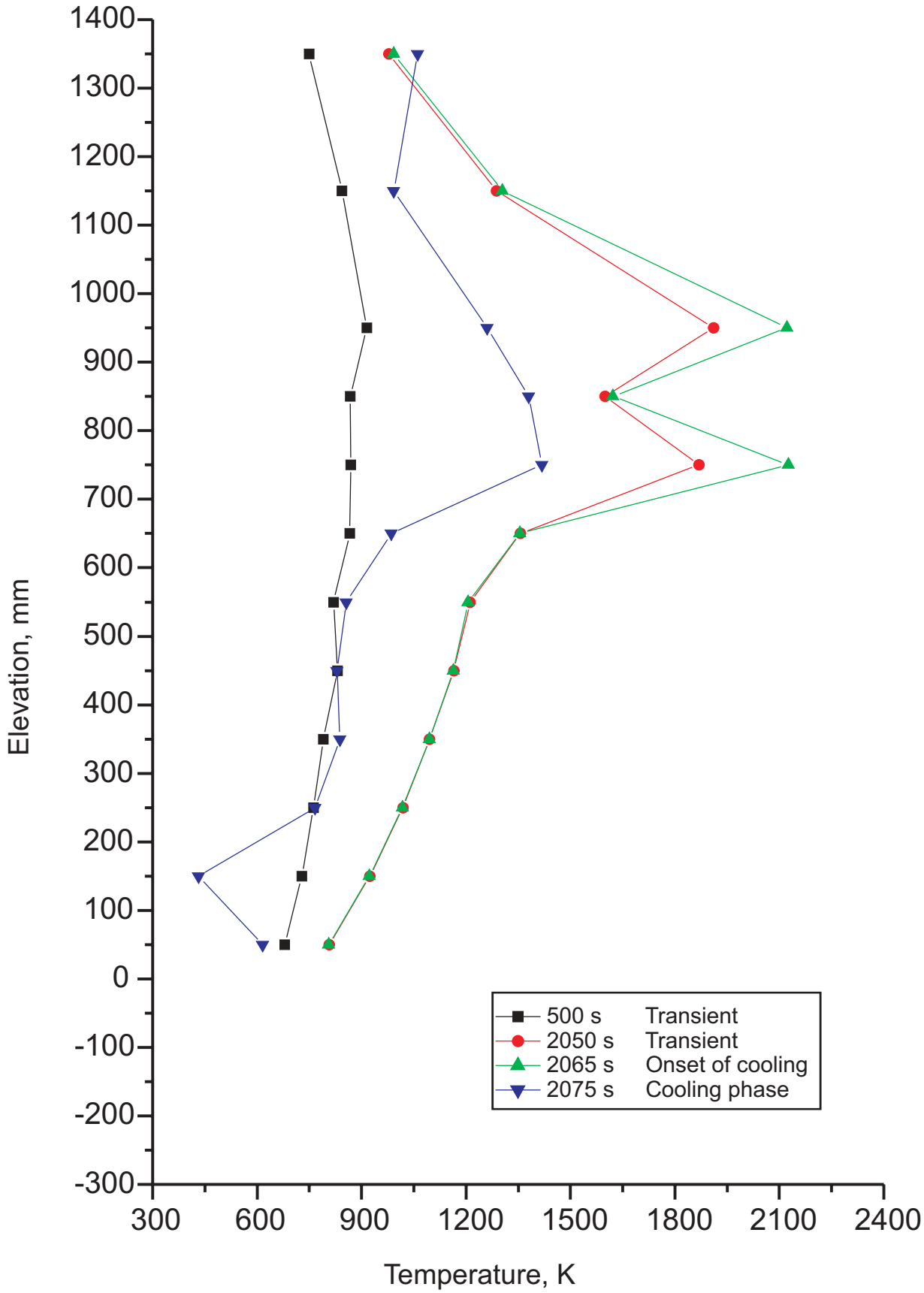

Fig. I-37: QUENCH-04; Axial temperature profile TFS 5 at 500 s, 2050 s 2065 s, 2075 s

Fig.37-QUE04-Axial TFS 5.cdr
08.10.01 - IMF

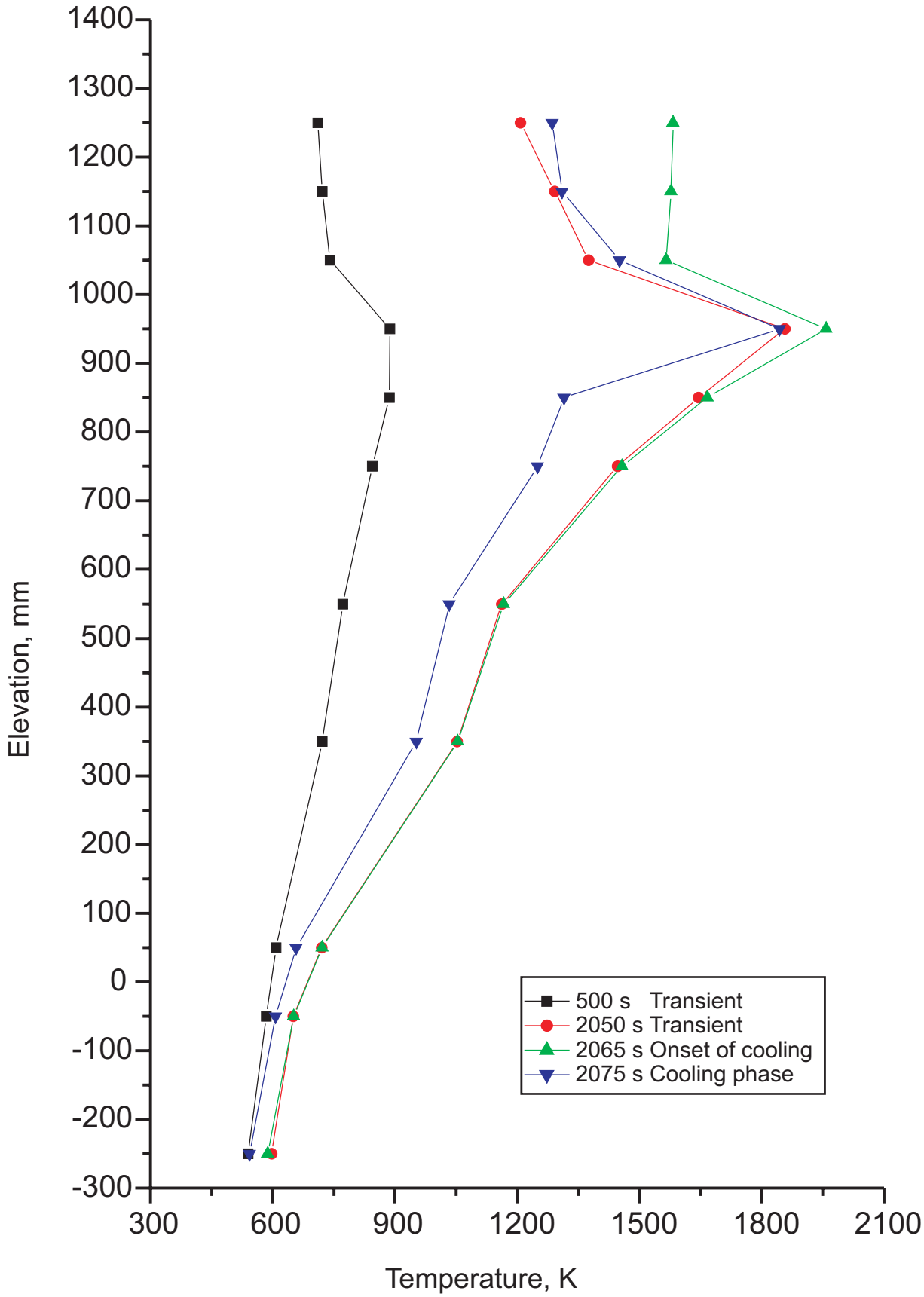

Fig. I-38: QUENCH-04; Axial temperature profile TSH at 500 s, 2050 s 2065 s, 2075 s

Fig.38-QUE04-Axial TSH.cdr
08.10.01 - IMF

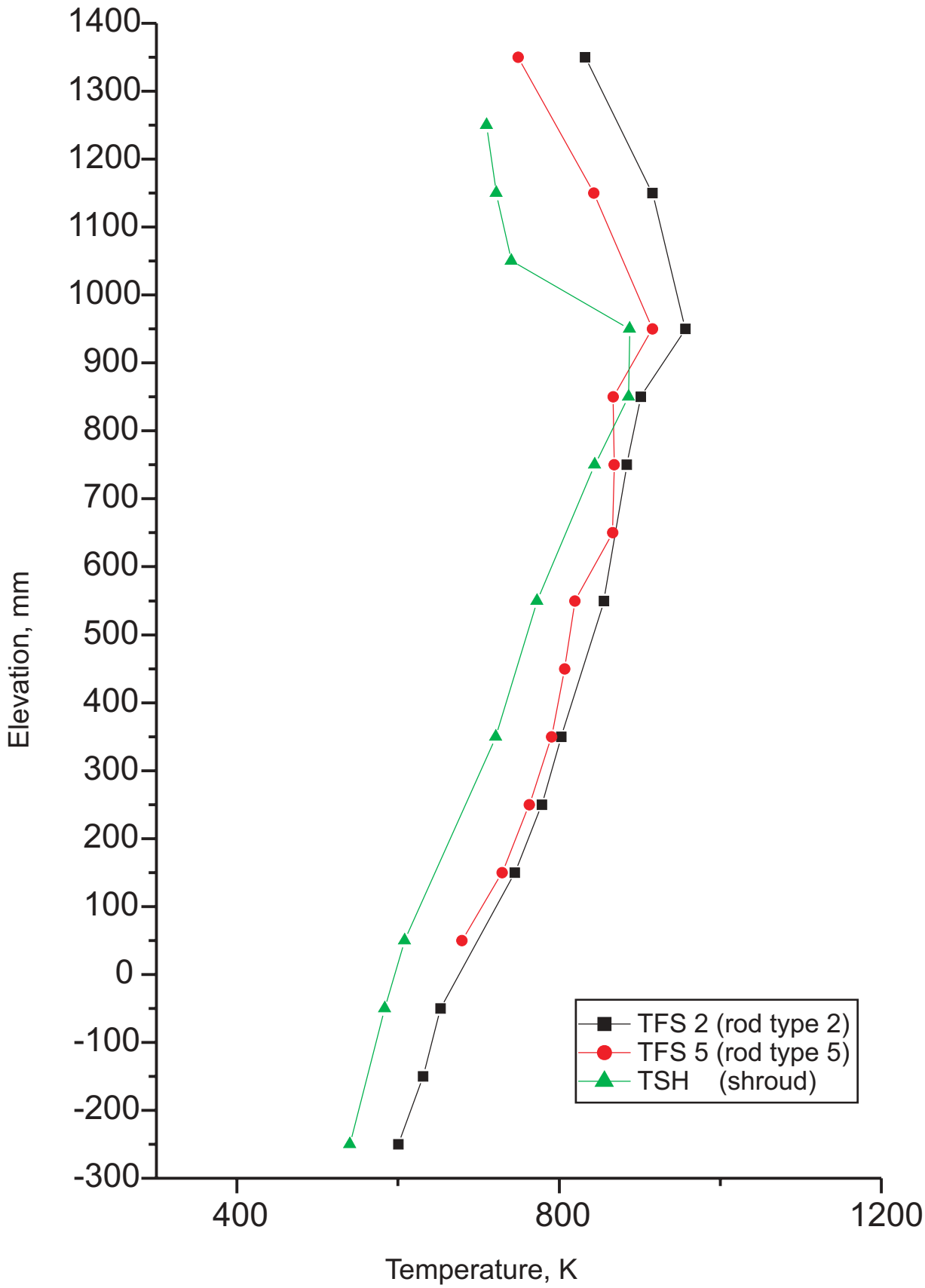

Fig. I-39: QUENCH-04; Axial temperature profile TFS 2, TFS 5,TSH at 500 s (transient)

Fig.39-QUE04-Axial 500s.cdr
08.10.01 - IMF

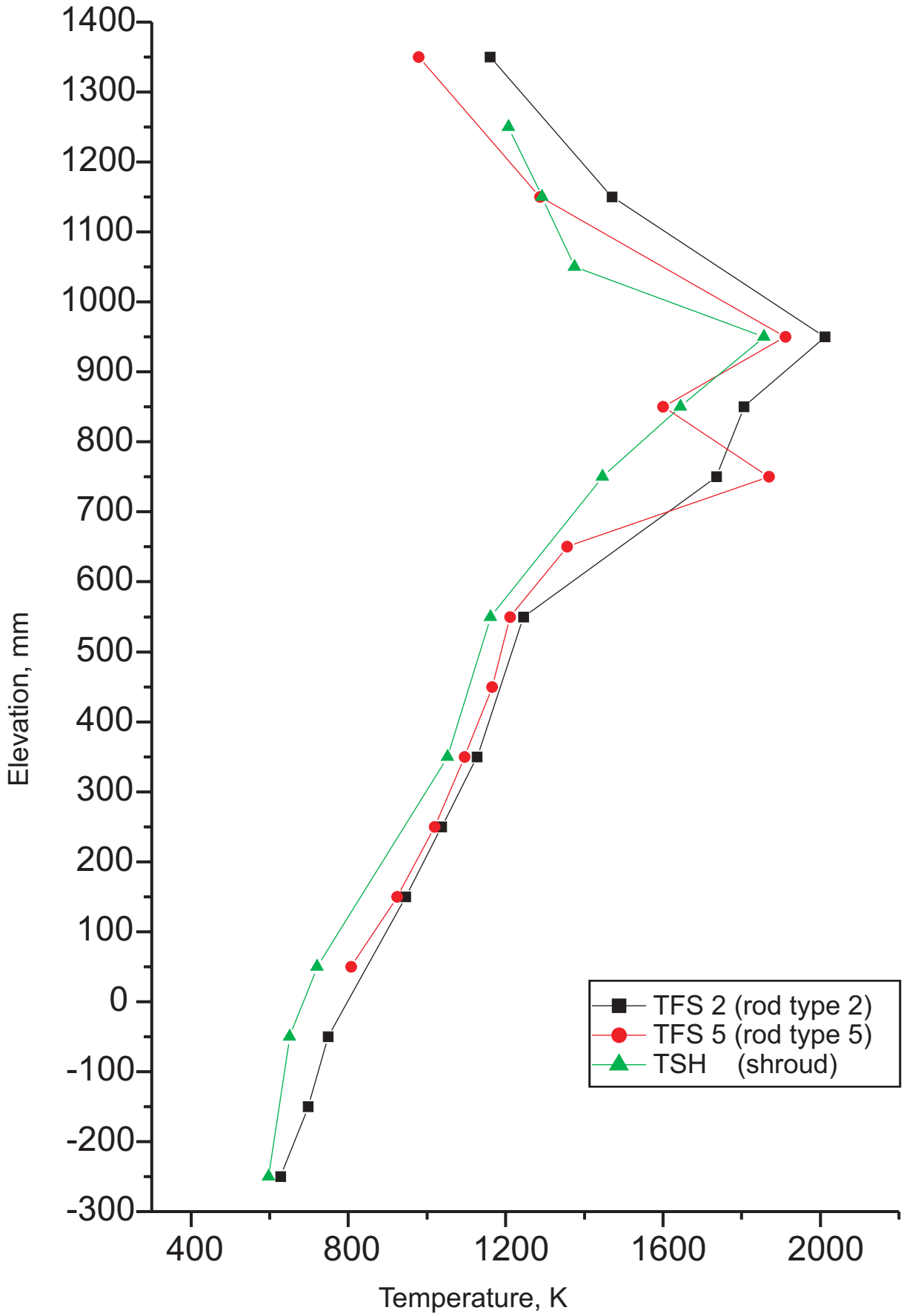

Fig. I-40: QUENCH-04; Axial temperature profile TFS 2, TFS 5,TSH at 2050 s (transient)

Fig.40-QUE04-Axial 2050s.cdr
08.10.01 - IMF

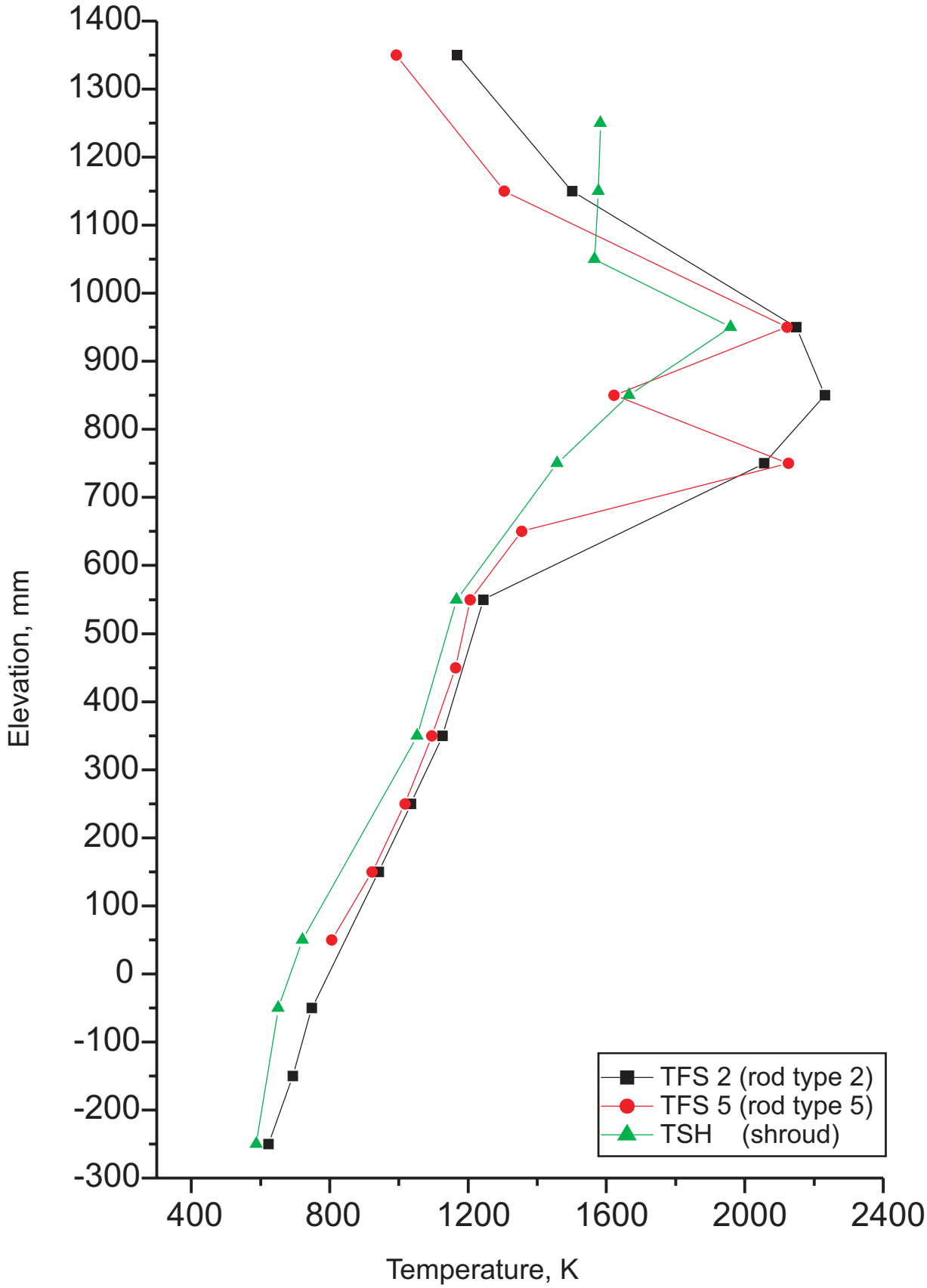

Fig. I-41: QUENCH-04; Axial temperature profile TFS 2, TFS 5,TSH at 2065 s (onset of cooling)

Fig.41-QUE04-Axial 2065s.cdr
08.11.01 - IMF

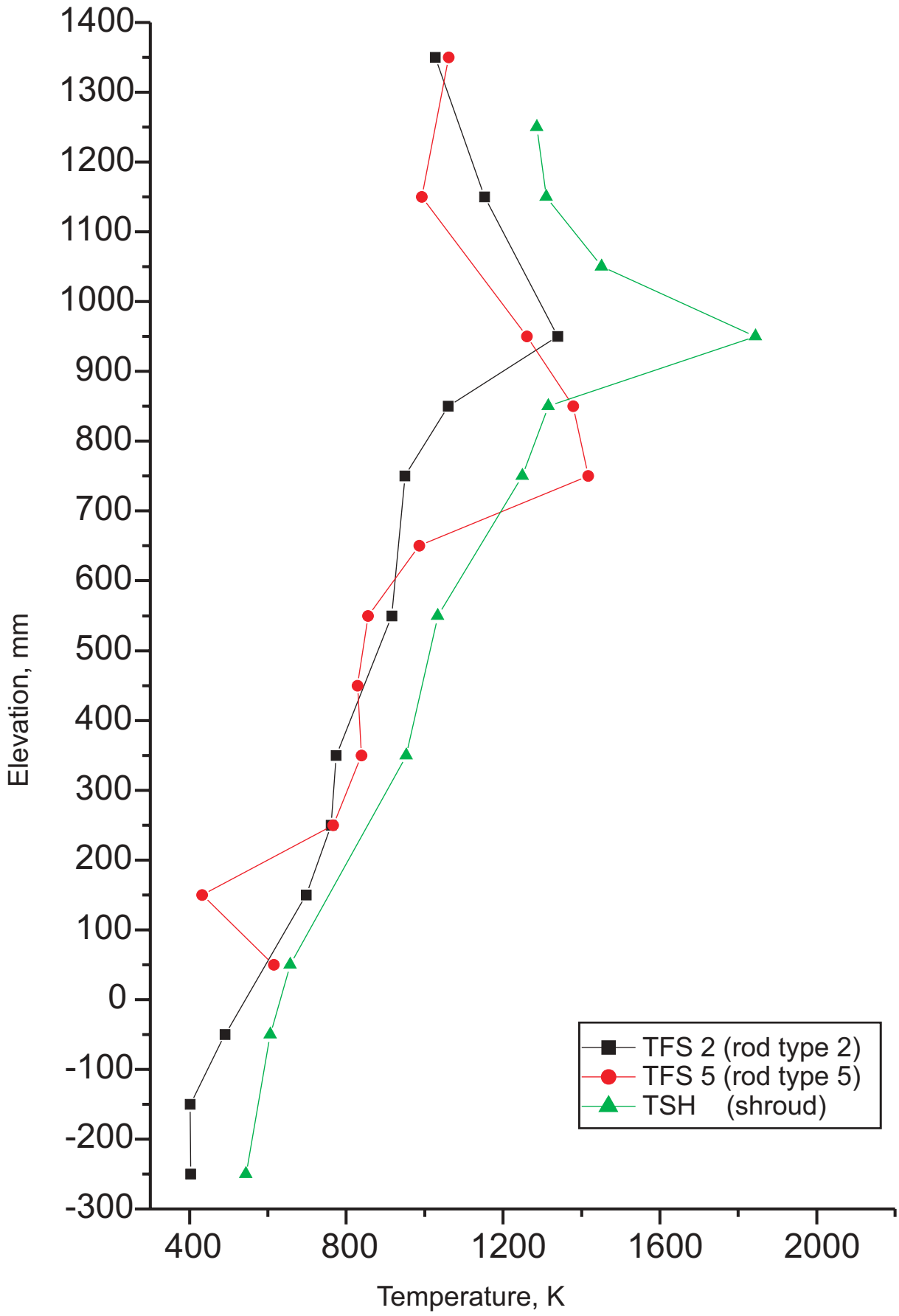

Fig. I-42: QUENCH-04; Axial temperature profile TFS 2, TFS 5,TSH at 2075 s (cooling phase)

Fig.42-QUE04-Axial 2075s.cdr
08.10.01 - IMF

Fig. I-43: QUENCH-04; Posttest appearance of the shroud between 780 mm and 1000 mm elevation

Fig 43 QUE04 Postttest a.cdr
08.11.01 - IMF

Fig. I-44: QUENCH-04; Molten shroud region 930 - 1000 mm

Fig 44 QUE04 Postttest b.cdr
23.10.01 - IMF

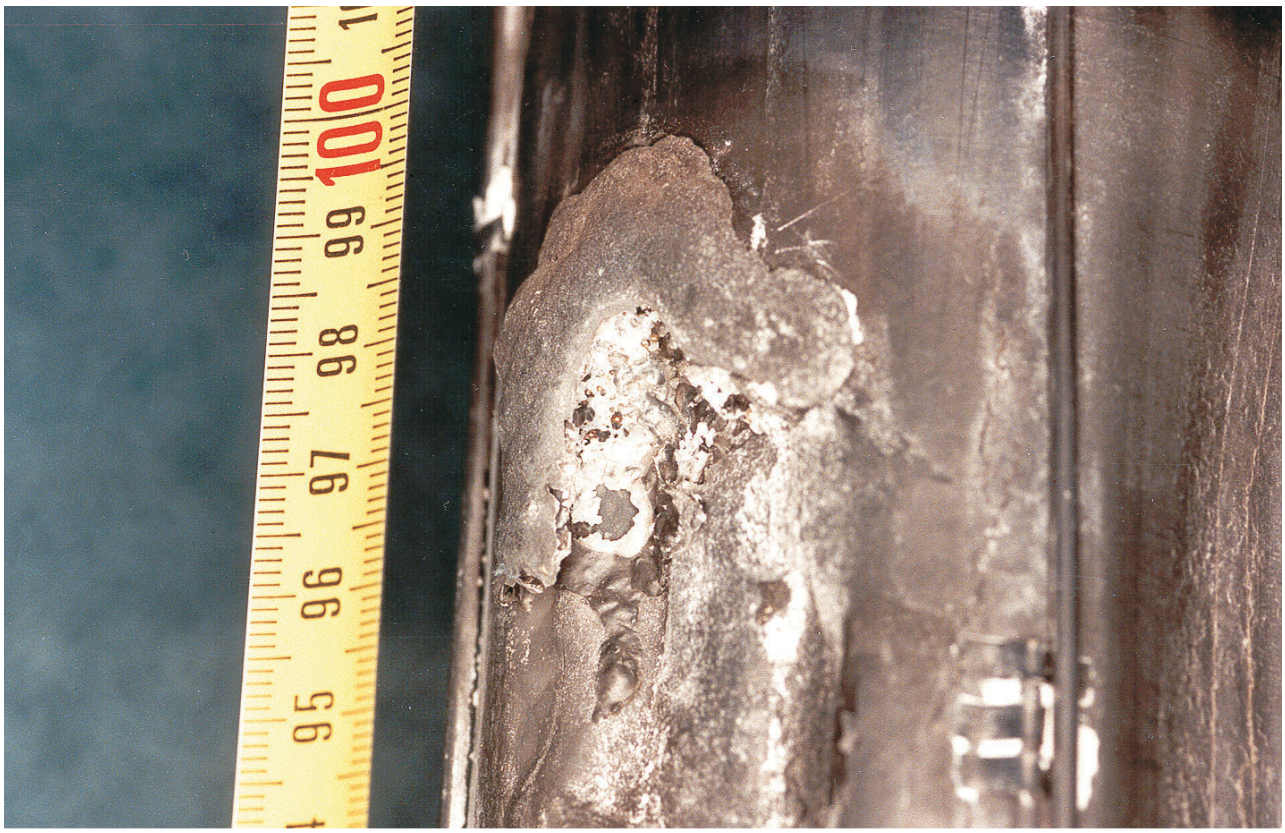

Fig. I-45: QUENCH-04; Molten shroud region

Fig 45 QUE04 Postttest c.cdr
23.10.01 - IMF

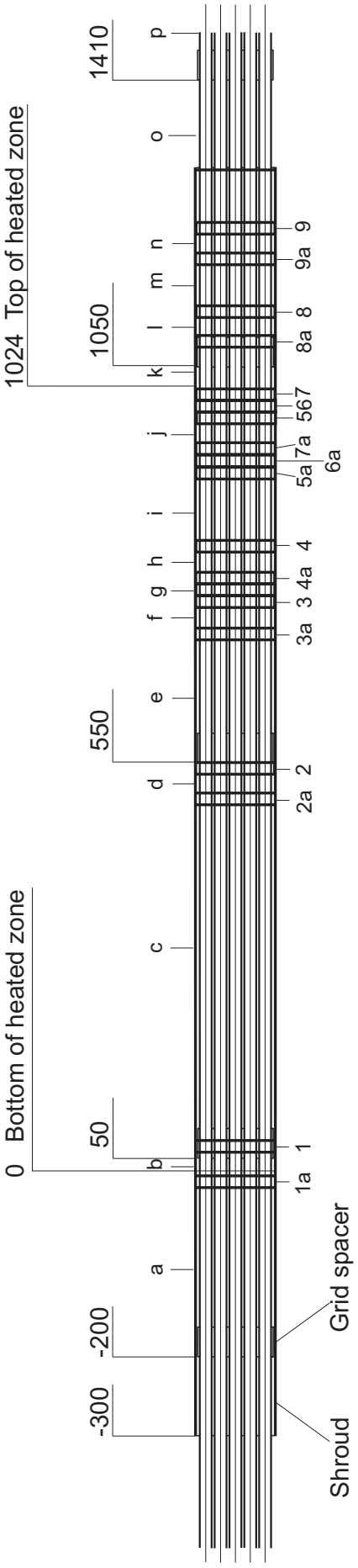

Fig. I-46: Sectioning of test bundle QUENCH-04

Fig.46-QUE04 Schnittplan.cdr
23.10.01 - IMF

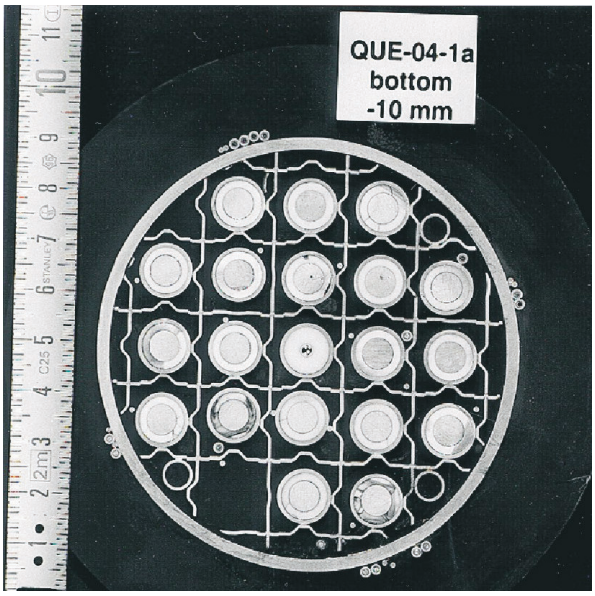

-10 mm shroud; 40 mm bundle

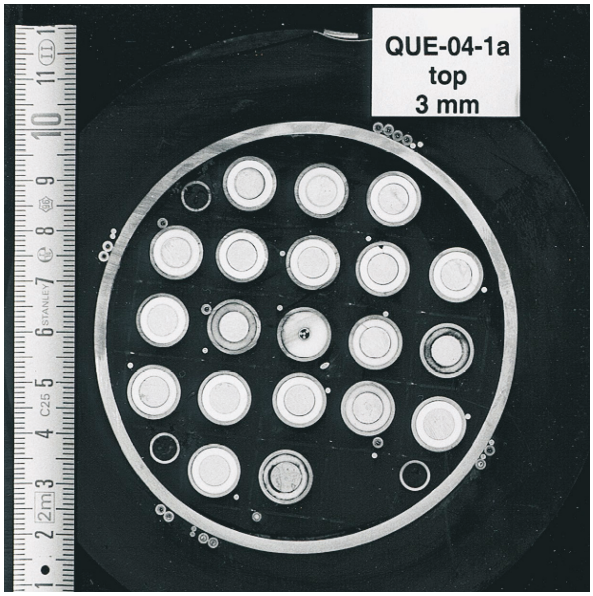

3 mm shroud; 53 mm bundle

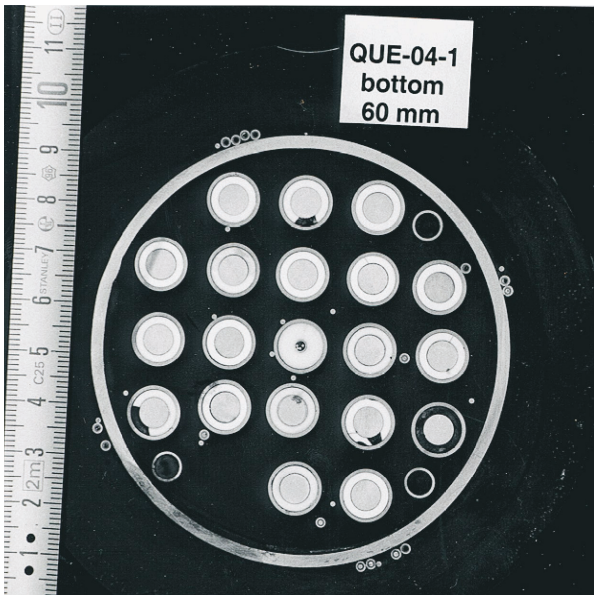

60 mm shroud; 110 mm bundle

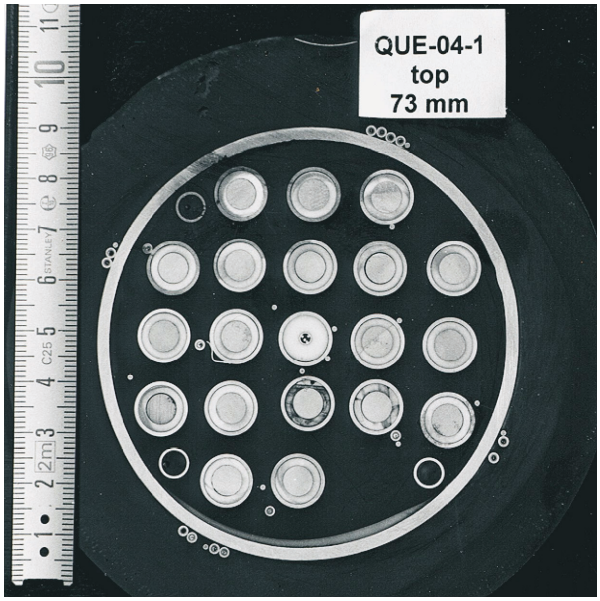

73 mm shroud; 123 mm bundle

Fig. I-47: QUENCH-04; Cross sections (unpolished)

Fig 47-QUE04 Foto-1.cdr
06.11.01 - IMF

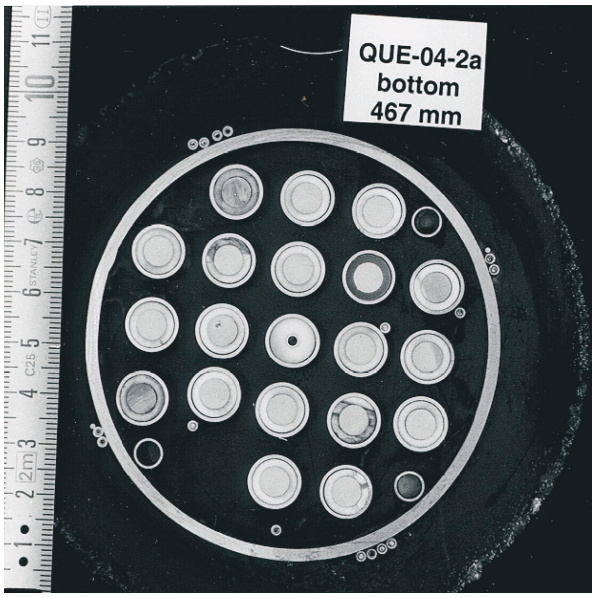

467 mm shroud; 517 mm bundle

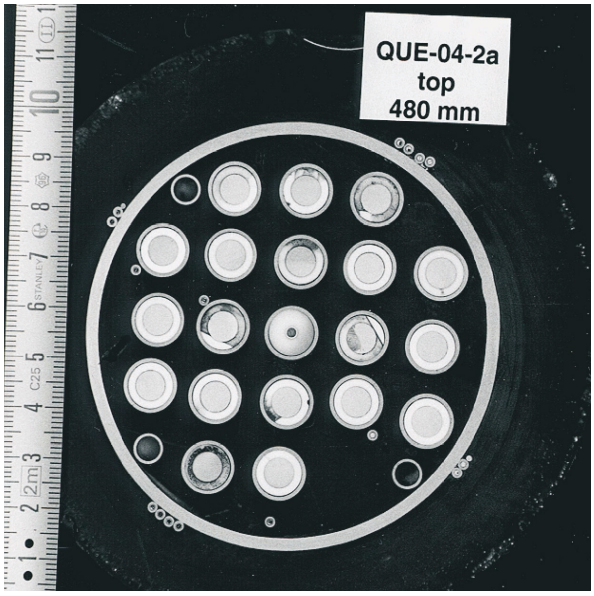

480 mm shroud; 530 mm bundle

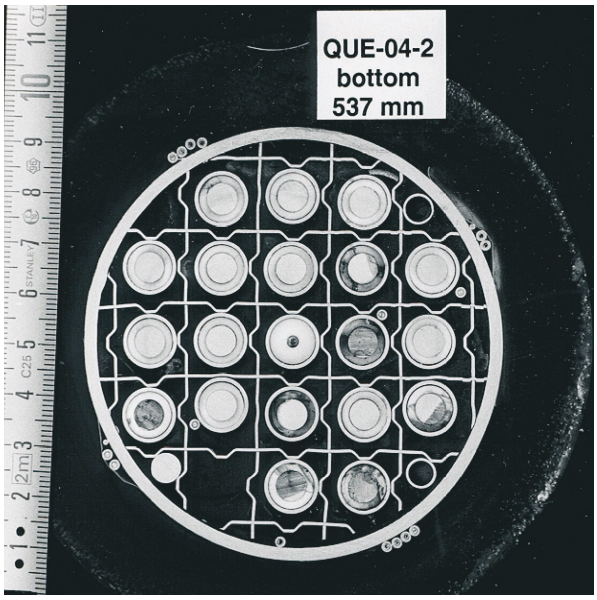

537 mm shroud; 587 mm bundle

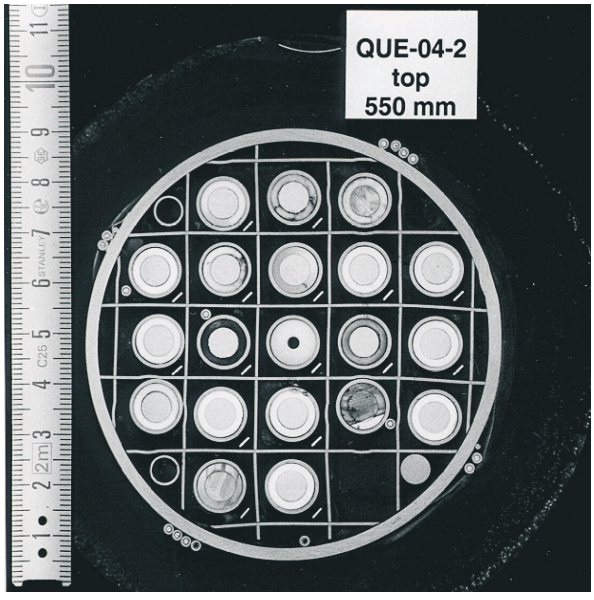

550 mm shroud; 600 mm bundle

Fig. I-48: QUENCH-04; Cross sections (unpolished)

Fig 48-QUE04 Foto-2.cdr
06.11.01 - IMF

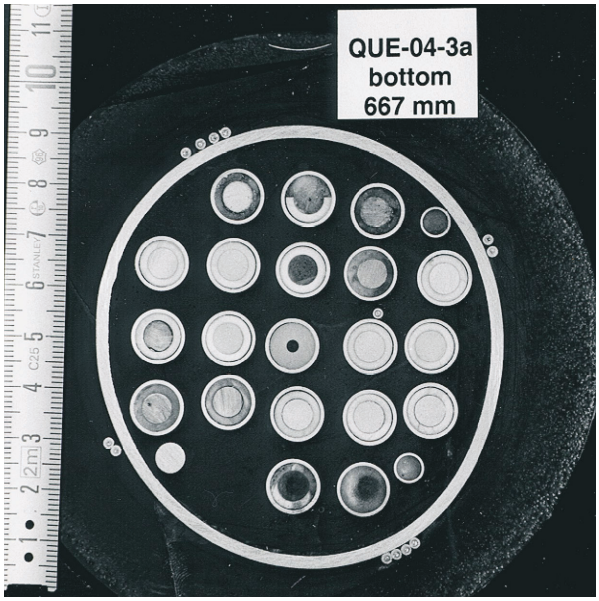

667 mm shroud; 717 mm bundle

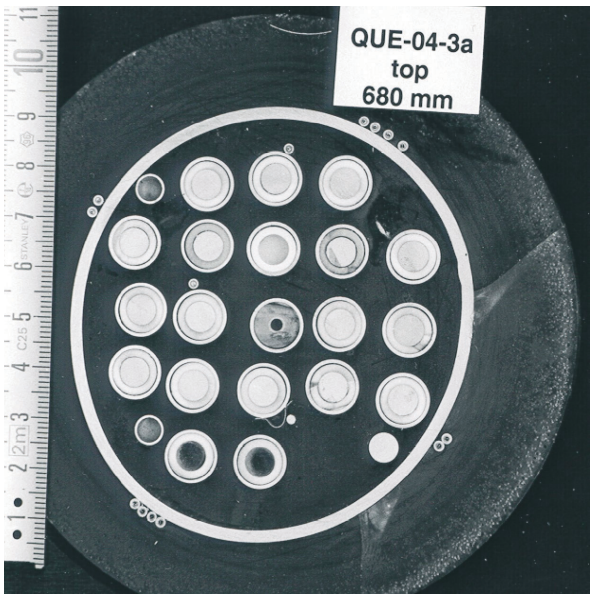

680 mm shroud; 730 mm bundle

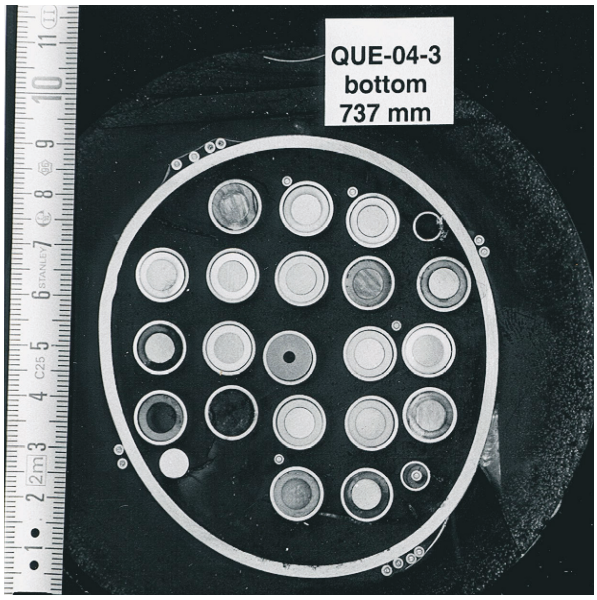

737 mm shroud; 787 mm bundle

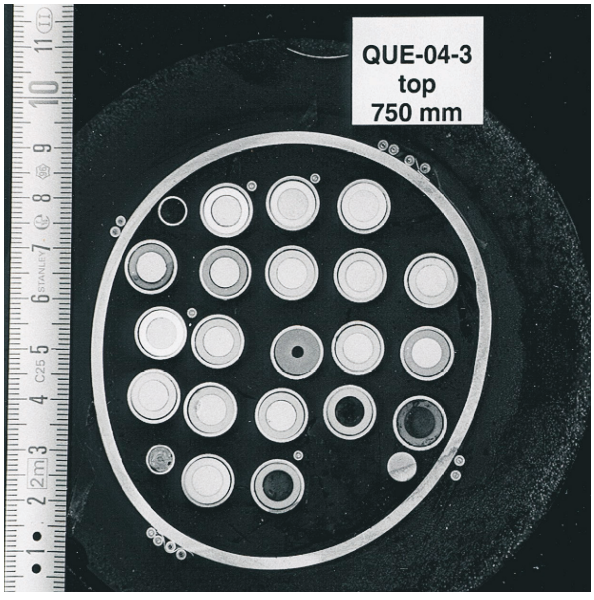

750 mm shroud; 800 mm bundle

Fig. I-49: QUENCH-04; Cross sections (unpolished)

Fig 49-QUE04 Foto-3.cdr
06.11.01 - IMF

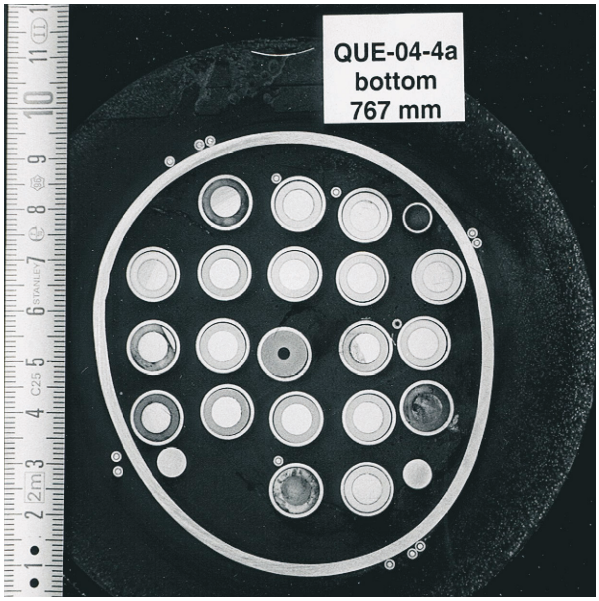

767 mm shroud; 817 mm bundle

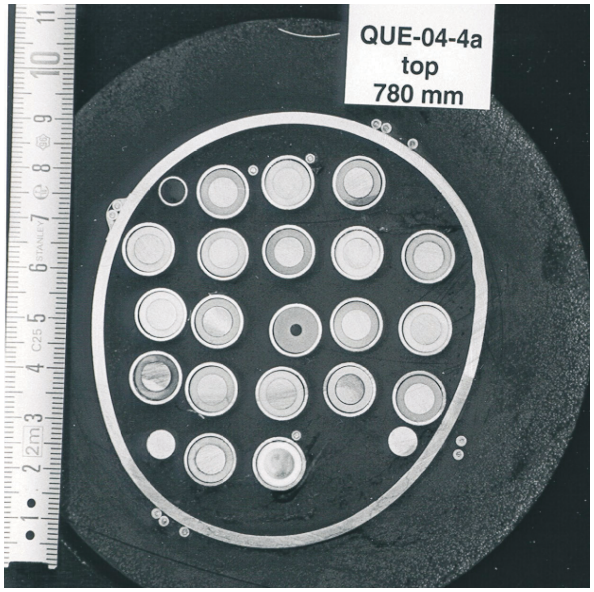

780 mm shroud; 830 mm bundle

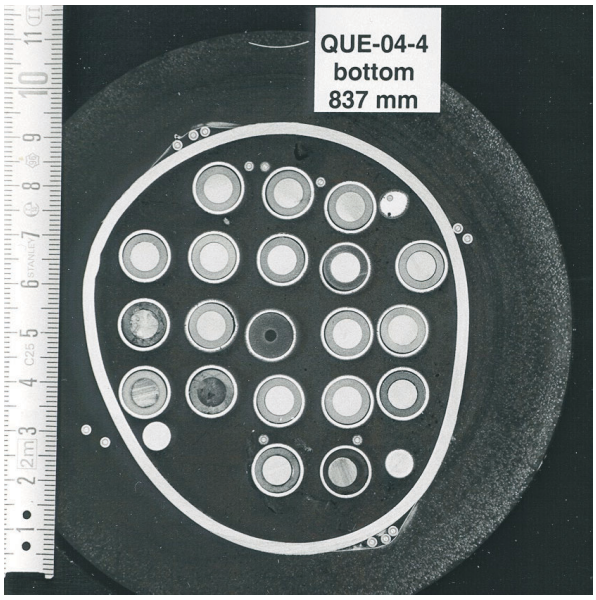

837 mm shroud; 887 mm bundle

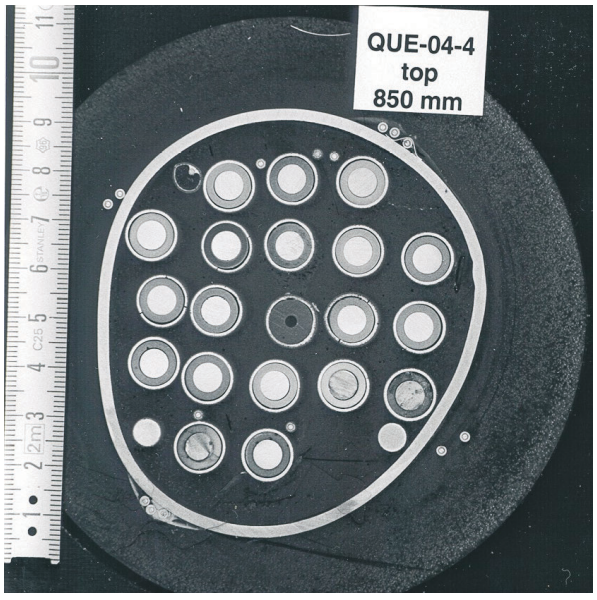

850 mm shroud; 900 mm bundle

Fig. I-50: QUENCH-04; Cross sections (unpolished)

Fig 50-QUE04 Foto-4.cdr
06.11.01 - IMF

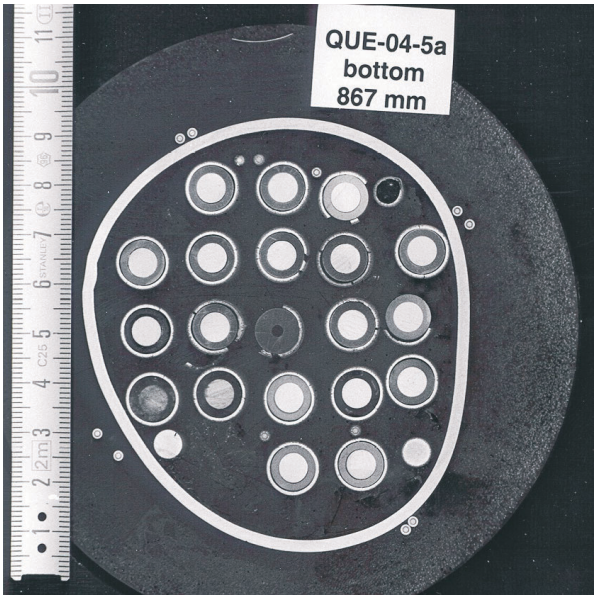

867 mm shroud; 917 mm bundle

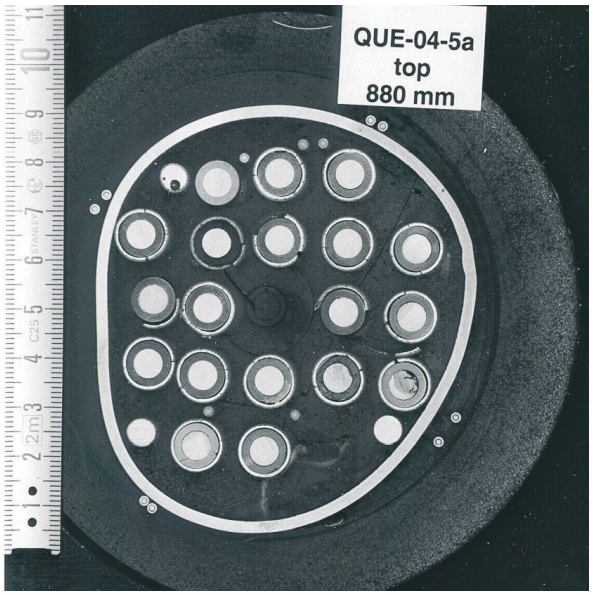

880 mm shroud; 930 mm bundle

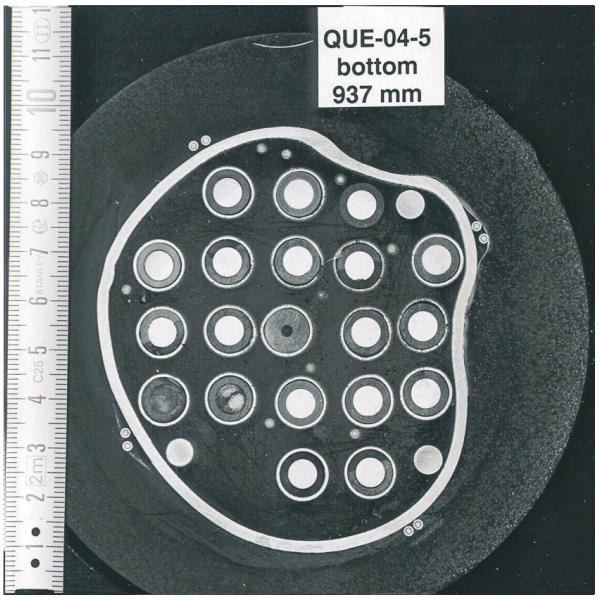

937 mm shroud; 987 mm bundle

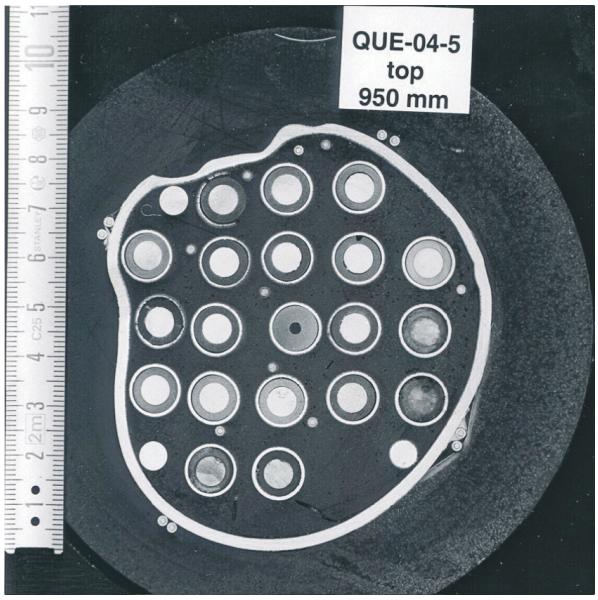

950 mm shroud; 1000 mm bundle

Fig. I-51: QUENCH-04; Cross sections (unpolished)

Fig 51-QUE04 Foto-5.cdr
06.11.01 - IMF

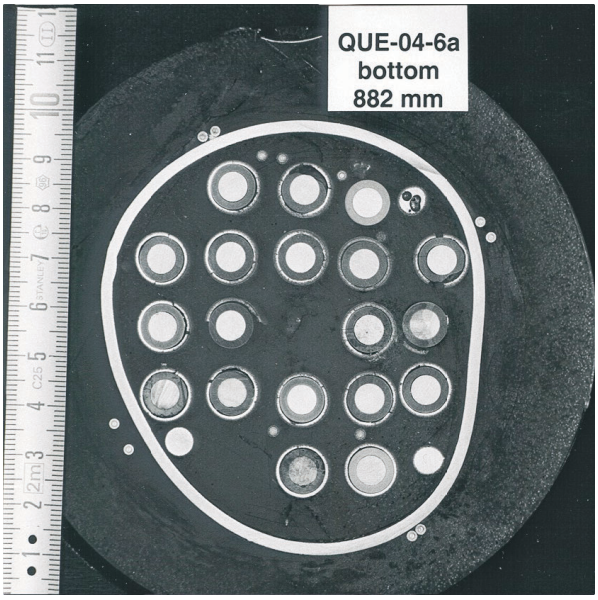

882 mm shroud; 932 mm bundle

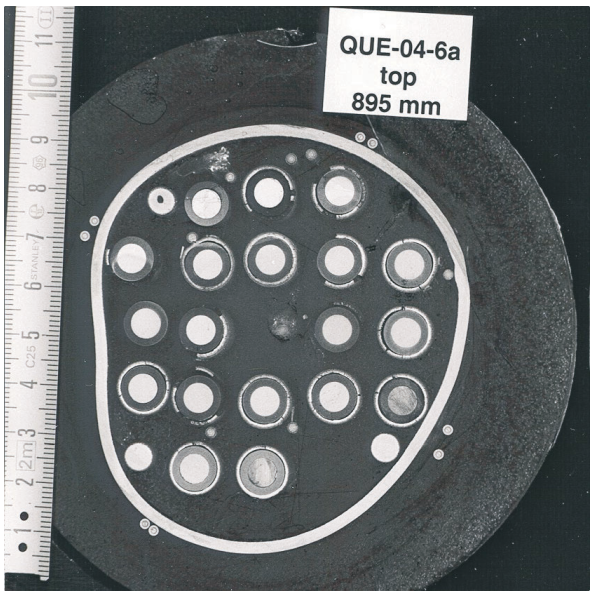

895 mm shroud; 945 mm bundle

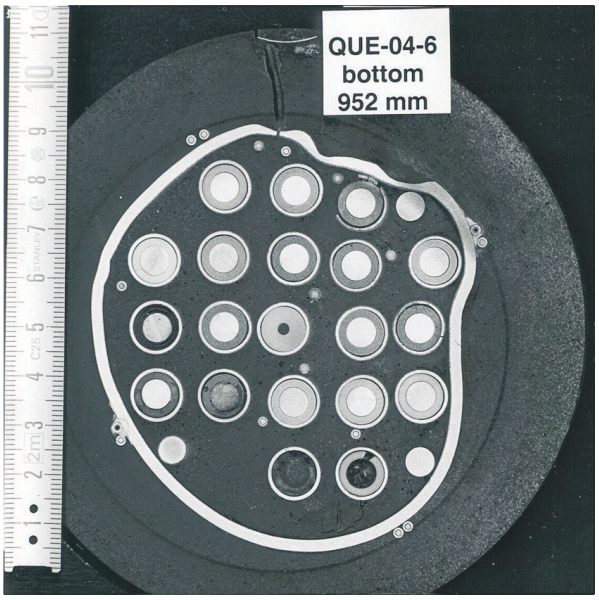

952 mm shroud; 1002 mm bundle

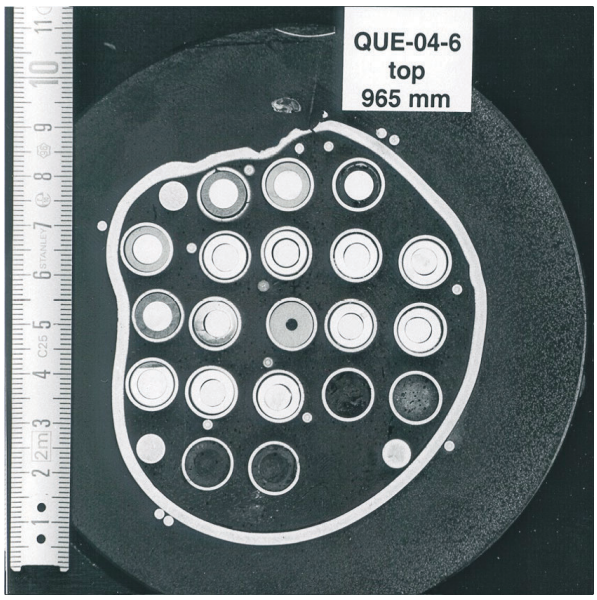

965 mm shroud; 1015 mm bundle

Fig. I-52: QUENCH-04; Cross sections (unpolished)

Fig 52-QUE04 Foto-6.cdr
06.11.01 - IMF

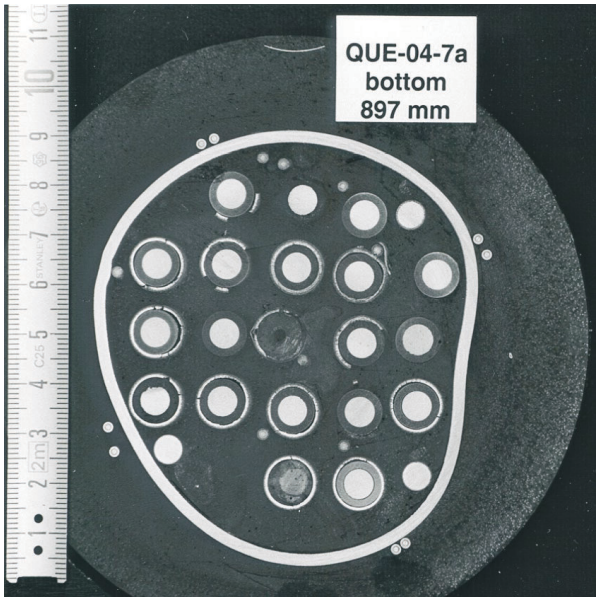

897 mm shroud; 947 mm bundle

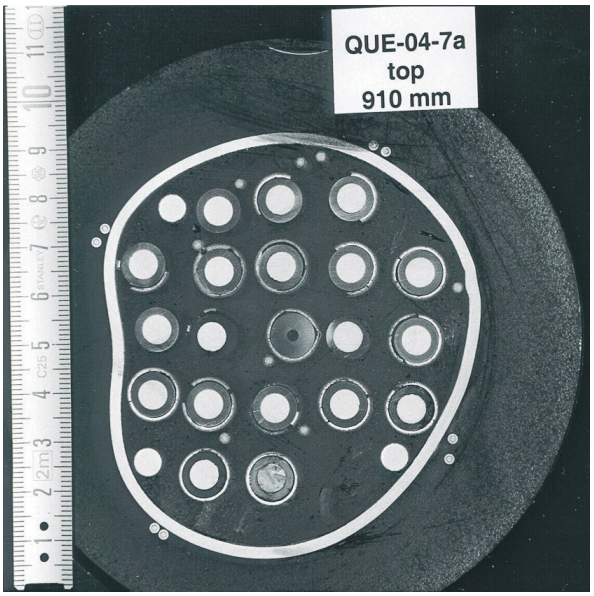

910 mm shroud; 960 mm bundle

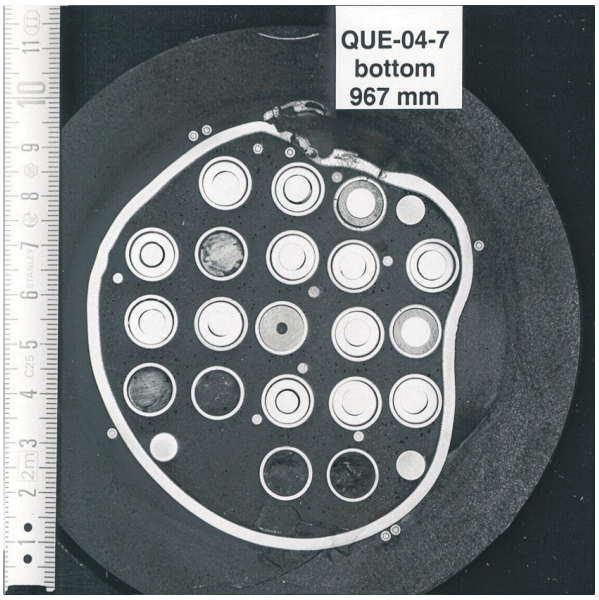

967 mm shroud; 1017 mm bundle

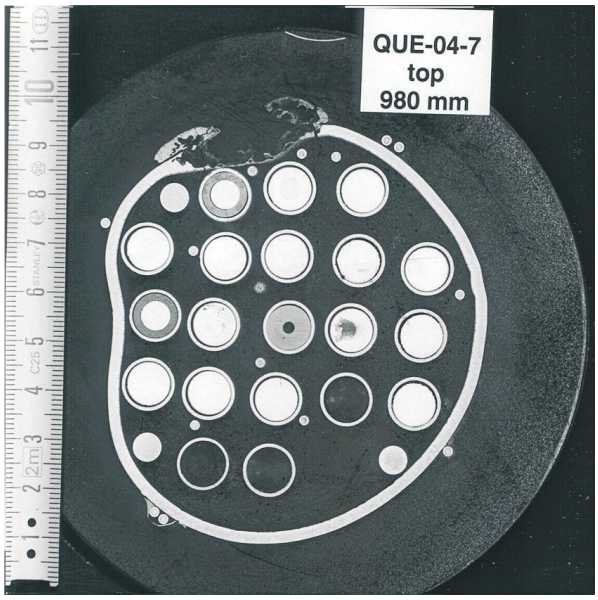

980 mm shroud; 1030 mm bundle

Fig. I-53: QUENCH-04; Cross sections (unpolished)

Fig 53-QUE04 Foto-7.cdr
06.11.01 - IMF

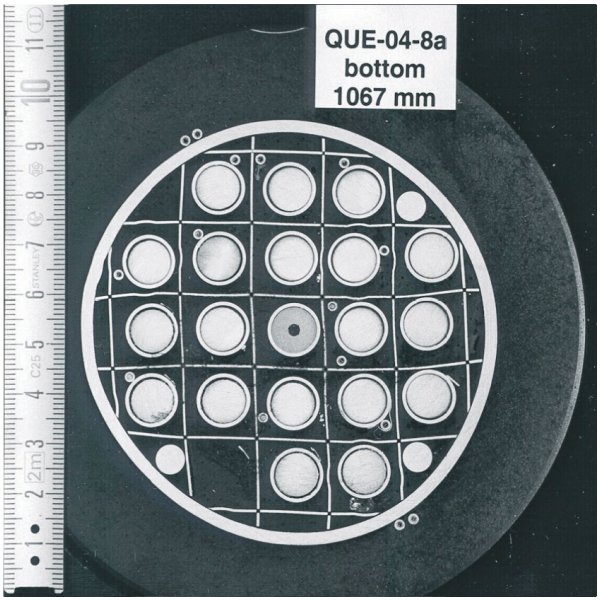

1067 mm shroud; 1117 mm bundle

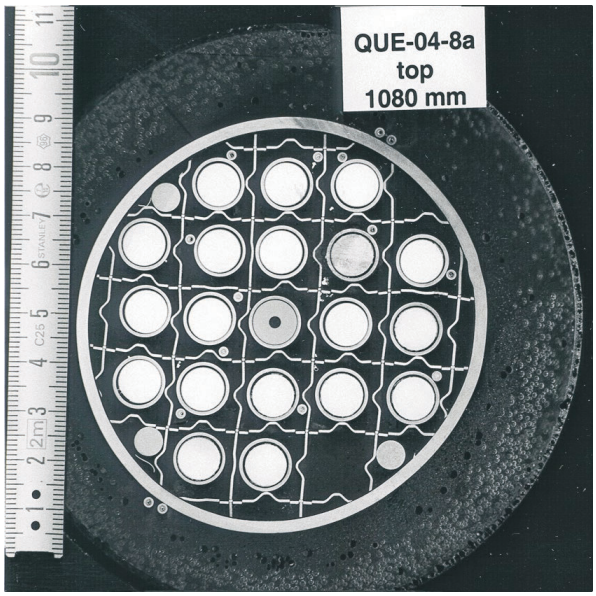

1080 mm shroud; 1130 mm bundle

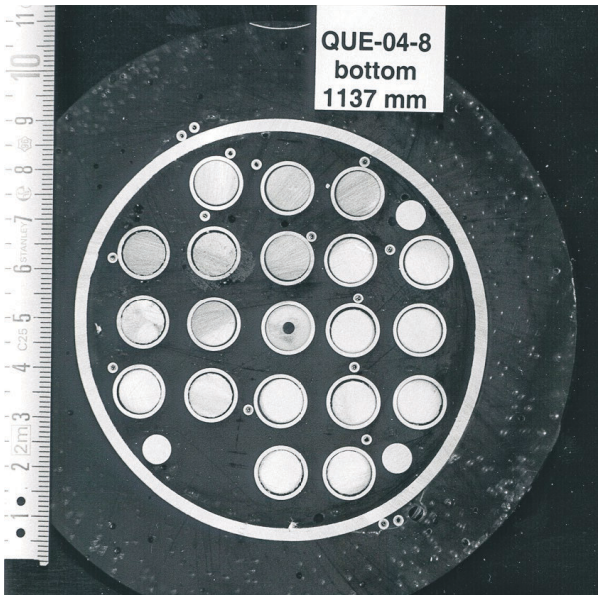

1137 mm shroud; 1187 mm bundle

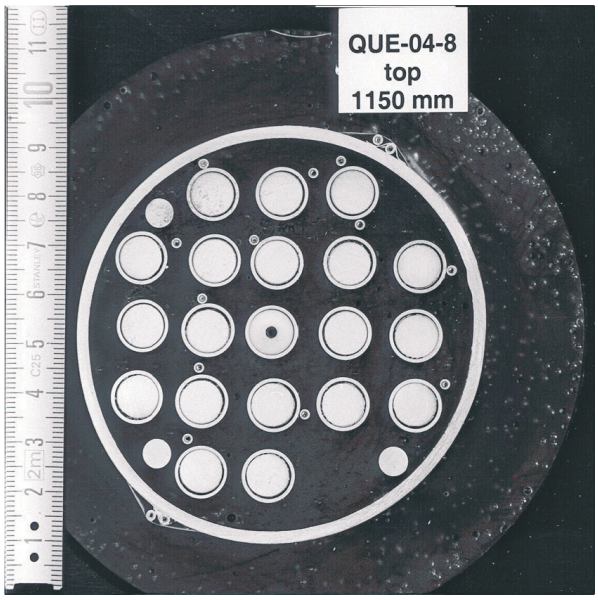

1150 mm shroud; 1200 mm bundle

Fig. I-54: QUENCH-04; Cross sections (unpolished)

Fig 54-QUE04 Foto-8.cdr
06.11.01 - IMF

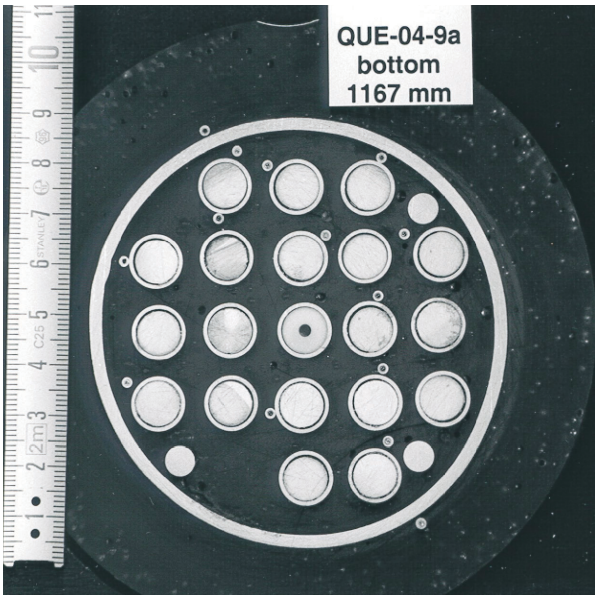

1167 mm shroud; 1217 mm bundle

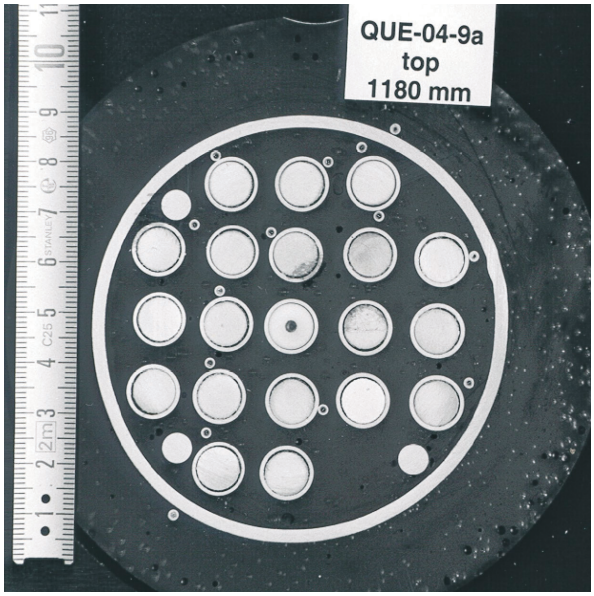

1180 mm shroud; 1230 mm bundle

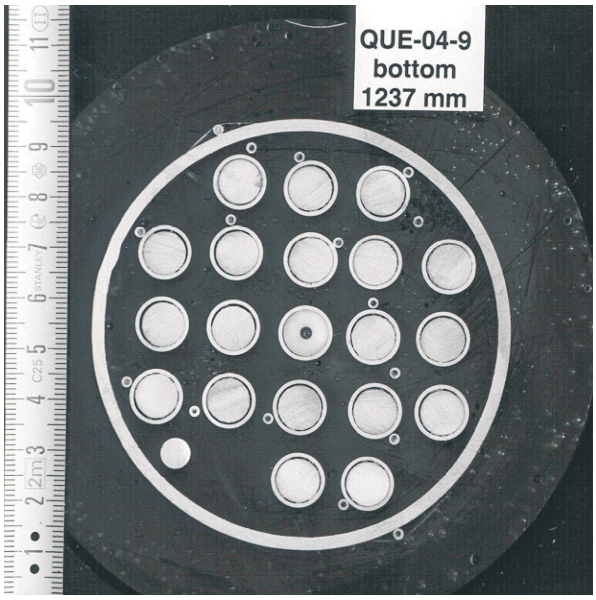

1237 mm shroud; 1287 mm bundle

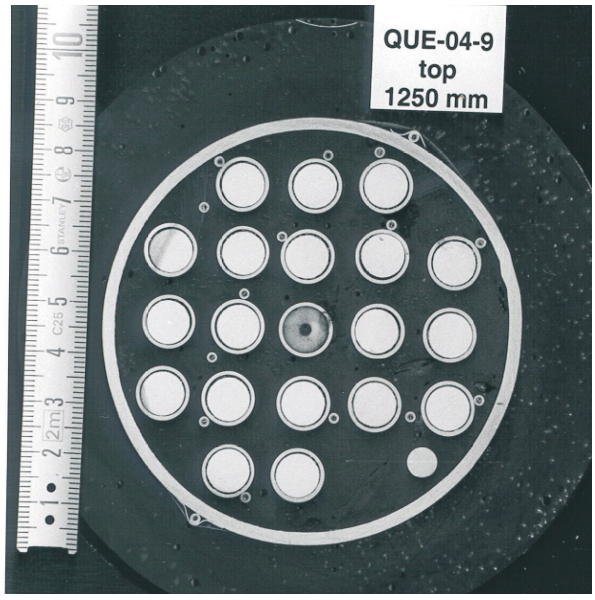

1250 mm shroud; 1300 mm bundle

Fig. I-55: QUENCH-04; Cross sections (unpolished)

Fig 55-QUE04 Foto-9.cdr
06.11.01 - IMF

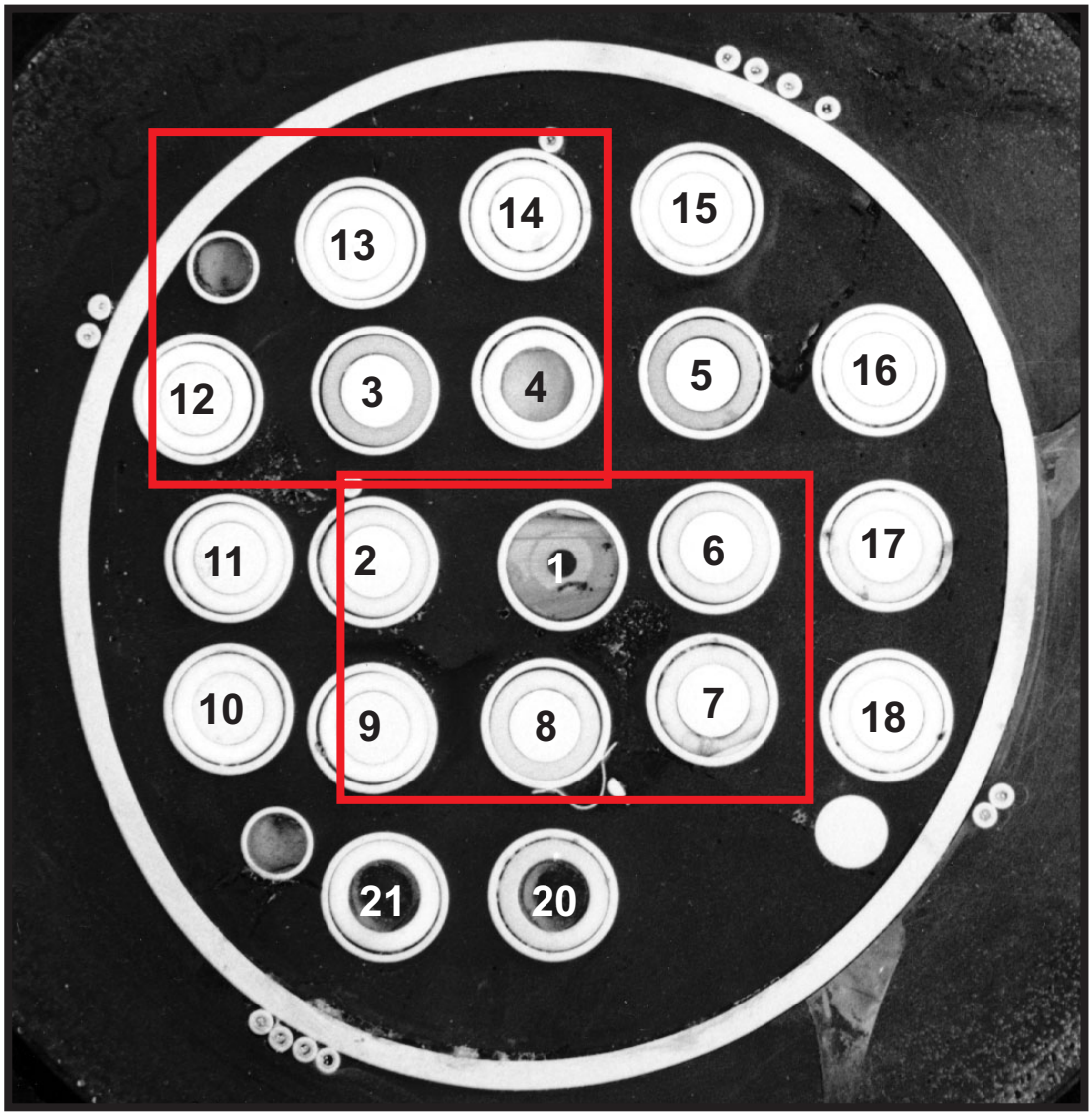

Fig. I-56: QUENCH-04; Cross section at bundle elevation 730 mm (QUE-04-3a, top); overview.

Fig 56-QUE04 Folie 13.cdr
30.10.01 - IMF

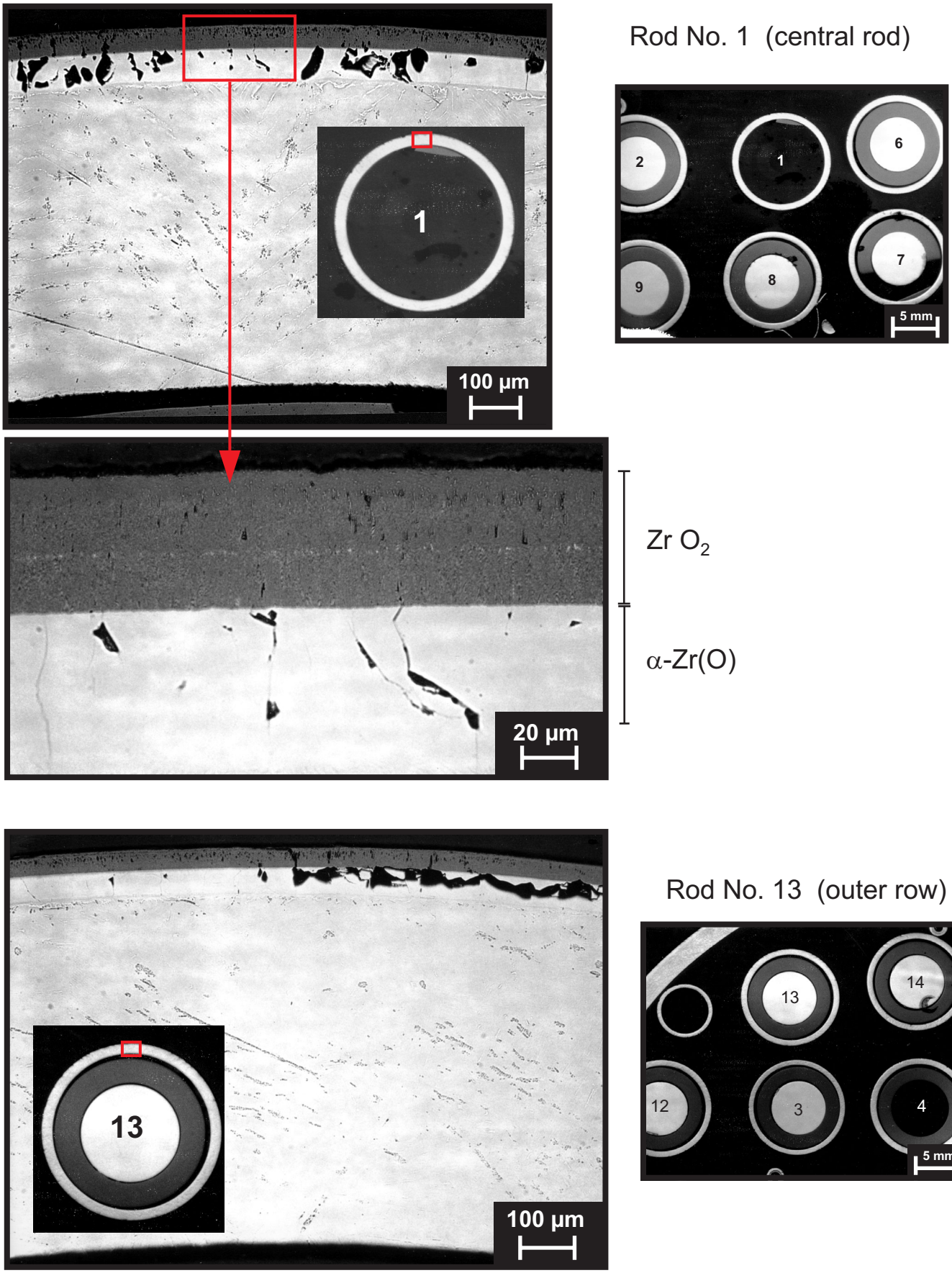

Fig. I-57: QUENCH-04; Cross section at bundle elevation 730 mm (QUE-04-3a, top); rod oxidation.

Fig 57-QUE04 Folie 14.cdr
30.10.01 - IMF

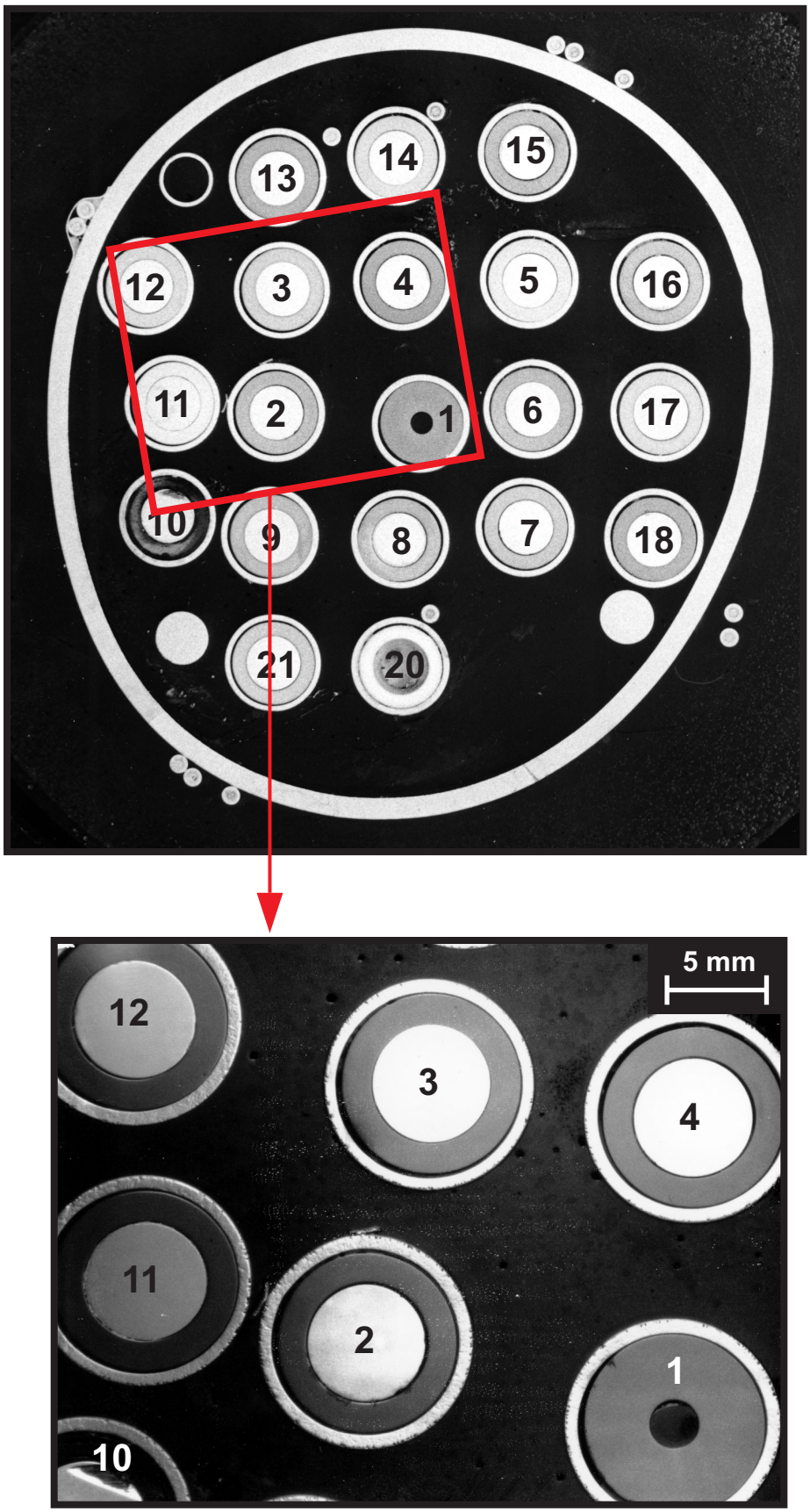

Fig. I-58: QUENCH-04; Cross section at bundle elevation 830 mm (QUE-04-4a, top); overview.

Fig 58-QUE04 Folie 15.cdr
30.10.01 - IMF

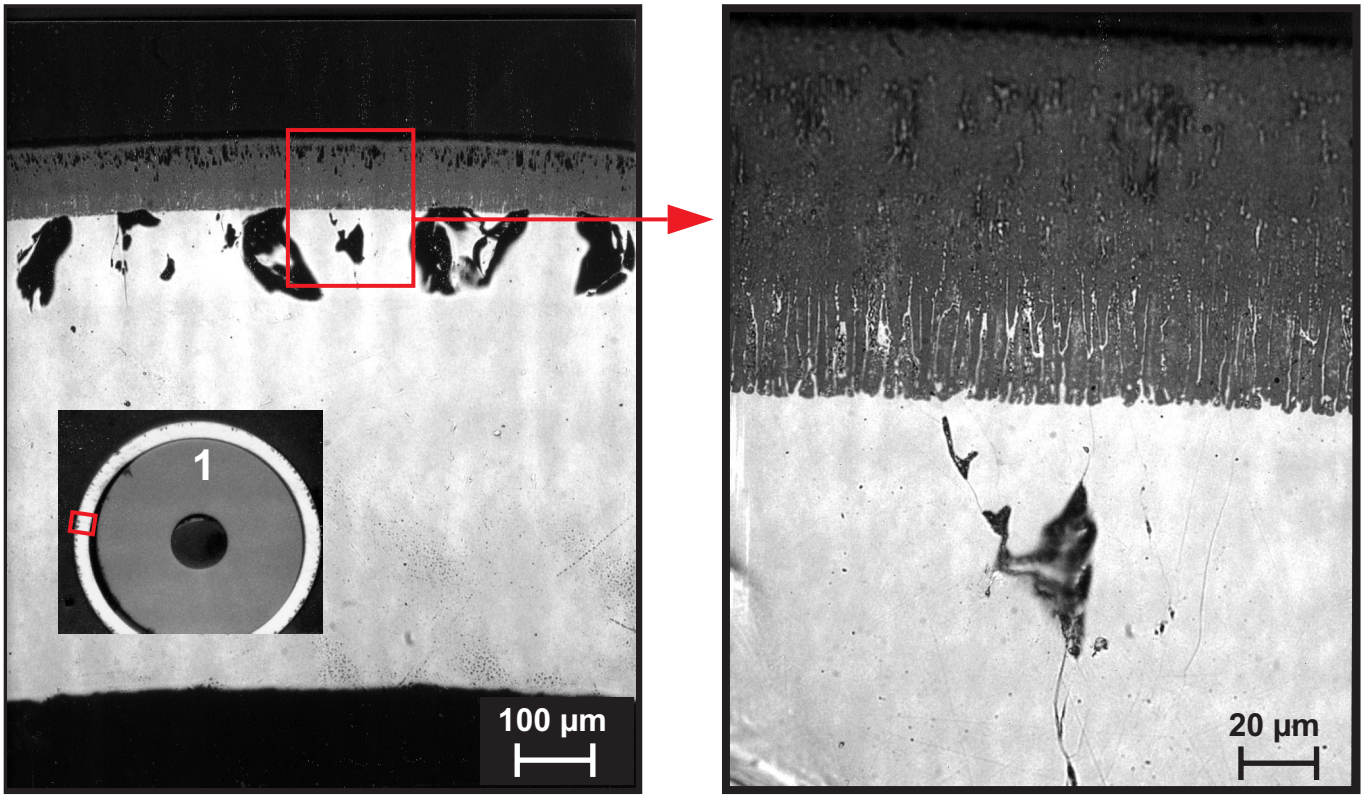

Rod No. 1 (central rod) , peak temperature above 1800 K.

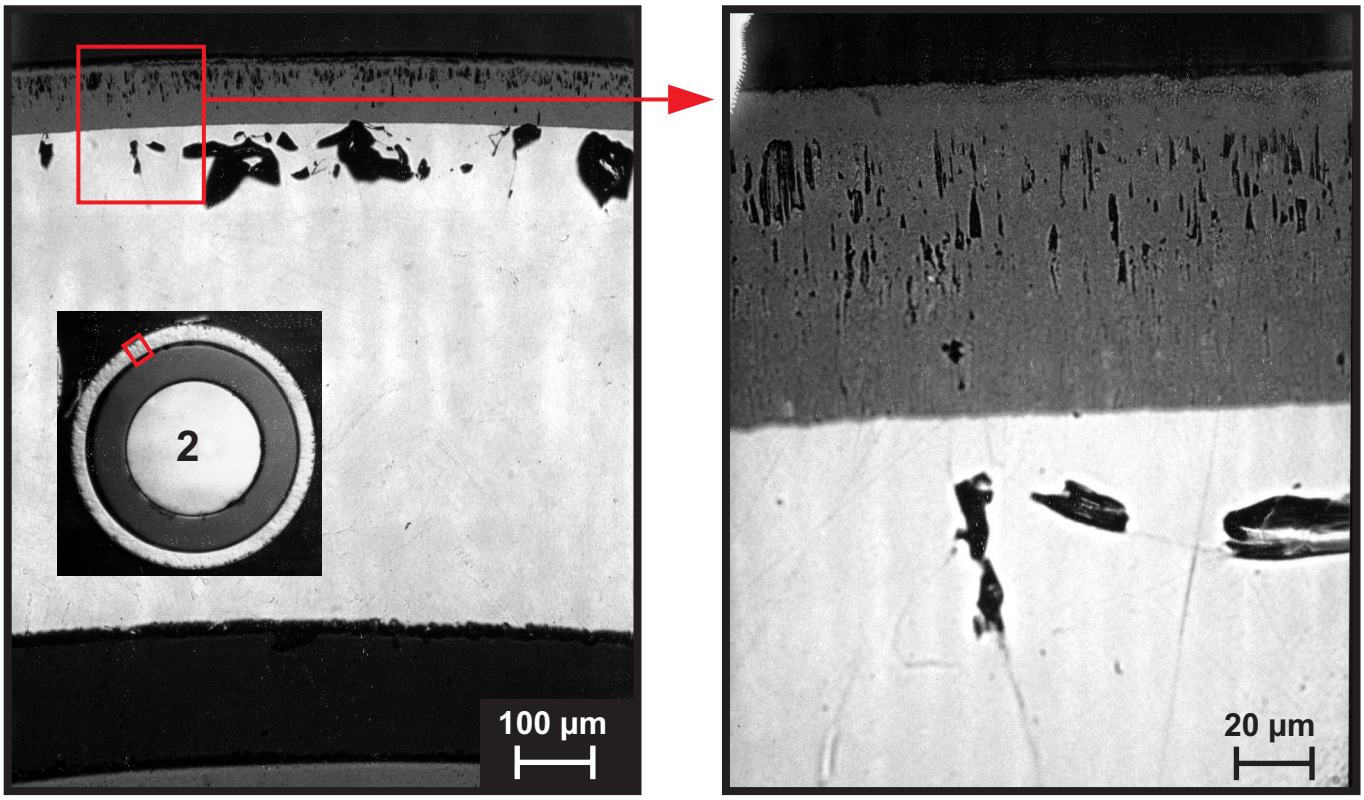

Rod No. 2 (inner row) , peak temperature below 1800 K.

Fig. I-59: QUENCH-04; Cross section at bundle elevation 830 mm (QUE-04-4a, top); slight peak temperature variation for neighbouring rods deduced from scale morphology difference and similar scale thickness.

Fig 59-QUE04 Folie 16.cdr
30.10.01 - IMF

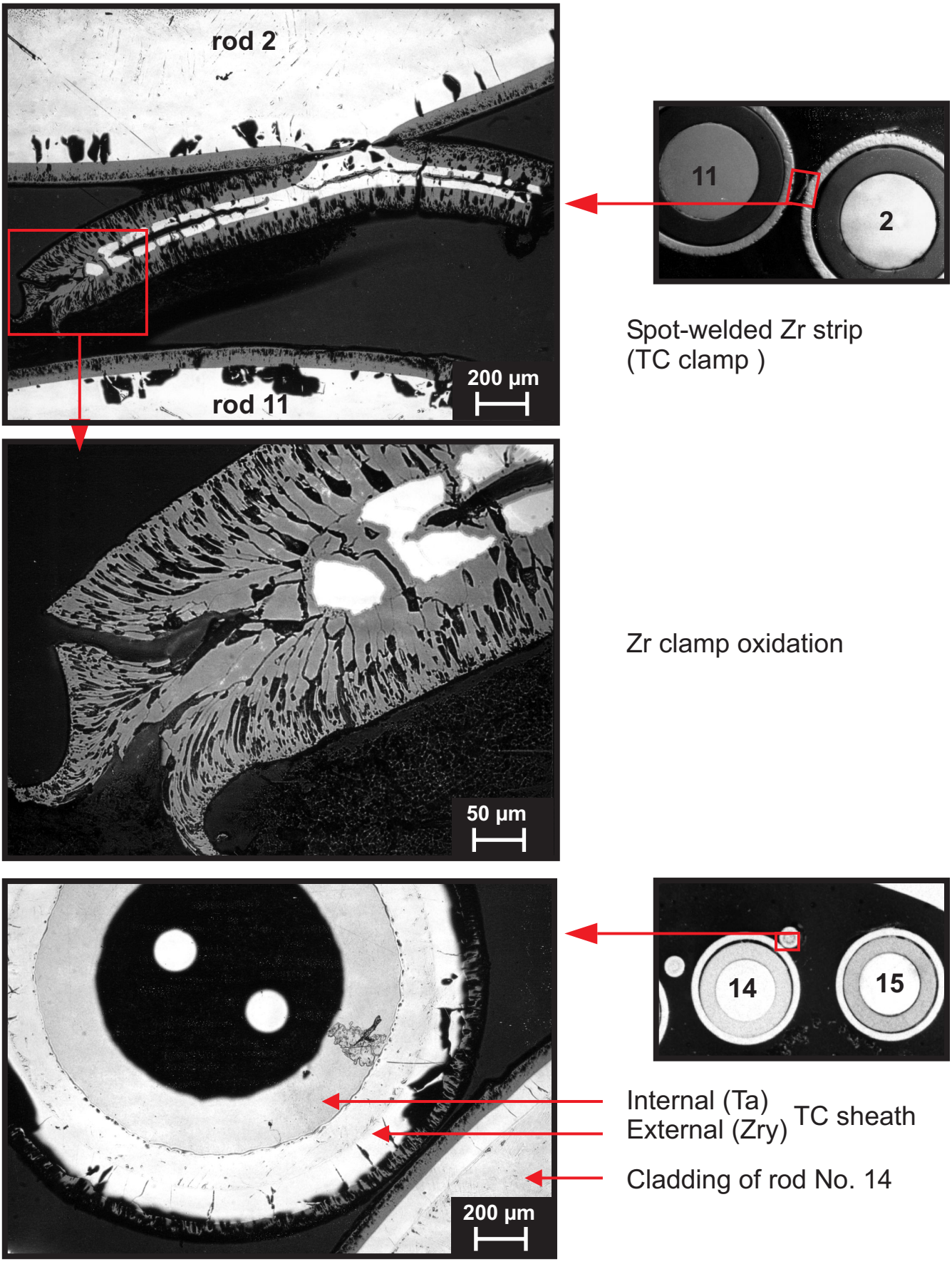

Fig. I-60: QUENCH-04; Cross section at bundle elevation 830 mm (QUE-04-4a, top); status of thermocouple fixing clamp and sheath.

Fig 60-QUE04 Folie 17.cdr
30.10.01 - IMF

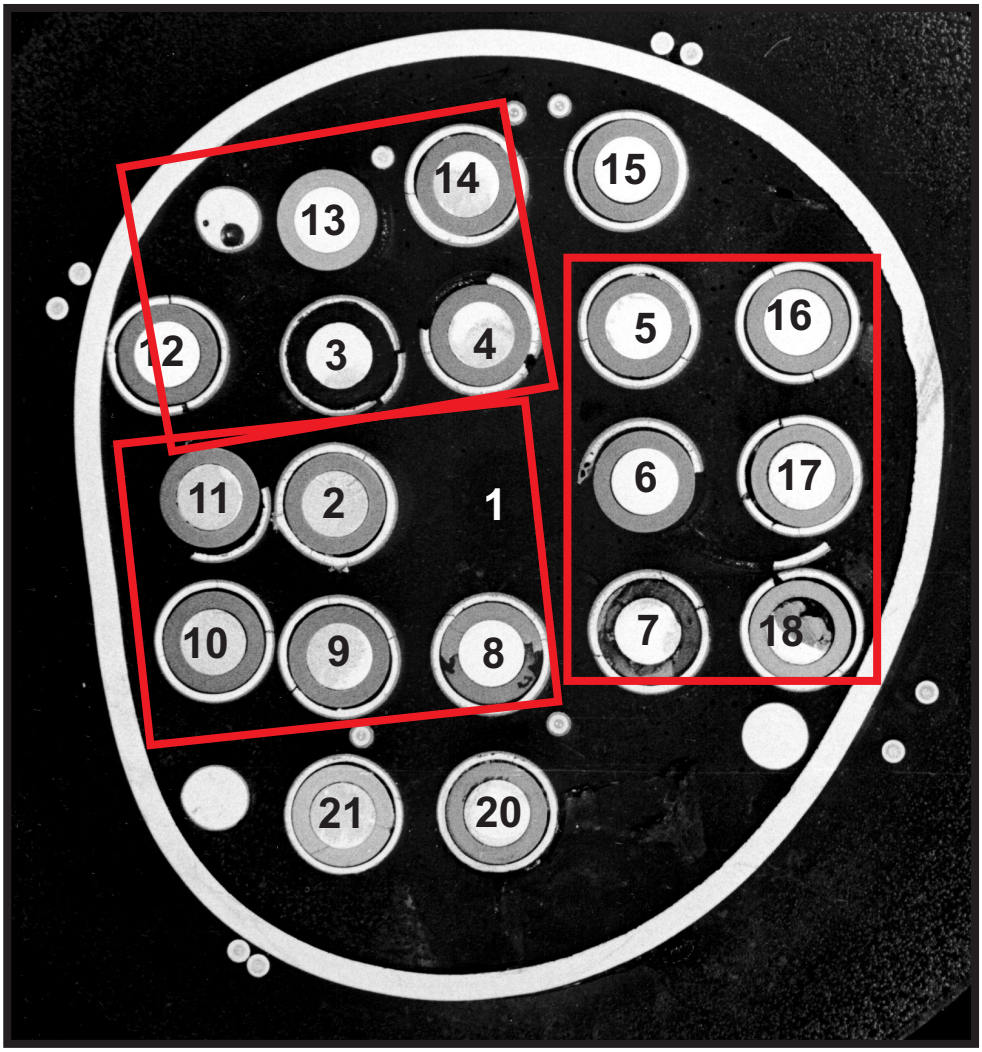

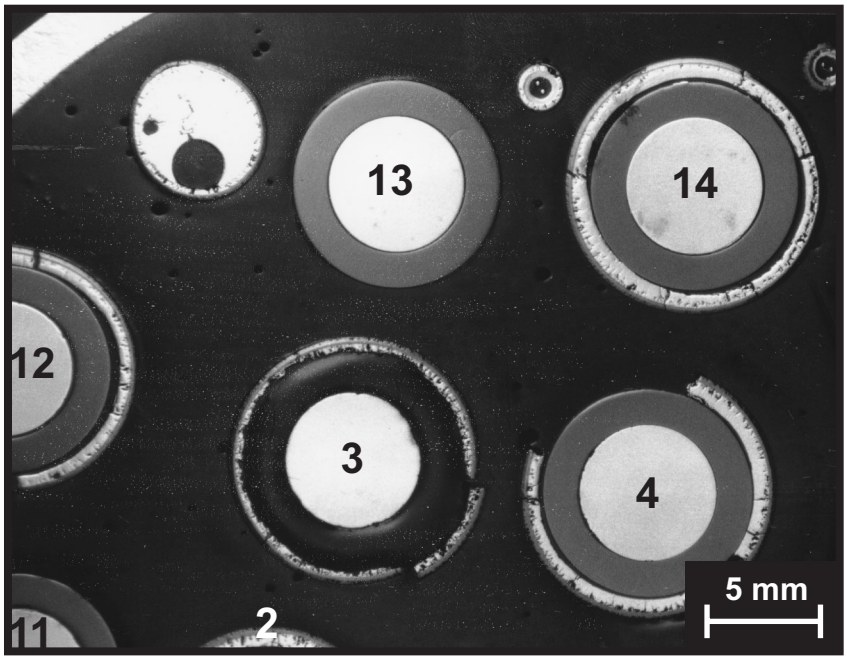

Fig. I-61: QUENCH-04; Cross section at bundle elevation 930 mm (QUE-04-5a, top); overview.

Fig 61-QUE04 Folie 18.cdr
30.10.01 - IMF

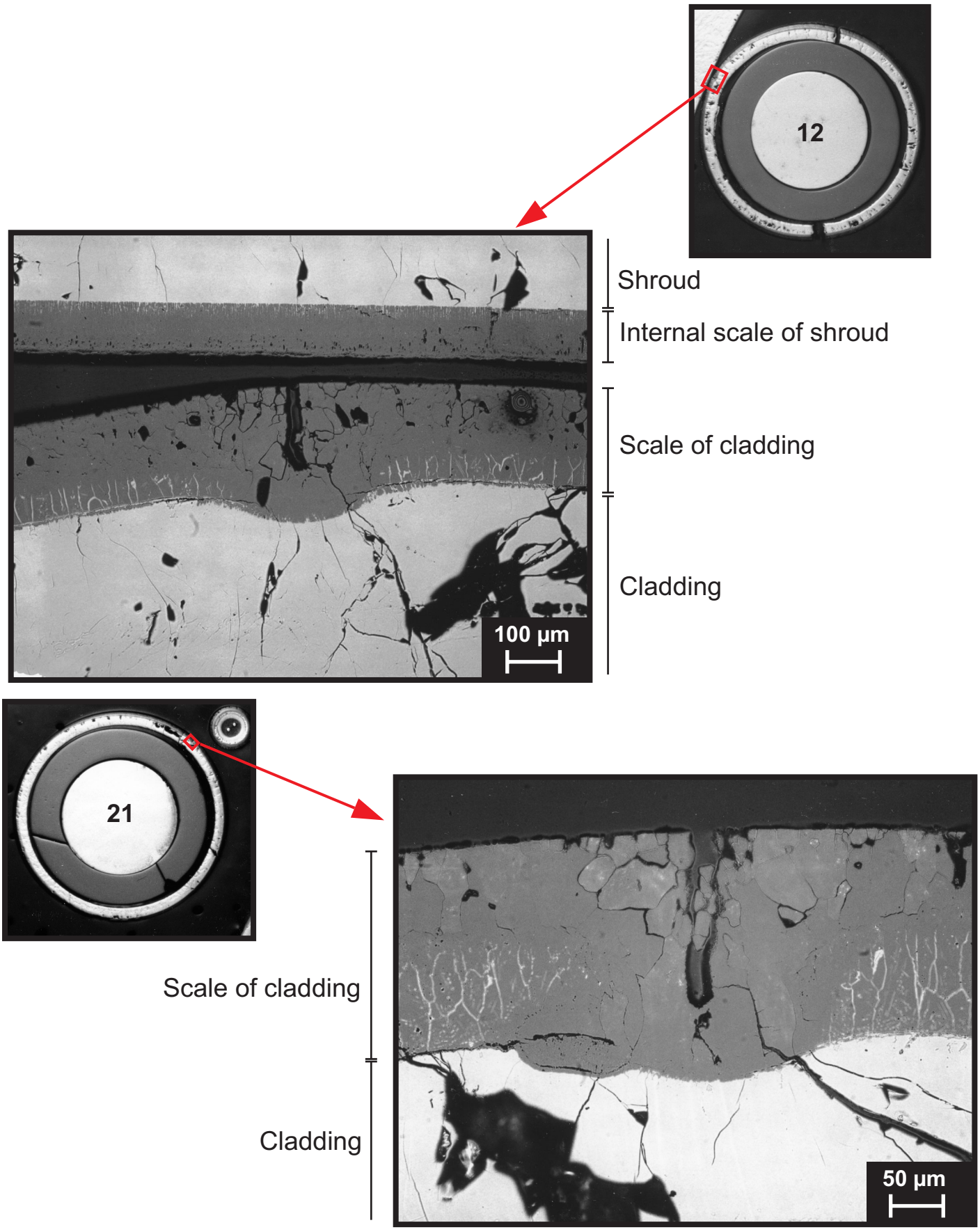

Fig. I-62: QUENCH-04; Cross section at bundle elevation 930 mm (QUE-04-5a, top); self-healing of cladding scale cracks.

Fig 62-QUE04 Folie 19.cdr
30.10.01 - IMF

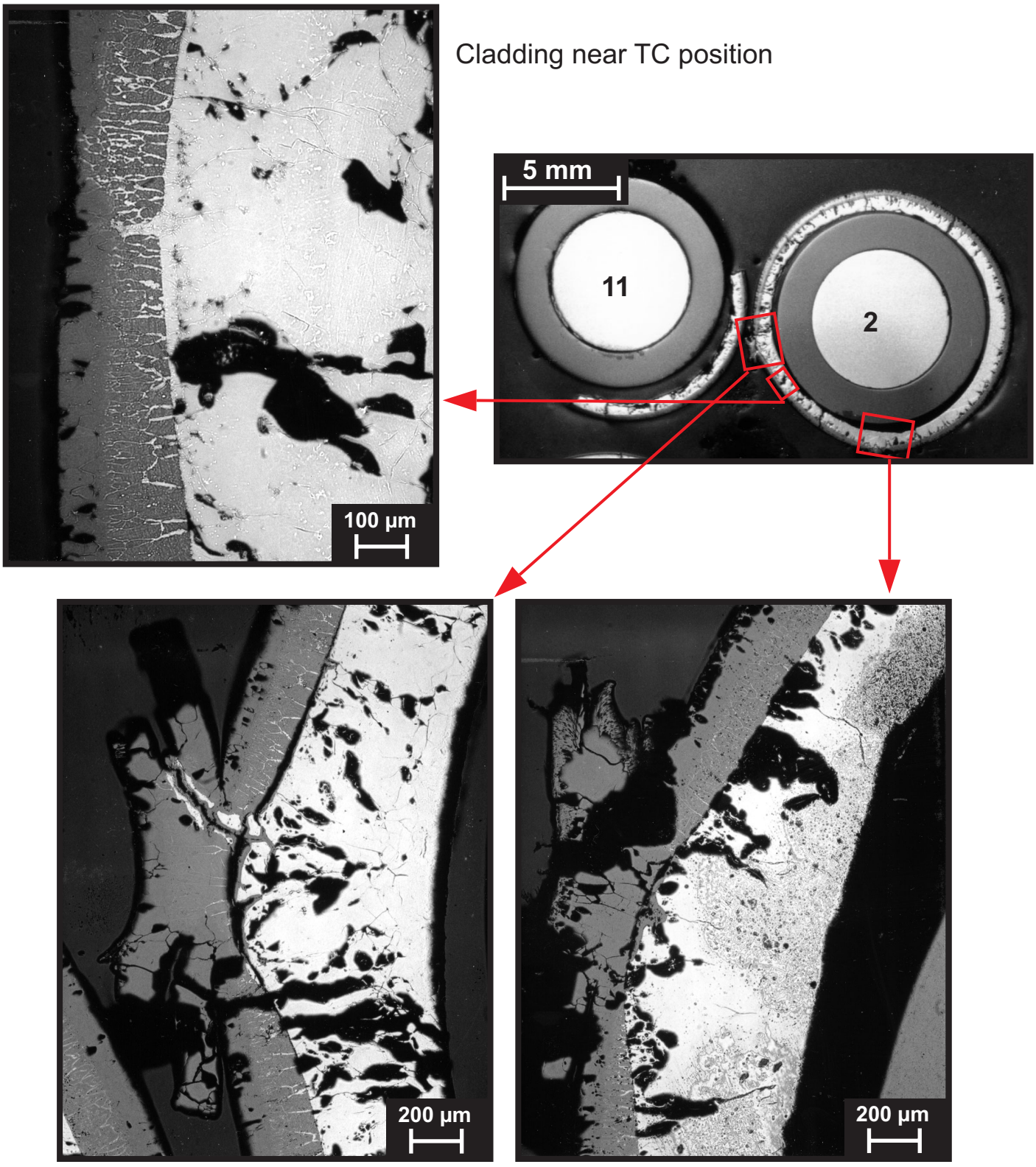

Spot weld positions of Zr strip for TC attachment.

Fig. I-63: QUENCH-04; Cross section at bundle elevation 930 mm (QUE-04-5a, top); slower cladding oxidation at thermocouple position and spot welds of attachment clamp, which itself is completely oxidized.

Fig 63-QUE04 Folie 20.cdr
30.10.01 - IMF

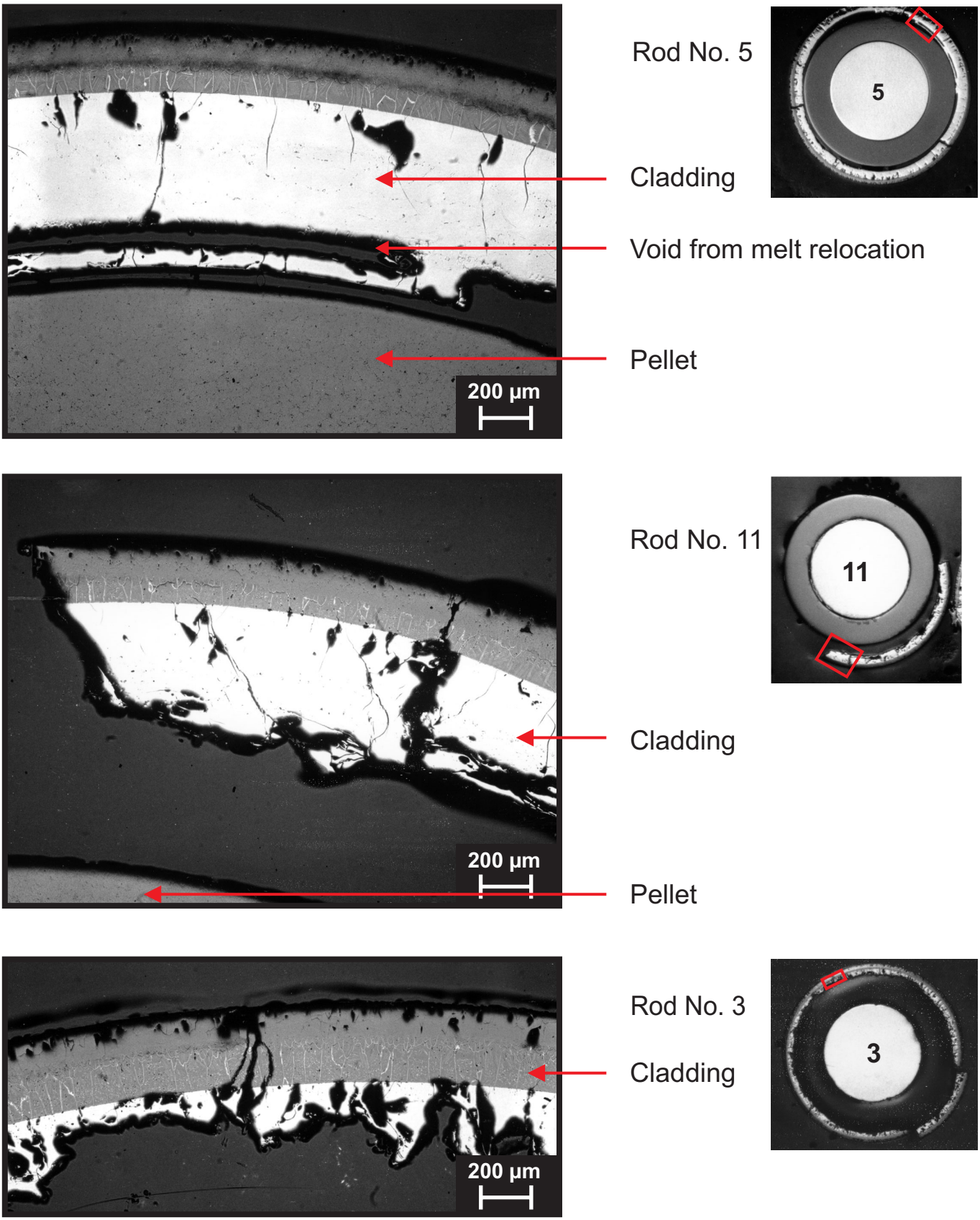

Fig. I-64: QUENCH-04; Cross section at bundle elevation 930 mm (QUE-04-5a, top); partial and advanced cladding melting and melt relocation.

Fig 64-QUE04 Folie 21.cdr
30.10.01 - IMF

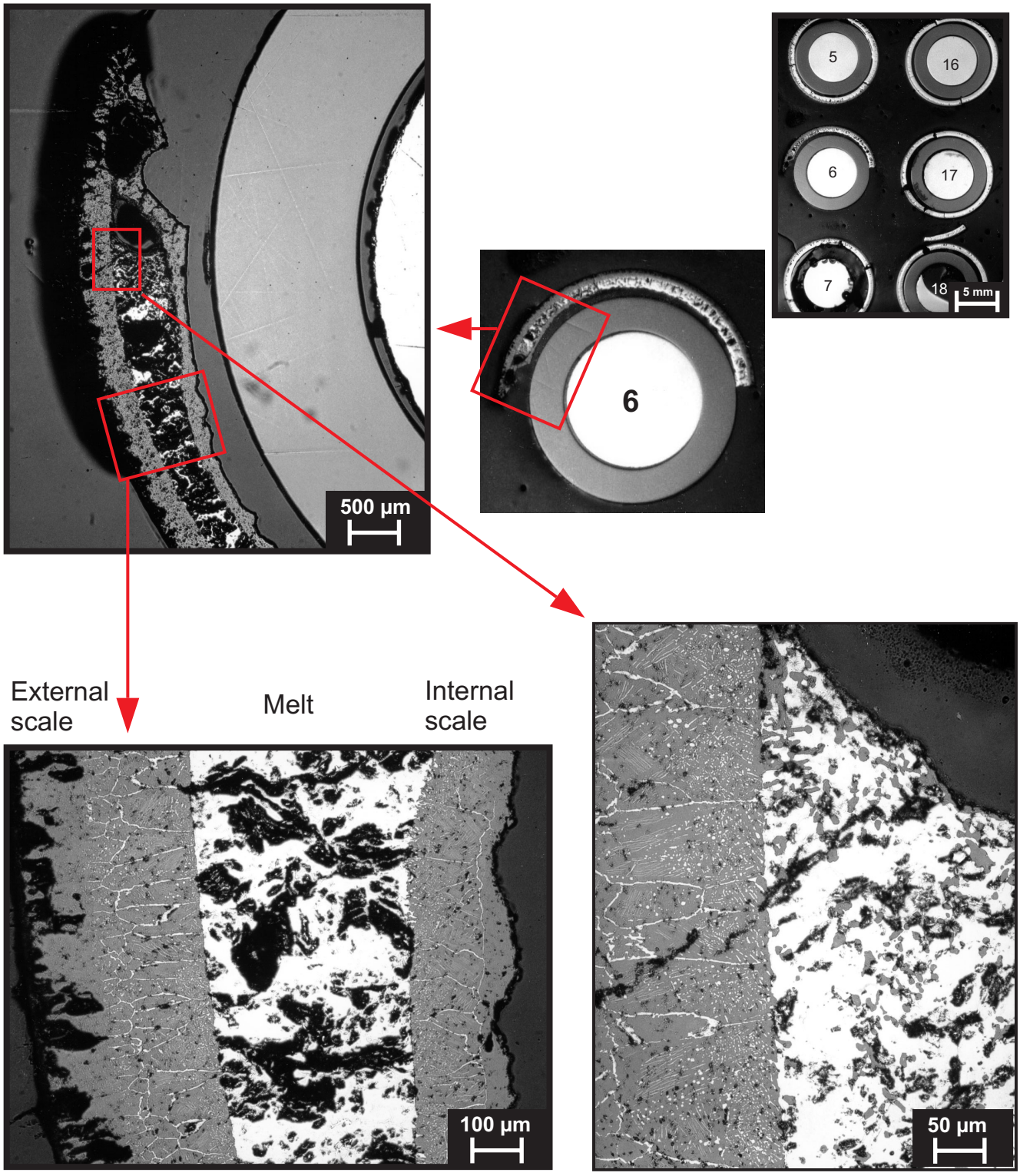

Fig. I-65: QUENCH-04; Cross section at bundle elevation 930 mm (QUE-04-5a, top); residual cladding and retained (Zr,O)-melt after partial melt relocation and internal steam oxidation.

Fig 65-QUE04 Folie 22.cdr
31.10.01 - IMF

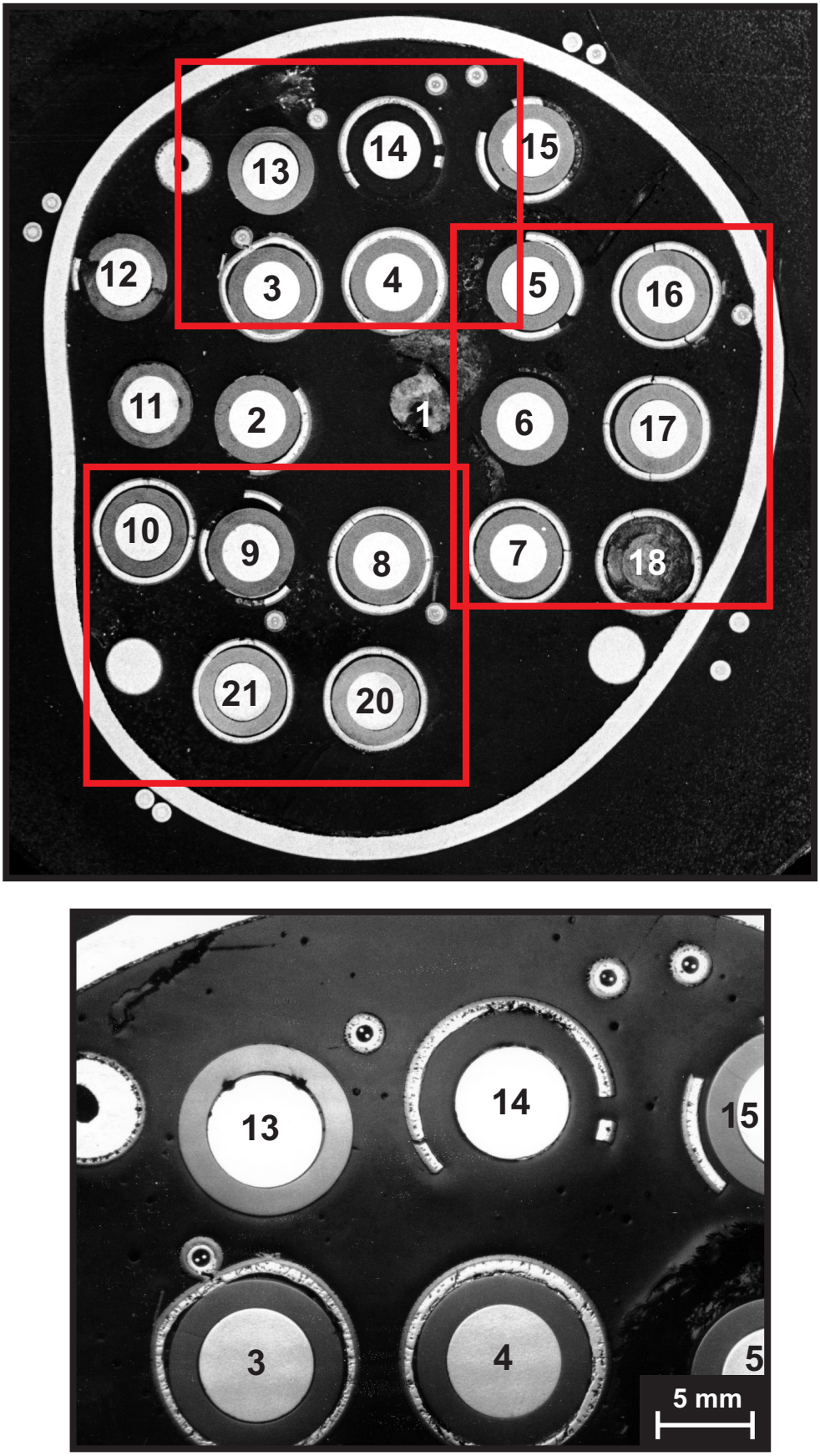

Fig. I-66: QUENCH-04; Cross section at bundle elevation 945 mm (QUE-04-6a, top); overview.

Fig 66-QUE04 Folie 23.cdr
31.10.01 - IMF

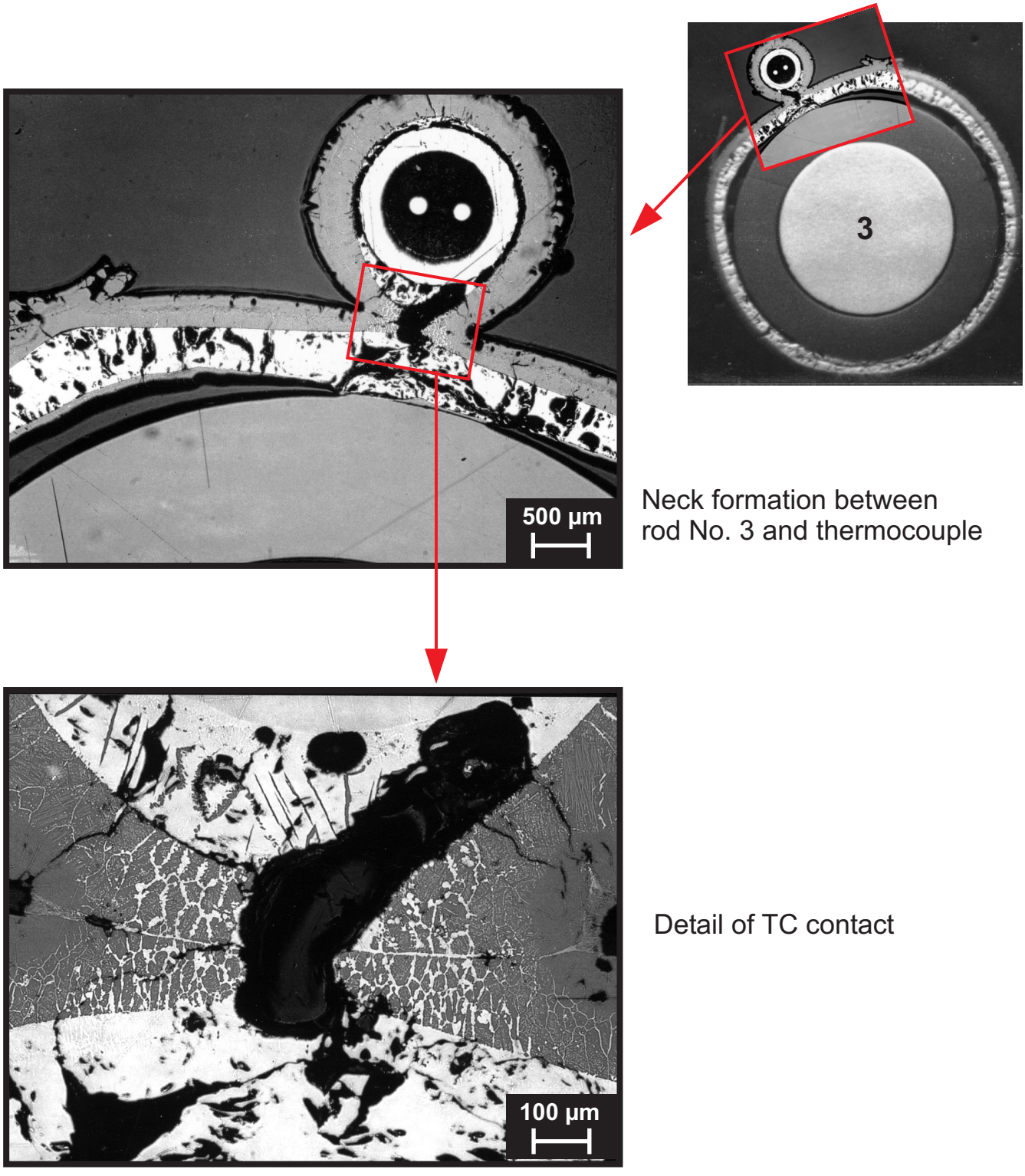

Fig. I-67: QUENCH-04; Cross section at bundle elevation 945 mm (QUE-04-6a, top); thermocouple status.

Fig 67-QUE04 Folie 24.cdr
31.10.01 - IMF

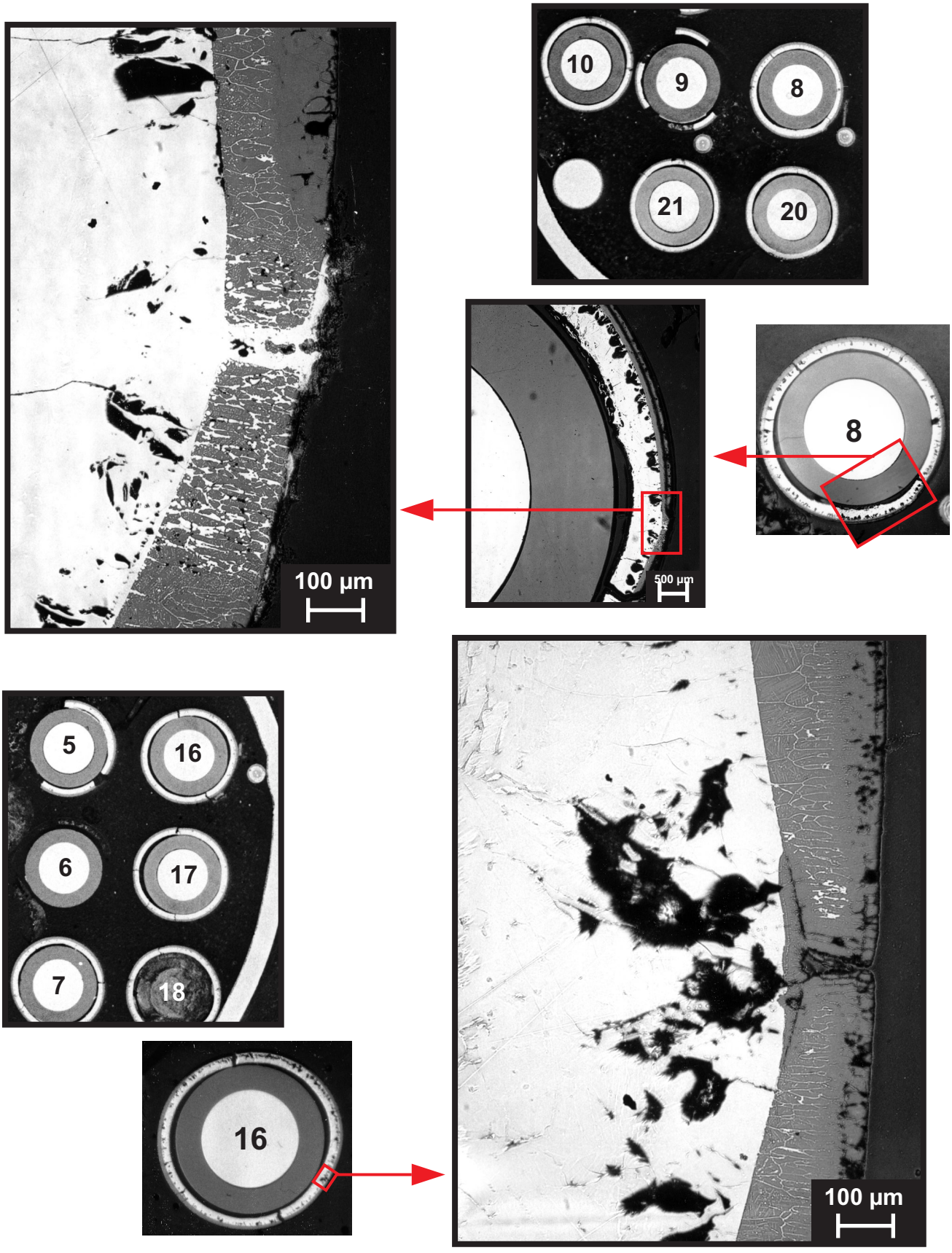

Fig. I-68: QUENCH-04; Cross section at bundle elevation 945 mm (QUE-04-6a, top); diminished cladding oxidation at positions of original thermocouple contact.

Fig 68-QUE04 Folie 25.cdr
31.10.01 - IMF

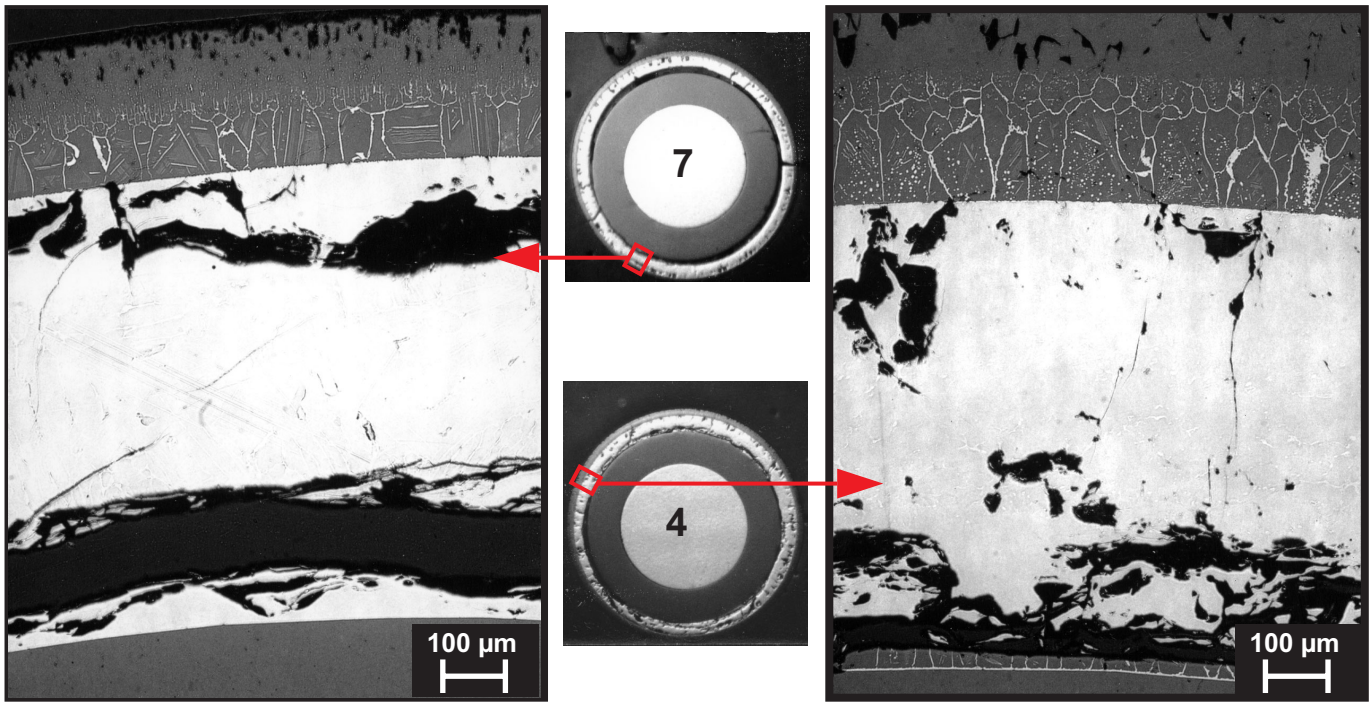

Rod No. 3 : No interaction detectable

Rod No. 4 : Interaction layer formed

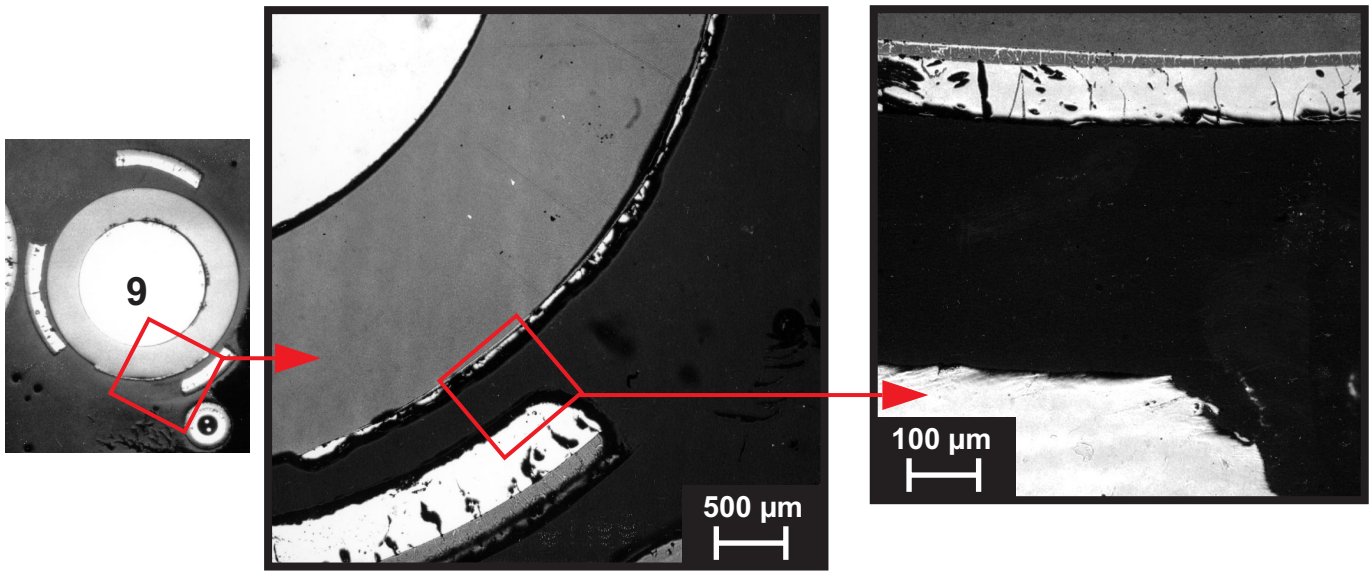

Rod No. 9 : Interaction layer and part of cladding adherent to pellet,
no internal steam oxidation detectable despite cladding fragmentation.

Fig. I-69: QUENCH-04; Cross section at bundle elevation 945 mm (QUE-04-6a, top); internal interaction of cladding and pellet.

Fig 69-QUE04 Folie 26.cdr
05.11.01 - IMF

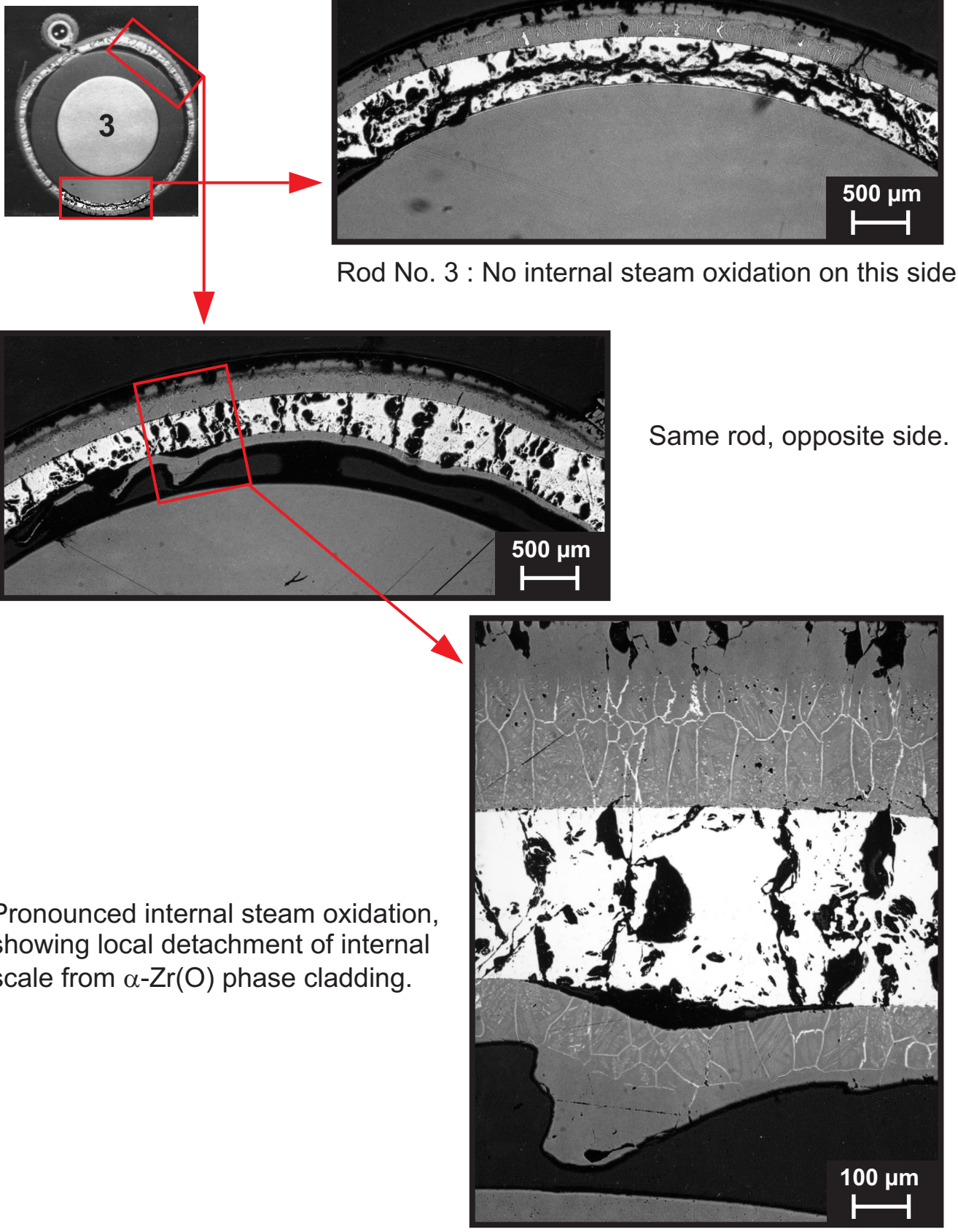

Fig. I-70: QUENCH-04; Cross section at bundle elevation 945 mm (QUE-04-6a, top); internal cladding oxidation by penetrated steam.

Fig 70-QUE04 Folie 27.cdr
05.11.01 - IMF

Overview of decomposed part of shroud, showing strain-related wall thinning.

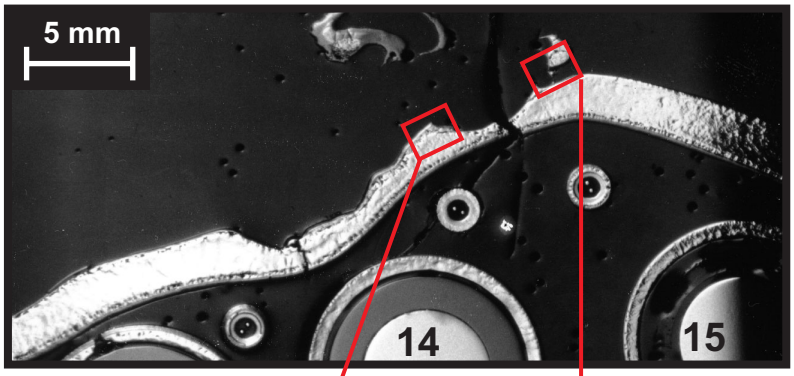

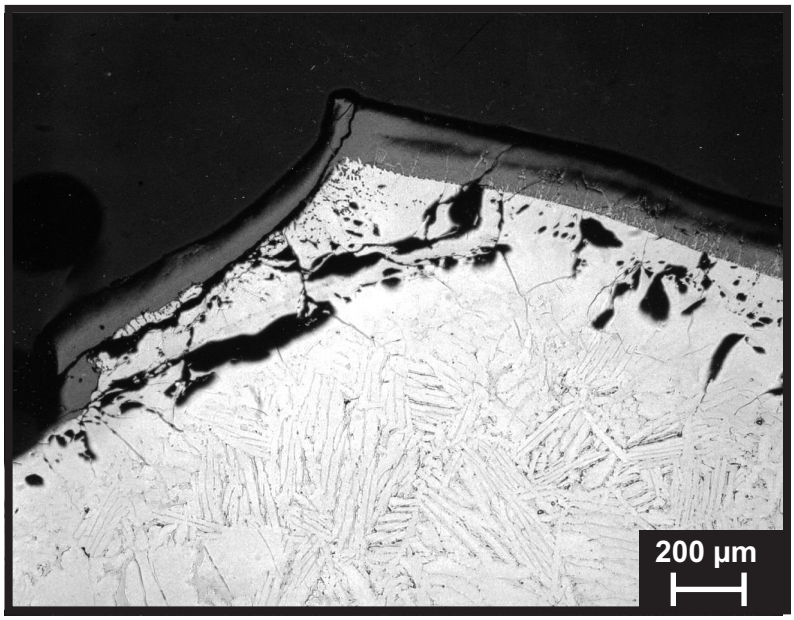

Strongly oxidized external shroud surface (right); deformation-related, less oxidized new surface (left).

Strongly oxidized melt droplet, bridge towards the shroud.

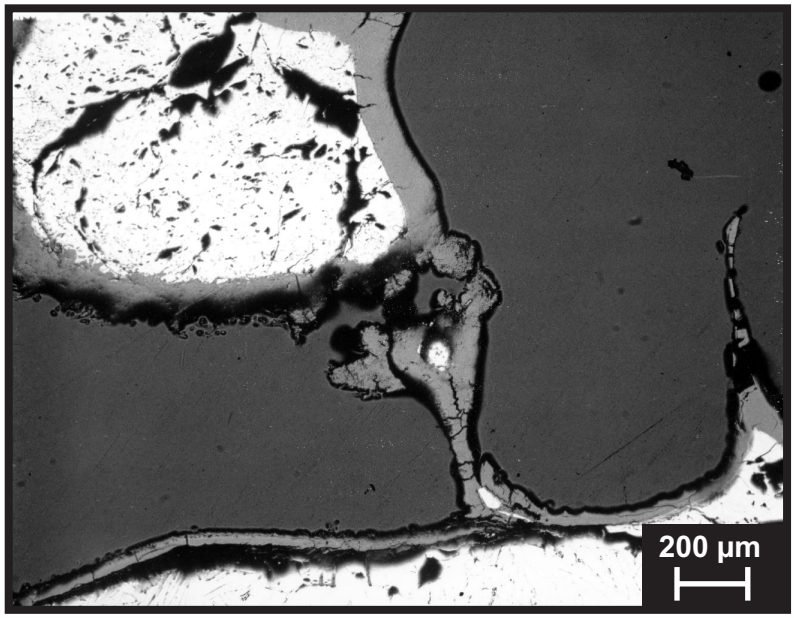

Fig. I-71: QUENCH-04; Cross section at shroud elevation 965 mm (QUE-04-6, top); shroud decomposition.

Fig 71-QUE04 Folie 28.cdr
05.11.01 - IMF

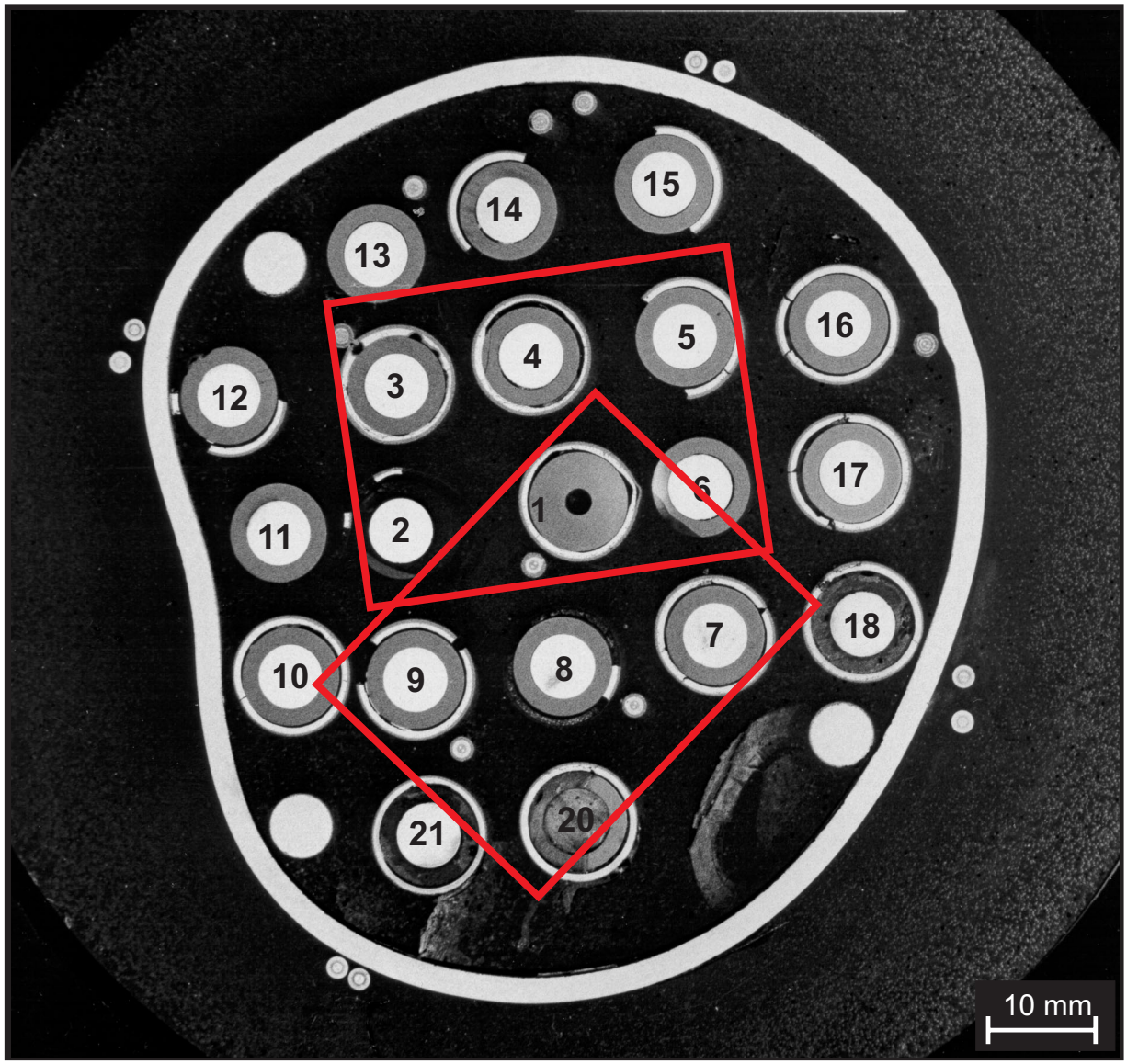

Fig. I-72: QUENCH-04; Cross section at bundle elevation 960 mm (QUE-04-7a, top); overview.

Fig 72-QUE04 Folie 1.cdr
05.11.01 - IMF

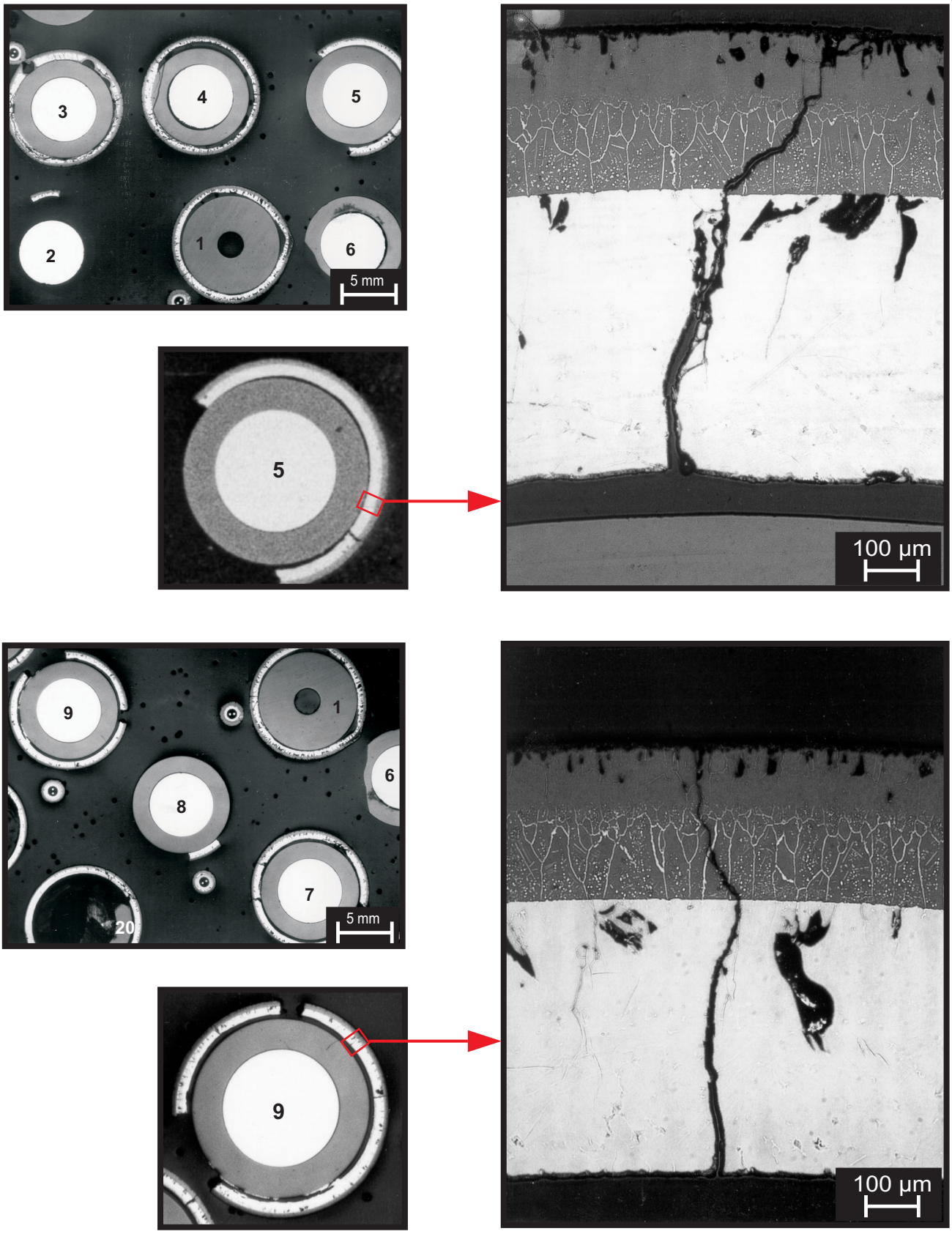

Fig. I-73: QUENCH-04; Cross section at bundle elevation 960 mm (QUE-04-7a, top); non-oxidized cladding through-wall cracks.

Fig 73-QUE04 Folie 2.cdr
05.11.01 - IMF

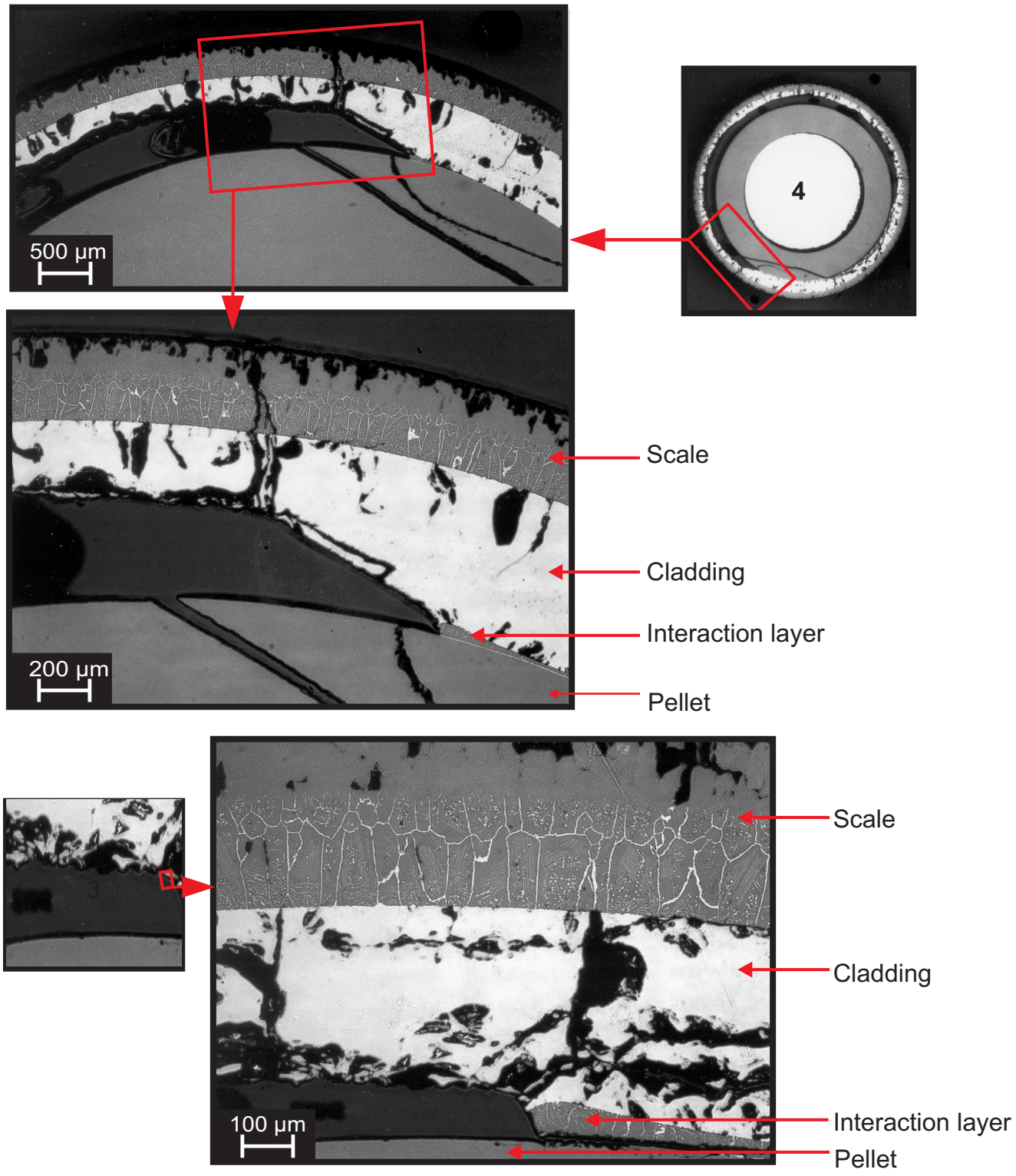

Fig. I-74: QUENCH-04; Cross section at bundle elevation 960 mm (QUE-04-7a, top); partial relocation of molten cladding, pellet interaction of remaining cladding.

Fig 74-QUE04 Folie 3.cdr
05.11.01 - IMF

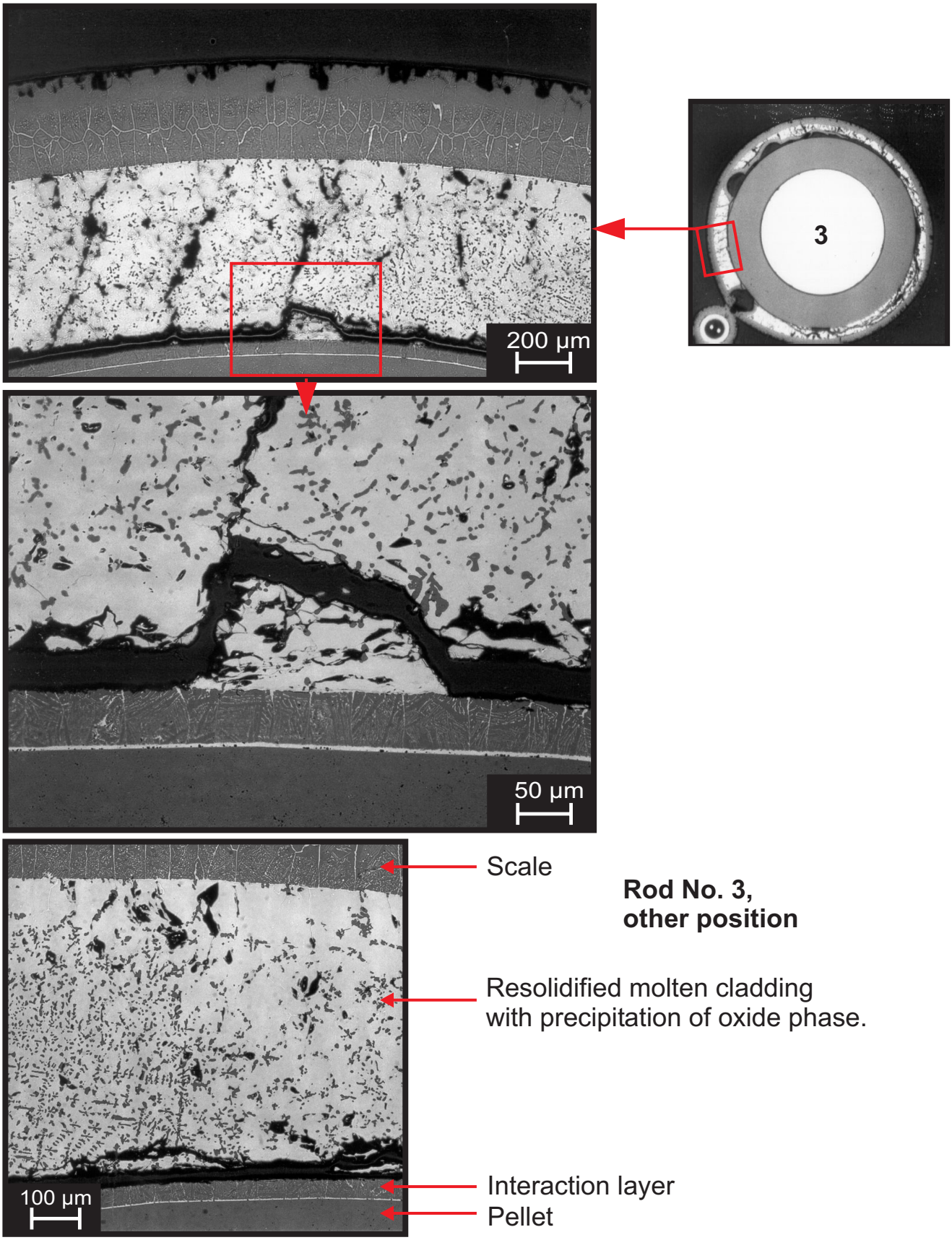

Fig. I-75: QUENCH-04; Cross section at bundle elevation 960 mm (QUE-04-7a, top); re-solidified cladding with oxide precipitates.

Fig 75-QUE04 Folie 4.cdr
05.11.01 - IMF

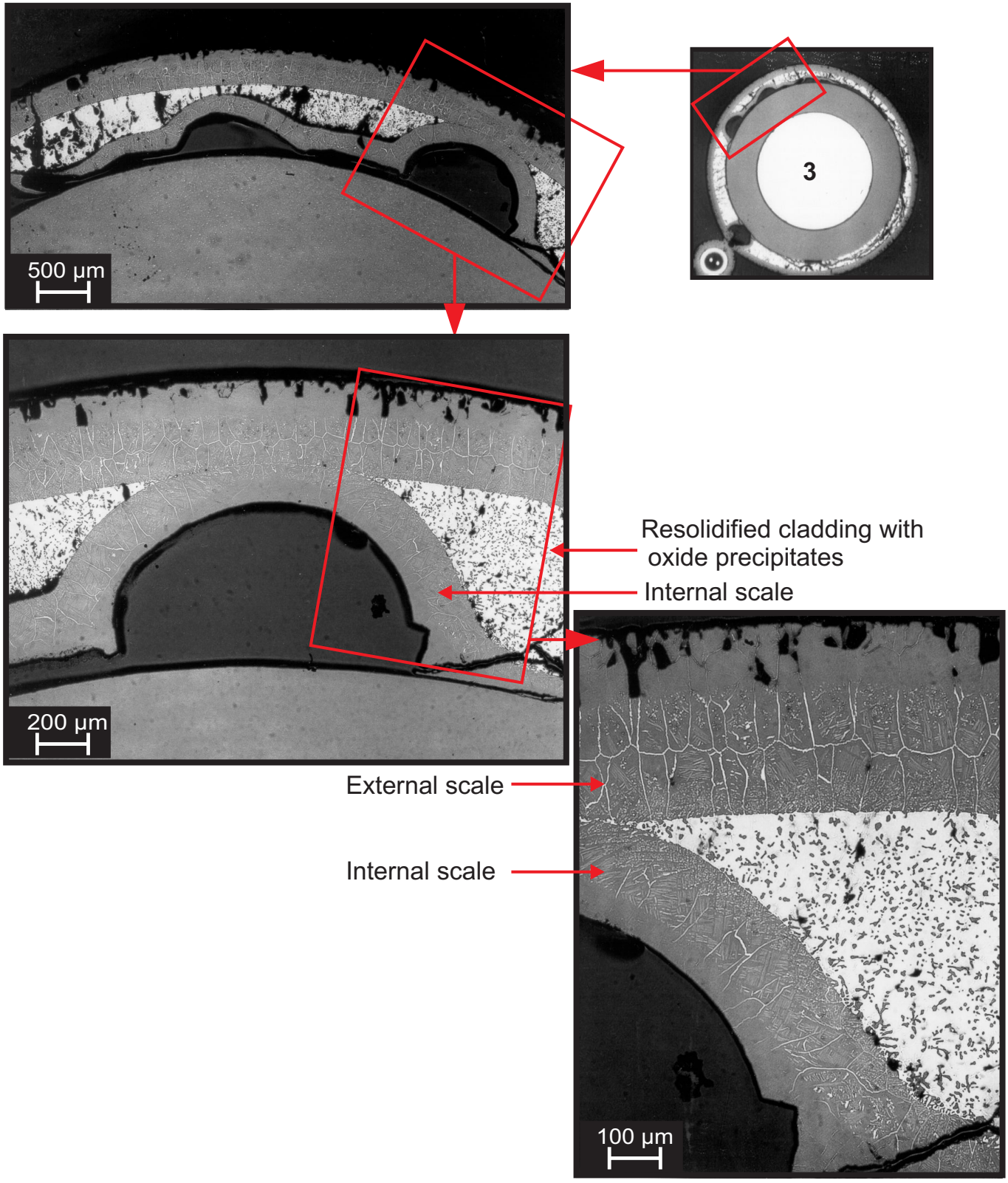

Fig. I-76: QUENCH-04; Cross section at bundle elevation 960 mm (QUE-04-7a, top); internal steam oxidation of cladding after partial relocation.

Fig 76-QUE04 Folie 5.cdr
05.11.01 - IMF

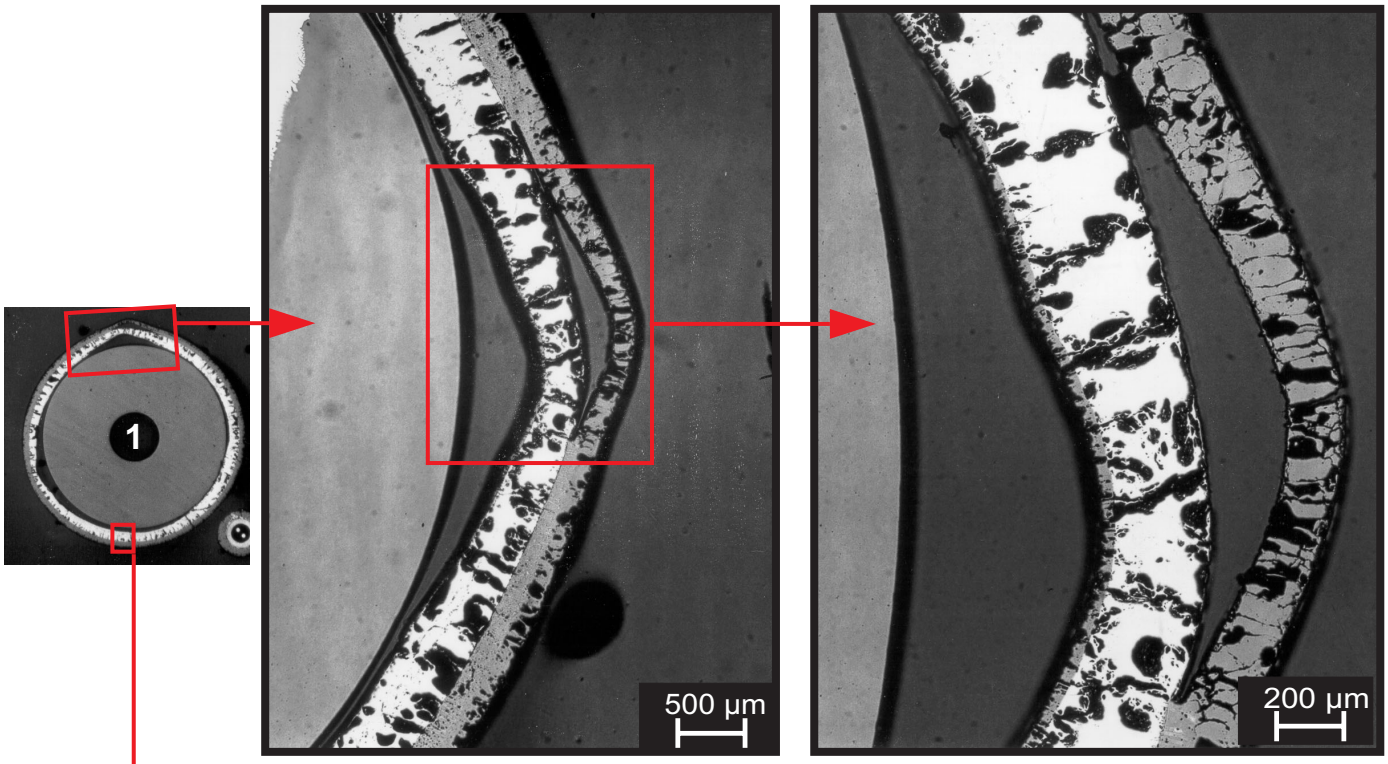

Bulged cladding and scale of central rod (No. 1)

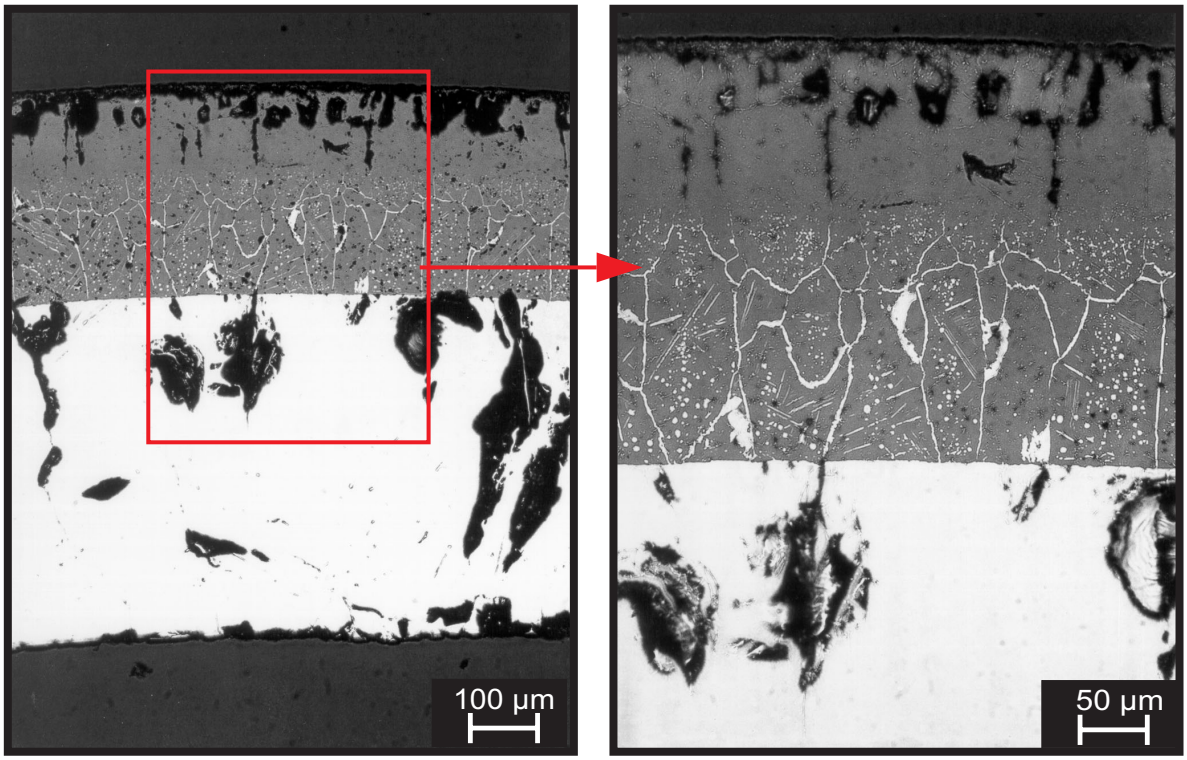

Opposite side of central rod

Fig. I-77: QUENCH-04; Cross section at bundle elevation 960 mm (QUE-04-7a, top); special form of cladding deformation.

Fig 77-QUE04 Folie 6.cdr
05.11.01 - IMF

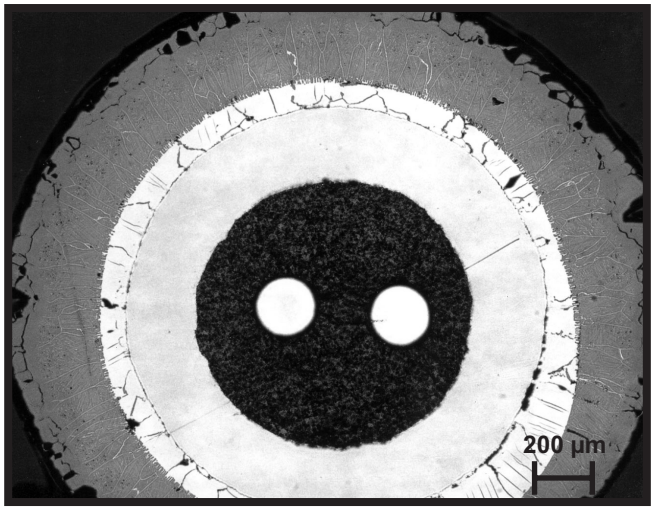

TC near rod No. 14

Partly oxidized
Zry sheath

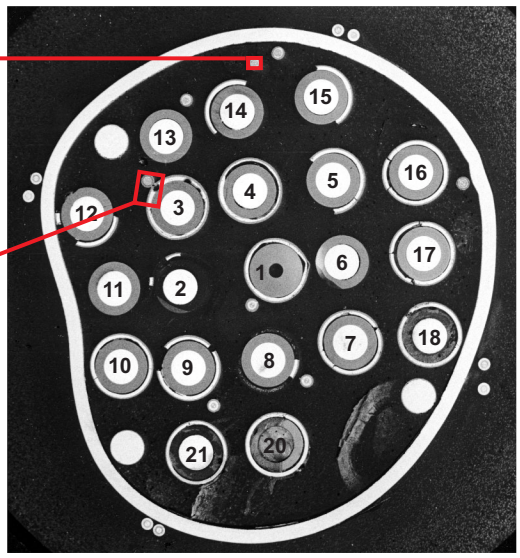

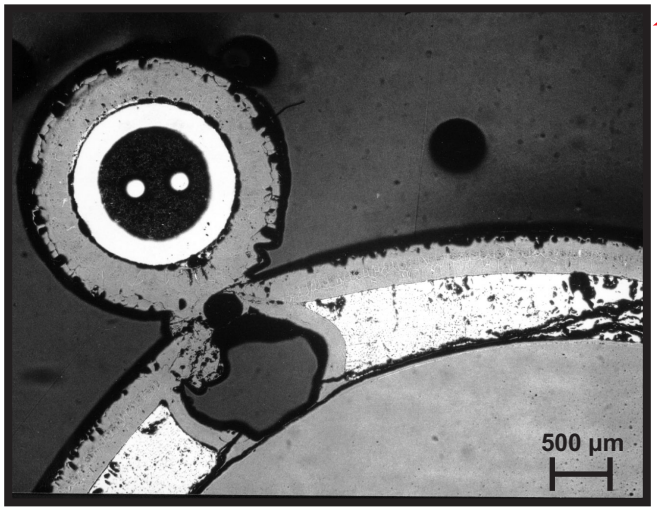

TC with rod No. 3

Completely
oxidized Zry sheath

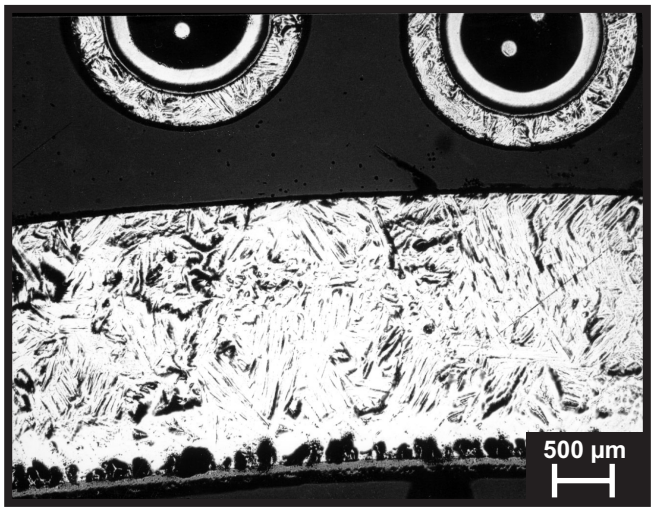

TCs at outer side of shroud
(see next figure, pos.1)

Non oxidized
Zry sheath

Shroud

Fig. I-78: QUENCH-04; Cross section at bundle elevation 960 mm (QUE-04-7a, top); thermocouple status.

Fig 78-QUE04 Folie 7.cdr
05.11.01 - IMF

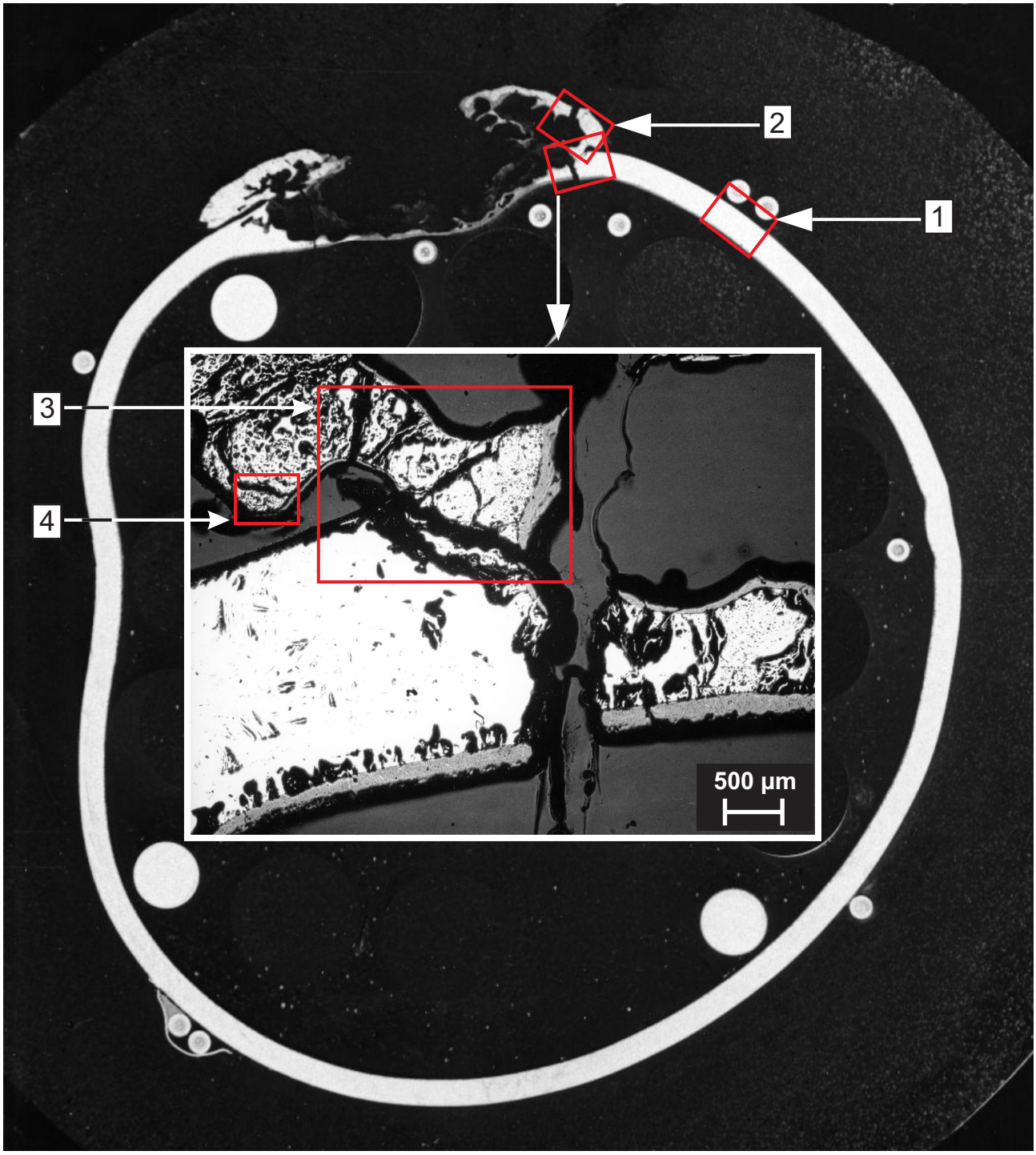

Fig. I-79: QUENCH-04; Cross section at shroud elevation 980 mm (QUE-04-7, top); overview of shroud.

Fig 79-QUE04 Folie 8.cdr
05.11.01 - IMF

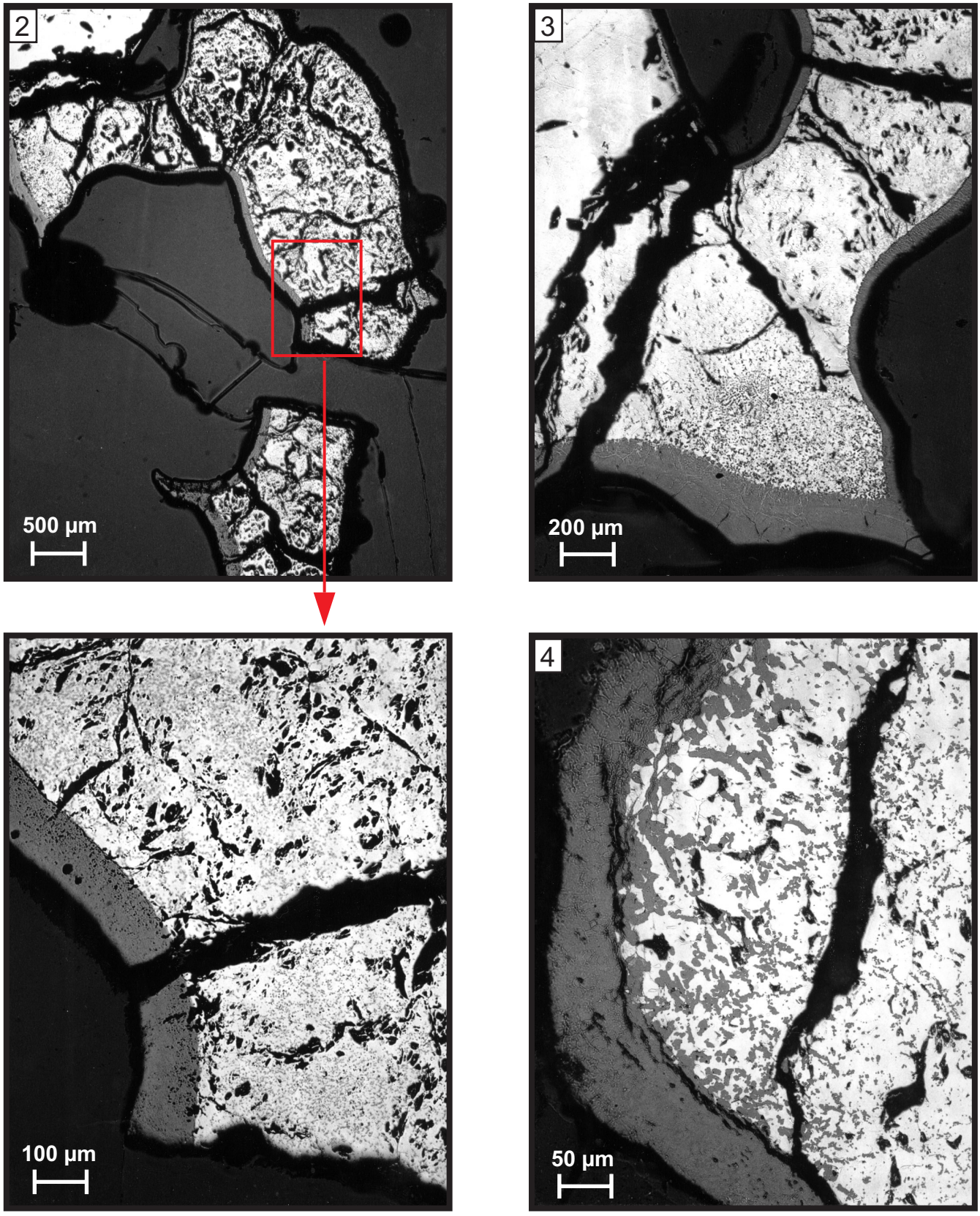

Fig. I-80: QUENCH-04; Cross section at shroud elevation 980 mm (QUE-04-7, top); partially oxidized shroud melt showing porosity and fragmentation.

Fig 80-QUE04 Folie 9.cdr
05.11.01 - IMF

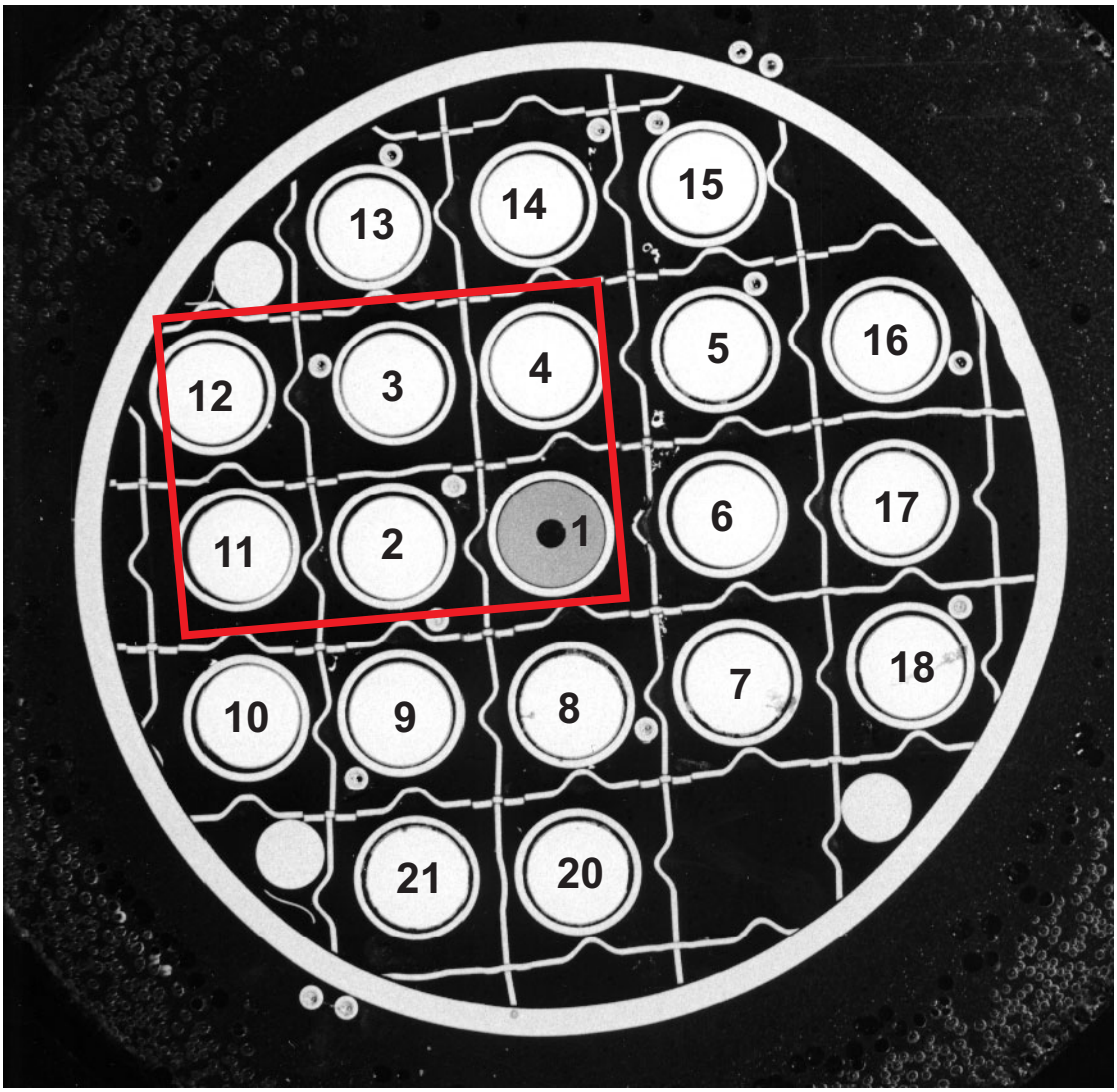

Fig. I-81: QUENCH-04; Cross section at bundle elevation 1130 mm (QUE-04-8a, top); overview bundle and spacer grid.

Fig 81-QUE04 Folie 10.cdr
05.11.01 - IMF

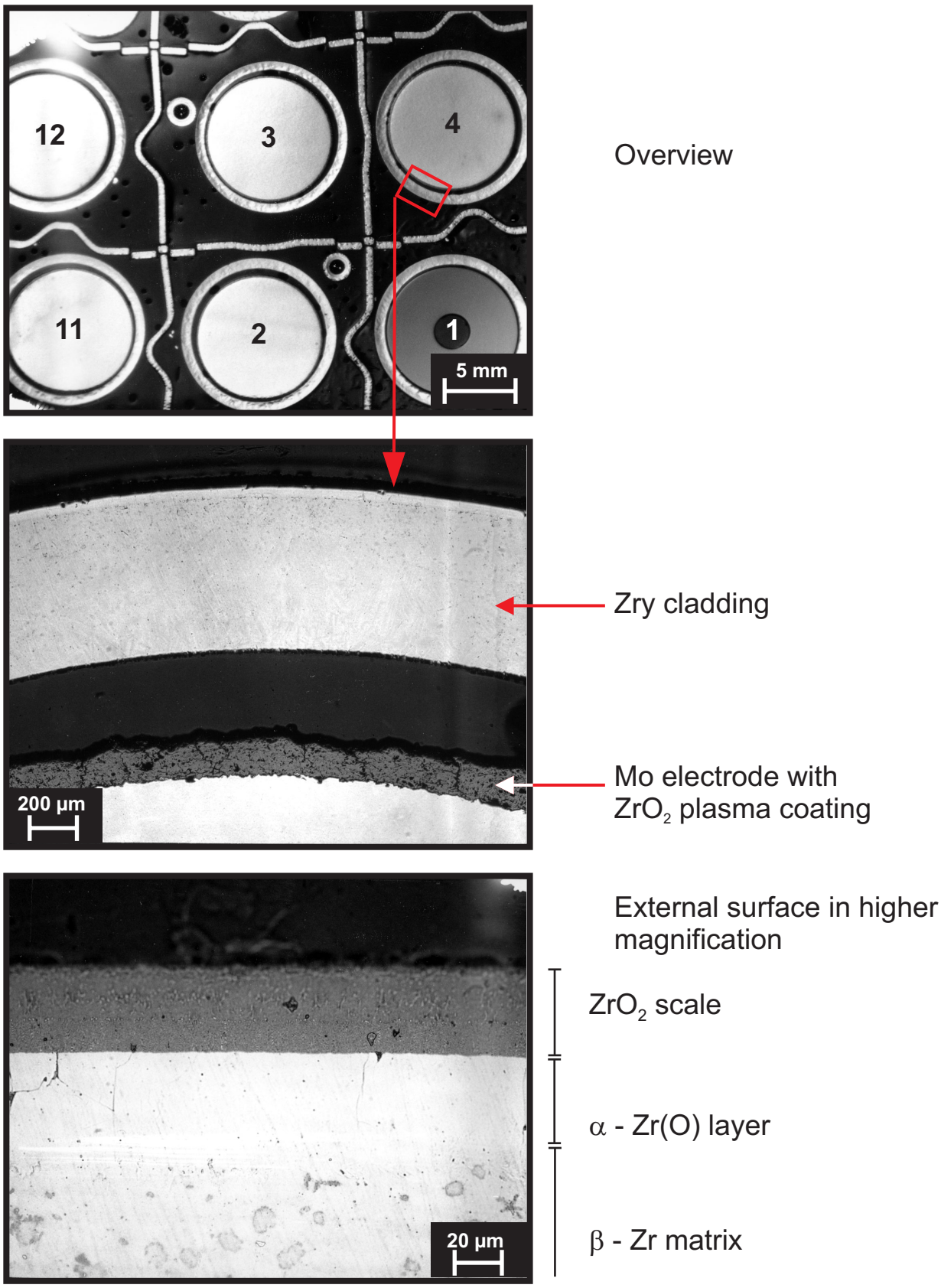

Fig. I-82: QUENCH-04; Cross section at bundle elevation 1130 mm (QUE-04-8a, top); Zry cladding oxidation.

Fig 82-QUE04 Folie 11.cdr
05.11.01 - IMF

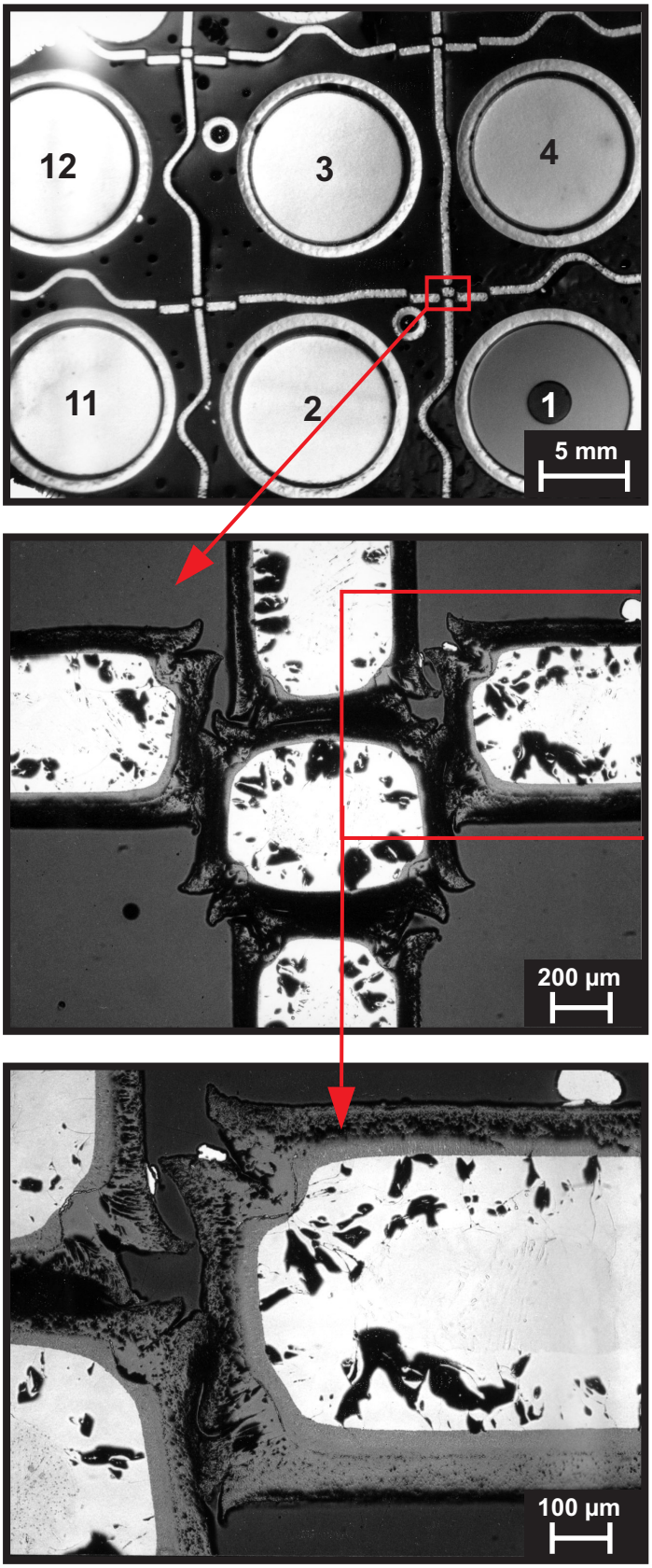

Overview

Spacer grid cross

Scale on spacer, showing break-awayrelated edge splitting effect.

Fig. I-83: QUENCH-04; Cross section at bundle elevation 1130 mm (QUE-04-8a, top); Zry spacer grid oxidation.

Fig 83-QUE04 Folie 12.cdr
05.11.01 - IMF

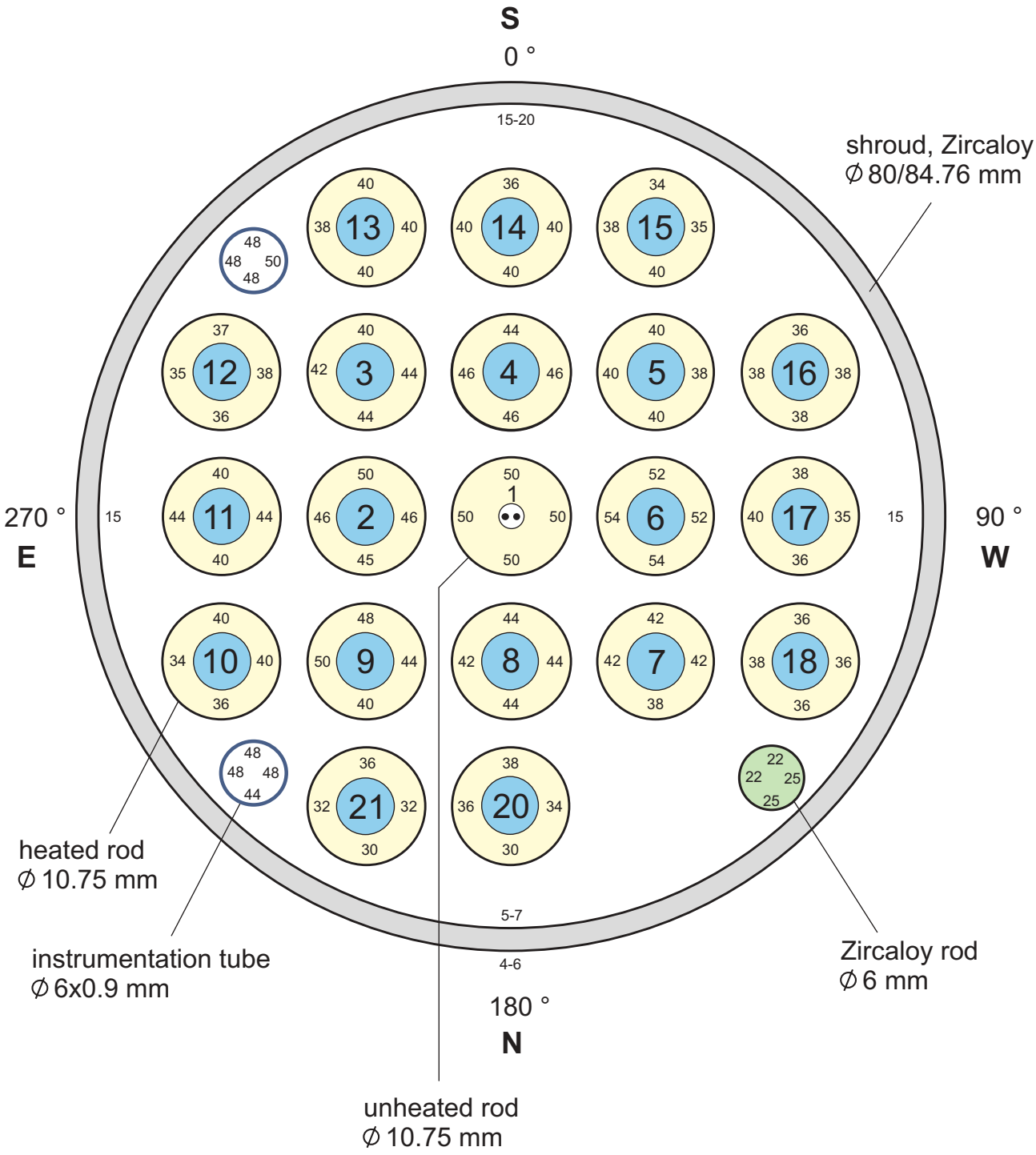

Fig. I-84: QUENCH-04; Oxide layer thicknesses of shroud at 750 mm, oxide layer thicknesses of bundle at 730 mm, cross section QUE-04-3a and QUE-04-3

Fig 84 QUE04 cross section-3.cdr
06.11.01 - IMF

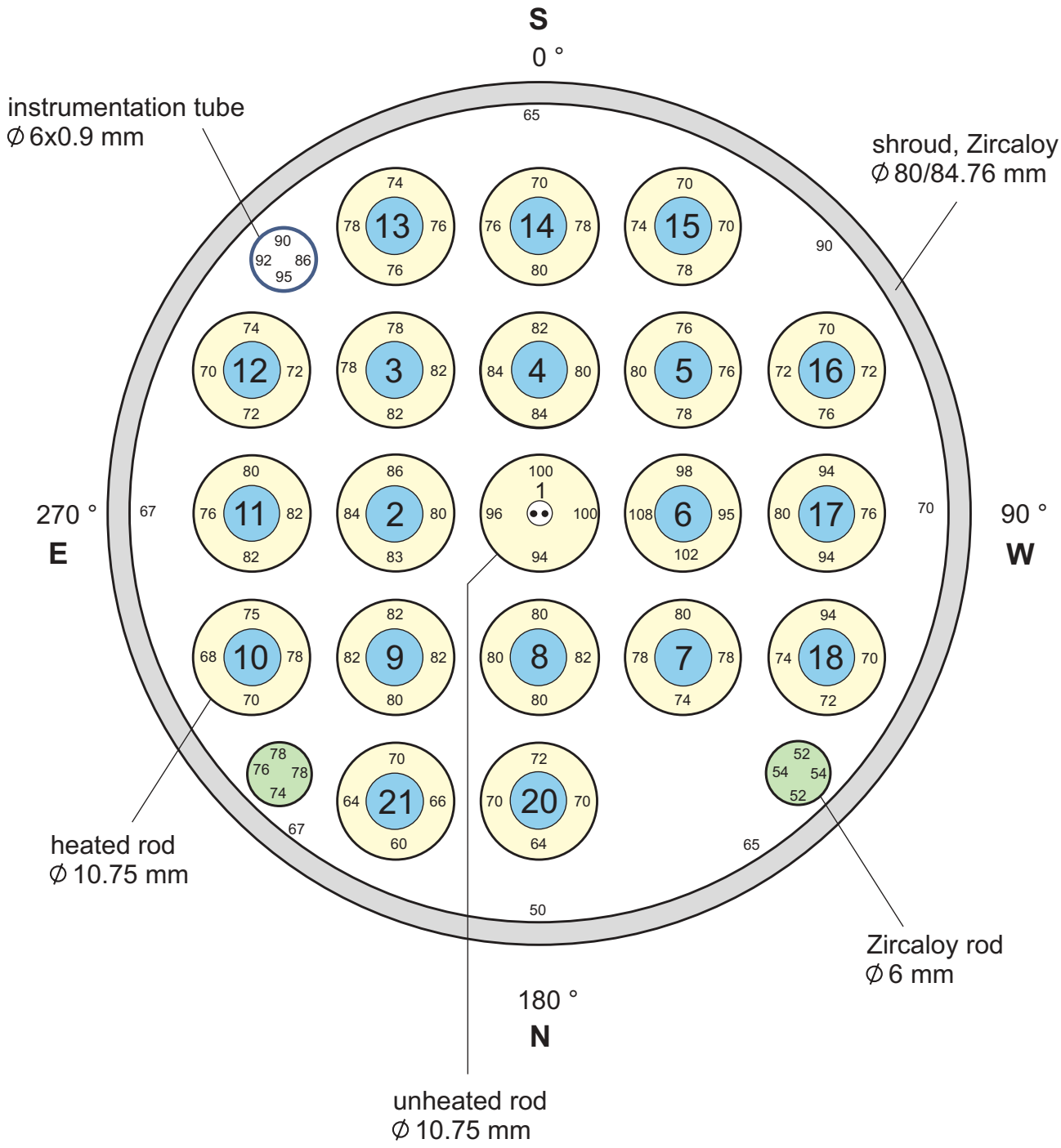

Fig. I-85: QUENCH-04; Oxide layer thicknesses of shroud at 850 mm, oxide layer thicknesses of bundle at 830 mm, cross section QUE-04-4a and QUE-04-4

Fig 85 QUE04 cross section-4.cdr
24.10.01 - IMF

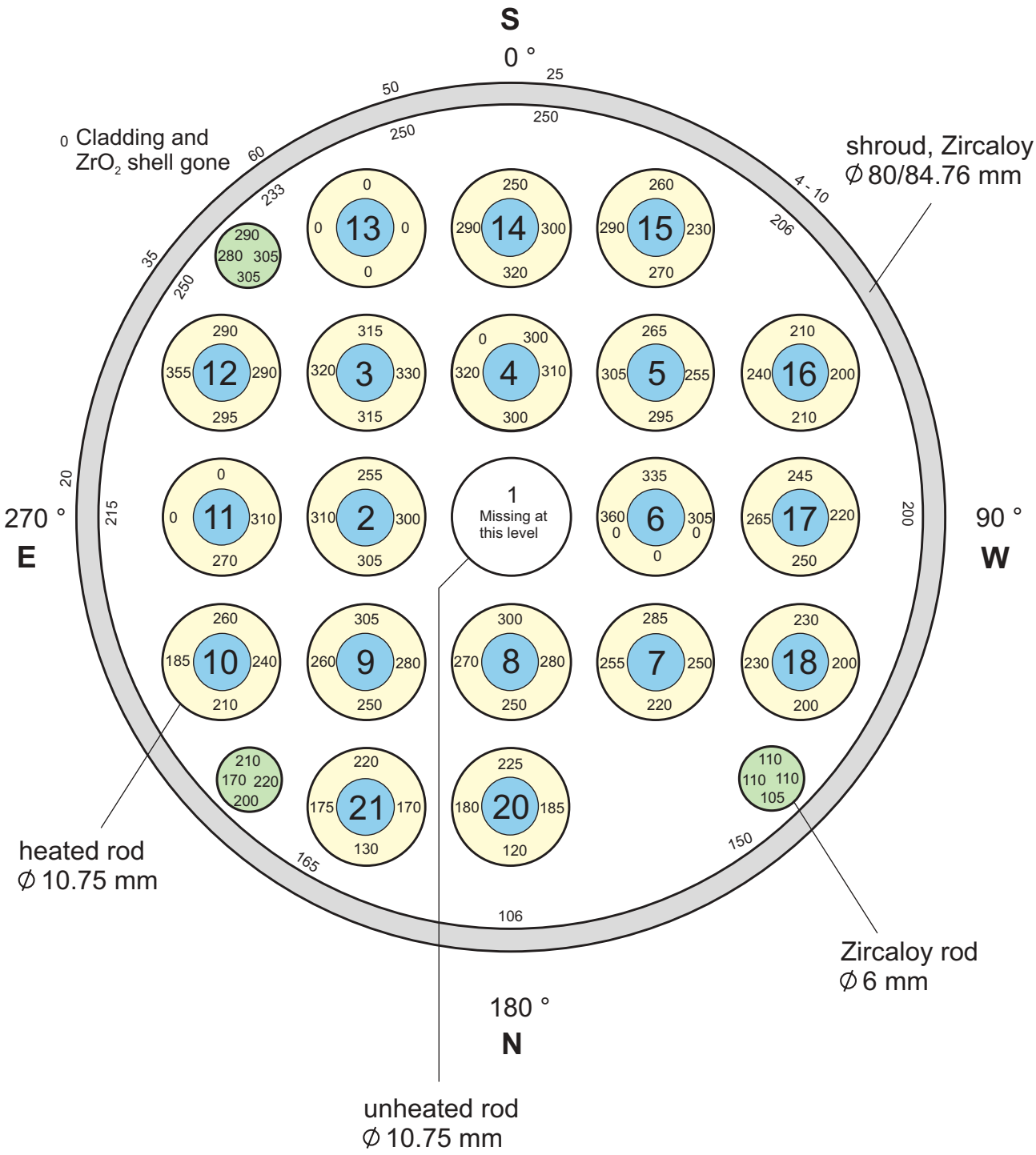

Fig. I-86: QUENCH-04; Oxide layer thicknesses of shroud at 950 mm, oxide layer thicknesses of bundle at 930 mm, cross section QUE-04-5a and QUE-04-5

Fig 86 QUE04 cross section-5.cdr
25.10.01 - IMF

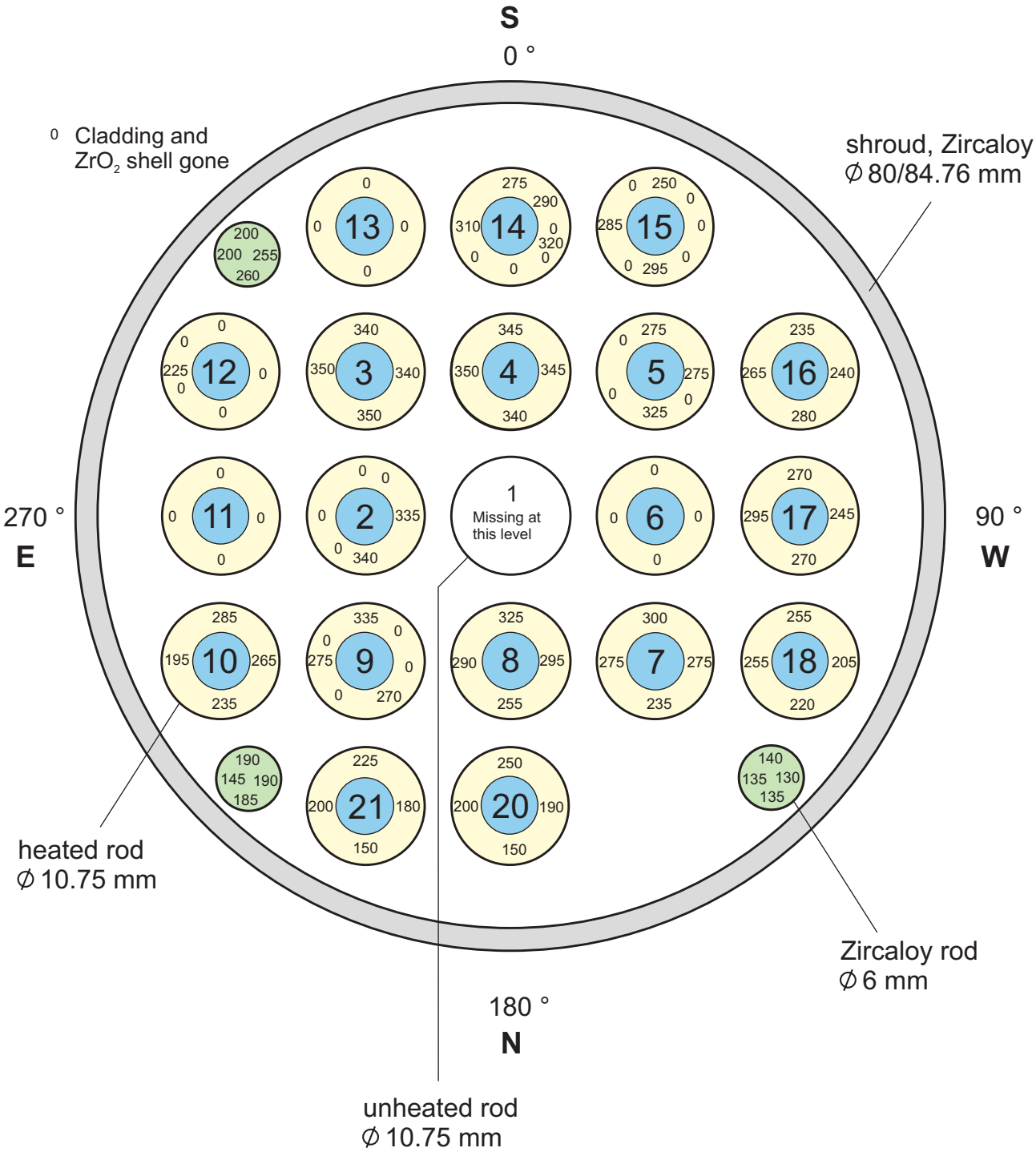

Fig. I-87: QUENCH-04; Oxide layer thicknesses of shroud at 965 mm, oxide layer thicknesses of bundle at 945 mm, cross section QUE-04-6a and QUE-04-6

Fig 87 QUE04 cross section-6.cdr
25.10.01 - IMF

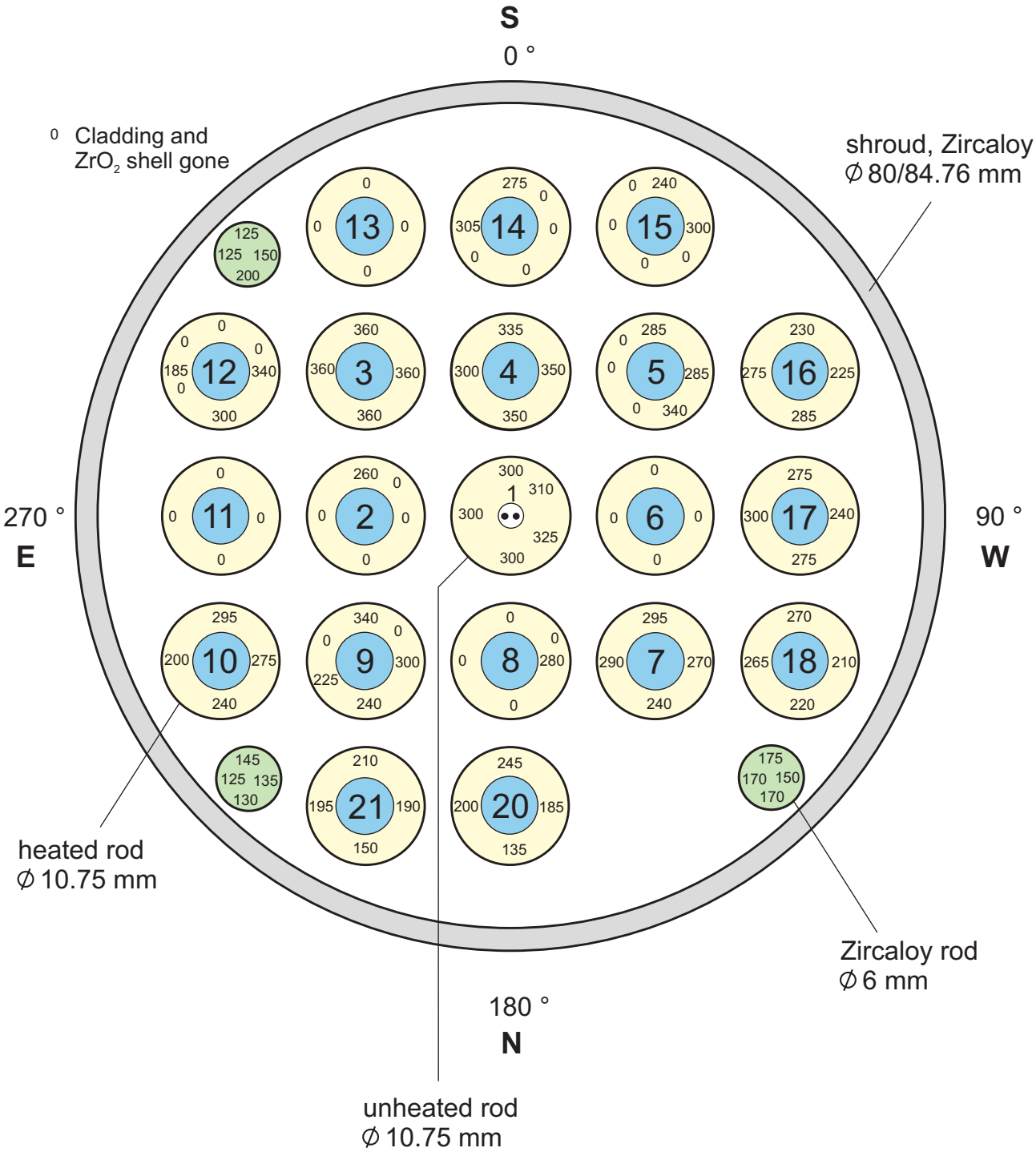

Fig. I-88: QUENCH-04; Oxide layer thicknesses of shroud at 980 mm, oxide layer thicknesses of bundle at 960 mm, cross sections QUE-04-7a and QUE-04-7

Fig 88 QUE04 cross section-7.cdr
25.10.01 - IMF

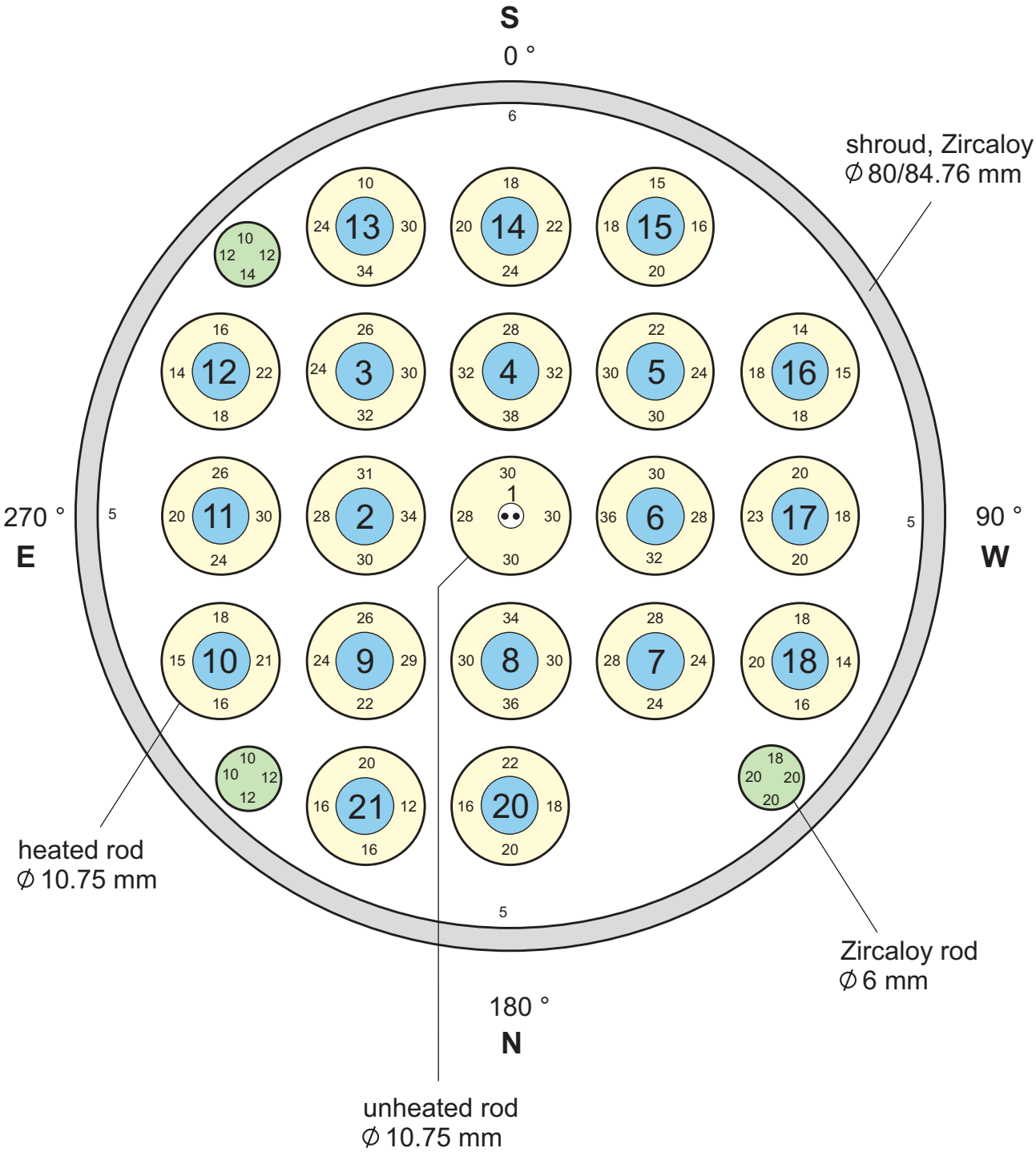

Fig. I-89: QUENCH-04; Oxide layer thicknesses of shroud at 1150 mm, oxide layer thicknesses of bundle at 1130 mm, cross sections QUE-04-8a and QUE-04-8

Fig 89 QUE04 cross section-8.cdr
25.10.01 - IMF

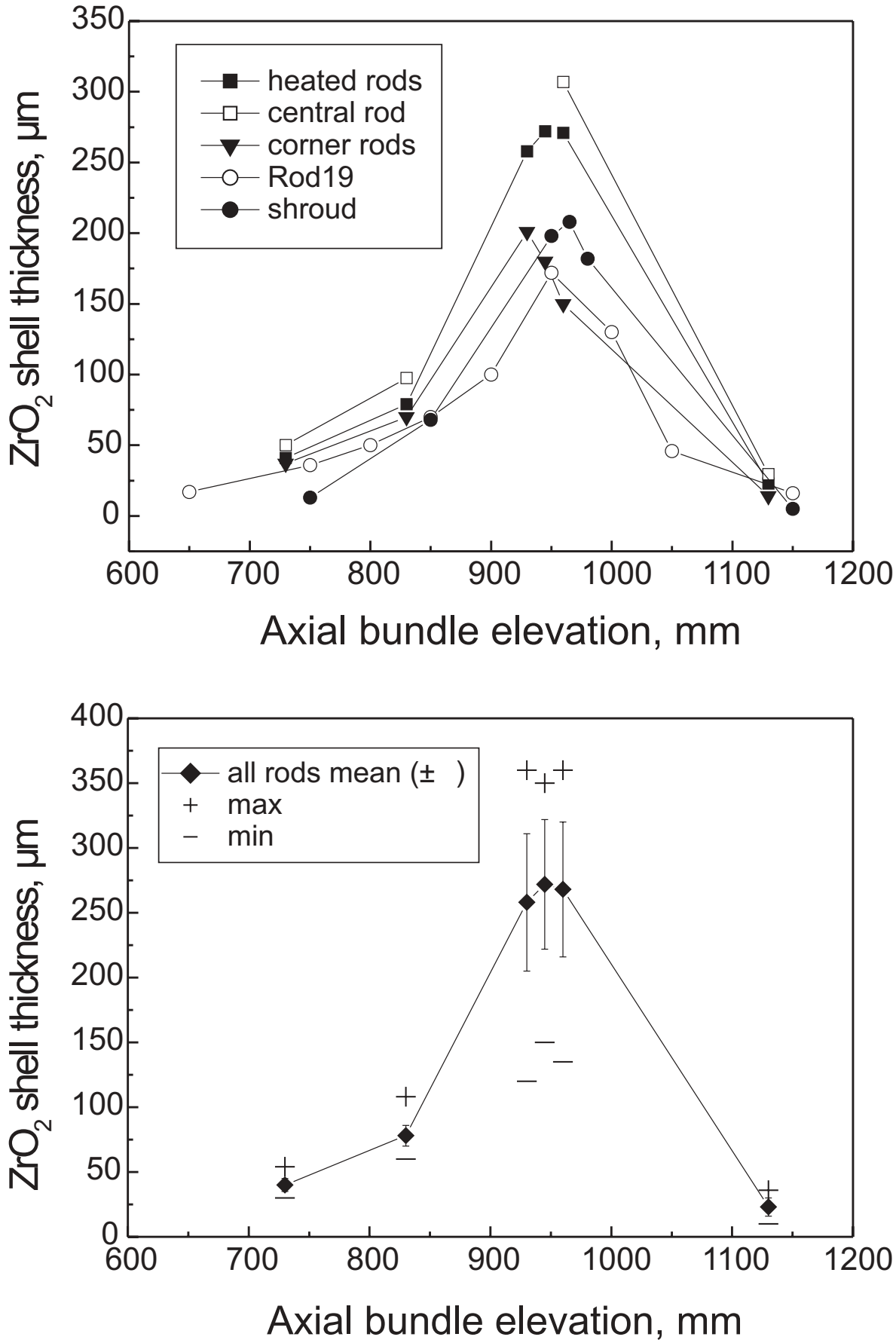

Fig. I-90: QUENCH-04; Axial oxide layer thicknesses distribution

Fig 90 QUE04 axial oxide layer 1.cdr
25.10.01 - IMF

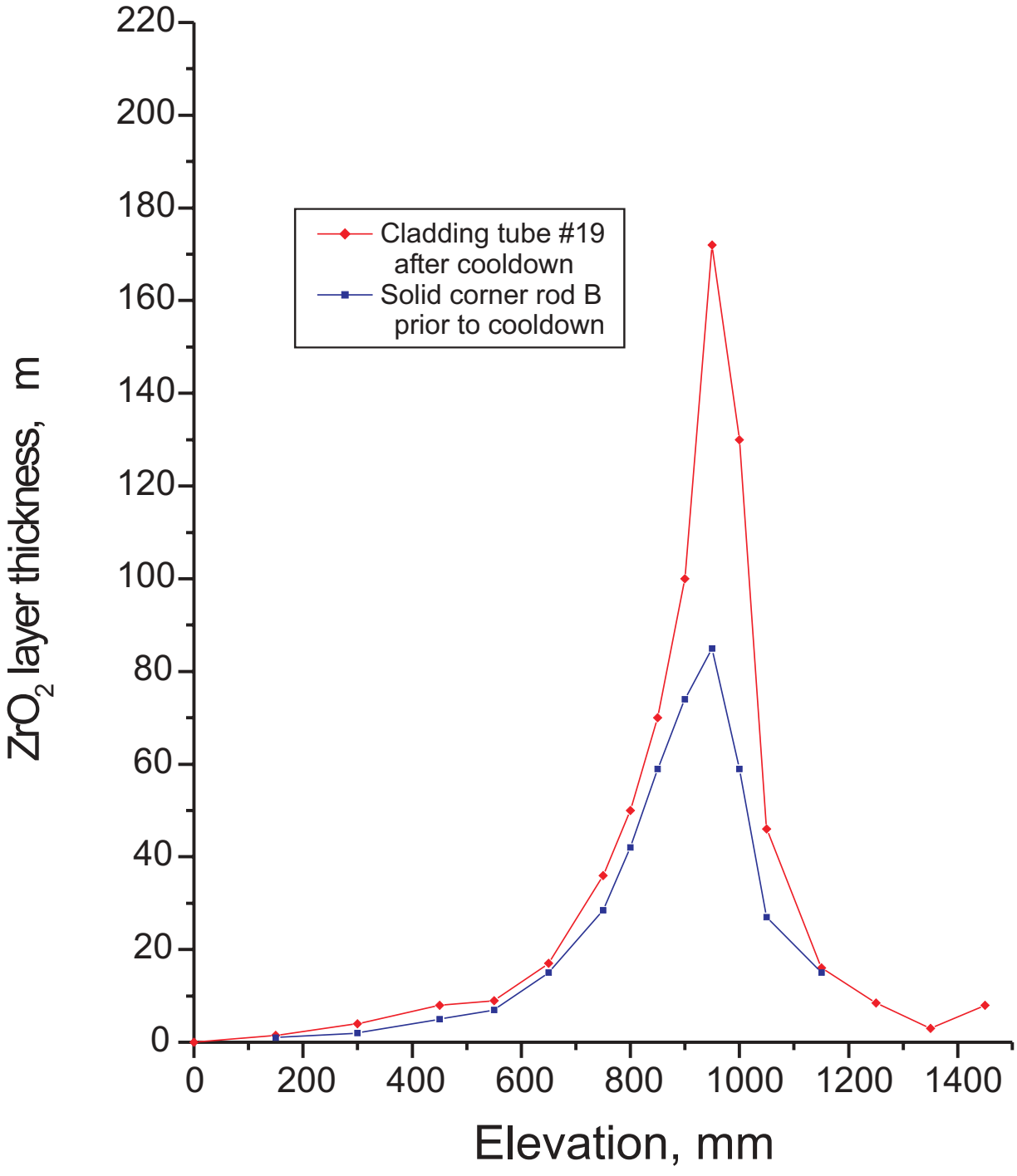

Fig. I-91: QUENCH-04; Axial oxide layer thicknesses profile of rod cladding #19 (entire test) and corner rod B (withdrawn during the transient, prior to cooldown)

Fig 91 QUE04 axial oxide layer 2.cdr
25.10.01 - IMF

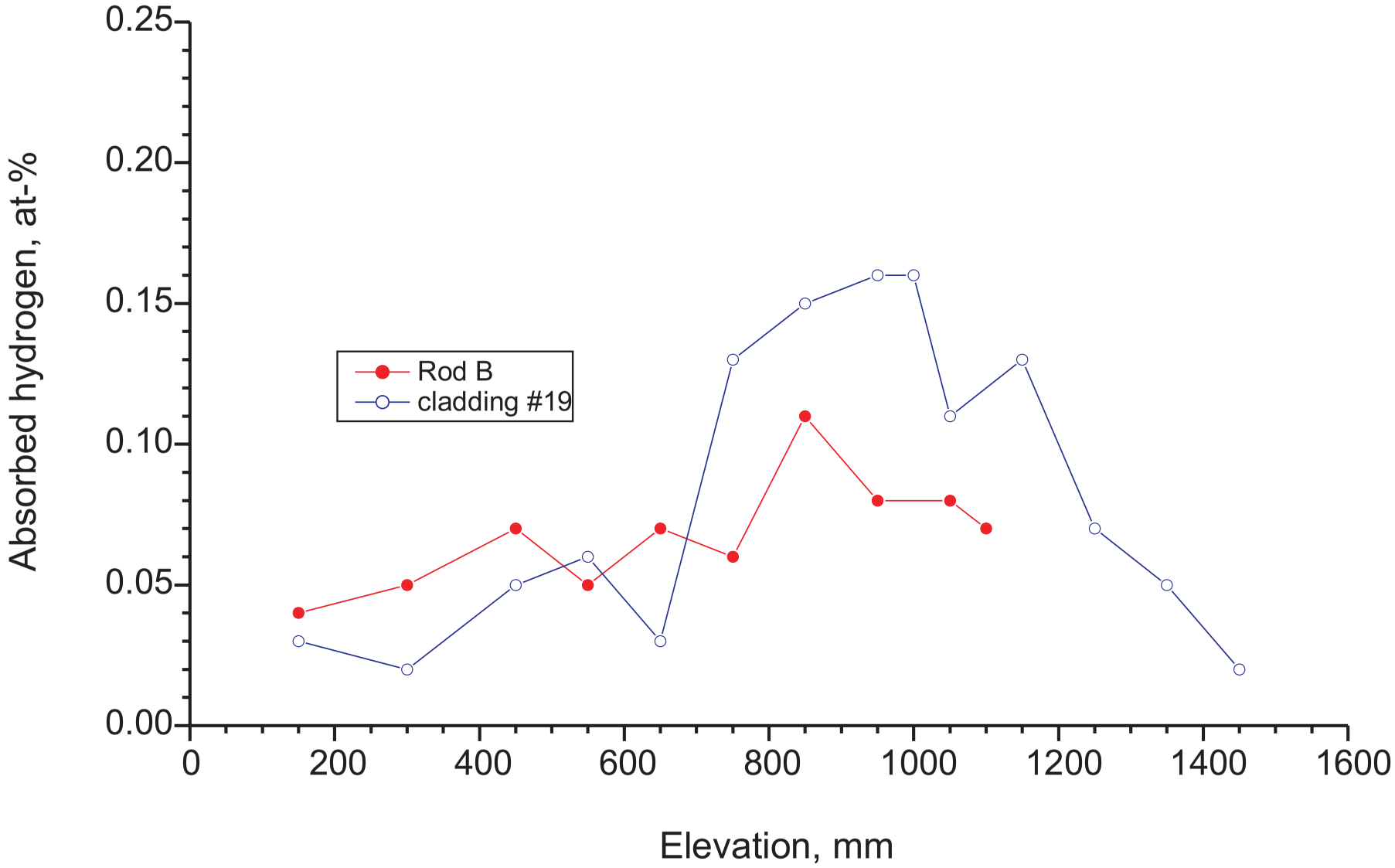

Fig. I-92: QUENCH-04; Absorbed hydrogen in the remaining Zry-4 metal of rod cladding #19 and corner rod B

Fig 92-QUE04 H2 absorb.cdr
25.10.01 - IMF

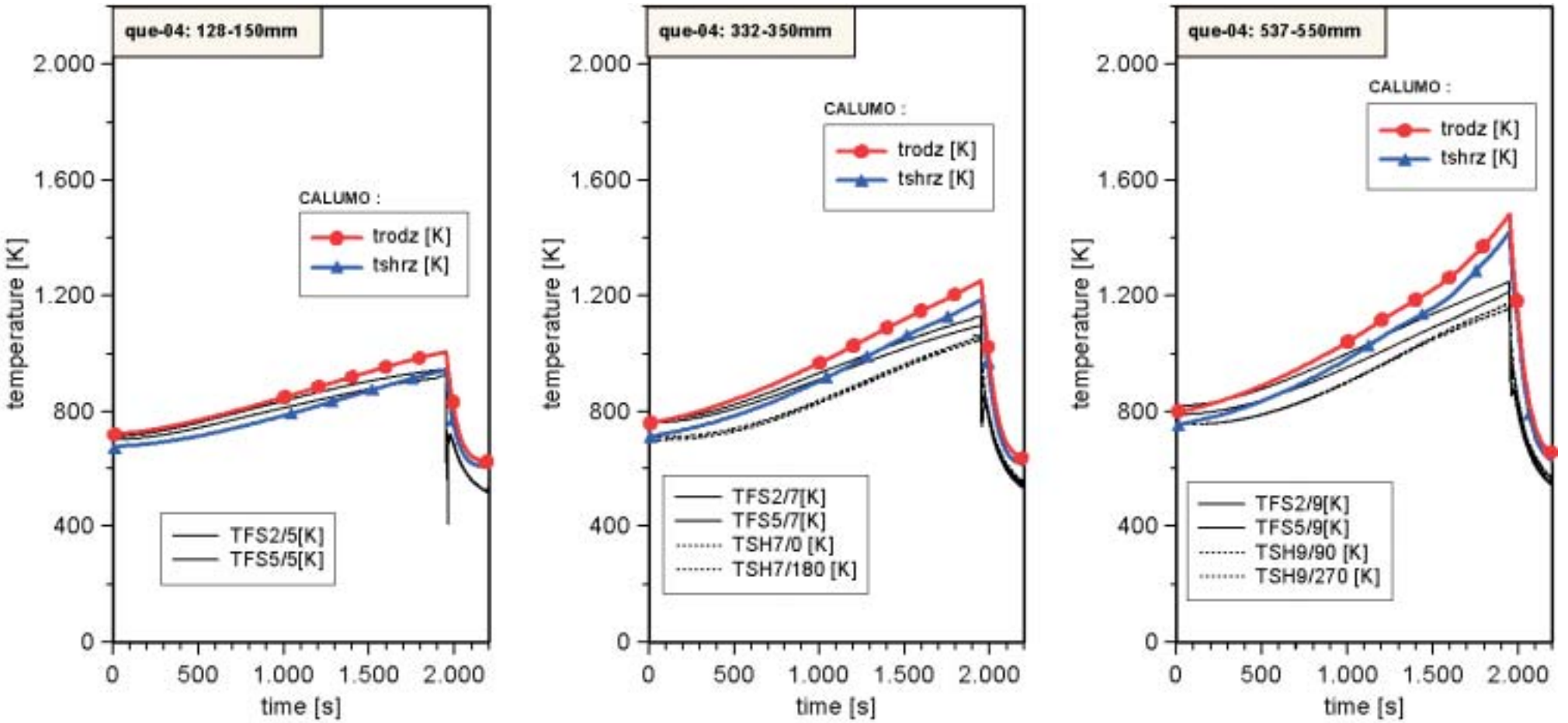

Fig. I-93: Evolution of rod and shroud temperatures of QUENCH-04 (low oxidation case) at different axial locations.

Fig 93-QUE04 Steiner 1.cdr
08.11.01 - IMF

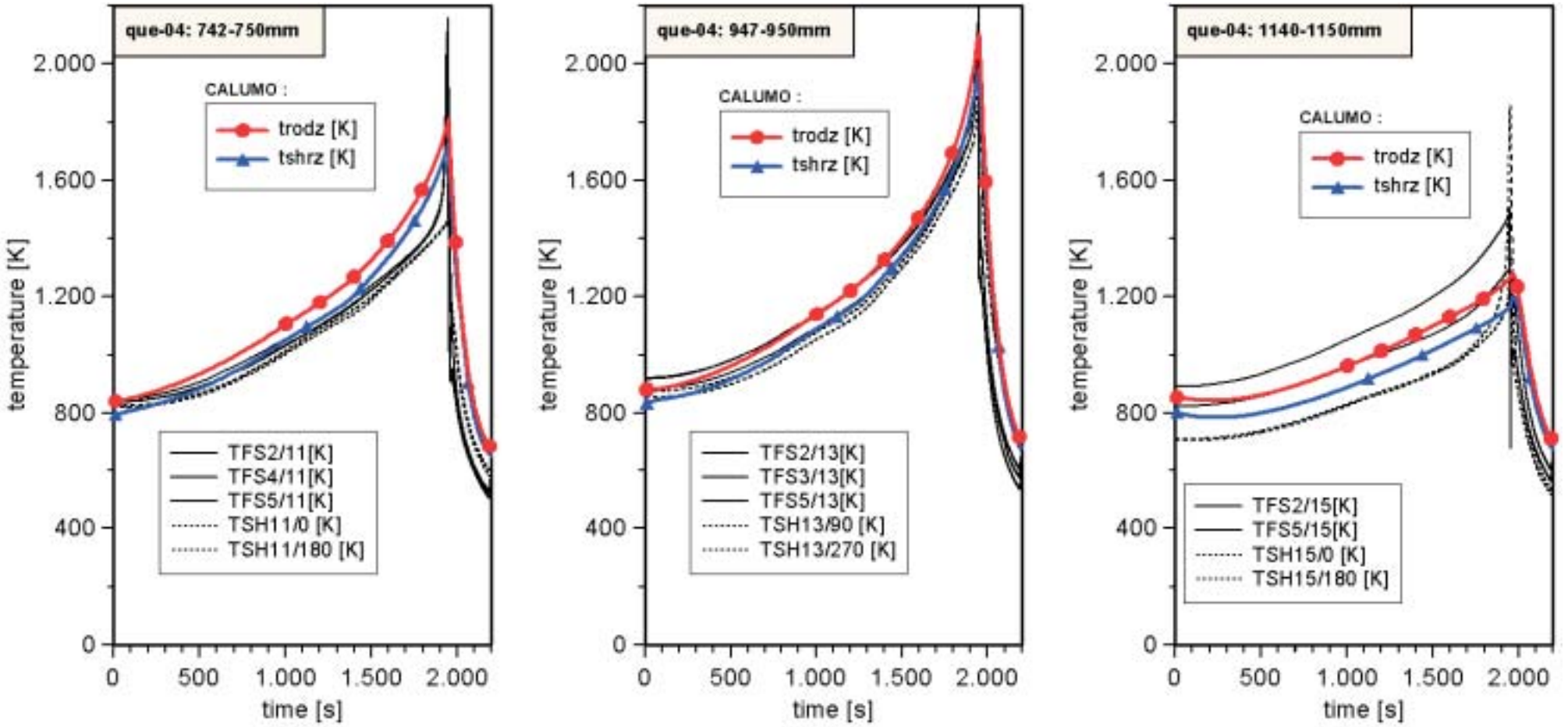

Fig. I-94: Evolution of rod and shroud temperatures of QUENCH-04 (low oxidation case) at different axial locations, continued.

Fig 94-QUE04 Steiner 2.cdr
08.11.01 - IMF

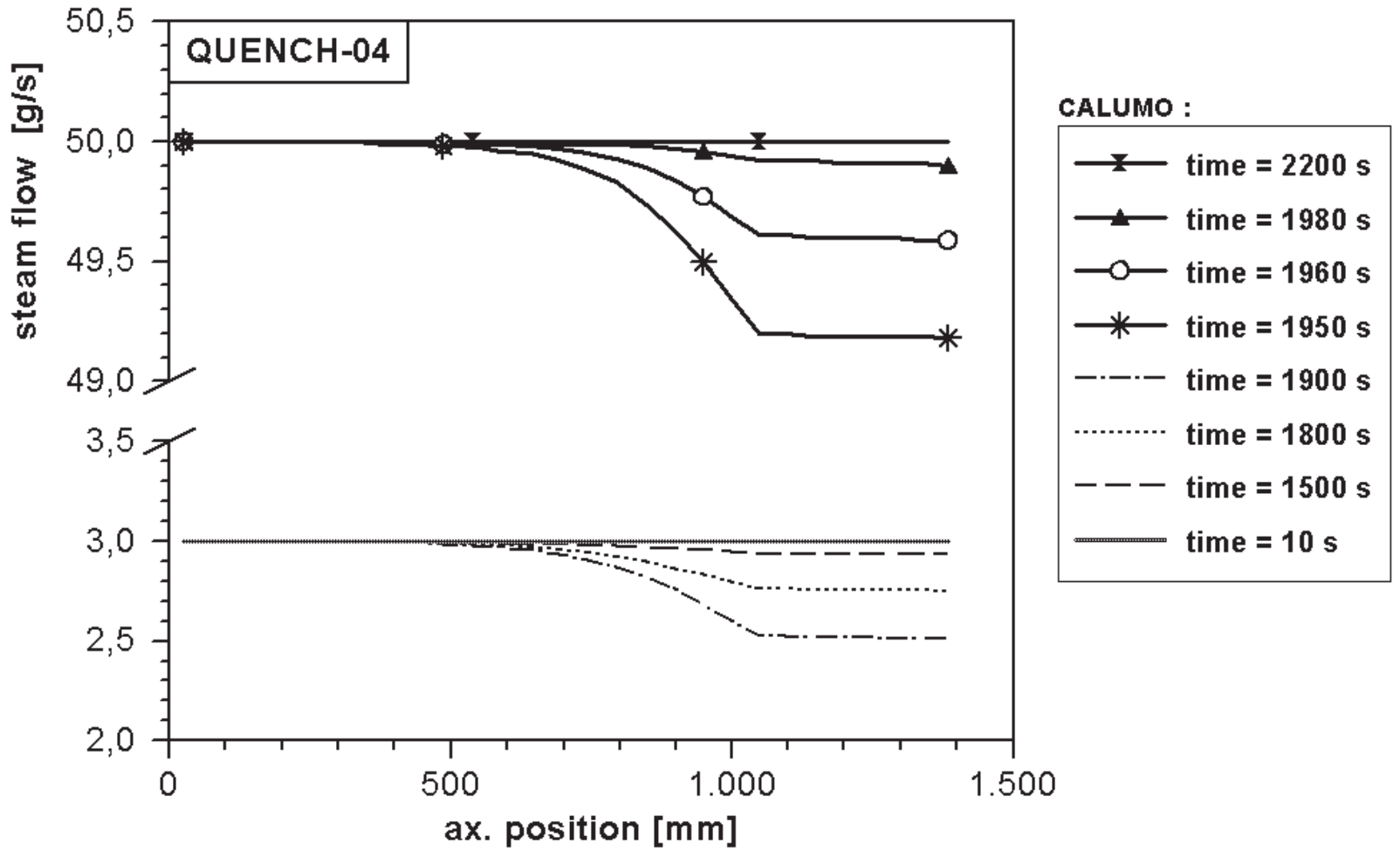

Fig. I-95: QUENCH-04; Axial distributions of the steam flow rate at different times into the transient (low oxidation case).

Fig 95-QUE04 Steiner 3.cdr
08.11.01 - IMF

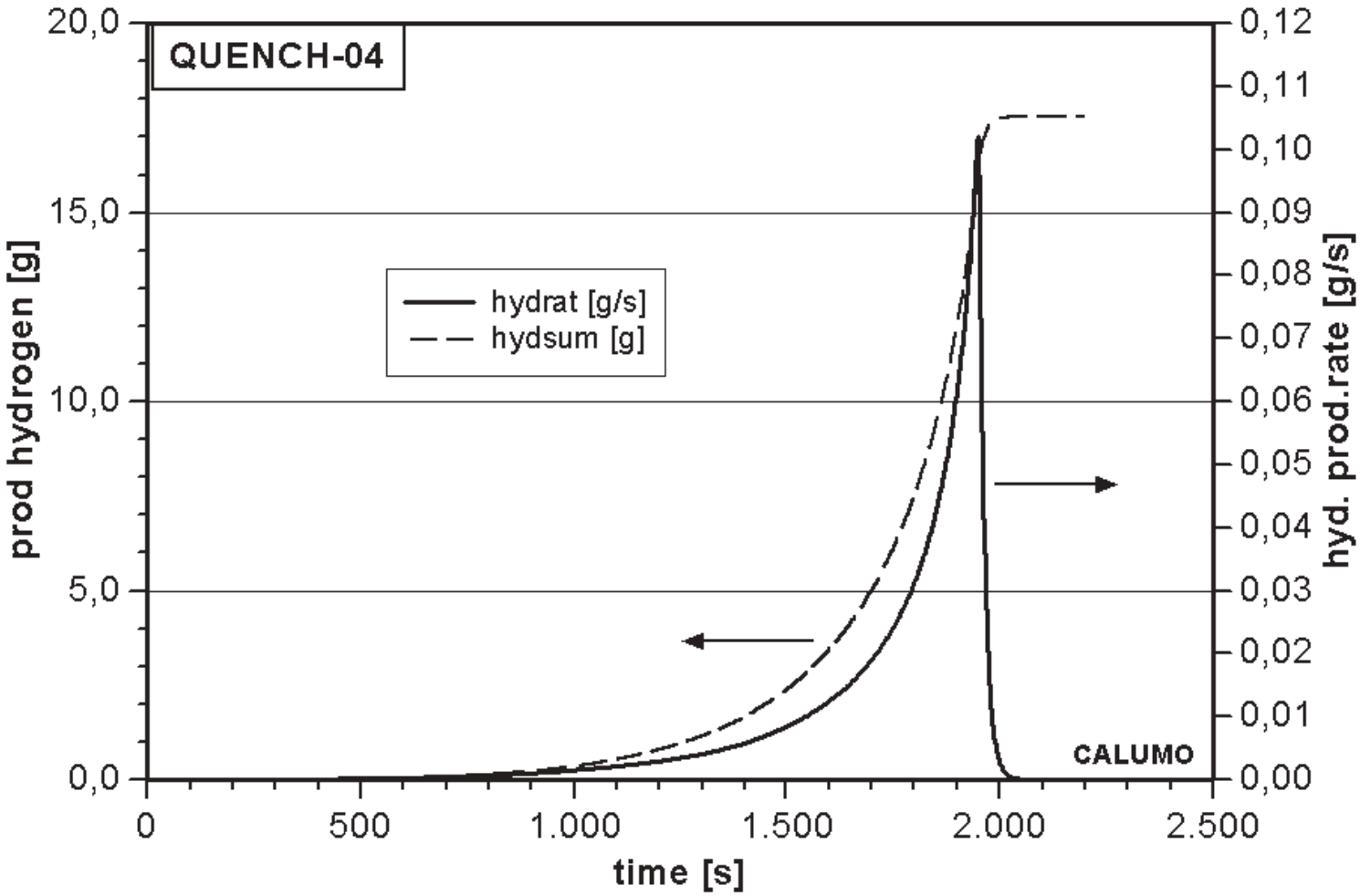

Fig. I-96: Evolution of the hydrogen production rate and produced hydrogen for QUENCH-04 (low oxidation case).

Fig 96-QUE04 Steiner 4.cdr
08.11.01 - IMF

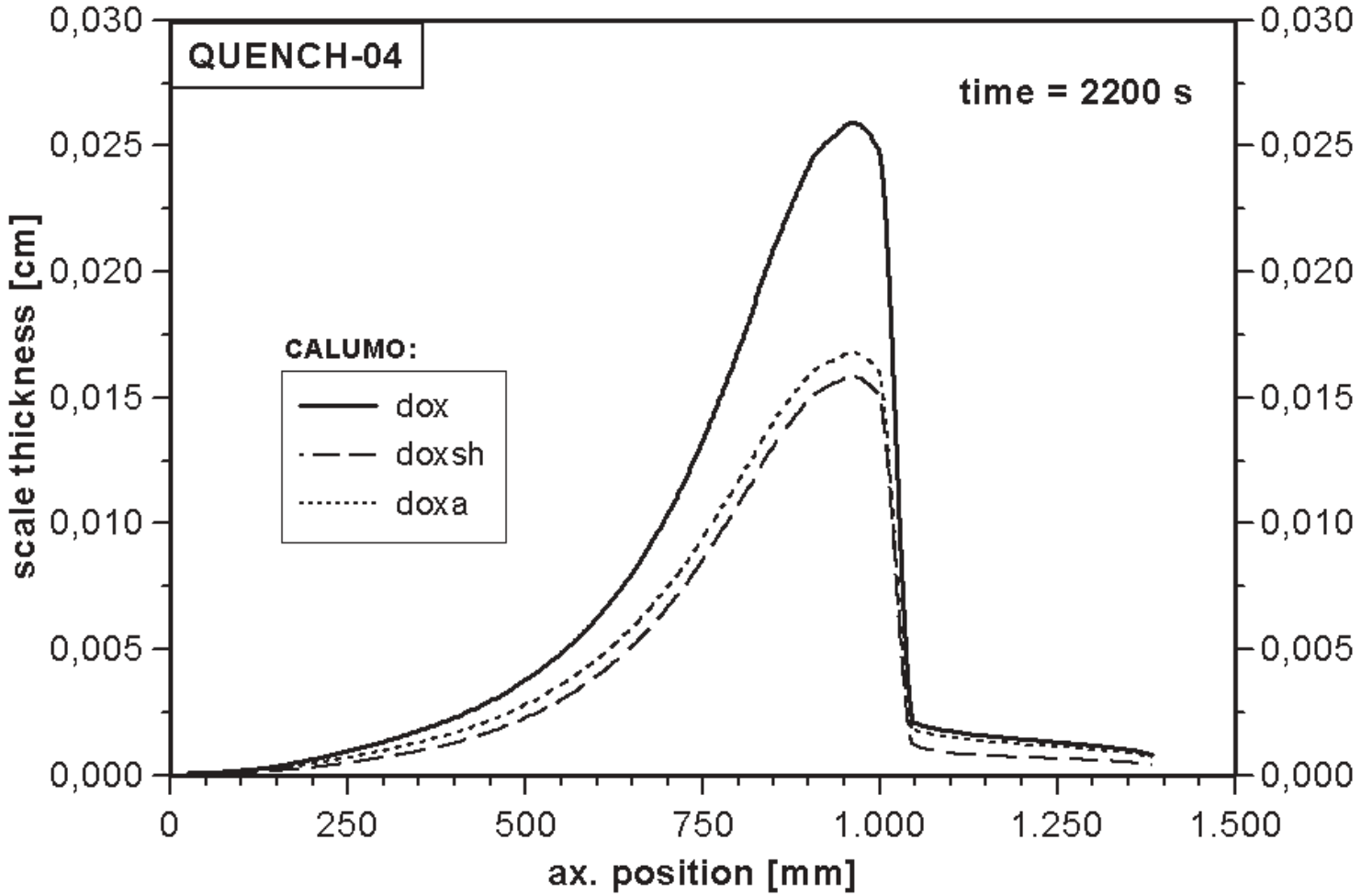

Fig. I-97: Axial distributions of the oxide scale thickness at the end of QUENCH-04 (low oxidation case).

Fig 97-QUE04 Steiner 5.cdr
08.11.01 - IMF

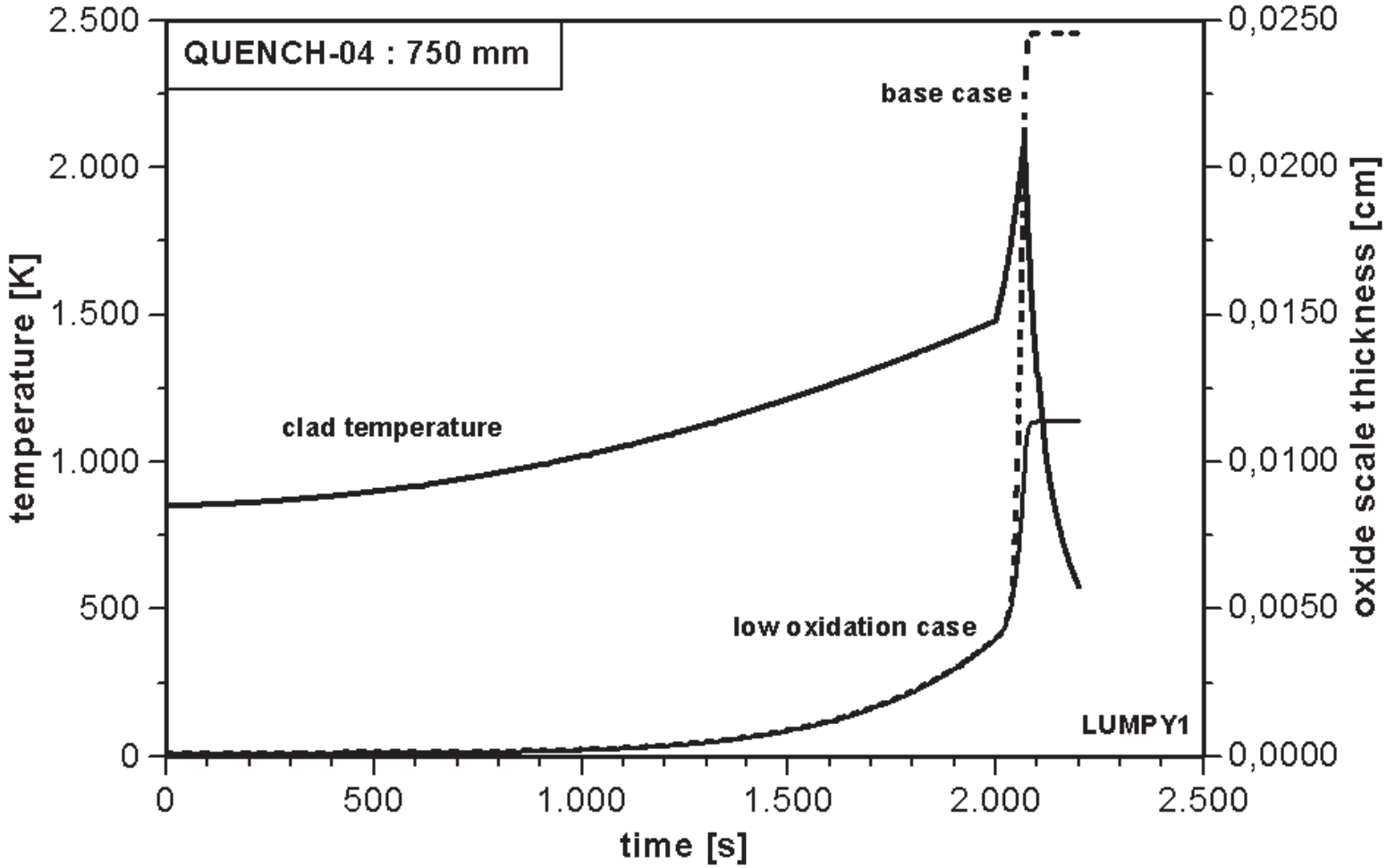

Fig. I-98: Evolution of clad temperature and oxide scale thickness at 750 mm acc. to LUMPY-1.

Fig 98-QUE04 Steiner 6.cdr
08.11.01 - IMF

Part II:

Application of the SVECHA/QUENCH Code to the Analysis of the QUENCH-01 and QUENCH-04 Bundle Tests

Contents

List of Tables

List of Figures

Introduction

Since the central rod of the bundle is not heated, its temperature evolution in the course of reflooding experiment is completely determined by thermal-hydraulic boundary conditions: temperatures of the surrounding heated rods and shroud and characteristics of the coolant flow (boiling regime, flooding rate, gas phase velocity and composition, etc.). In the case of full-scale simulation of the bundle test the temperatures of the heated rods and shroud are calculated by specifying the electric power time evolution and thus, the boundary conditions for the central rod are determined by the code. At the same time, there exists another possibility to determine the boundary conditions for the central rod: instead of calculation, the temperatures of the heated rods and shroud may be taken from the experiment.

From the viewpoint of the solution of the heat conduction problem inside the central rod both ways are equivalent. Specification of the boundary conditions on the basis of the experimentally measured temperatures even has certain advantages as it describes the thermal regime around the central rod very close to that in the experiment.

Within the framework of SVECHA/QUENCH (S/Q) code [1-5] the thermal boundary conditions for the central rod may be predetermined by specifying the temperatures of the "effective channel" inner wall on the basis of experimentally measured temperatures. The inner surface of the effective channel represents the surfaces of the heated rods surrounding the central rod.

The heat exchange between the central rod and the effective channel is affected via radiation and heat transfer through the water-gas media filling the channel. The thermal-hydraulic characteristics of the effective channel (cross-section, hydraulic diameter) are determined on the basis of geometrical parameters of the bundle (total cross-section, number of rods and their diameters).

The appropriate determination of the effective channel parameters and temperature evolution makes it possible to reproduce very closely the experimental thermal conditions around the central rod. Since the S/Q code uses fine adaptive meshing and accounts for all the details of the heat conduction process (layers thickness variation, different thermal properties of different layers, etc. [1]) it allows a correct solution of the temperature problem inside the rod on the basis of such boundary conditions.

The correct reproduction of the rod temperature evolution in its turn allows a detailed description of cladding mechanical deformation, oxidation and hydrogen absorption processes during reflooding, which can be currently treated by the S/Q in the most advanced mechanistic approach. Different stages of the bundle quenching test (preheating, preoxidation, reflooding) can be analysed by the S/Q code. A number of important parameters (rod temperature axial distribution, gas outlet temperature, oxide layer thickness, hydrogen production rate, etc.) can be calculated and compared with the experimentally

measured ones. In order to help the future experiments conductance, the effective pre-test calculations may be also carried out.

The present work is concerned with the results of the S/Q code application to the FZK QUENCH bundle tests simulation. The adaptation of the S/Q code to such kind of calculations is described. The numerical procedure of the test temperature data recalculation and preparation for the S/Q code input is presented. The results of Q-01 and Q-04 tests simulation are discussed.

The main attention was paid to the central rod temperature history modelling in every phase of the tests from the pre-oxidation up to the flooding and steam-cooling, respectively, since it strongly influences progression of other processes.

The main results were obtained for the central rod. However, some results such as the hydrogen generation rate and the total hydrogen production were extrapolated to the whole bundle, in order to compare the calculations with integral values measured by mass spectrometer (MS GAM) and the Caldos device.

1 S/Q code adaptation to the bundle tests simulation

1.1 Code adaptation basic features

Originally S/Q code was developed for the simulation of the single fuel rod quenching tests. For the simulation of the FZK bundle tests some special improvements and modifications were made. These modifications mainly concern the driver and heat exchange modules of S/Q code. The other modules of S/Q code (thermal conductivity, oxidation, mechanical behaviour, hydriding) were not modified since these modules are sufficiently versatile to be applied to the bundle test simulation. The main aim of the code adaptation was to make it possible to account for the detailed temperature distribution evolution of the rod surroundings using corresponding experimental data. The basic actions of the S/Q code adaptation were as follows:

- development of **new routines** for the driver module **(DRIVER)** for reading and updating of input data**;**
- **modification** of head routine of the driver module **(DRIVER);**
- **modification** of routines of the heat exchange module **(BOIL);**
- formation of special **input files** from experimental temperature data.

1.2 New routines function

Two new routines were developed for **DRIVER** module for reading and updating of experimental temperature data.

The functions of the new routine **quen1i.for** are:

- reading of the temperature input files **tc-coord.dat, tc-temp.dat** (see below, subsection 3.5);
- temperature input files check up;
- thermocouples coordinates recalculation from original experimental form to the code coordinate system;
- thermocouples data sorting from original free order to increasing order with respect to axial position;
- thermocouples data recalculation from degree centigrade (°C) to Kelvin (K);
- averaging of TC data relating to the same elevation.

The function of the new routine **quen1t.for** is:

- calculation of time dependence of temperature in the thermal mesh nodes.

1.3 Existing routines modification

- Several modifications of the existing S/Q code routines were also made. The most important modifications were made in the head routine of the **DRIVER** module and in routine of the heat exchange module **BOIL,** which calculate boundary heat flows.

In the routine **boilqf.for** of the heat exchange module:

- spatial dependence of surrounding temperature field was taken into account when calculating the heat flows from cladding surfaces.

In the routine **quen.for** of the driver module:

- implementation of new routines, modification of routines callings, modification and addition of new output files were realised.

2 Recalculation of the Q-01 bundle test temperature data

2.1 Rod and shroud thermocouples data

During the QUENCH-01 test [6] the temperature was continuously measured at different locations of the bundle. 35 thermocouples were attached to the cladding of the rods at 17 different elevations between -250 mm and 1350 mm, two more thermocouples were inserted in the centre of the unheated rod simulator at 570 mm and 950 mm elevations. The TCs data were processed by the FZK experimental team, incorrect data were deleted, and at the moment the data of 32 rod TCs are available in the electronic format. Table II-1 presents these TCs designations, corresponding rod numbers and elevations.

26 thermocouples were located at the shroud outer surface at 11 different elevations between -250 mm and 1250 mm. Since the TCs were protected by the shroud wall from direct contact with steam and water, all of them survived throughout the test. Table II-2 presents designations and elevations of the shroud thermocouples, available in the electronic format.

The above mentioned TCs data were used for the simulation of the effective channel internal surface. The numerical procedure of the rod TCs data recalculation includes smoothening, averaging and interpolation. These operations are described below.

2.2 Irregular behaviour of the thermocouples

At the reflooding phase of the Q-01 test thermocouples located at the surface of heated rods show noisy, irregular behaviour with sharp drops and increases of temperature by hundreds of degrees in a split second (Fig. II-1). The consideration based on the estimated heat capacity of the rod simulator and maximal heat flows occurring under nucleate boiling conditions leads to the conclusion, that the rod surface can not be cooled down so sharply due to rewetting and following nucleate boiling. Other important point is the temperature of the rod surface at the moment when the drop occurs. This temperature is too high for rewetting under Q-01 test conditions (pressure 2.2 atm).

Sharp drop of the TC-measured temperature may be explained by the temporary loss of contact between the TC and the rod surface (thermal de-coupling) due to interaction with the surrounding water-steam media. Because of its small size thermocouple has very small heat capacity. On losing the contact with the rod surface TC rapidly cools down in the steam flow. Correspondingly, sharp rise of the TC-measured temperature is a result of re-establishing of the contact with the hot rod surface. Such temporary failures of the TC readings should be excluded from the consideration.

Table II-1. Locations of the TCs used for the fuel rod simulators temperature measurement in the QUENCH-01 bundle test

	Channel	TC	Rod	Elevation
1	KAN:04	TFS2/17	6 FRS *)	1350 mm
2	KAN:49	TFS5/17	10 FRS	1350 mm
3	KAN:37	TFS3/16	7 FRS	1250 mm
4	KAN:48	TFS5/16	21 FRS	1250 mm
5	KAN:47	TFS5/15	19 FRS	1150 mm
6	KAN:03	TFS2/15	4 FRS	1150 mm
7	KAN:09	TFS3/14	5 FRS	1050 mm
8	KAN:16	TFS5/14	18 FRS	1050 mm
9	KAN:02	TFS2/13	2 FRS	950 mm
10	KAN:11	TFS4/13	20 FRS	950 mm
11	KAN:15	TFS5/13	16 FRS	950 mm
12	KAN:08	TFS3/13	3 FRS	950 mm
13	KAN:14	TFS5/12	15 FRS	850 mm
14	KAN:07	TFS3/12	9 FRS	850 mm
15	KAN:10	TFS4/11	14 FRS	750 mm
16	KAN:01	TFS2/11	8 FRS	750 mm
17	KAN:13	TFS5/11	13 FRS	750 mm
18	KAN:12	TFS5/10	12 FRS	650 mm
19	KAN:41	TFS5/9	10 FRS	550 mm
20	KAN:05	TFS3/8	5 FRS	450 mm
21	KAN:82	TFS5/7	19 FRS	350 mm
22	KAN:23	TFS2/7	6 FRS	350 mm
23	KAN:76	TFS2/6	4 FRS	250 mm
24	KAN:81	TFS5/6	18 FRS	250 mm
25	KAN:22	TFS2/5	2 FRS	150 mm
26	KAN:80	TFS5/5	16 FRS	150 mm
27	KAN:79	TFS5/4	21 FRS	50 mm
28	KAN:74	TFS 2/3	8 FRS	-50 mm
29	KAN:73	TFS 2/2	6 FRS	-150 mm
30	KAN:72	TFS 2/1	4 FRS	-250 mm
31	KAN:0	TCR 13	1 FRS	950 mm
32	KAN:33	TCRC 13	1 FRS	950 mm

*) Fuel rod simulator

2.3 Processing of the Q-01experimental data

In order to use the temperature measurement data as input information for the S/Q code calculations these data were processed and recalculated. Consecutive steps of TFS3/16 and TFS5/16 thermocouples data processing are presented in Figs. II-2 to II-4. In Fig. II-2 the original TC readings (thin lines) and corrected data (thick lines) are shown. The correction procedure includes cutting off the failure parts of the temperature evolution curves and smoothing of the noisy data with the help of **Mathcad 2000** `medsmooth` and `ksmooth` functions. In Fig. II-3 the result of cubic spline interpolation of the smoothed data is presented.

Finally, the averaging of smoothed and recalculated data was performed and the final curve which describes the temperature evolution of the bundle at 1250 mm elevation was obtained (Fig. II-4).

Similar procedure was applied to the temperature data measured by TCs located at 1350 mm (TFS2/17 and TFS5/17, Fig. II-5), at 1150 mm (TFS2/15 and TFS5/15, Fig. II-6) and at 1050 mm (TFS3/14 and TFS5/14, Fig. II-7).

Table II-2. Locations of the TCs used for the shroud temperature measurement in the QUENCH-01 bundle test

	Channel	TC	Elevation
1	KAN: 17	TSH 16/180	1250 mm
2	KAN: 67	TSH 16/0	1250 mm
3	KAN: 66	TSH 15/0	1150 mm
4	KAN: 57	TSH 15/180	1150 mm
5	KAN: 19	TSH 14/90	1050 mm
6	KAN: 53	TSH 14/270	1050 mm
7	KAN: 18	TSH 13/90	950 mm
8	KAN: 52	TSH 13/270	950 mm
9	KAN: 56	TSH 13/180	950 mm
10	KAN: 65	TSH 13/0	950 mm
11	KAN: 21	TSH 12/0	850 mm
12	KAN: 55	TSH 12/180	850 mm
13	KAN: 20	TSH 11/0	750 mm
14	KAN: 51	TSH 11/270	750 mm
15	KAN: 54	TSH 11/180	750 mm
16	KAN: 60	TSH 11/90	750 mm
17	KAN: 50	TSH 9/270	570 mm
18	KAN: 59	TSH 9/90	570 mm
19	KAN: 86	TSH 7/180	350 mm
20	KAN: 90	TSH 7/0	350 mm
21	KAN: 83	TSH 4/270	50 mm
22	KAN: 85	TSH 4/180	50 mm
23	KAN: 87	TSH 4/90	50 mm
24	KAN: 89	TSH 4/0	50 mm
25	KAN: 84	TSH 3/180	- 50 mm
26	KAN: 88	TSH 1/0	-250 mm

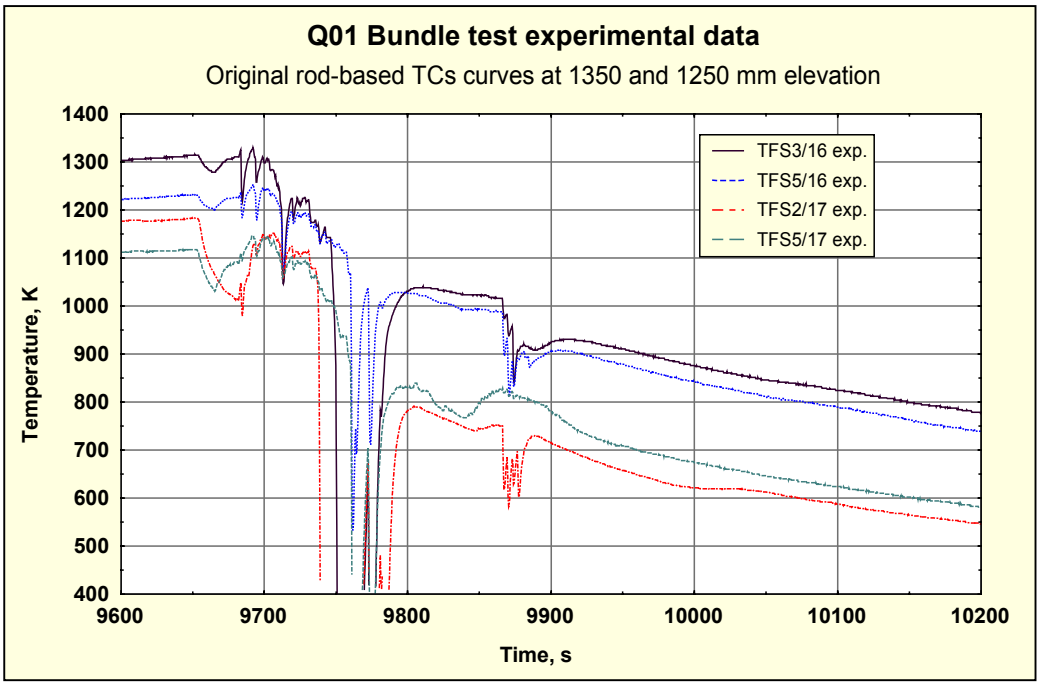

Fig. II-1. Original readings of the thermocouples located at 1350 and 1250 mm elevations (TFS2/17, TFS5/17, TFS3/16, TFS5/16) at the flooding phase of the Q-01 experiment.

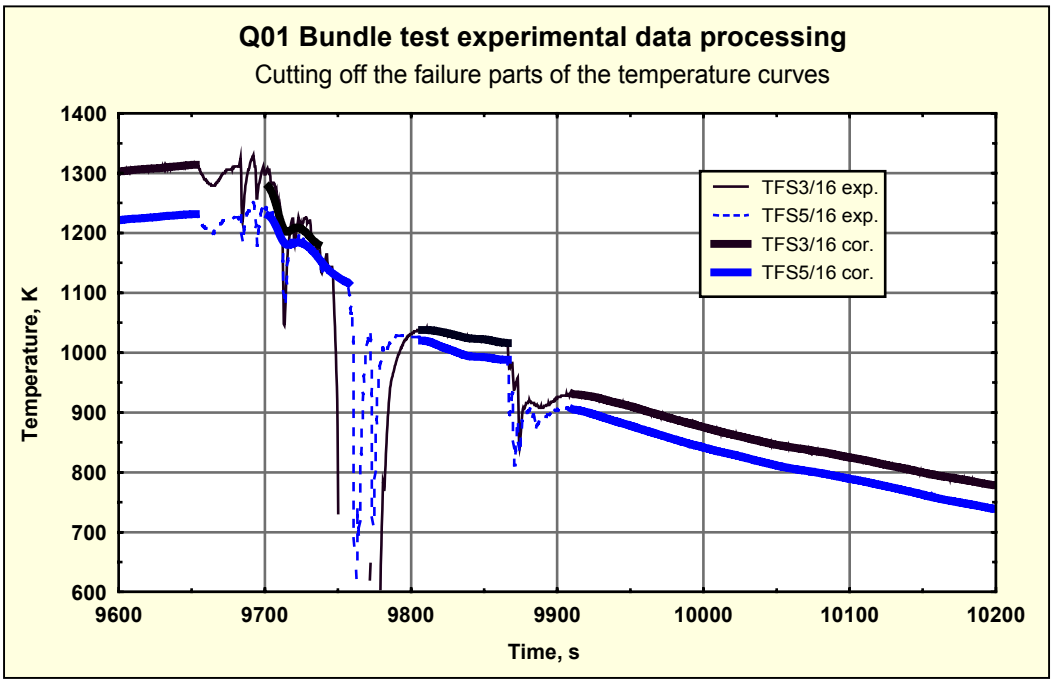

Fig. II-2. Cutting off the failure parts of the temperature curves and smoothing. Original readings of the thermocouples TFS3/16, TFS5/16 (thin lines) and corrected data (thick lines).

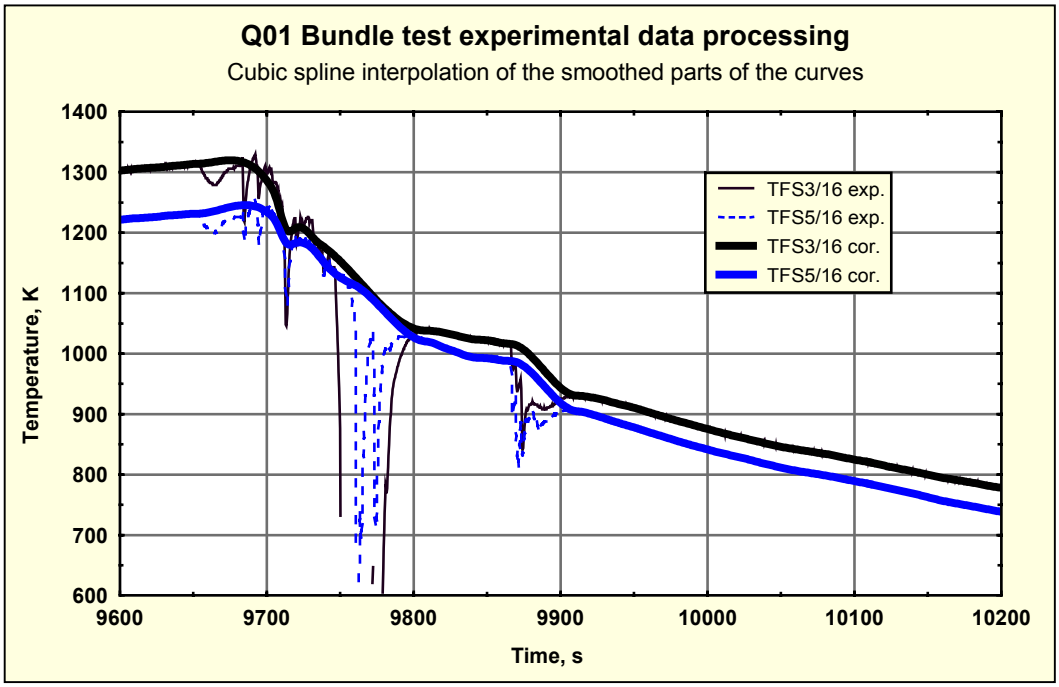

Fig. II-3. Cubic spline interpolation of the smoothed data. Original readings of the thermocouples TFS3/16, TFS5/16 (thin lines) and corrected data (thick lines).

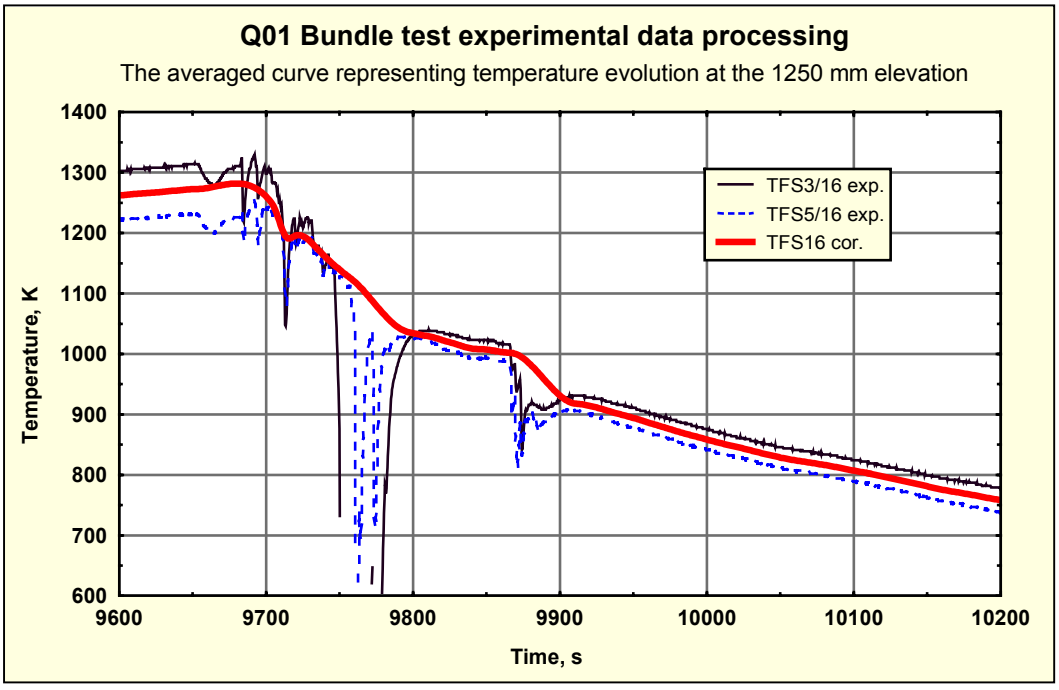

Fig. II-4. The averaged curve representing temperature evolution at the 1250 mm elevation. Original readings of the thermocouples TFS3/16, TFS5/16 (thin lines) and corrected data (thick line).

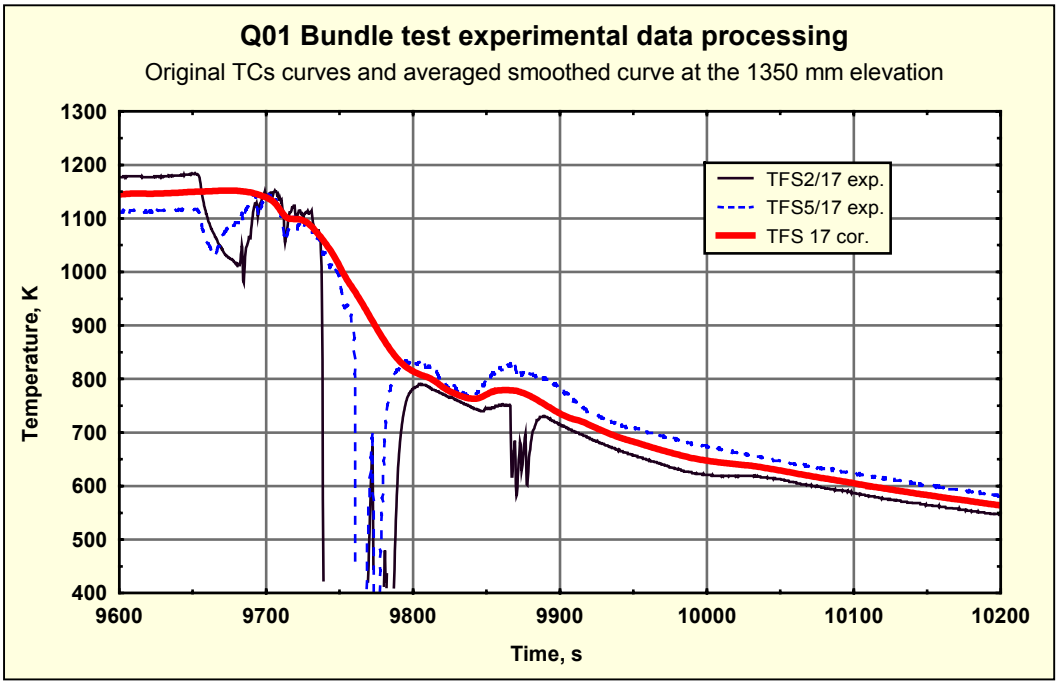

Fig. II-5. The averaged curve representing temperature evolution at the 1350 mm elevation. Original readings of the thermocouples TFS2/17, TFS5/17 (thin lines) and corrected data (thick line).

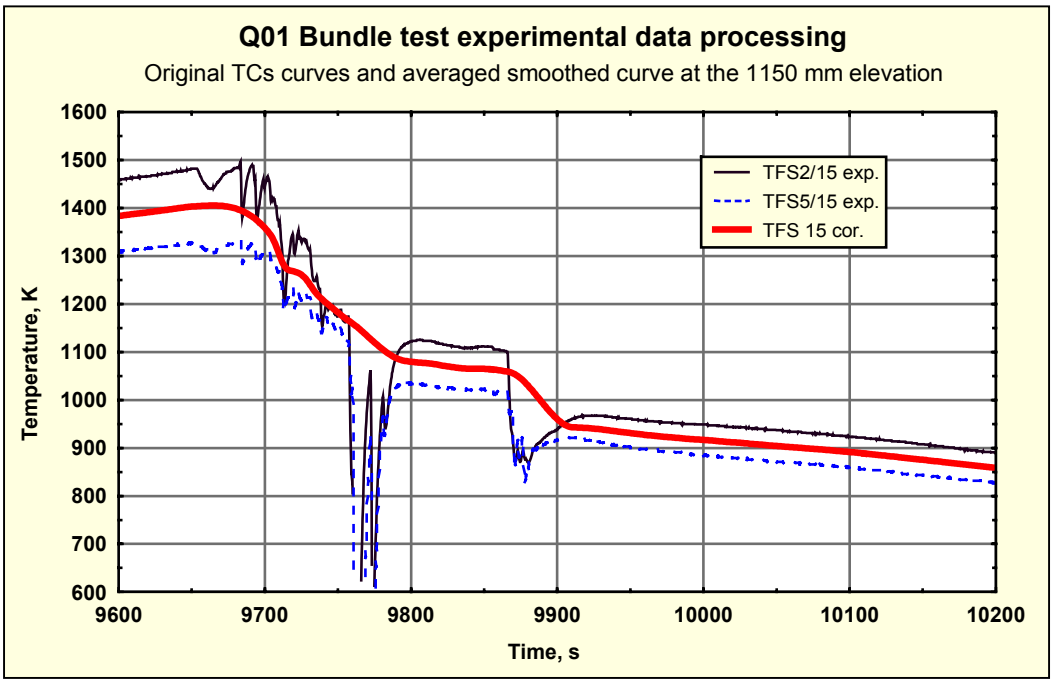

Fig. II-6. The averaged curve representing temperature evolution at the 1150 mm elevation. Original readings of the thermocouples TFS2/15, TFS5/15 (thin lines) and corrected data (thick line).

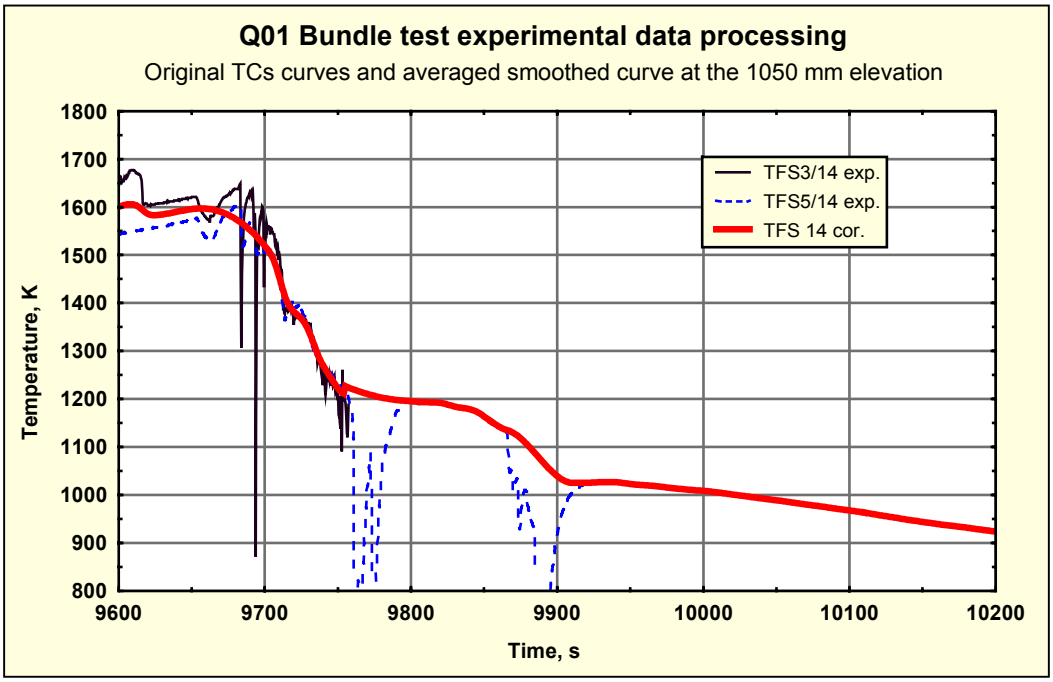

Fig. II-7. The averaged curve representing temperature evolution at the 1050 mm elevation. Original readings of the thermocouples TFS3/14, TFS5/14 (thin lines) and corrected data (thick line).

Owing to high temperatures in the hottest region of the bundle, thermocouples located at the elevations 750 mm, 850 mm and 950 mm (11, 12 and 13 levels) failed during preheating and transient phases of the test. In order to describe temperature evolution of the bundle at these elevations during whole test the shroud-based thermocouples data were used.

In Fig. II-8 the rod-based and the shroud-based TC data measured at 750 mm elevation are presented. Up to the time moment 7527 s all three rod-based TCs located at this elevation (TFS2/11, TFS4/11, TFS5/11) show rather smooth and close time evolution. The average temperature shown by these three TCs may be considered as representative bundle temperature at 750 mm in the time period from the beginning of the test to 7527 s. We note, that the shroud-based TCs (TSH11/0, TSH11/90, TSH11/180, TSH11/270) also show smooth and close evolution in this time period with average shroud temperature being lower then the average temperature of the rods. The difference between rod and shroud temperatures gradually increases reaching approximately 60 K at 7527 s.

After 7527 s global time TFS2/11 thermocouple reading shows sharp oscillations, TFS4/11 and TFS5/11 thermocouples also demonstrate unsTable II-behaviour (probably, due to losing of tight contact with the rod surface). Thus, one has not got reliable rod-based TC data in this time period. On the other hand, shroud-based TC show just the same smooth and close evolution as before up to the end of the test, due to the fact that they are protected by the shroud from direct contact with the water-steam mixture.

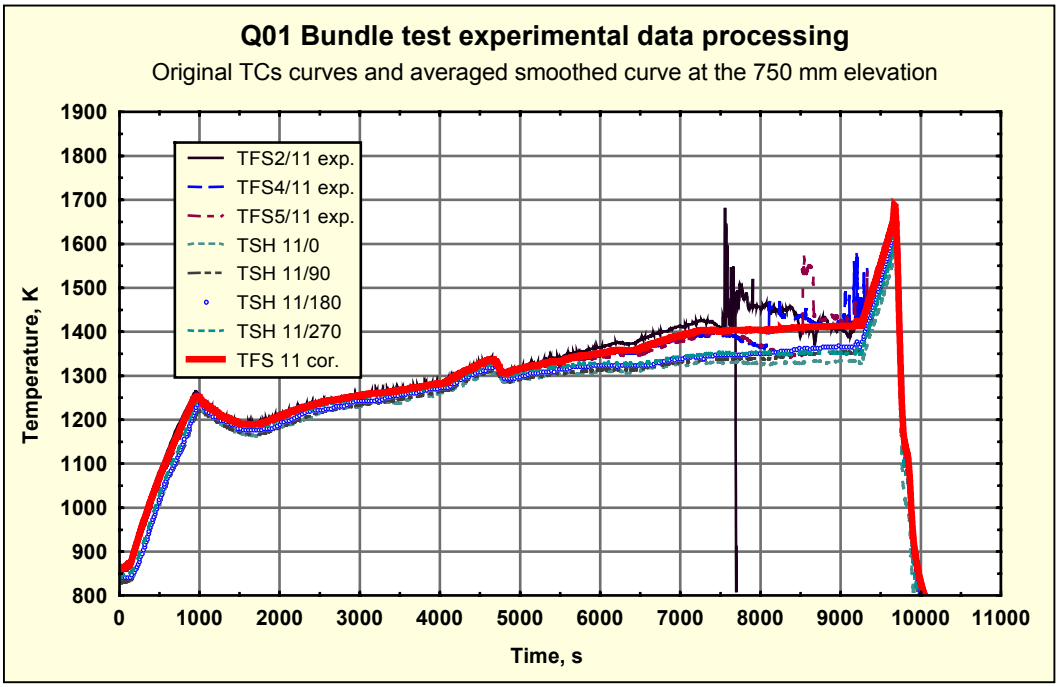

Fig. II-8. The averaged curve representing temperature evolution at the 750 mm elevation. Original readings of the rod-based thermocouples TFS1/11, TFS4/11, TFS5/11; shroud based thermocouples TSH11/0, TSH11/90, TSH11/180, TSH11/270 (thin lines) and corrected data (thick red line).

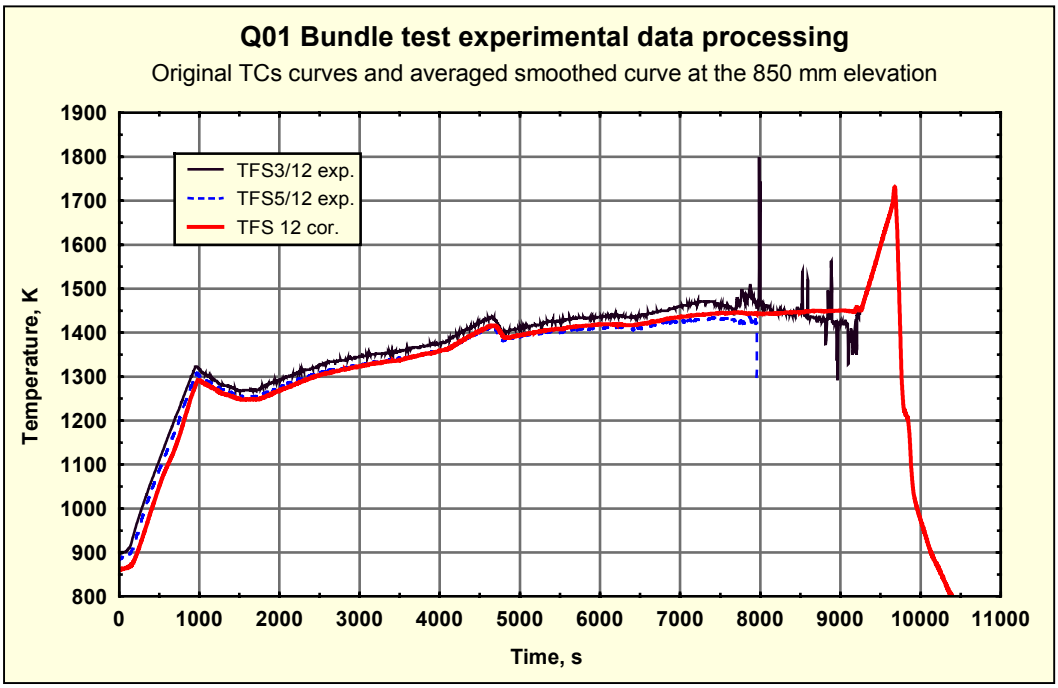

Fig. II-9. The averaged curve representing temperature evolution at the 850 mm elevation. Original readings of the rod-based thermocouples TFS3/12, TFS5/12 (thin lines) and corrected data (thick red line).

One can assume, that the real temperature evolution in the central part of the bundle at the considered elevation should be similar to the shroud temperature evolution corrected for the mentioned above temperature difference (60 K). The resulting temperature evolution curve obtained on the basis of the above considerations is shown in Fig. II-8 (thick red line).

Similar procedure was applied to the temperature data measured by TCs located at 850 mm (TFS3/12 and TFS5/12, Fig. II-9). Up to the moment of TFS5/12 thermocouple failure (7947 s global time) the average temperature evolution curve was determined on the basis of the smoothed rod-based TC data, and in the time period after 7947 s – on the basis of shroud-based TC data.

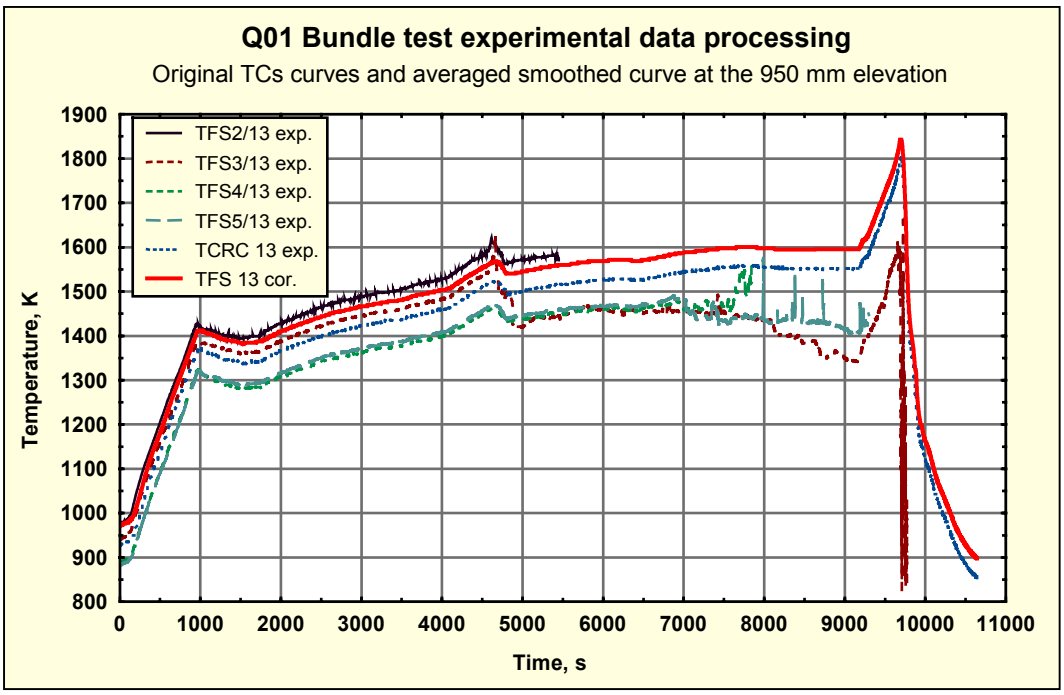

Fig. II-10. The averaged curve representing temperature evolution at the 950 mm elevation. Original readings of the rod-based thermocouples TFS2/13, TFS3/13, TFS4/13, TFS5/13 and TCRC13 (thin lines) and corrected data (thick red line).

Four rod-based thermocouples located at 950 mm elevation (TFS2/13, TFS3/13, TFS4/13, TFS5/13) at the initial phase of the experiment show quite similar behaviour. However, difference between the temperatures measured by TFS2/13 thermocouple and by TFS5/13 thermocouple was about 150-200 K (Fig. II-10). Temperature of the 2-nd and the 3-rd rods (measured by TFS2/13 and TFS3/13, respectively) which were arranged more closely to the central rod, appear to be noticeably higher than the temperature of the 20-th and 16-th rods (measured by TFS4/13 and TFS5/13) arranged at the bundle's periphery (for the rod designation see Fig. 9 and Fig. 11 in [6]).

Because of their position in the bundle, the temperature of the 2-nd and the 3-rd rods may be considered as representing more adequately thermal regime around the central rod than the temperature of the 20-th and 16-th rods. Accounting for all four measured temperatures will give the average temperature values well below the real temperatures of the rods

surrounding central rod and forming the walls of the effective channel. That is why in such situation of big difference between the 'first row' rods and the peripheral rods temperatures the 'first row' rods temperature evolution was used for the effective channel description.

In the time interval from the beginning of the experiment to 4563 s global test time the average bundle temperature at the 950 mm elevation was determined on the basis of TFS2/13 and TFS3/13 data. At 4563 s limited local escalation started, followed by unsTable II-behaviour of the TFS2/13 and TFS3/13 thermocouples with subsequent failure of TFS2/13 at 5450 s. For this reason the average bundle temperature at considered elevation in the time interval from 4563 s to the end of the test was determined on the basis of shroud TCs data corrected for corresponding temperature difference value (44 K at 4563 s).

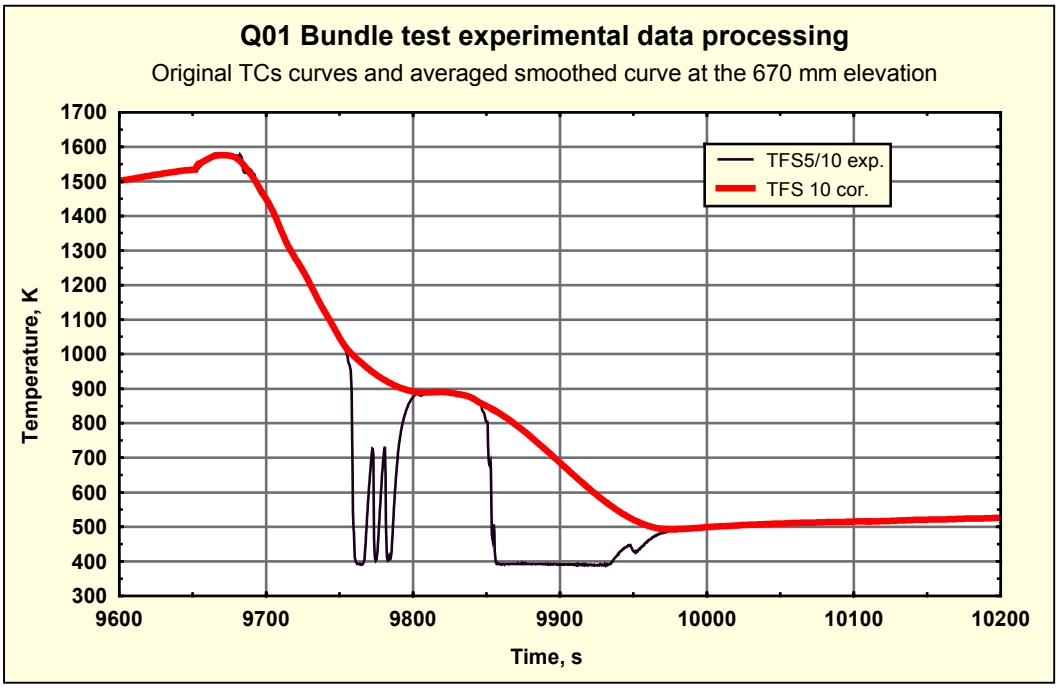

Fig. II-11. The averaged curve representing temperature evolution at the 670 mm elevation. Original reading of the rod-based thermocouple TFS5/10 (thin line) and corrected data (thick red line).

At the 670 mm elevation only one thermocouple (TFS5/10) was located. The behaviour of this TC is quite similar to the ones located above the hottest region of the bundle at 17, 16, 15 and 14 levels: there were two temporary TC failures (Fig. II-11). Correspondingly, the same numerical procedure as at the mentioned levels was applied and the resulting smoothed temperature evolution curve was obtained.

Thermocouples located below 670 mm show quite different behaviour as compared with the upper ones. One of the examples is presented in Fig. II-12. Rod-based thermocouple TFS5/9 (570 mm elevation) experienced sharp drop at 9714 s due to interaction with water-steam mixture. At the same time, two shroud-based TCs located at this elevation (TSH9/90 and TSH9/270) show gradual cooling down up to the 9840 s, when at temperatures 570 – 620 K rewetting of the shroud surface occurs. As contrasted to the shroud-based TCs, the rod-

based TFS5/9 thermocouple drops from 1100 K. Rewetting of massive rod with such high temperature is not possible. On the other hand, in the case if thermocouple looses tight contact with the rod, it can be cooled down very quickly because of its small size and small amount of heat stored. Thus, sharp drop of the TFS5/9 at 9714 s should be interpreted as thermocouple effect, but not real rod behaviour.

Having regard to the above considerations, average bundle temperature at the 570 mm elevation was determined on the basis of TFS5/9 data in the time interval from the beginning of the test to 9714 s, and on the basis of shroud TCs in the time interval from 9714 s to the end of the test.

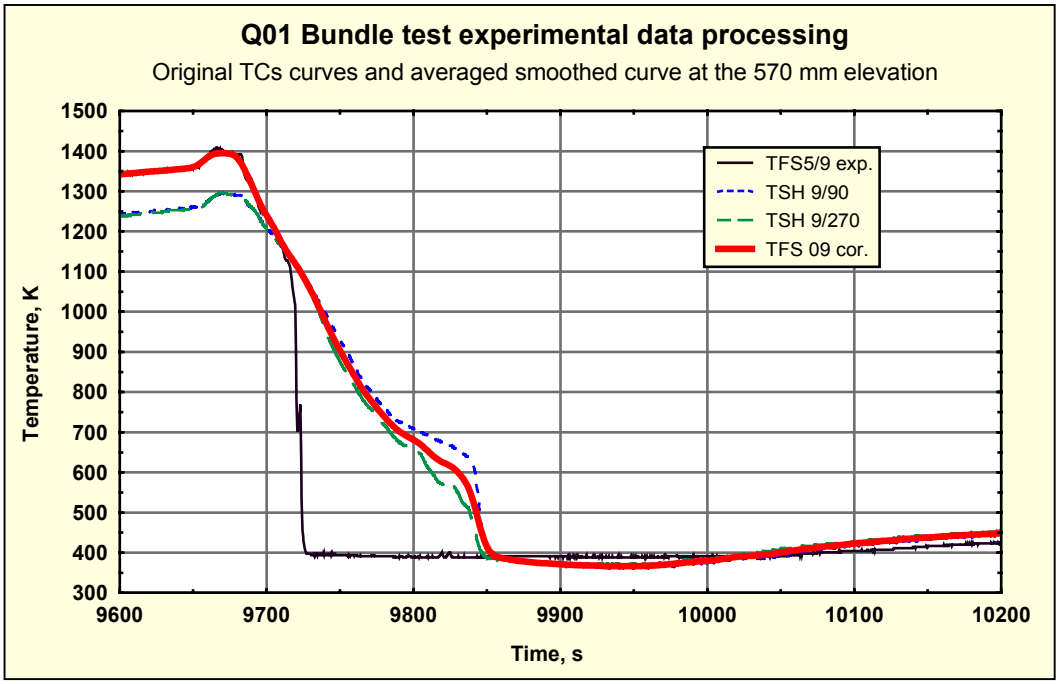

Fig. II-12. The averaged curve representing temperature evolution at the 570 mm elevation. Original reading of the rod-based thermocouple TFS5/9, shroud-based thermocouples TSH9/90 and TSH9/270 (thin lines) and corrected data (thick red line).

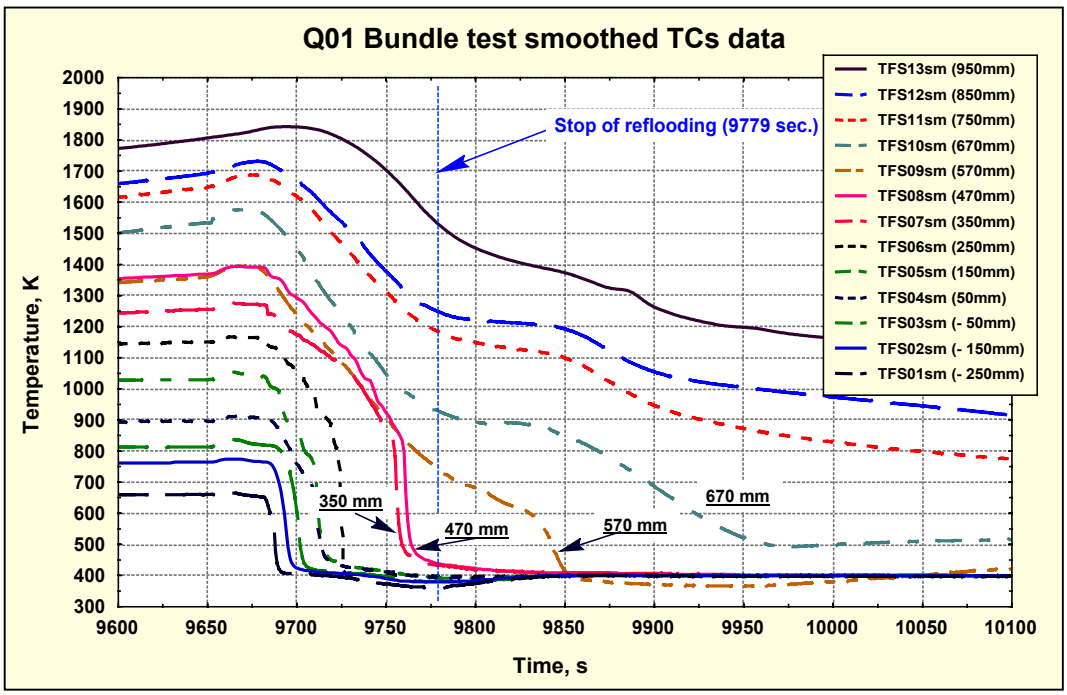

Fig. II-13. Averaged and smoothed curves representing temperature evolution of the bundle at the elevations from –250 mm to 950 mm.

Similar procedure was applied to the temperature data measured at 470 mm, 350 mm, 250 mm, 150 mm, 50 mm, -50 mm, -150 mm, -250 mm elevations.

These corrected data for the lower part of the bundle are presented in Fig. II-13. Analysis of the obtained temperature curves allows making certain conclusions about flooding stage of the Q-01 bundle test.

2.4 Analysis of the Q-01 temperature evolution data

As one can see, temperature evolution curves, presented in Fig. II-13 can be classified into two groups. Curves of the first group belong to the thermocouples located in the lower half of the bundle at the elevations below 600 mm. All these curves show more or less smooth fall to the value of approximately 400 K at different time moments. Since the saturation temperature in the Q-01 test conditions was about 400 K (396 K at test pressure 2.2 atm), such temperature evolution can be naturally explained by transition from film boiling to the nucleate boiling, intensification of heat exchange and subsequent rewetting of the corresponding area of the rod surface.

Curves that correspond to the thermocouples located at the elevations above 600 mm show quite different behaviour. Such time evolution can be characterised as slow cooling without any indications of rewetting throughout the whole flooding phase and long after the end of the flooding. The time moment at which water injection was stopped (9779 s, shown by vertical dashed line in Fig. II-13) quite well correlates with the end of rewetting process. With the only exception (temperature curve TFS09sm, 570 mm) all the curves show ‘rewetting fall’ before the end of flooding. As one can see in Fig. II-13, the ‘stop of flooding’ vertical line

represents a kind of border between temperature evolution curves of rewetting and non-rewetting types.

On the basis of the above consideration one can determine the water level position at the end of flooding: between 570 mm and 670 mm, i.e. in the middle of the bundle (lower end – 475 mm, upper end 1500 mm). It should be noted, that based on the Q-01 flooding parameters (flow rate 52 g/s, bundle cross-section 30 cm^2, total flooding duration 89 s) one can expect, that at the end of flooding water reached the bottom of the upper plenum ([6], p.11). The explanation of the above contradiction consists in the fact that water is intensively evaporated in the course of flooding. Roughly half of the total amount of water injected in the bundle during main flooding phase (4.6 litre) was evaporated. Correspondingly, at the end of flooding water filled only half of the bundle instead of the whole bundle.

On the basis of S/Q code simulation of the Q-01 test (see below, Sect. 4) it is possible to give an estimation of the evaporation rate during flooding phase of the test. Average calculated steam velocity at the outlet of the film boiling region (where steam was assumed to be at the saturation temperature) was 4.6÷5.8 m/s. With account for the bundle cross-section (30 cm^2) such steam velocities correspond to the total evaporation rates 17÷21 g/s. Comparison with Q-01 test flooding rate (50 g/s) confirms the above conclusion that approximately half of the water injected in the bundle during flooding phase was evaporated.

2.5 Temperature data input files

The axial coordinates of calculated effective channel wall TCs and their temperatures represent the input information for the S/Q code. These data are specified in the two new input files **`tc-coord.dat`** and **`tc-temp.dat.`** The examples of these files for the case of the rod-based calculation are presented in the Appendix.

It should be noted that the possibility of thermocouple data averaging and interpolation is implemented in the S/Q code as well. That is why the input temperature data may contain several TCs relating to the same elevation. Such possibility minimises preliminary data processing and facilitates the input of uncorrupted temperature data (i.e. without TCs failures, missing values, noisy behaviour etc.).

3 Q-01 bundle test simulation

3.1 Effective channel parameters determination

For the correct description of the heat- and mass-exchange processes taking place in the bundle within the framework of the effective channel approach it is very important to determine correctly the parameters of the effective channel. In the present subsection the determination of the effective channel hydraulic parameters developed earlier for the channel gas heating model verification [4] is briefly described.

The following bundle parameters were used for the channel determination:

Shroud inner diameter	D_{sh} = 80.0 mm;
Rod outside diameter	D_r = 10.75 mm;
Instrumentation tube diameter	D_t = 6.0 mm;
Number of rods	N_r = 21;
Number of tubes	N_t = 4.

The total bundle cross-section is given by the expression:

$$A_{tot} = \frac{1}{4}\pi \cdot D_{sh}^2 - N_r \cdot \frac{1}{4}\pi \cdot D_r^2 - N_t \cdot \frac{1}{4}\pi \cdot D_t^2 \quad (1)$$

The value of A_{tot} is equal to 30.07 cm^2.

Four variants of the effective hydraulic perimeter determination may be considered. According to the 1-st variant all available surfaces (shroud, fuel rod simulators and instrumentation tubes) were taken into account:

$$L_1 = \pi \cdot D_{sh} + N_r \pi \cdot D_r + N_t \pi \cdot D_t \ . \quad (2)$$

In the 2-nd variant, the instrumentation tubes were excluded from the consideration:

$$L_2 = \pi \cdot D_{sh} + N_r \pi \cdot D_r \quad (3)$$

In the 3-rd variant only the fuel rod simulators were considered:

$$L_3 = N_r \pi \cdot D_r \ . \quad (4)$$

On the basis of the above effective perimeters, Eqs. (2)-(4) and the total bundle cross-section, Eq. (1), the effective hydraulic diameter is determined in accordance with the usual definition:

$$h_k = \frac{A_{tot}}{L_k} \ , \quad k = 1,2,3 \ . \tag{5}$$

The effective channel inner radius can be found from the following obvious relation:

$$\frac{\pi R_{eff,k}^2 - \frac{1}{4}\pi D_r^2}{\pi D_r} = h_k \ \Rightarrow \ R_{eff,k} = \sqrt{D_r h_k + \frac{1}{4} D_r^2} \ , \quad k = 1,2,3 \tag{6}$$

The other approach to the determination of effective channel parameters (4-th variant) is based on the value of the channel cross-section per one rod

$$A_{eff} = \frac{A_{tot}}{N_r + N_t} \tag{7}$$

The effective channel inner radius is connected with the value of A_{eff} by:

$$\pi R_{eff,4}^2 - \frac{1}{4}\pi D_r^2 = A_{eff} \ \Rightarrow \ R_{eff,4} = \sqrt{\frac{A_{eff}}{\pi} + \frac{D_r^2}{4}} \tag{8}$$

The effective hydraulic diameter is given by:

$$h_4 = \frac{A_{eff}}{\pi \cdot D_r} \tag{9}$$

The values of the calculated hydraulic parameters are collected in the following table:

Table II-3. Hydraulic parameters of the effective channel.

Variant	Hydraulic diameter	Channel inner radius
1	2.903 mm	7.752 mm
2	3.131 mm	7.909 mm
3	4.241 mm	8.630 mm
4	3.562 mm	8.197 mm

By now four above variants of the effective channel parameters determination were considered and the main attention was paid to the fourth variant as it seems to be rather realistic from the point of view of the local flow [4].

On the basis of the above parameters the argon and steam mass flows at the preheating and transient phases were determined. By definition, gas flow in the effective channel is connected with the total gas flow by:

$$J_{eff} = J_{tot} \frac{A_{eff}}{A_{tot}} \quad (10)$$

The value of argon and steam flows during preheating and preoxidation phases in the Q-01 test was 3 g/s each. So, in terms of effective channel (4-th variant) argon and steam mass flows were 0.12 g/s.

3.2 The main assumptions used for the Q-01 bundle test simulation

In this subsection the main assumption regarding test conduct and internal S/Q code parameters (time steps, meshing, etc.) are briefly described.

Regarding test conduct it was assumed that transient phase began at 9188 s global time. Flooding began at 9660 s global time (472 s quenching time). During first 30 s the flooding rate was 80 g/s (2.67 cm/s). At 9690 s global time (502 s) flooding rate was changed to 52 g/s (1.73 cm/s) for the next 89 s. At 9779 s global time (591 s) the flooding was stopped.

Time step values were:

1.0 s up to 9660 s,

0.1 s up to 10600 s.

The bundle nodalization is characterised by the following values:

Heat conduction module

- The total nodes number in the radial direction: 35
- Pellet nodes number in the radial direction: 21
- External layer (oxide) nodes number: 7
- Total nodes number in the vertical direction: 150

(The vertical grid used in the heat conduction module is adaptive one, with maximum density in the region of the maximum temperature gradients).

Total number of meshes used by oxidation, mechanical deformation and hydrogen absorption modules was 73. The total central rod length considered was 1975 mm – from the upper point 1500 mm (adjacent to the Al_2O_3 plate thermal shield) to the lower point -475 mm (adjacent to the lower SS plate).

3.3 Calculation results

In the Section only temperature-relating results of the Q-01 test simulation by the S/Q code are described. The results concerning oxidation, mechanical deformation and hydrogen release are discussed in the Section 5.

As it was described above, on the basis of TC data the temperature of the effective channel inner wall was determined. In Fig. II-14 the effective channel temperature axial profile for different time moments (1000 s, 3000 s, 6000 s, 9000 s and 9660 s) is presented.

Due to heat exchange with effective channel (by radiation) and with flowing argon/steam mixture (by convection) the central rod is heated up in the course of preoxidation and transient phases. The axial profiles of the central rod surface temperature at different time moments are presented in Fig. II-15.

Gas flow plays an important role in the heat transfer from the heated rods to the central rod. At the channel inlet the gas temperature is lower then the channel wall temperature. The heat flow is directed from the channel wall to the gas and from the gas to the central rod. While flowing, gas is heated and its velocity is increased. Since the channel wall temperature axial profile is not uniform, above some elevation (corresponding to the maximum bundle temperature) gas temperature appears to become higher than the channel wall one. Starting from this elevation, the heat flow is directed from the gas to surrounding structures, gas temperature and velocity commence to decrease. The latter means that gas mixture carries out not only radial, but also axial heat transfer leading to the shift of the maximum temperatures to the upper part of the bundle.

The following figures illustrate these well-recognised considerations about the heat exchange in the bundle. Fig. II-16 presents gas temperature axial profiles at different time moments. Fig. II-17 shows gas velocity axial profiles at these moments. In Fig. II-18 the comparison between gas and channel temperature axial profiles at 3000 s is presented. Above 1000 mm elevation gas temperature is higher than the channel one and so the heat flow is directed from the gas to the rods.

The comparison of the calculated temperature evolution with the measured one is of special interest. The only thermocouple attached to the central rod, which survived in the Q-01 test is TCRC13, which was located in the centre of the rod at the 950 mm elevation. In Figs. II-19 and II-20 the calculated central rod temperature evolution at this elevation (in the centre of the pellet and on the outer surface of the cladding) and the TCRC13 experimental data are presented during whole experiment and during quenching phase.

One can see good agreement between the calculated temperature evolution and measured one. At the preheating, preoxidation and transient phases of the test one can hardly distinguish between the experimental data TCRC13 and calculated temperature in the centre of pellet (Fig. II-19). It should be noted that the difference between the calculated temperatures at the outer surface of the rod and inside the pellet is very small during preheating, preoxidation and transient phases (only several degrees). This fact indicates that radial temperature distribution inside central rod was practically uniform during these test phases (at least, at the considered elevation).

Quite satisfactory agreement between the calculated and measured temperatures was also obtained at the quenching phase of the test (Fig. II-20). As one can see, at the quenching phase of the test temperature difference between pellet centre and rod outer surface

exceeded 100 K, leading to high temperature gradients in the radial direction. Consideration of these gradients is important for the description of cladding mechanical behaviour.

Although it is not possible to perform direct comparison of calculated results with experimental data at other central rod elevations (since only 950 mm elevation data are available), the consideration of general picture of the calculated central rod surface temperature evolution is of big interest (Fig. II-21). As one can see, calculated central rod surface temperature evolution is in qualitative agreement with experimentally measured bundle temperature evolution (Fig. II-13). (Direct comparison of the data presented in Fig. II-13 and II-21 does not make much sense as they refer to different locations in the bundle). At the same time, there are some differences, mainly relating to the motion of “rewetting front” along the central rod surface. Thus, further development of the S/Q code thermal-hydraulic model (especially description of transition boiling and rewetting process in the bundle conditions) is necessary.

On the whole, the above comparison of calculation results with experimental data shows that ‘effective channel’ approach to the bundle tests simulation and developed data recalculation procedure allow adequate description of the central rod heat exchange under flooding conditions. Modelling of cladding oxidation and mechanical deformation in Q-01 test performed on the basis of central rod temperature evolution description is presented in the following Section 5.

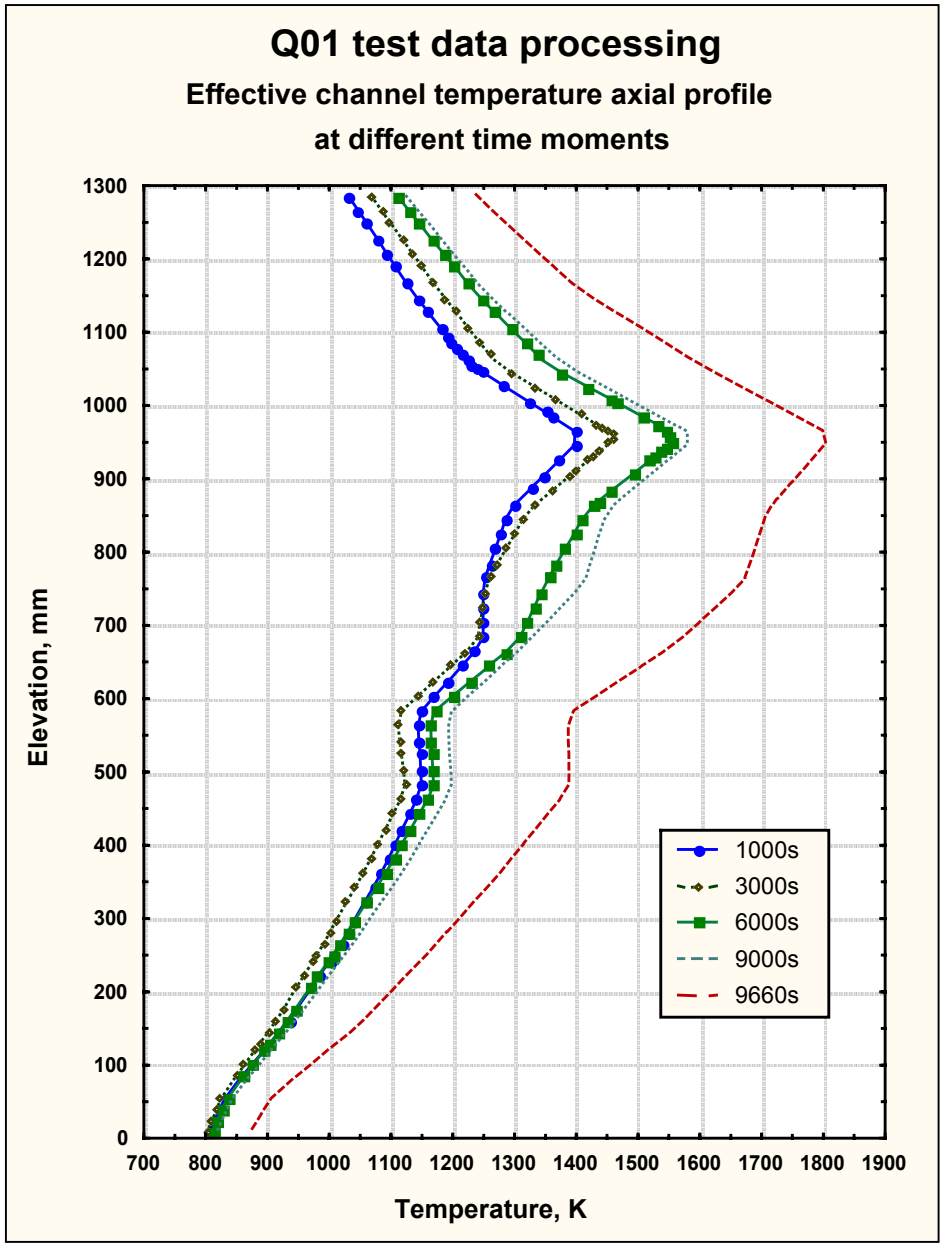

Fig. II-14 Effective channel inner wall temperature axial profile at different time moments.

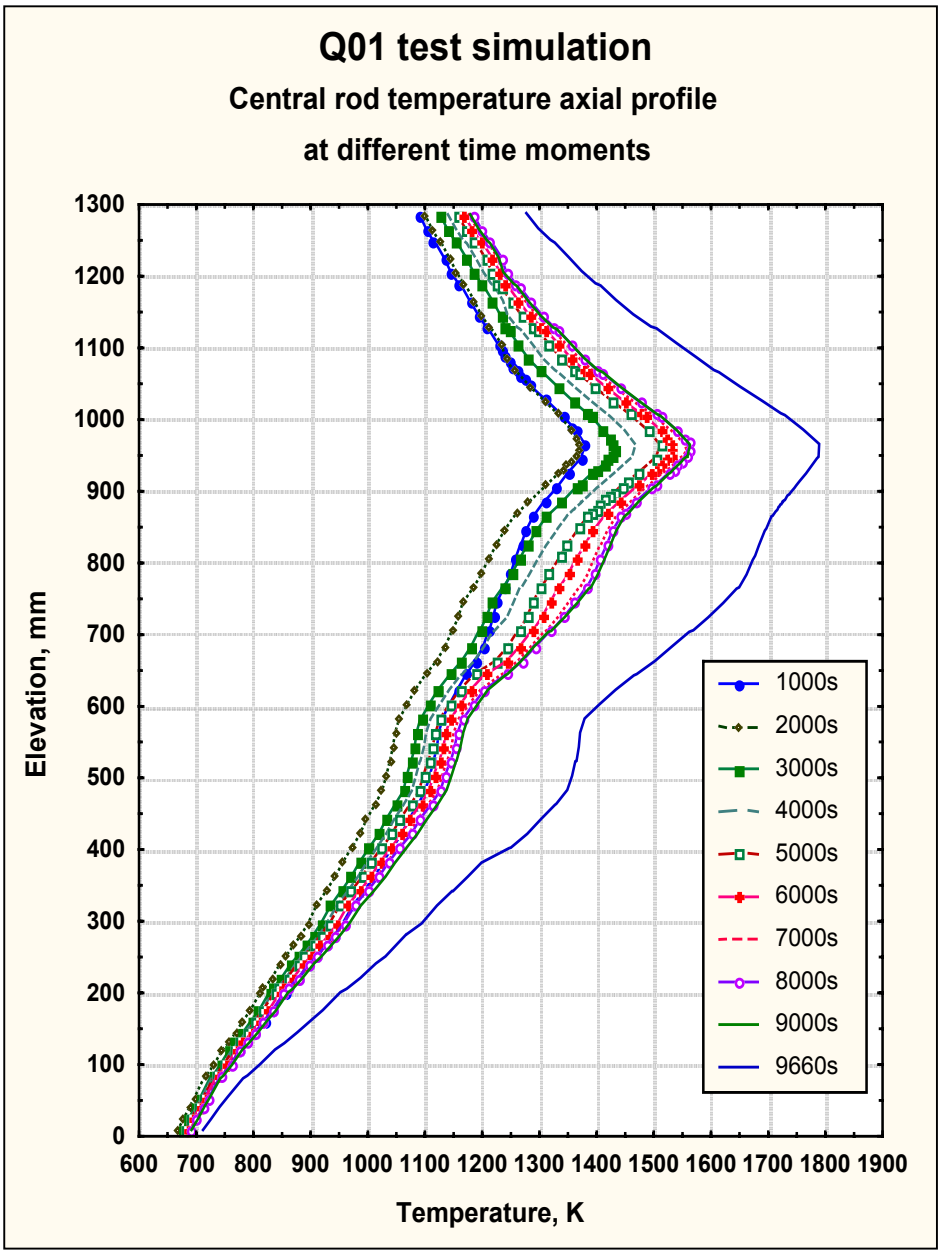

Fig. II-15. Central rod temperature axial profile at different time moments.

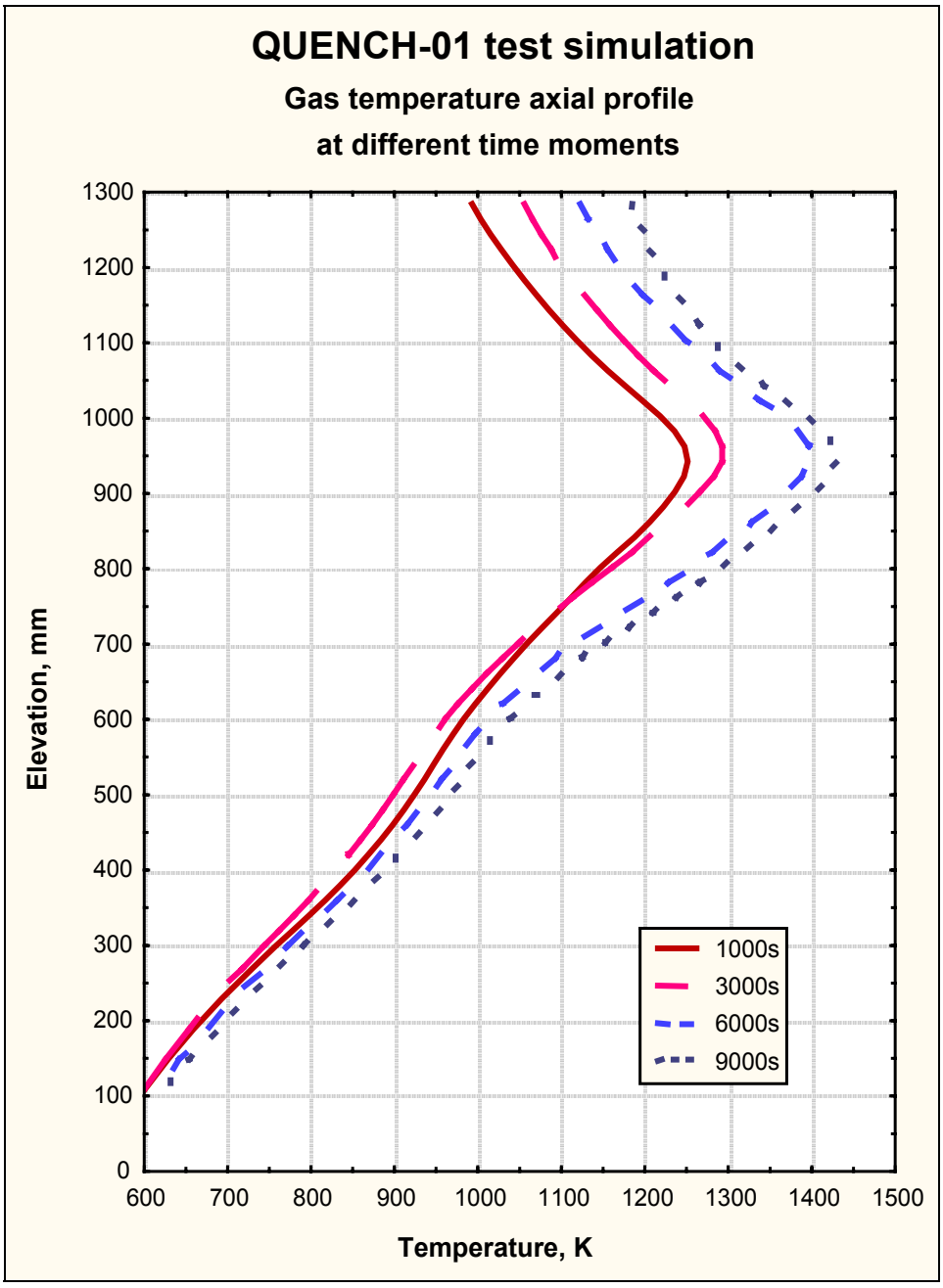

Fig. II-16. Gas temperature axial profile at different time moments.

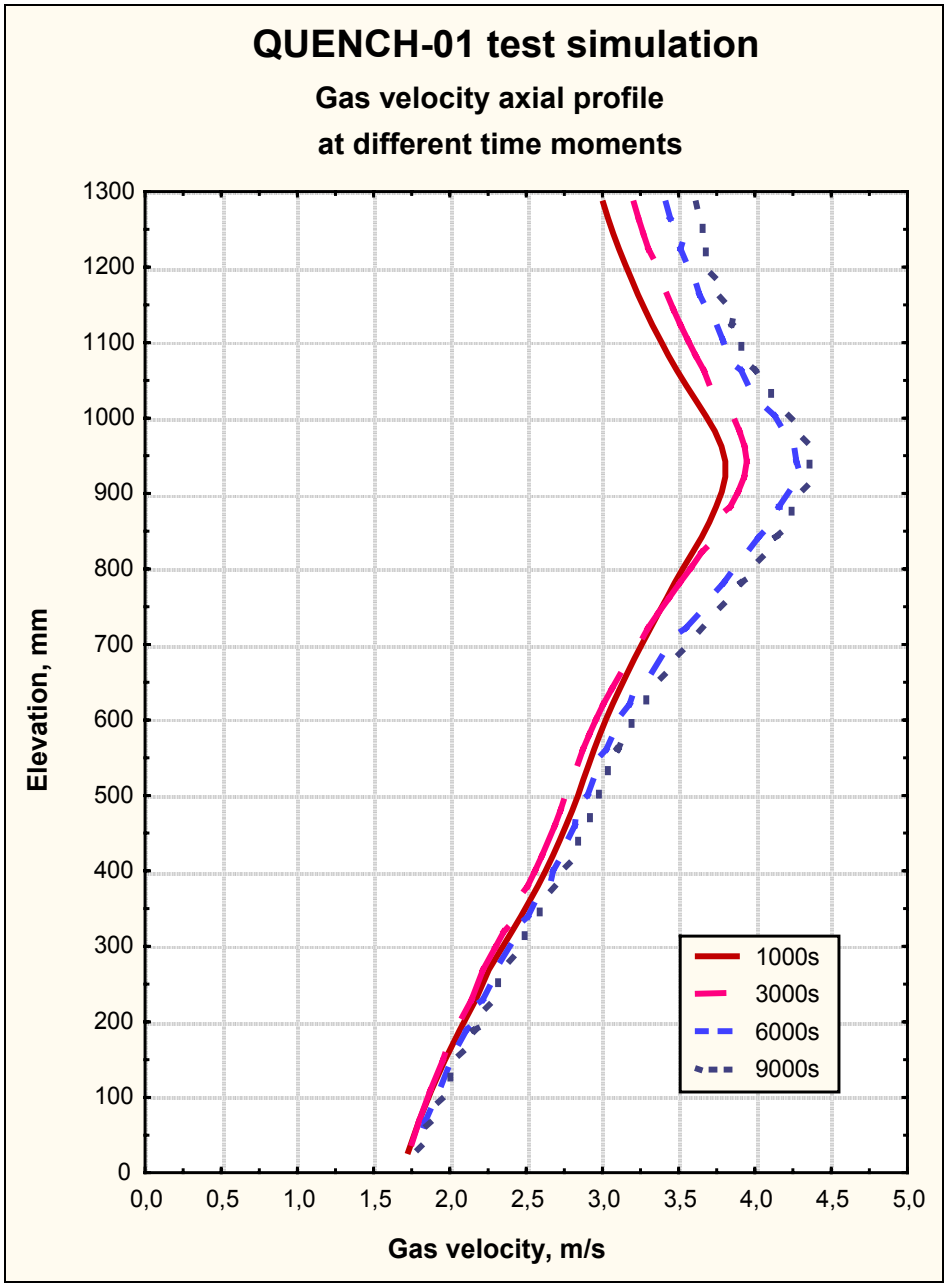

Fig. II-17. Gas velocity axial profile at different time moments.

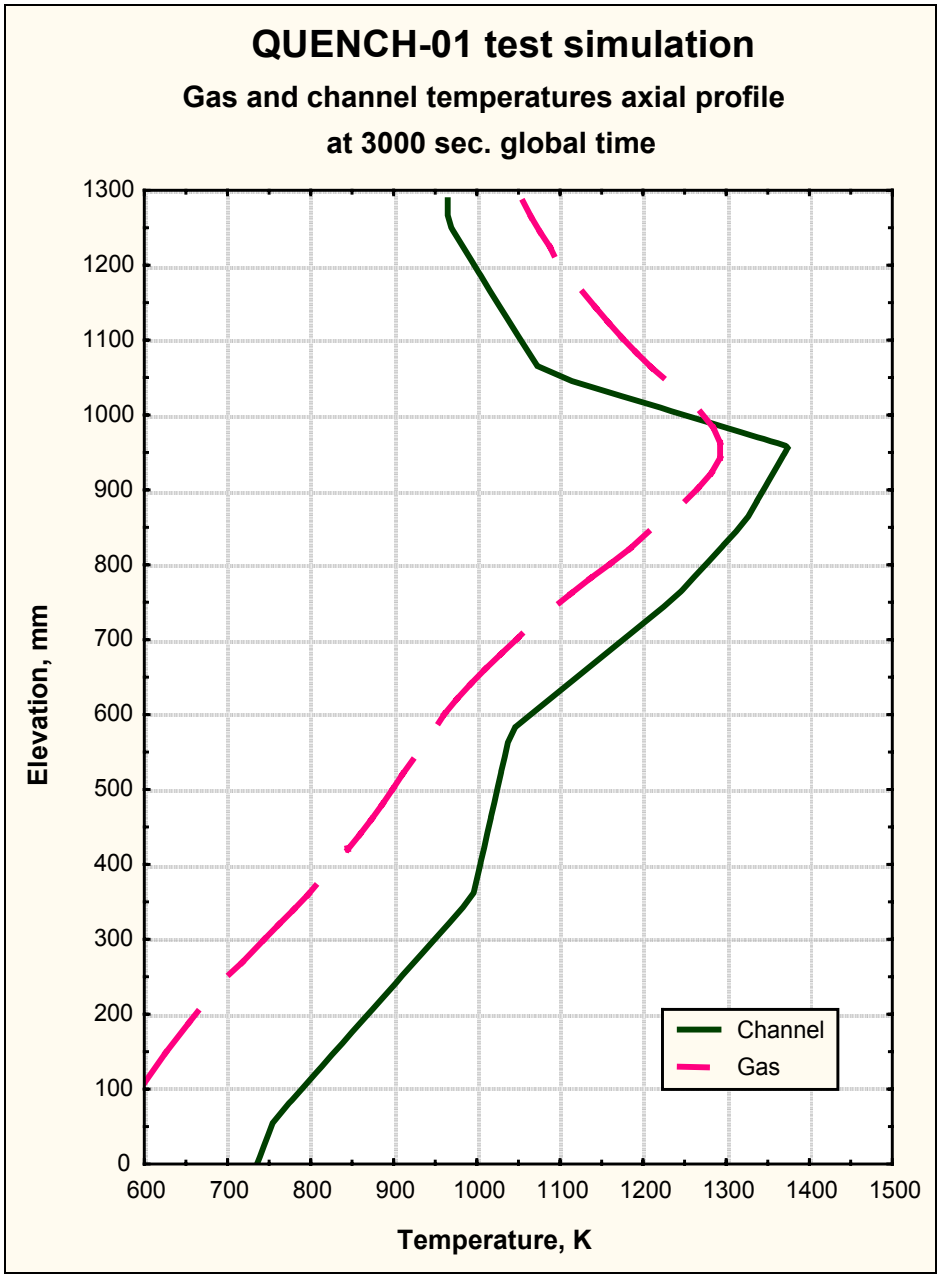

Fig. II-18. Comparison of the gas and channel axial profiles at 3000 s.

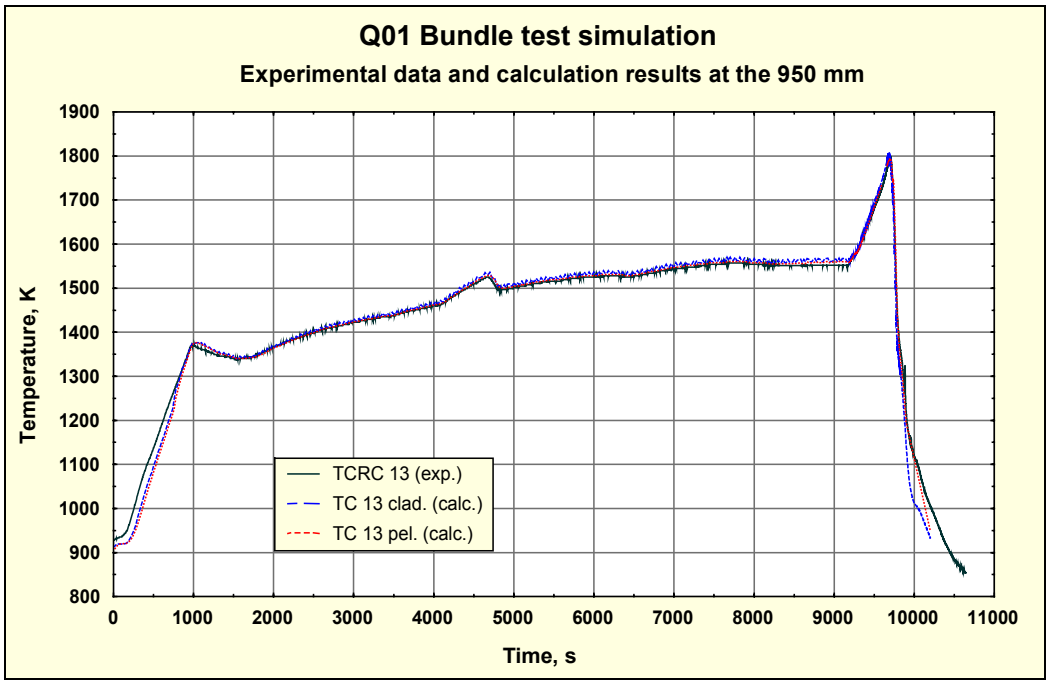

Fig. II-19. Central rod temperature evolution at 950 mm elevation.

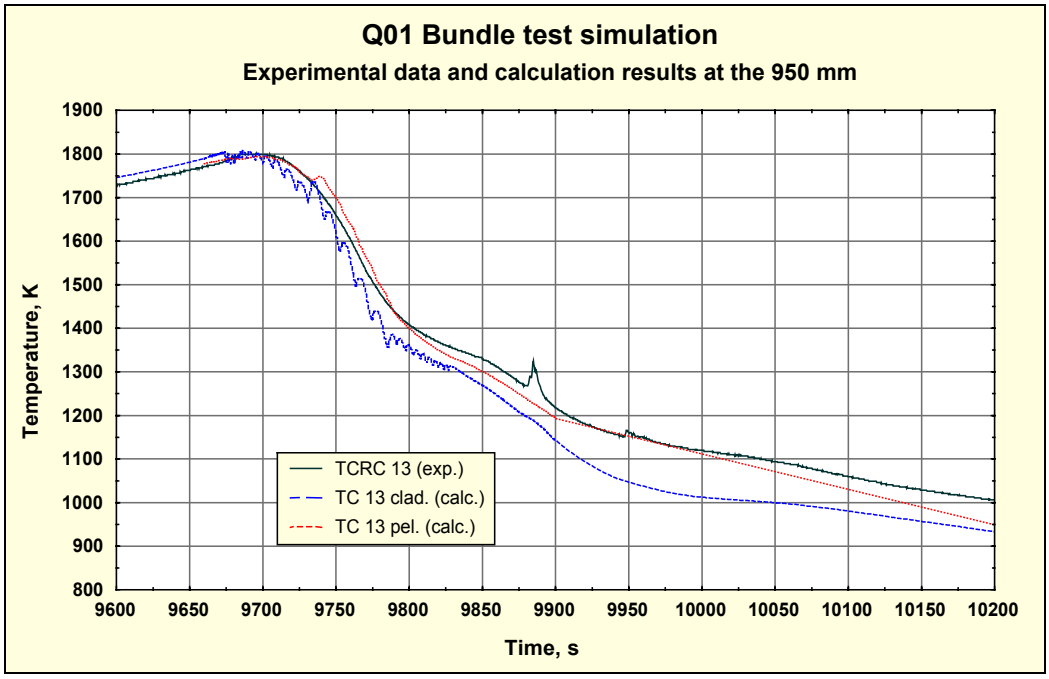

Fig. II-20. Central rod temperature evolution at 950 mm elevation. Quenching phase.

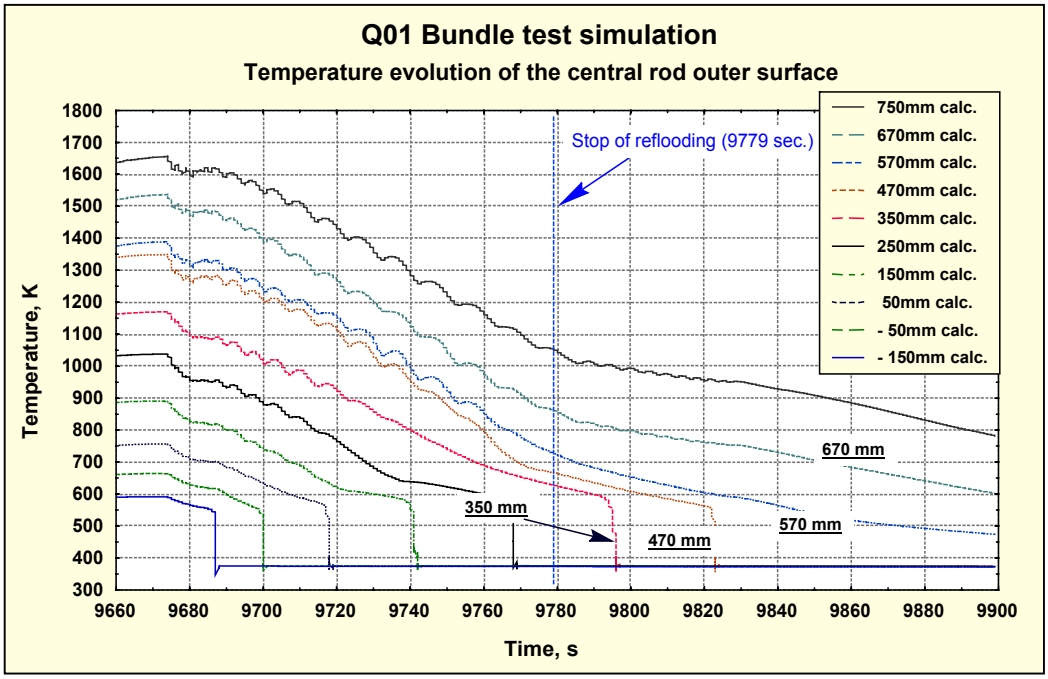

Fig. II-21 Calculated central rod temperature evolution at different elevations. Quenching phase.

4 Analysis of Q-01 bundle test simulation results

4.1 Experimental observations

To compare the obtained calculation results with the experimental data, the main observations are summarised in the present section. The post-test examination of the bundle after the test conduction reveals the following main features of the test bundle behaviour [6]:

- the post-test appearance of the bundle shows no signs of any melt;
- significant oxidation of the bundle occurred between 700 and 1000 mm elevation, Figs. II-22a to II-22c;
- in this region the oxide layer has grey colour and through-wall cracks in the cladding have formed, Figs. II-22b and II-22c;
- the central rod in the lack of the support from the heating element is broken and pellets are found outside the cladding;
- no or only few through-wall cracks form if ZrO_2 layer thickness $\leq$ 200 μm, Fig. II-22a;
- oxidation of the through-wall crack surfaces occurred during flooding, Figs. II-22b and II-22c;
- internal cladding oxidation is associated with the through-wall cracks, Figs. II-22b and II-22c;
- strong internal localised cladding oxidation is observed at some locations;
- the shroud is intact and non-deformed;
- the regions of the shroud above the heated zone that is without insulation exhibits a bronze-like colour, this is the region where a slight temperature escalation of the shroud might have taken place.

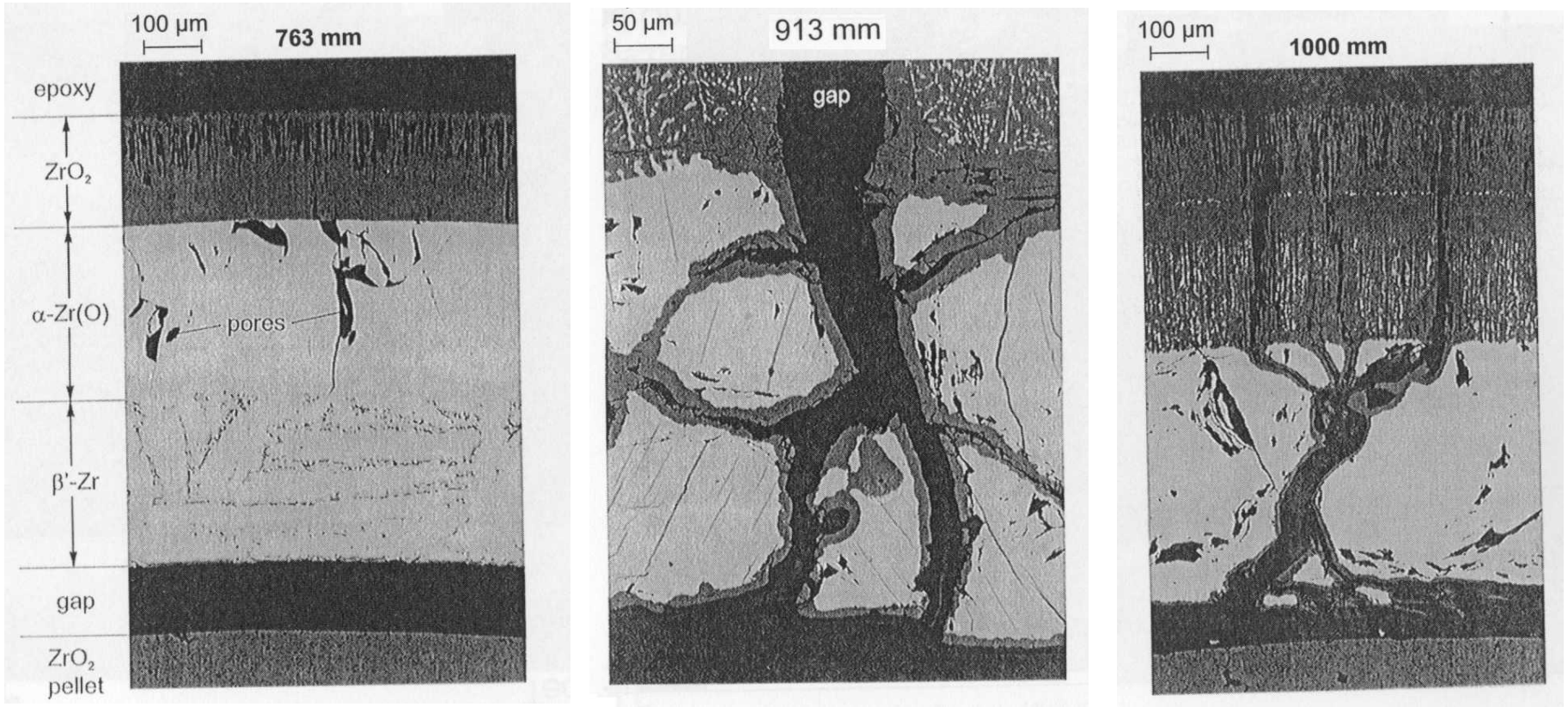

a b c

Fig. II-22 Oxidation of Zircaloy cladding at different axial bundle elevation

4.2 Calculation results

4.2.1 Boundary conditions for temperature simulation

To simulate the temperature history of the central rod the experimentally measured boundary conditions (see Section 3 of the present report), were used. As it was demonstrated in Section 4, the usage of the central rod environment temperature history gives the calculated temperature evolution, which is very similar to experimental one.

In Fig. II-23 the calculated temperatures of the central rod at the axial elevation 950 mm are presented along with experimental temperature, measured by thermocouple located in the pellet centre of the central rod at the same axial elevation. In this figure the calculated temperatures of the pellet centre, the outer pellet surface, the inner and the outer surface of the cladding and the input temperature of the inner shroud surface are plotted.

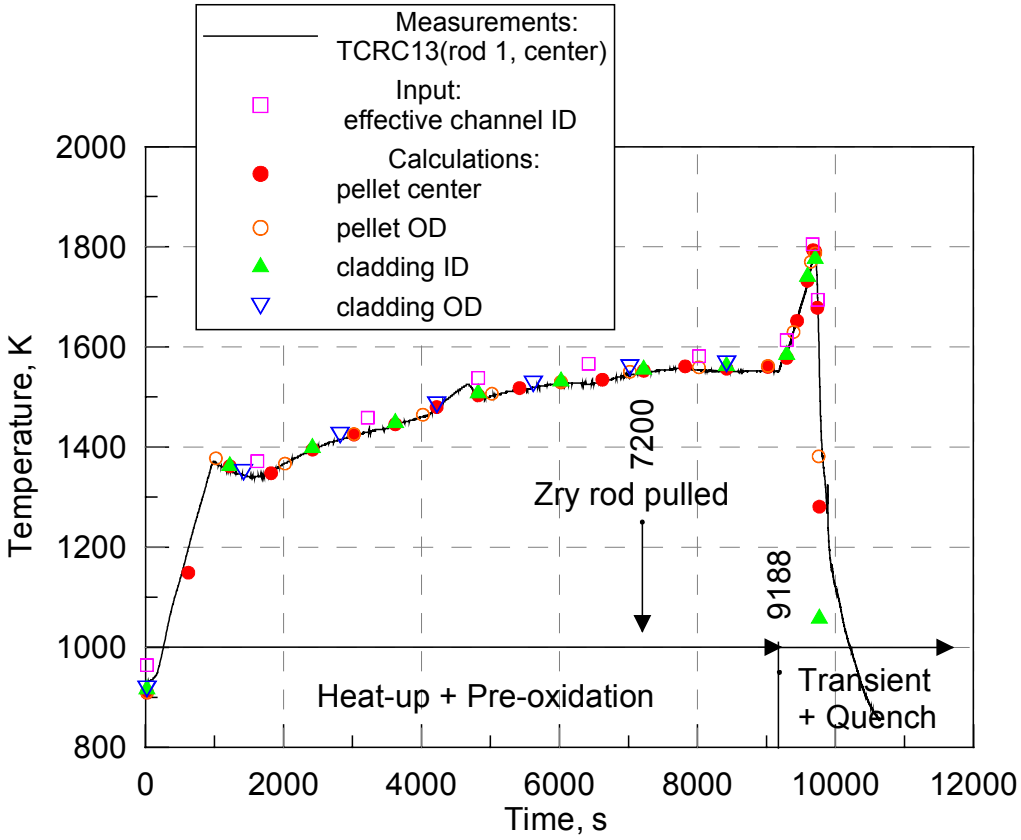

Fig. II-23 Comparison of the calculated and measured temperature evolution at 950 mm axial elevation of the central rod.

One can see from Fig. II-23 that the radial temperature gradient for the central rod up to the reflooding phase is negligible. It means that the measured temperature evolution may be used as input data to evaluate the oxide layer thickness at the given bundle elevation.

4.2.2 Axial oxide layer profile of the removed Zircaloy rod

The pre-oxidation phase started after the second heat up period with a ramp rate of 0.5 K/s and lasted for 8280 s at maximum temperatures of about 1400 – 1600 K to attain the required maximum oxide layer thickness of 300 μm at 900 mm elevation. At about 6300 s in the pre-oxidation phase one of the solid Zircaloy rods was pulled from the bundle to check the extent of the attained oxidation. In Fig. II-24 the calculated and measured axial oxide layer profiles are presented.

The calculated oxide thickness is plotted for the time instant 7200 s. This time interval is obtained by summation of 6300 s measured from the beginning of the pre-oxidation phase and 900 s duration of the second heat up phase. This total time does not include the first heat up phase and the phase at ca. 1000 K in which well defined amounts of helium were injected into the test section at 700 mm elevation to determine delay times for the hydrogen transport to the mass spectrometer and the Caldos device. Everywhere, if it is not specially indicated, this total time was used, for instance in Fig. II-23.

Fig. II-24 shows that the calculated oxide layer axial profile at 7200 s is slightly lower than the measured one. The main difference is observed for the lower part of the central rod, where temperature is lower than in the upper part. It is explained by the limitation to the minimal temperature, 1235 K at which the oxidation module starts operation.

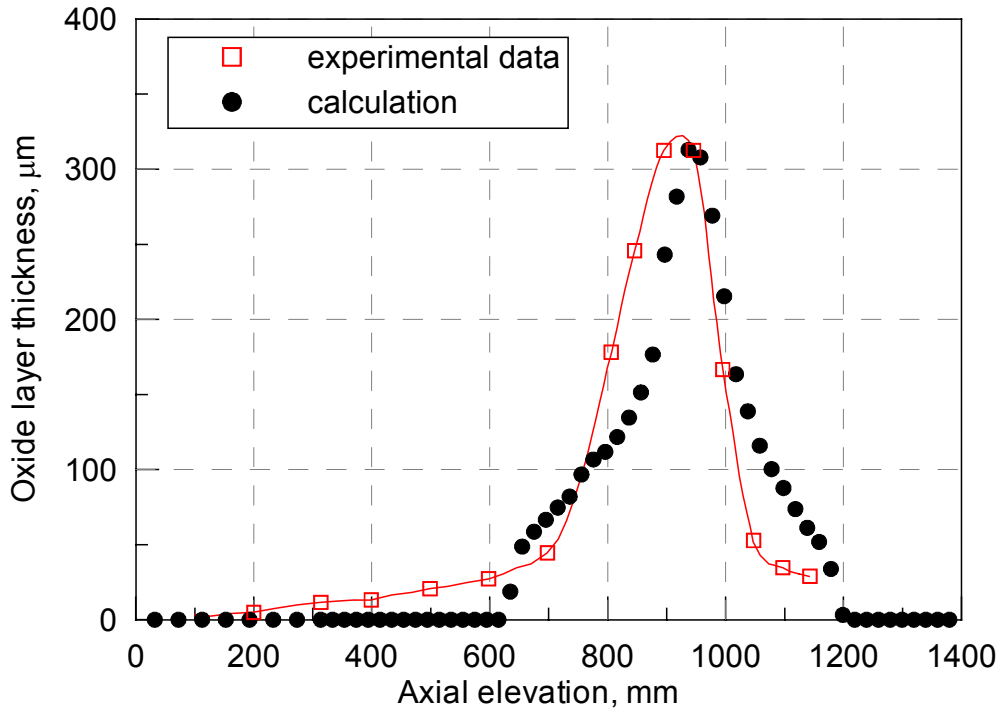

Fig. II-24 Comparison of the calculated and measured oxide layer axial profile in the end of the pre-oxidation phase

4.2.3 The calculated state of the central rod after reflooding

After the oxide layer axial profile was calculated up to the end of pre-oxidation phase and a good agreement with the experimental results was attained, the transient and the quenching phases were simulated. The final state of the central rod is presented in Table II-4.

Table II-4. Calculated state of central rod after quenching at different axial elevation

.Elevation	Outer oxide	Cladding state	Inner oxide	Crack surfaces oxide
mm	μm		μm	μm
1400	1	intact	0	0
1300	12	intact	0	0
1200	41	intact	0	0
1100	140	intact	0	0
1060	191	intact	0	0
1040	228	cracked	15	16
1020	279	cracked	19	20
1000	365	cracked	23	26
980	399	cracked	31	33
960	459	cracked	41	43
940	488	cracked	46	47
920	424	cracked	39	40
900	405	cracked	29	31
880	336	cracked	21	24
860	268	cracked	16	17
840	240	cracked	13	14
820	224	cracked	11	12
800	208	cracked	10	11
780	199	cracked	8	9
760	186	intact	0	0
700	124	intact	0	0
600	31	intact	0	0
500	22	intact	0	0
400	7	intact	0	0
300	0	intact	0	0
200	0	intact	0	0
100	0	intact	0	0
0	0	intact	0	0

The first column of this Table II-presents the axial elevation of the central rod. The second column presents the oxide layer thickness formed under external oxidation. The third shows the state of the cladding wall; if through-wall cracks formed at this elevation then the state is termed "cracked", otherwise the state is "intact". The fourth column presents the oxide layer thickness formed under internal oxidation after through-wall cracks formation. And the last column presents the oxide layer thickness formed on the through-wall crack surfaces; for the case of two metal layers at the given elevation, i.e. prior β-Zr and α-Zr(O), the average oxide layer thickness is indicated.

For comparison the final (after reflooding) outer calculated oxide layer thickness profile along the axial direction is plotted in Fig. II-25 along with the measured data.

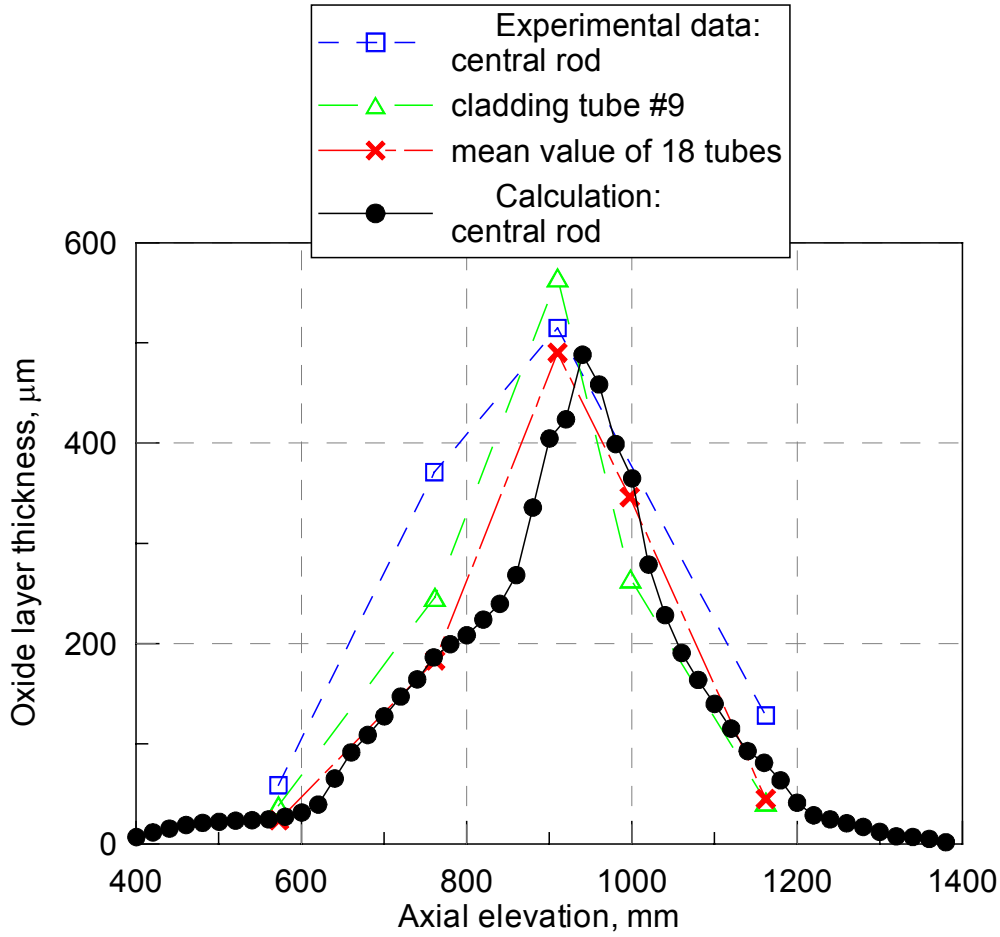

Fig. II-25 Calculated and measured outer oxide layer thickness profile along the axial direction after reflooding.

From Fig. II-25 one can see that the calculated profile of the oxide layer for the central rod is closer to the mean values for the other 18 cladding tubes. However, some underestimation is observed and this should lead to some underestimation of the integral hydrogen production.

The calculation predicts the through-wall cracks formation at the elevation between 780 and 1040 mm, for other elevations a relatively thick layer of β phase prevents the cracks propagation.

To calculate the internal cladding oxidation, the same oxygen flux as for the outer surface was applied to the inner cladding surface. Comparison of the calculated and measured oxide layer thickness profiles for the internal cladding oxidation is shown in Fig. II-26. One can see overestimation of the calculated profile in comparison with measured one. The possible reason is the overestimation of the penetrated oxygen flux accessible to the inner surface.

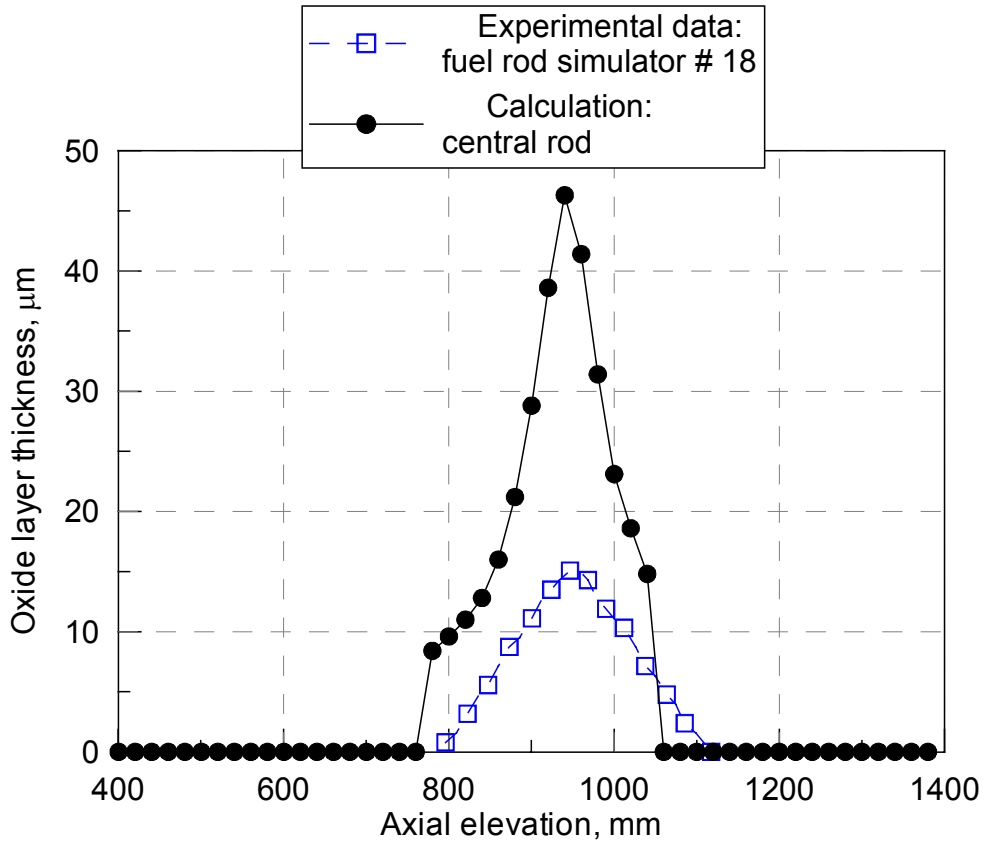

Fig. II-26 Calculated and measured inner oxide layer thickness profiles along the axial direction after reflooding.

The approach to calculate the oxidation of through-wall crack surfaces was described in [5]. The main features of this approach are the following:

- new virtual oxidation meshes with outer surfaces equal to the total crack surfaces are introduced for each metal layer of the oxidized cladding, the height of these meshes is the same as the height of the real oxidation mesh;
- the mass of each virtual mesh is equal to the mass of corresponding metal layer and, hence, the inner radius and the layer thickness are obtained from this condition;
- initial oxygen distribution is assumed to be uniform along the radius of the virtual mesh and determined by oxygen dissolved in the corresponding metal layer;

- temperature of the virtual mesh corresponds to an average temperature of the corresponding metal layer;
- virtual meshes are subjected only to the outer oxidation, the oxygen flux is the same as for the outer mesh surface;
- it is assumed that oxidation of the real and the virtual meshes occurs independently.

Calculations predict that the density of the through-wall cracks is about of 0.8-0.9 mm^{-1}, hence, the total cracks surface is very close to the inner cladding surface: if the oxide thickness is greater than 300 μm (thickness of α layer is about 500 μm) the total cracks surface is slightly smaller than the inner surface, and if the oxide thickness is less than 300 μm, the total cracks surface is slightly greater than the inner surface.

A similar surface area and the same oxygen flux lead to the oxide layer thickness of the through-wall cracks similar to the inner cladding oxidation, see Table II-4. The oxide thickness on the cracks surfaces was not measured after the test, but the visual metallographic examination of the cladding cross-sections gives the values comparable with the inner surface oxide thickness, see Figs. II-22b and II-22c. Hence, it was assumed that Fig. II-26 may be used for comparison of the calculated oxide layer thickness formed on the through-wall crack surfaces and measured values. Overestimation of the oxide thickness may be related to the unaccounted steam starvation effect on the inner surface, since the available oxygen flux firstly reaches the crack surfaces and then the inner surface.

Another important conclusion may be derived from consideration of the measured profile of the inner oxide. It was observed that the inner oxidation took place at the elevation where the through-wall cracks were formed, and the upper parts of the inner surface were not oxidised. In calculations it was assumed that formation of the first crack leads to the oxide cracking at the neighbouring axial elevations if the embrittlement of the cladding is higher than the critical value. Then cracking propagates along the cladding until the cladding embrittlement becomes lower than the critical value. Hence, if it is the case, the through-wall cracks formed at the same time in the cladding and the absence of oxidation at the upper enough heated parts means that the oxygen flux did not reach these elevations and was absorbed by the crack and lower inner surfaces.

4.2.4 Hydrogen absorption and generation

The calculated results of the total hydrogen generation and hydrogen absorption for the central rod are shown in Fig. II-27.

One can see that the simulation predicts release of hydrogen dissolved in the beginning of the transient phase and then desorbed after temperature increase and decrease of hydrogen solubility. Measurement of hydrogen absorbed in the remaining Zircaloy-4 metal of the rod # 18 gives the maximum value of about 5%. The total hydrogen generation increases during transient phase due to intensive oxidation and this contribution to the total hydrogen production is greater than the hydrogen generation during reflooding.

In order to compare simulations with the measured total hydrogen production in the bundle, the central rod calculated results were extrapolated to the bundle. It was assumed that contribution in the hydrogen production is proportional to the number of structures, the oxide layer thickness and the oxidised surface of the structure. There were three types of structures: the fuel rod simulator, the solid Zircaloy-4 rod and the shroud. Under the assumption that contribution of each fuel rod simulator is the same, the total hydrogen production for the bundle may be obtained in the following manner:

$$M^H_{bundle}(t) = N_{fuel\_rod} \cdot M^H_{central}(t) + N_{solid\_rod} \cdot \frac{R_{solid\_rod}}{R_{fuel\_rod}} \cdot M^H_{central}(t) +$$

$$+ N_{shroud} \cdot \frac{R_{shroud}}{R_{fuel\_rod}} \cdot \frac{th^{ox}_{\max,shroud}}{th^{ox}_{\max,fuel\_rod}} \cdot M^H_{central}(t) \ , \qquad (11)$$

where:

$M^H_{bundle}(t)$ is the mass of the total hydrogen production for the bundle as a function of time;

N_{fuel_rod}, N_{solid_rod} and N_{shroud} are the number of the fuel rod simulators, the solid rods and shroud, respectively;

$M^H_{cenral}(t)$ is the mass of the total hydrogen production for the central rod as a function of time;

R_{solid_rod}, R_{fuel_rod} and R_{shroud} are the outer radii of the solid and fuel rods, and the inner radius of the shroud, respectively;

$th^{ox}_{max,shroud}$, $th^{ox}_{max,fuel\_rod}$ are the maximum oxide layer thickness for the shroud and fuel rod simulator, respectively.

It was assumed that the extent of the solid rod oxidation is equal to the central rod one.

Eq. (11) was applied to each stage of the test. The final view for the bundle hydrogen generation and hydrogen generation rate up to 7200 s, when one of the solid rods was removed, is given by:

$$M^H_{bundle}(t) = 28 \cdot M^H_{central}(t)$$

$$\frac{dM^H_{bundle}(t)}{dt} = 28 \cdot \frac{dM^H_{central}(t)}{dt} \ , \qquad (12)$$

For the time interval up to the reflooding onset, from 7200 to 9660 s, the bundle hydrogen production is given by:

$$M^H_{bundle}(t) = M^H_{bundle}(7200) + 27.3 \cdot \left(M^H_{central}(t) - M^H_{central}(7200)\right)$$

$$\frac{dM^H_{bundle}(t)}{dt} = 27.3 \cdot \frac{dM^H_{central}(t)}{dt} \ , \qquad (13)$$

For the reflooding phase it was assumed that the main contribution to the hydrogen generation gives the fuel rod simulator due to oxidation of the inner and crack surfaces, hence, for the time after the onset of the reflooding, i.e. after 9660 s:

$$M^H_{bundle}(t) = M^H_{bundle}(9660) + 21 \cdot \left(M^H_{central}(t) - M^H_{central}(9660) \right)$$

$$\frac{dM^H_{bundle}(t)}{dt} = 21 \cdot \frac{dM^H_{central}(t)}{dt} , \qquad (14)$$

In Fig. II-28 the total hydrogen generation extrapolated to the bundle is plotted along with the measured values. Since the experimental estimation of the absorbed hydrogen is about 3 % of the hydrogen totally produced during the test, then the experimental data may be considered as the total hydrogen generation.

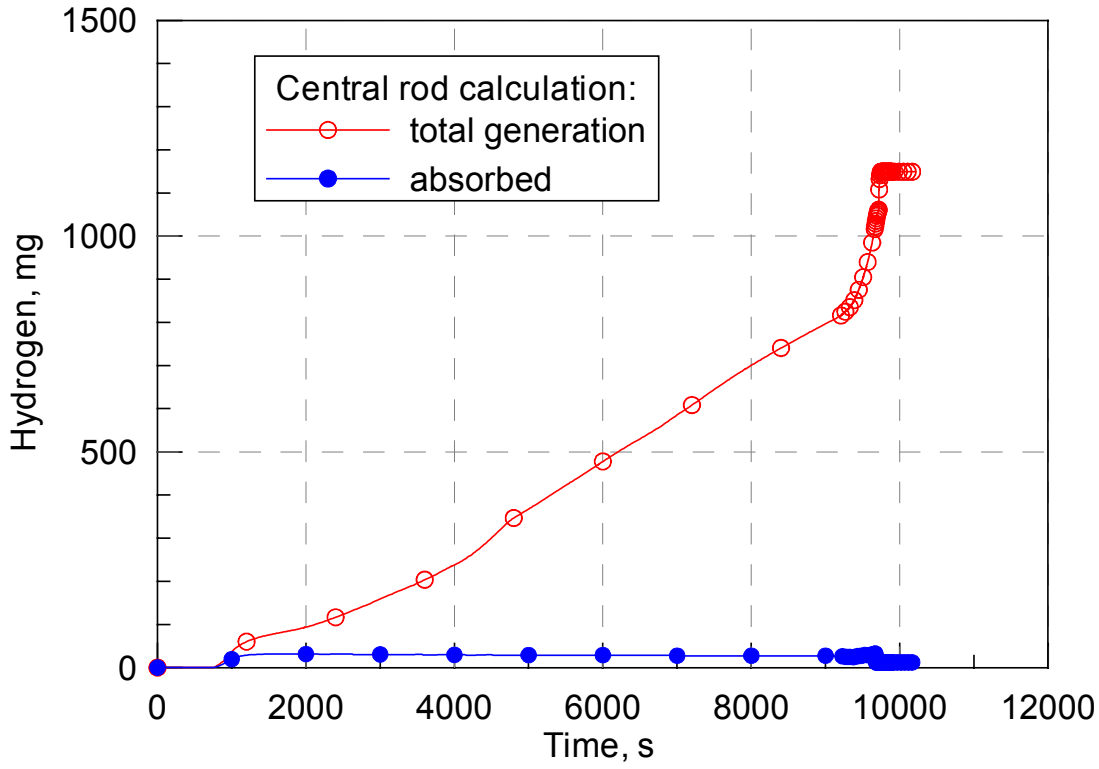

Fig. II-27 Calculation results for hydrogen absorption and generation in the central rod.

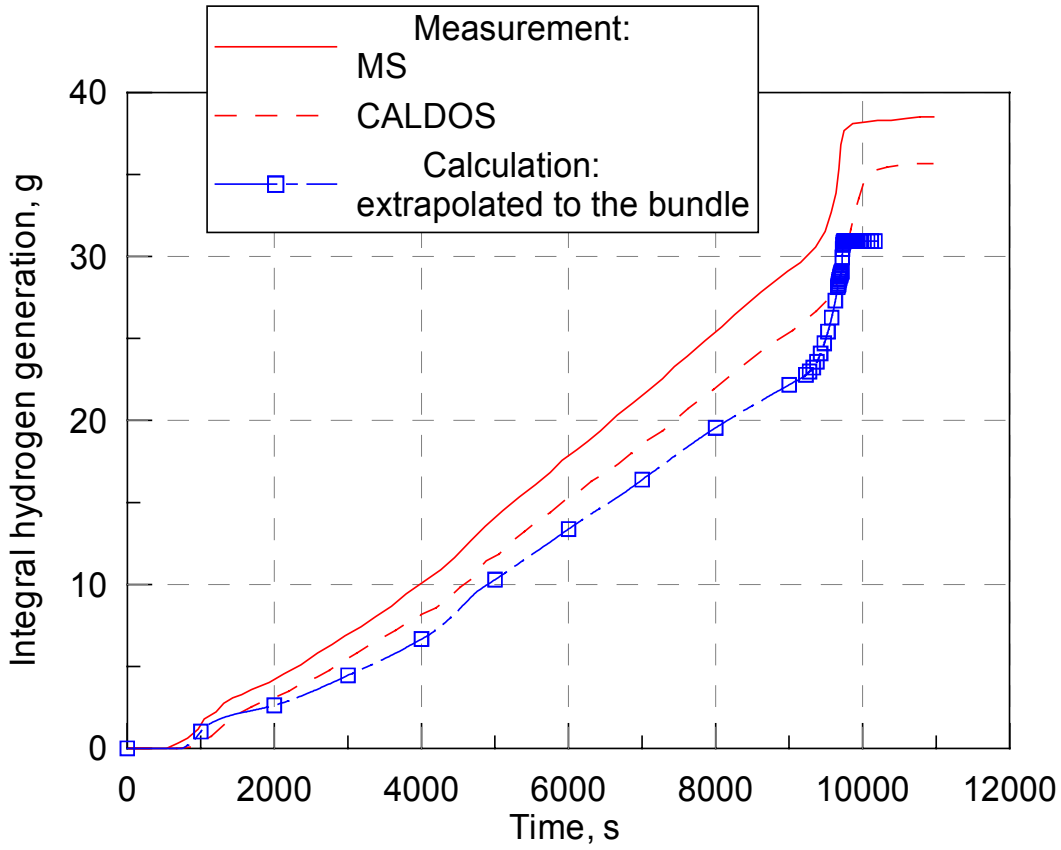

Fig. II-28 Comparison of the calculation result for hydrogen generation in the central rod extrapolated to the bundle and the bundle measured values.

Comparison of the calculated and measured hydrogen generation rates is presented in Fig. II-29 and Fig. II-30. In Fig. II-29 the hydrogen generation rate in the pre-oxidation phase is plotted. The measured value of the mass spectrometer and Caldos device and the calculated ones are in good agreement. In the case of transient and quenching phases (Fig. II-30) the measurements of mass spectrometer are used, owing to the absence of the delay in the measurements.

From Fig. II-28 and II-29 one can see that the calculated value for the total hydrogen generation and the generation rate are slightly less than the measured ones in the pre-oxidation stage. This is explained by the thinner oxide layer thickness predicted by simulation, see Fig. II-24. The increase of the hydrogen production during transient is higher for the calculated value, see Fig. II-28, the final calculated hydrogen production is very close to the measured values.

The calculated hydrogen generation rate presented in Fig. II-30 has a local maximum, which is the result of the through-wall cracks formation and the intensive oxidation of the inner and crack surfaces.

The measured hydrogen generation rate has a local maximum too. The measured increase of hydrogen production occurred after the start of the power reduction from 20 kW to 4 kW and, hence, after the rapid cool down of the bundle. Therefore, the possible reason of this peak is the through-wall cracks formation and oxidation.

Instants of the measured and the calculated peaks do not coincide and the measured one is smoother than the calculated. The possible reason is the extrapolation of the results obtained for the central rod to the entire bundle. Since the radial and the axial temperature distributions during flooding depend on the rod locations, in the pre-oxidation phase these differences are negligible. Nevertheless, the calculated integral hydrogen production in the transient and quench phase is very close to the measured one.

To find the contribution of the inner and crack surfaces oxidation to the total hydrogen production, the test simulation without possibility of the through-wall cracks formation was performed. The results are presented in Fig. II-31 and II-32.

The oxide layer thickness profiles before and after the quench phase are plotted in Fig. II-31. This growth of the outer oxide layer thickness is the source of the hydrogen generation without cracks formation, represented by the lower curve in Fig. II-32. The upper curve in Fig. II-32 corresponds to the hydrogen generation under QUENCH-01 conditions. The difference between these two curves is the contribution of the inner and crack surfaces oxidation to the hydrogen production.

The quantitative analysis shows that the calculated total hydrogen generation during quenching is about 3 g, an experimental estimation of the total hydrogen generation during quenching is also about 3 g. This amount of 3 g is formed by 1.4 g due to further external oxidation, inner (0.6 g) and through-wall crack (1 g) surfaces oxidation. Hence, the through-wall cracks formation and oxidation gives considerable contribution into hydrogen generation during quenching.

The detailed calculated and measured data according to the hydrogen generation are presented in Tables II-5 and II-6.

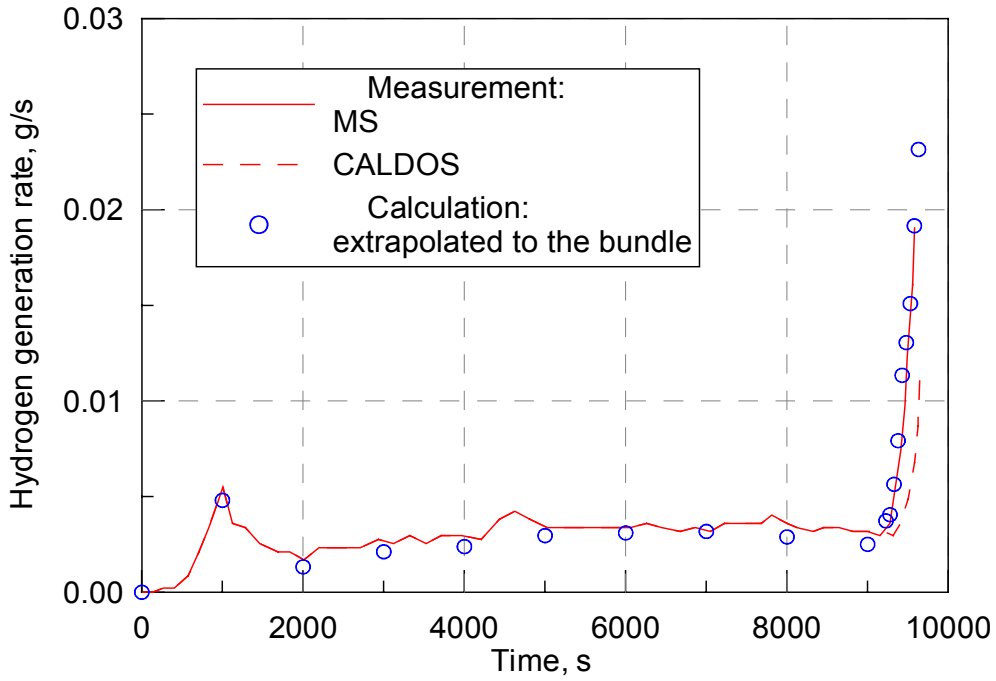

Fig. II-29 Calculation results for hydrogen generation rate in the central rod extrapolated to the bundle during pre-oxidation phase.

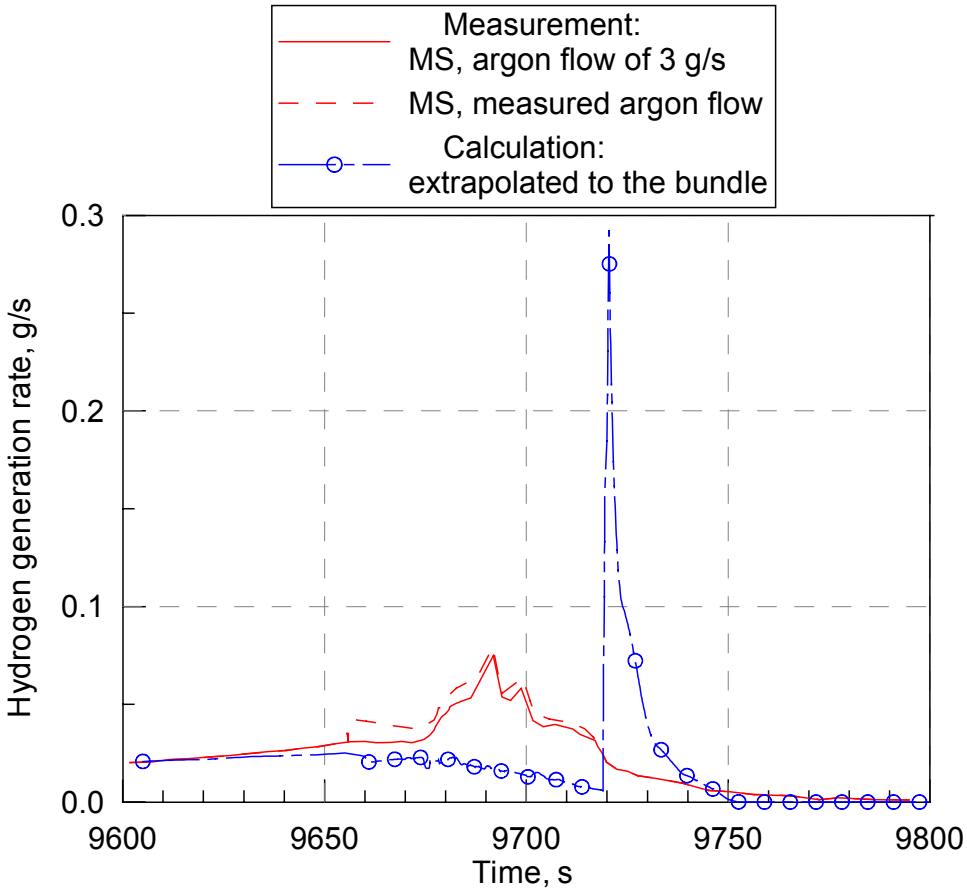

Fig. II-30 Calculation results for hydrogen generation rate in the central rod extrapolated to the bundle during transient and quenching phases

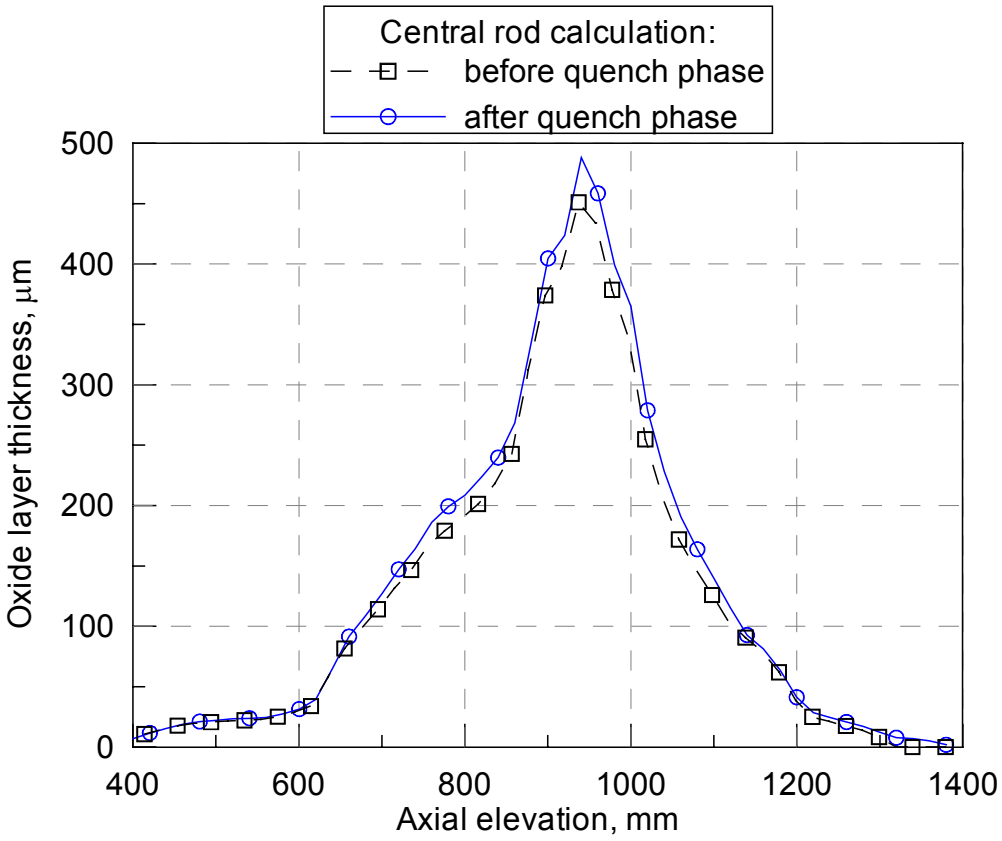

Fig. II-31 Calculated thickness of oxide layer for central rod after pre-oxidation and transient phase.

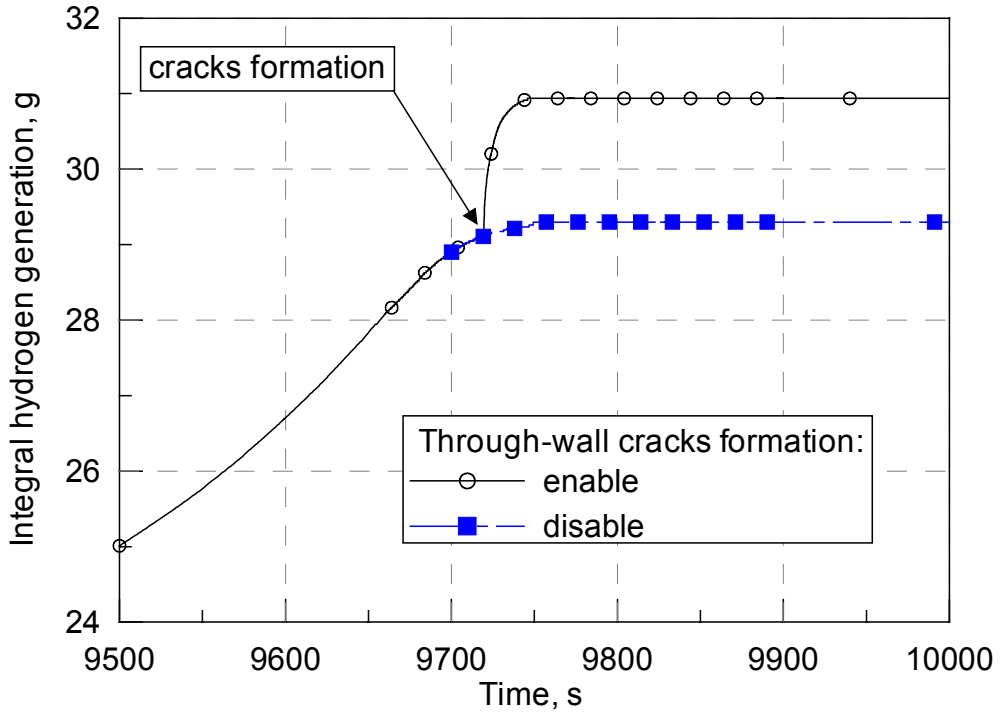

Fig. II-32 Calculated hydrogen generation for central rod during quench phase due to through-wall cracks formation.

Table II-5. Hydrogen generation, experimental data, g.

Test phase	Mass spectrometer	Caldos system
1 st heat-up	0.5	-
He injection	0.5	-
2 nd heat & pre-oxidation	30	27
Transient & quench	8	8
Total	39	35
	Estimation	
Quench	3	
Absorbed hydrogen	1	

Table II-6. Hydrogen generation, calculated data, g.

Test phase	Calculation	
1 st heat-up	0	
He injection	0	
2 nd heat & pre-oxidation	23	
Transient & quench	8	
Total	31	
Quench	3	
	external oxidation	1.4
	internal oxidation	0.6
	crack surfaces oxidation	1.0
Absorbed hydrogen	0.3	

5 Analysis of Q-04 bundle test temperature data

5.1 TFS thermocouples data

Contrary to Q-01 test in Q-04 test [7] quenching phase was performed with steam injection (average flow rate 50 g/s), rather than with water. All the thermocouples located at rod outer surfaces (TFS type thermocouples) survived throughout the whole experiment. Many of these thermocouples show similar behaviour during quenching phase.

At the upper part of the bundle at the elevations 1350, 1250, 1150 and 1050 mm well-pronounced minimum just after the beginning of the quenching phase (2065 s) can be recognised (Fig. II-33). In the hottest region of the bundle at the elevations 950, 850 and 750 mm local temperature escalation up to the values 2200 - 2300 K was observed in the time period just prior to quenching start with following decrease of temperature (Figs. II-34-35). At lower elevations TC data also shows fast decreasing of the rod surface temperatures after 2065 s (Figs. II-36 and II-37). Some of the TCs show 'partial recovery', i.e. limited increase of temperature in the time period 2270-2285 s (TFS5/5 in Fig. II-36; TFS2/2 and TFS2/3 in Fig. II-37).

Limited temperature increase measured by the TCs located in the upper part of the bundle (Fig. II-33) and in the lower part (Figs. II-36 and II-37) may be explained by the fact that the inlet temperature of injected steam was not constant but varied from 410 K at 2066 s to 585 K at 2088 s (see Fig. II-38). It should be noted, that in Q-04 test inlet gas temperature was measured not only by thermocouple T511 located in the steam supply pipe at the bundle inlet, but also by thermocouple TFS2/1, located at the –250 mm elevation at the heated rod surface and bent out to the channel. Obvious correlation between two curves in Fig. II-38 confirms the reliability of these data. Variation of the inlet gas temperature leads to corresponding variation of the rod surface temperature.

At the same time, some TCs show much more pronounced response to the inlet gas temperature variation than the other ones at the same elevation (for example, TFS5/5 and TFS2/5 in Fig. II-36). Behaviour of TFS5/5 and TCR9 (located at the outer surface of the central rod at the 550 mm elevation, see Fig. II-40) bears some resemblance to the temporary failures of the thermocouples in the Q-01 test, discussed in the Section 3 of the present part of the report. In order to clarify whether TC data show the real temperature evolution of the cladding surface or represent temperature evolution of the thermocouple itself, a set of auxiliary calculations with S/Q code was performed. These calculations are described in the following subsection.

5.2 Central rod thermocouples data analysis

In Q-04 test central rod thermocouples were located not only on the outer surface of the cladding (TCR7 (350 mm), TCR9 (550 mm), TCR13 (950 mm)), but also in the centre of the pellet (TCRC7 (350 mm), TCRC9 (550 mm), TCRC13 (950 mm)) and in the gap between the pellet and the cladding (TCRI7 (350 mm), TCRI9 (550 mm)). The availability of temperature evolution data measured at the same elevation at different radial locations inside central rod

makes it possible to verify the reliability of the surface temperature data. As discussed above in the Section 3, the surface-located thermocouples under certain conditions may loose tight contact with the rod due to interaction with the channel flow. If this takes place, thermocouple represents its own temperature evolution different from rod surface temperature evolution. At the same time, thermocouple located inside the pellet is protected from direct contact with channel flow, and thus gives trustworthy information. (We note that TC located in the gap is in contact either with pellet outer surface or cladding inner surface, and thus shows some average temperature. That is why it is difficult to use gap-located TCs for the temperature data evaluation).

Using temperature data measured in the centre of pellet one can verify the data measured at the rod surface. As it is well known, specification of the temperature on the surface of a body completely determines temperature distribution inside this body. Thus, by setting rod surface temperature equal to the experimentally measured temperature and solving heat conduction problem inside the rod, one can calculate the temperature evolution at the centre of the pellet and compare it with the experimental data. If there is an agreement between calculated and measured temperatures in the centre of the pellet, one can conclude, that surface TC measurements adequately represent the real temperature evolution of the rod surface. The discrepancy between calculated and measured data will indicate that the 'TC effect' took place in the considered time interval and thus, measured rod surface temperature evolution is inadequate.

In the present work such experimental data analysis was performed with respect to the central rod temperature data. It should be noted, that the description of the rod heat exchange process that is realised in the current version of the S/Q code is based on the specification of the *heat flow* from the rod surface. Within the framework of the S/Q thermal-hydraulic model the heat flow from the rod surface is determined as a function of flow parameters, boiling regime, rod surface temperature, etc. From the mathematical point of view specification of the heat flow from the surface (more accurately, specification of the temperature radial gradient on the surface at the heat conduction module time step) represents boundary condition of the *second kind*. Direct specification of the rod surface temperature as boundary condition for the heat conduction problem (boundary conditions of the *first kind*) requires serious modification of numerical scheme of the S/Q code heat conduction module. This is not foreseen by current research project program. However, by introducing minor modifications in the S/Q code description of the rod heat exchange process with the effective channel walls it is possible to specify the rod surface temperature indirectly.

The results of such specification and corresponding solution of the heat conduction problem inside the central rod are presented in Figs. II-39 and II-40. In Fig. II-39 simulation of the central rod temperature evolution in the vicinity of 350 mm elevation during quenching phase is shown. Experimentally measured rod surface temperature (TCR7, solid line) was used as the boundary condition for the heat conduction problem. As one can see, there is a good agreement between experimentally measured pellet centre temperature (dashed line) and calculated pellet centre temperature (doted line). The remaining minor discrepancies may be explained by inexact determination of the initial radial temperature distribution inside the rod (in the current version of S/Q code it is not possible to specify non-uniform initial radial temperature distribution inside the rod). Thus, one may conclude, that TCR7 thermocouple

more or less adequately represents the temperature evolution of the rod surface at 350 mm elevation.

The situation is quite different at the 550 mm elevation (Fig. II-40). Here the TCR9 thermocouple response to the inlet gas temperature variation is much more pronounced (solid line). The difference between experimentally measured pellet centre temperature (dashed line) and pellet centre temperature calculated on the basis of TCR9 data (doted line) points to the fact that a 'TC effect' takes place here and that real rod surface temperature evolution at 550 mm elevation was different from the TCR9 temperature evolution.

5.3 Effective channel inner wall temperature determination

On the basis of the considerations described in the above subsection, the full set of the TFS data was analysed, selected and averaged and the temperature distribution of the effective channel inner walls was determined. Since all the TCs survived throughout the test and show rather smooth behaviour, it was not necessary to take recourse to additional mathematical recalculation procedures (smoothing, cutting off of the failure parts of the curves, interpolation) as in the case of Q-01 data (Sec. 3). The main attention was paid to throwing away inadequate data referring to the quenching phase of the test (e.g. TFS5/5). Also, in the case of big discrepancies between the TCs data of the same elevation, preference was given to the data measured at the surface of the rods located more closely to the central rod (i.e. the rod types 2 and 3 rather than 4 and 5).

The obtained effective channel temperature evolution used for the Q-04 test simulations is presented in Fig. II-41. The effective channel wall axial profile is shown at the time moments 500 s, 1000 s, 1500 s, 2000 s, 2030s, 2040 s, 2050 s, 2060 s. One can see well-pronounced temperature escalation at 750-950 mm elevations in the time interval just before the beginning of quenching (2065 s). On the basis of the obtained effective channel temperature evolution the input temperature data files **`tc-coord.dat`** and **`tc-temp.dat`** were created in a way similar to the Q-01 case.

The thermal-hydraulic parameters of the effective channel were determined identical to that for the Q-01 test simulation (subsec. 4.1).

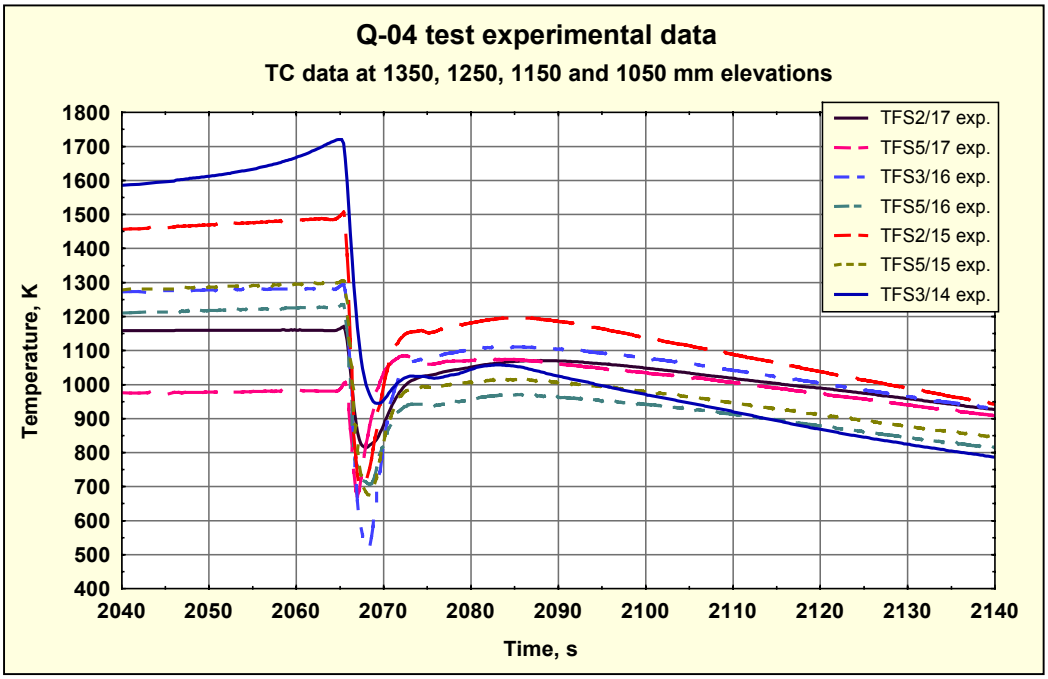

Fig. II-33. Q-04 test bundle temperature evolution at 1350, 1250, 1150, 1050 mm elevations. Quenching phase.

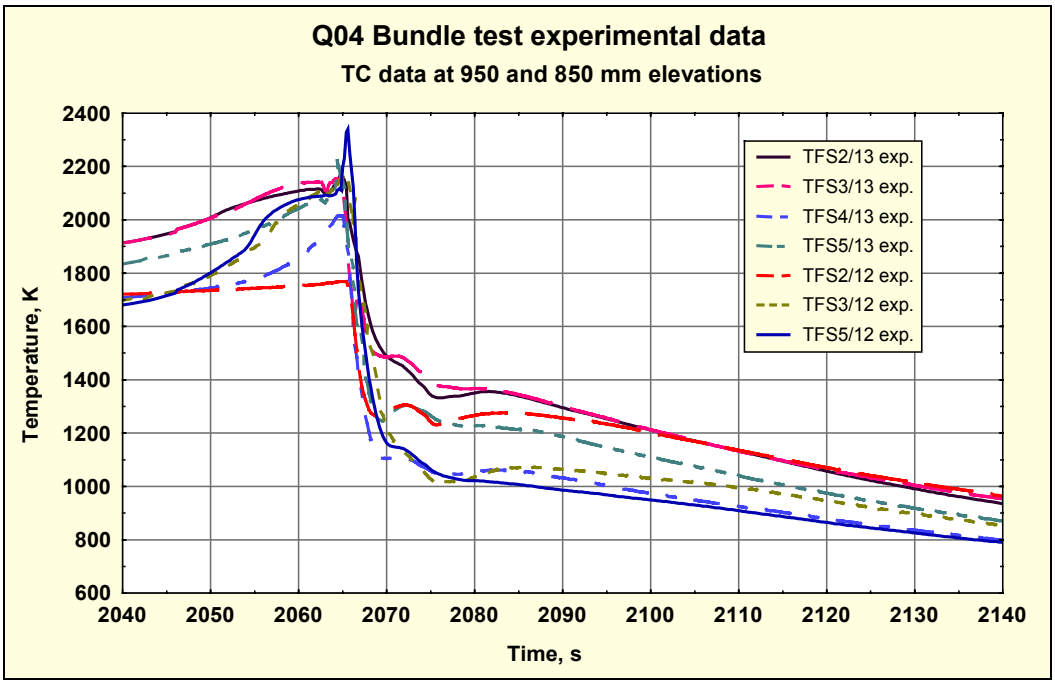

Fig. II-34 Q-04 test bundle temperature evolution at 950 and 850 mm elevations. Quenching phase.

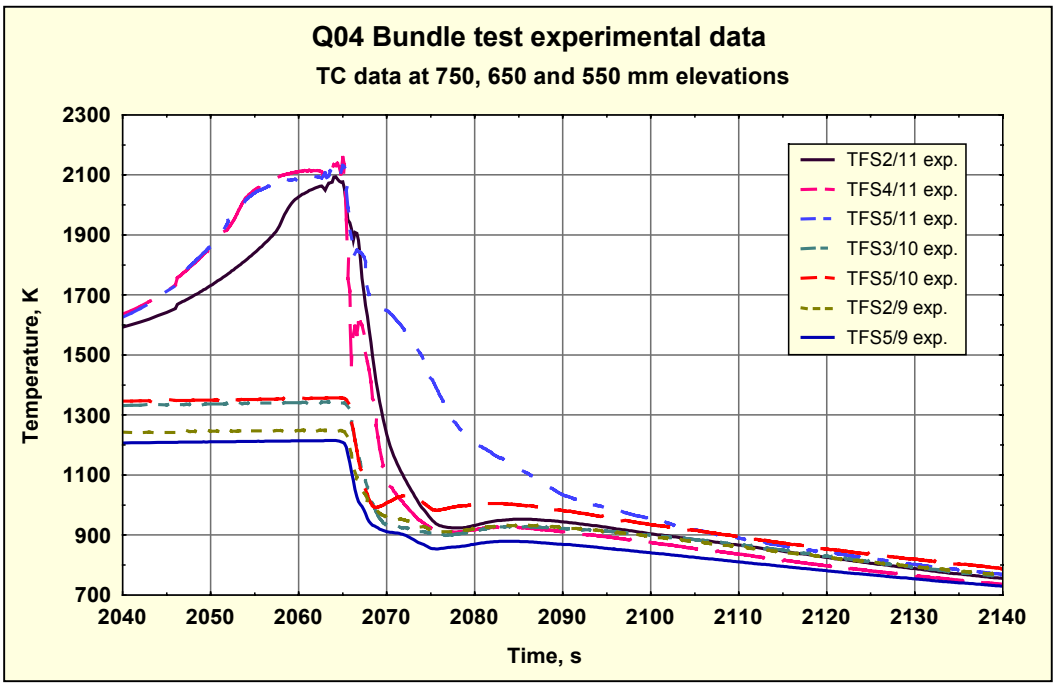

Fig. II-35. Q-04 test bundle temperature evolution at 750, 650 and 550 mm elevations. Quenching phase.

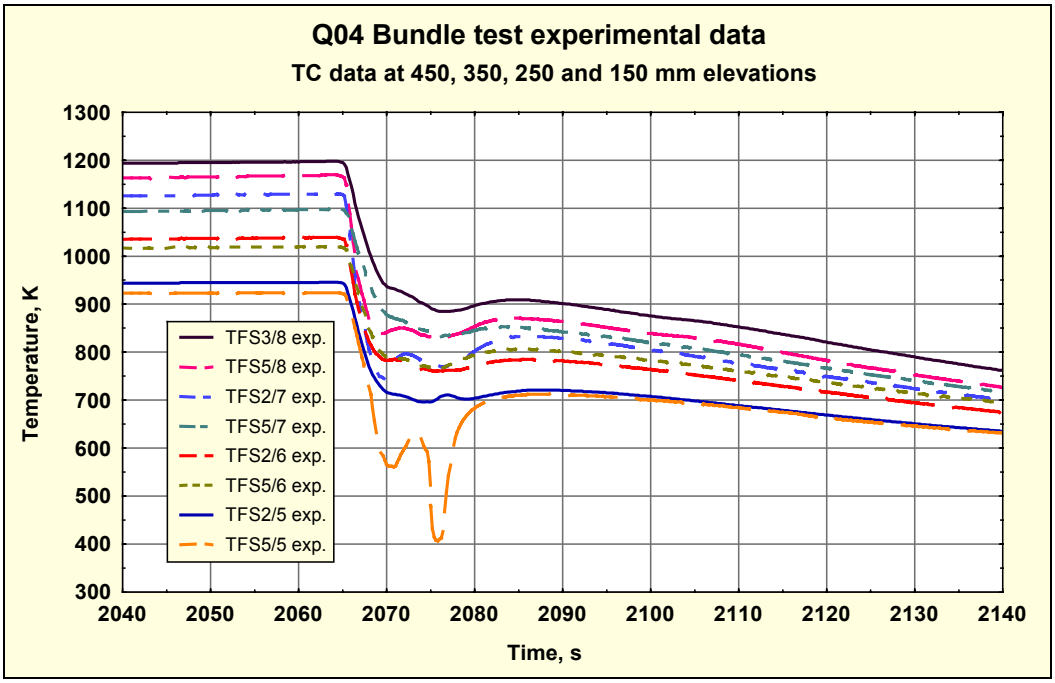

Fig. II-36. Q-04 test bundle temperature evolution at 450, 350, 250 and 150 mm elevations. Quenching phase.

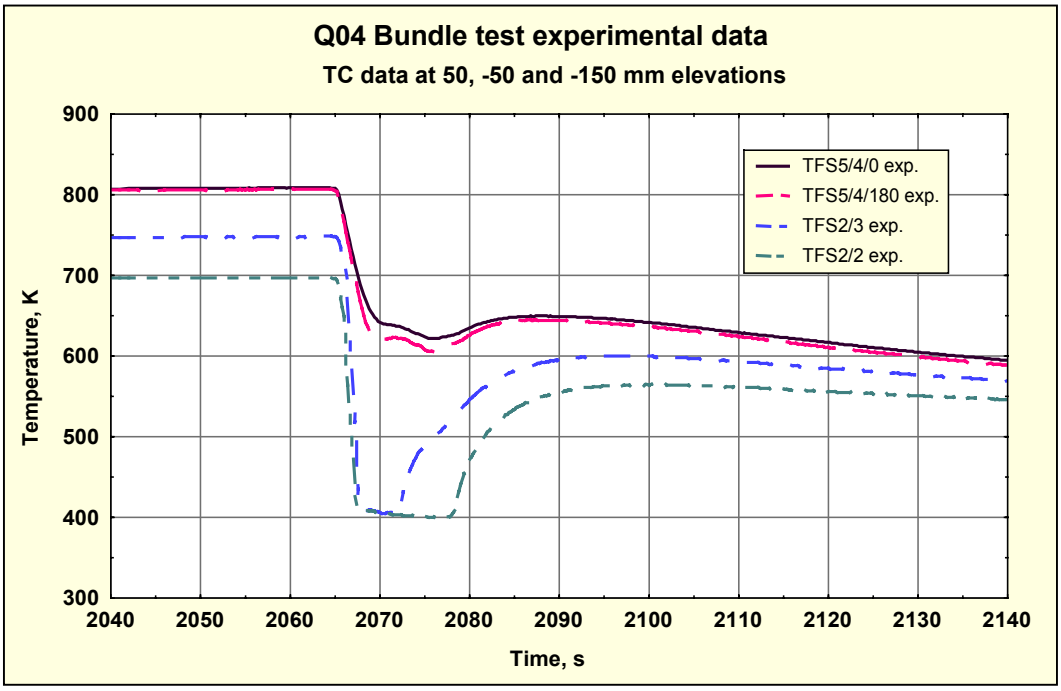

Fig. II-37. Q-04 test bundle temperature evolution at 50, -50 and -150 mm elevations. Quenching phase.

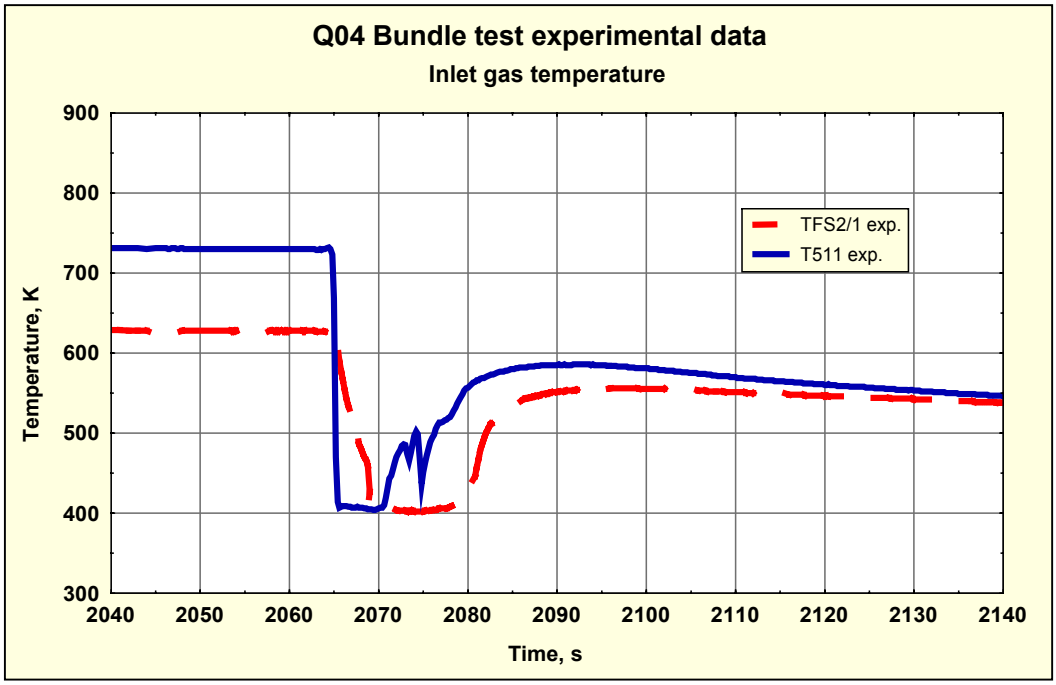

Fig. II-38. Q-04 test gas inlet temperature variation. Quenching phase.

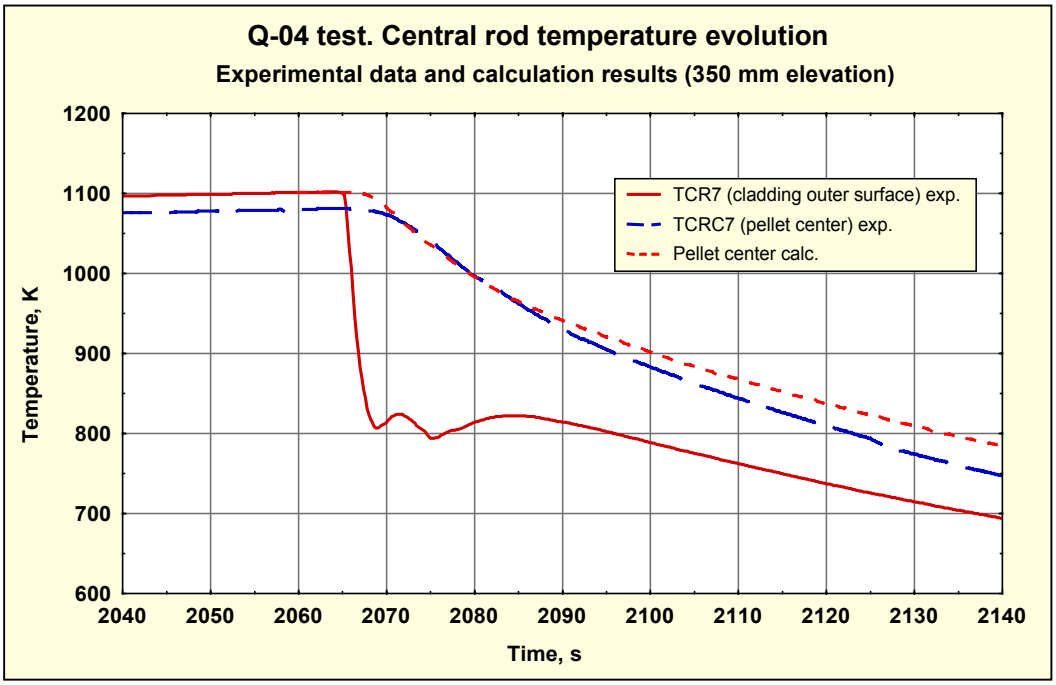

Fig. II-39. Simulation of the central rod temperature evolution at the vicinity of 350 mm elevation by specifying rod surface temperature using experimental data. Rod surface temperature (solid line), experimentally measured pellet centre temperature (dashed line), calculated pellet centre temperature (doted line).

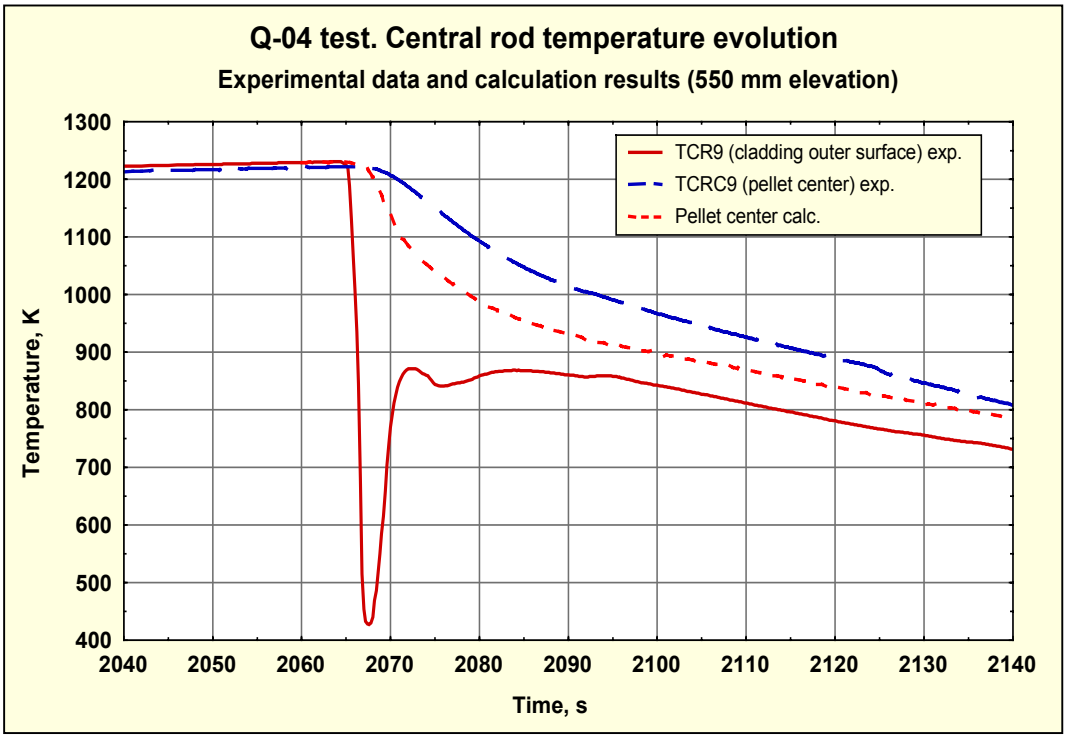

Fig. II-40. Simulation of the central rod temperature evolution at the vicinity of 550 mm elevation by specifying rod surface temperature using experimental data. Rod surface temperature (solid line), experimentally measured pellet centre temperature (dashed line), calculated pellet centre temperature (dotted line).

6 Q-04 bundle test simulation

6.1 The main assumptions used for the Q-04 test simulation

Regarding test conduct it was assumed that quenching phase began at 2065 s global time. Since, as demonstrated above, inlet gas temperature variation had large effect on the bundle temperature evolution, the real time dependence of gas temperature measured at the bundle inlet by T511 thermocouple (Fig. II-38) was used in the S/Q code input file (**q-global.inp**) instead of the average fixed value. To make the input information more detailed and representative, the real time dependence of the steam and argon mass flow rates at the quenching phase (data sets **fm 204** and **fm 401** available in electronic format) were also used in the input file.

Time step values were:

1.0 s up to 2040 s,

0.01 s from 2040 s to 2080 s,

0.1 s from 2080 s to 2400 s.

The bundle nodalization is characterised by the following values:

Heat conduction module

- The total nodes number in the radial direction: 35
- Pellet nodes number in the radial direction: 21
- External layer nodes number: 7
- Total nodes number in the vertical direction: 180

In contrast to Q-01 test simulation, the total number of nodes in the vertical direction used by heat conduction module was increased from 150 to 180. The total number of meshes used by oxidation, mechanical deformation and hydrogen absorption modules was also increased from 73 to 98 with the mesh height in the hottest bundle region (from 700 mm to 1400 mm elevations) equal to 10 mm. Meshing refining and decreasing of the time step in the time period from 2040 s to 2080 s to 0.01 s was performed in order to give more detailed description of the bundle behaviour during temperature escalation and quenching phases.

6.2 Calculation results

In the present Section only temperature-relating results of the Q-04 test simulation by the S/Q code are described. The results concerning oxidation, mechanical deformation and hydrogen release are discussed below in the Section 8.

Due to heat exchange with effective channel and with flowing argon/steam mixture, the central rod is heated up during preoxidation phase. The axial profiles of the central rod surface temperature at different moments are presented in Fig. II-42.

In Figs. II-43 and II-44 the calculated central rod temperature evolution at 950 mm elevation (in the centre of the pellet and on the outer surface of the cladding) and corresponding experimental data (TCR13 and TCRC13) are presented during the whole experiment and during the quenching phase.

As one can see, there is a good agreement between the calculated temperature evolution of the rod surface and measured one both at preoxidation and quenching phases of the test. In contrast to Q-01 test, here one has a considerable difference between temperatures on the surface of the rod and in the centre of pellet at the preoxidation phase. Calculated central temperature curve resembles the measured one, however, it is overestimated at the preoxidation phase and underestimated at the quenching phase of the test. Currently the reason of these discrepancies is unclear. Probably, they are due to some local effects (for example, non-symmetrical position of the pellet at this elevation).

We note, that at the lower elevations (550 mm and 350 mm) the agreement between calculated central temperatures and measured ones is much better. In Figs. II-45 and 46 the calculated central rod temperature evolution at 550 mm elevation (in the centre of the pellet and on the outer surface of the cladding) and corresponding experimental data (TCR9 and TCRC9) are presented during whole experiment and during quenching phase. As one can see, calculated and measured central temperatures are close to each other at the preoxidation phase and practically coincide at the quenching phase of the test.

As for the temperature on the surface of the rod, here calculated and measured temperatures show quite different behaviour at the quenching phase. Temperature evolution of the central rod at 550 mm elevation was already analysed in the present part of the report (subsec. 6.2, Fig. II-40). On the basis of the S/Q code auxiliary calculation it was concluded, that experimental surface temperature data represent local thermocouple effect, but not the real temperature evolution of the bundle. The calculation results presented in Fig. II-45 provide an additional support for this conclusion. In contrast to experimental curve, calculated one shows rather smooth behaviour without any oscillations in the time period from 2065 s to 2085 s, whereupon both curves are close to each other.

Similar situation takes place at the 350 mm elevation (see Figs. II-47 and 48). Here one has underestimation of calculated temperature at the preoxidation phase and reasonable correlation between calculation results and experimental data at the quenching phase. Calculated surface temperature generally agrees with measured one, in line with the conclusion made above in subsection 6.2, about reliability of TCR7 thermocouple data. At the same time, we note that minor “TC effect” is involved here.

In general, the presented calculation results show reasonable agreement with experimental data and provide the basis for the adequate description of cladding behaviour (oxidation, mechanical deformation, hydrogen absorption) under quenching conditions.

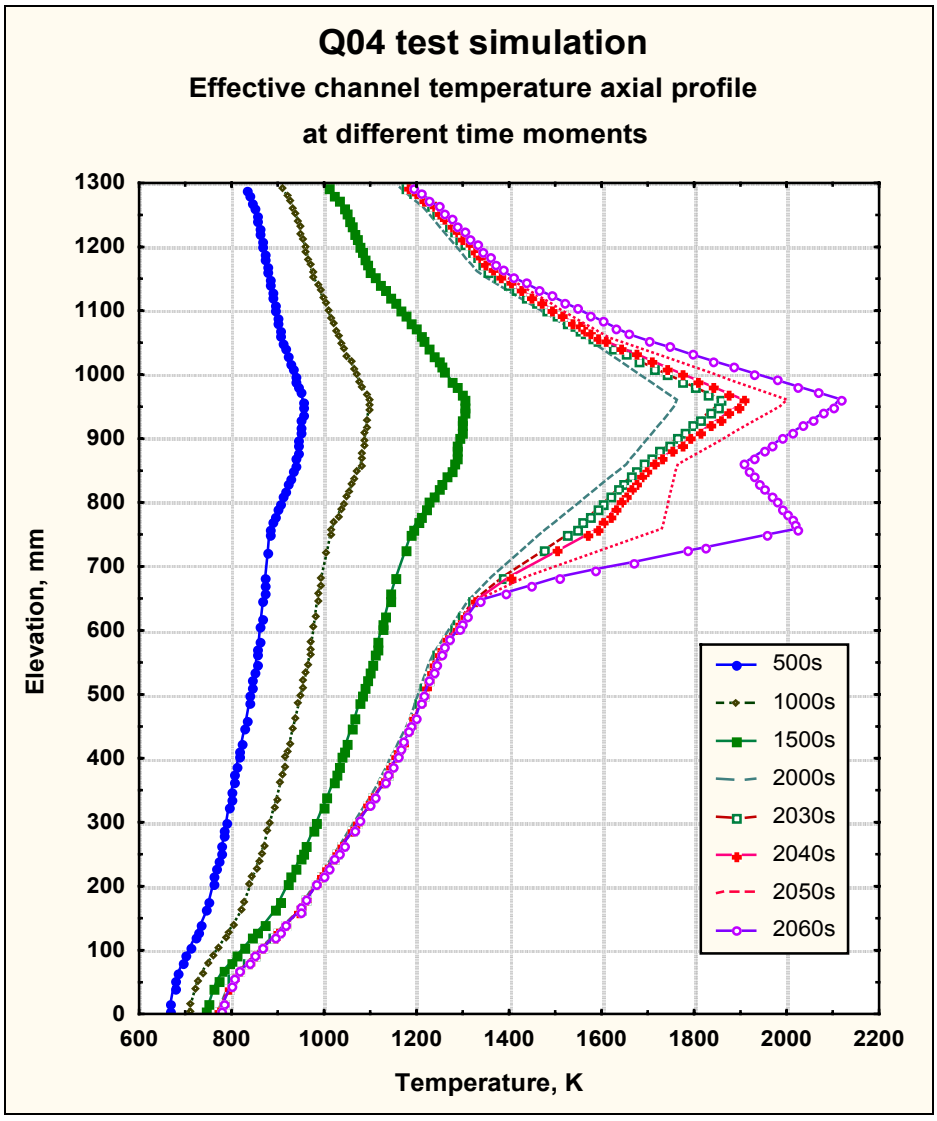

Fig. II-41. Effective channel inner wall temperature axial profile at different time moments.

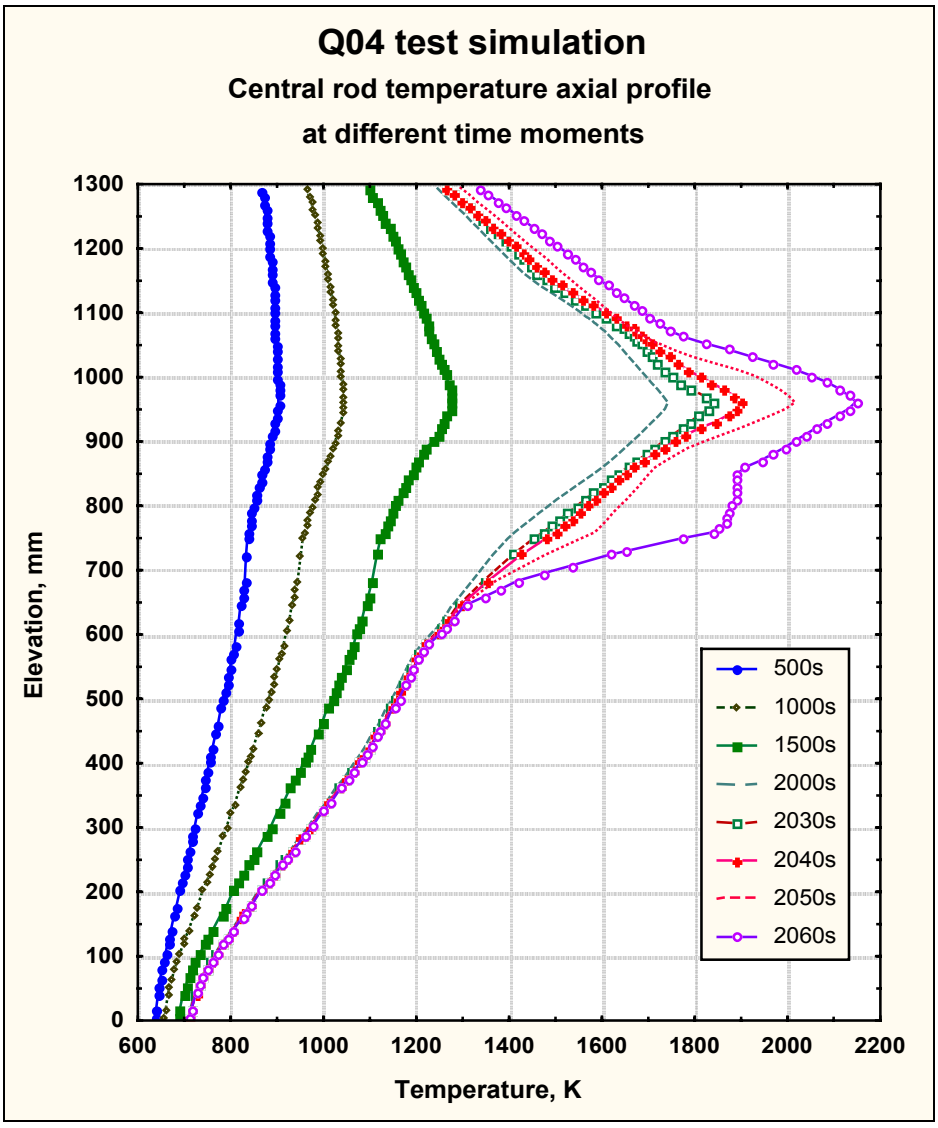

Fig. II-42. Central rod temperature axial profile at different time moments.

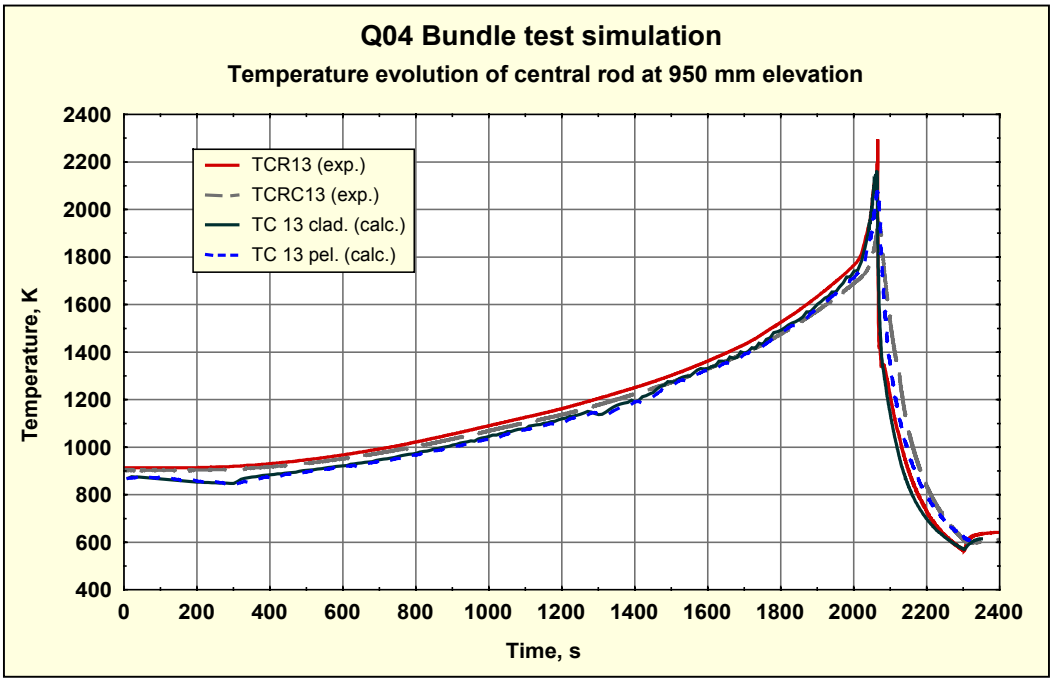

Fig. II-43. Central rod temperature evolution at 950 mm elevation.

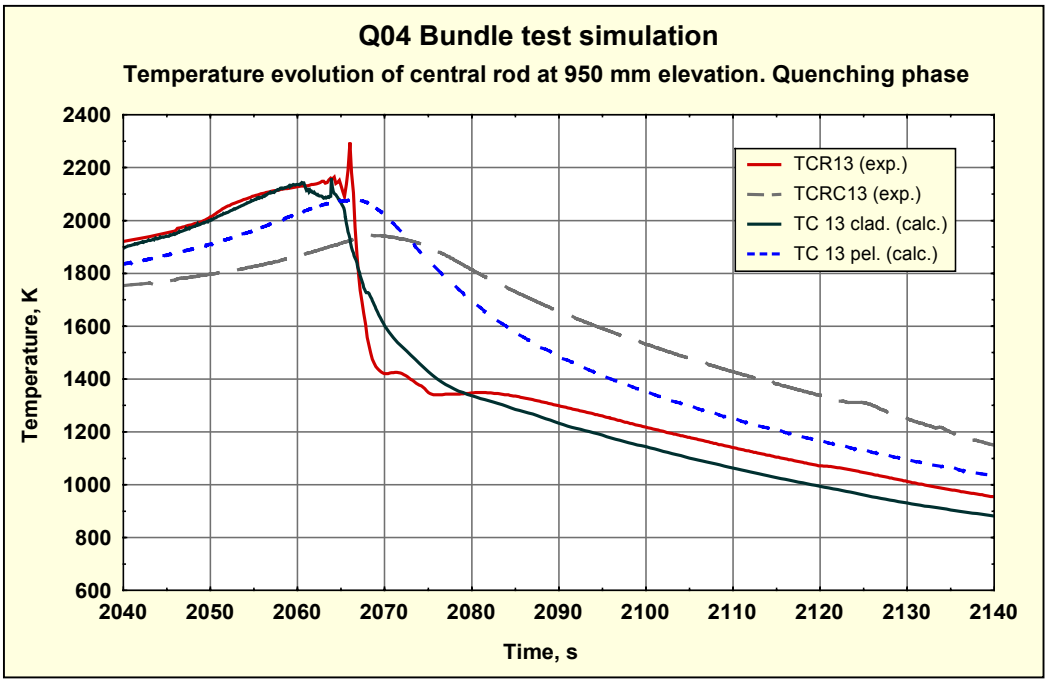

Fig. II-44. Central rod temperature evolution at 950 mm elevation. Quenching phase.

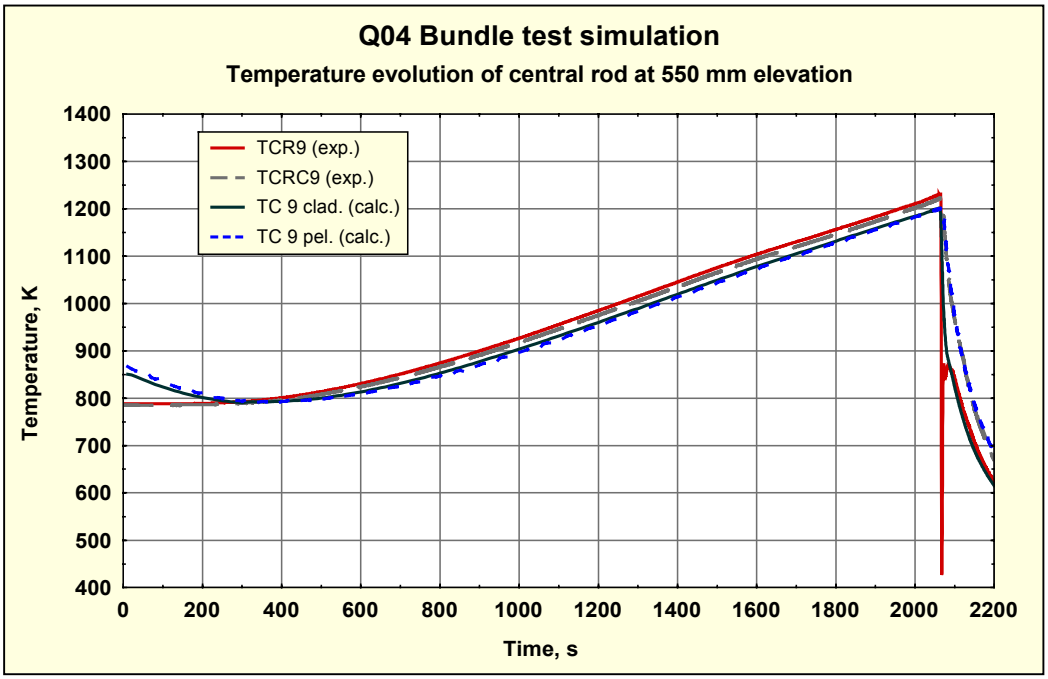

Fig. II-45. Central rod temperature evolution at 550 mm elevation.

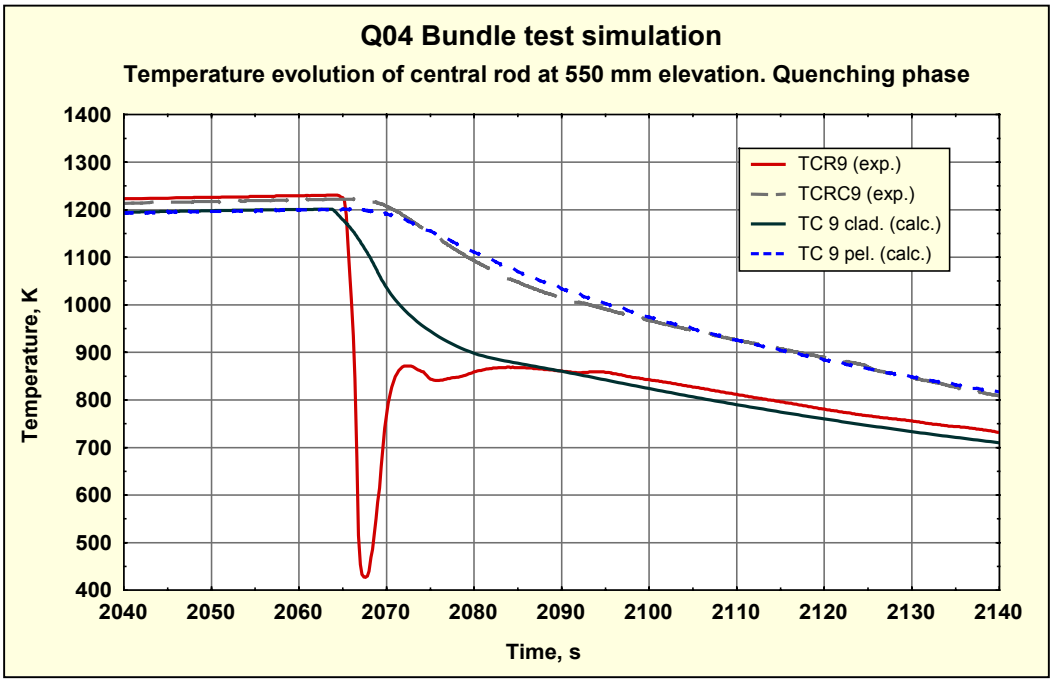

Fig. II-46. Central rod temperature evolution at 550 mm elevation. Quenching phase.

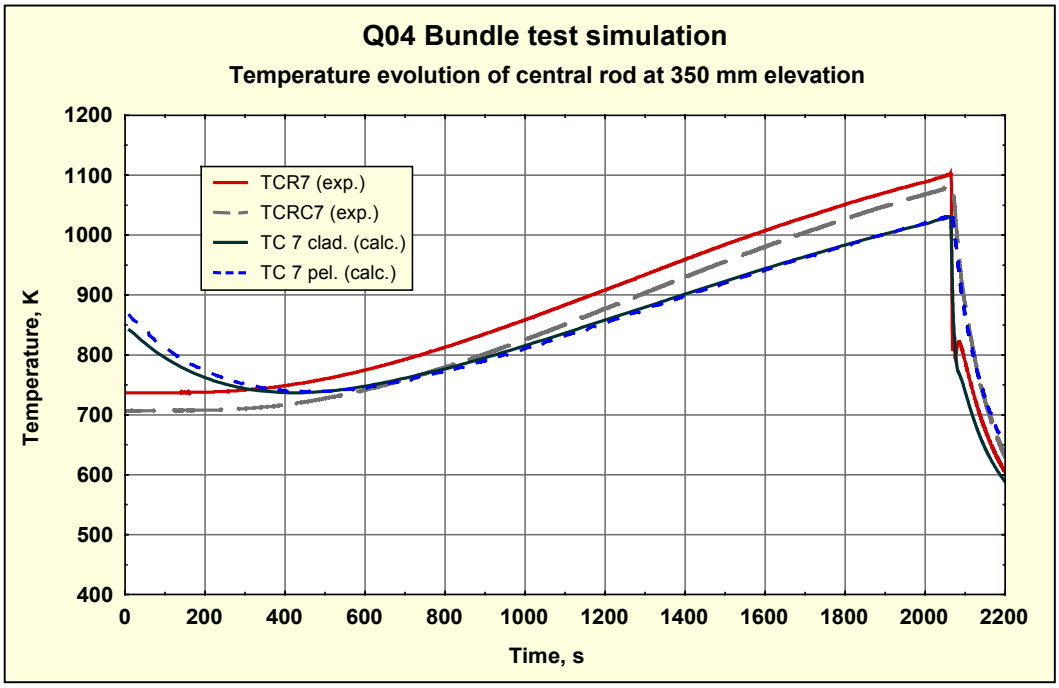

Fig. II-47. Central rod temperature evolution at 350 mm elevation.

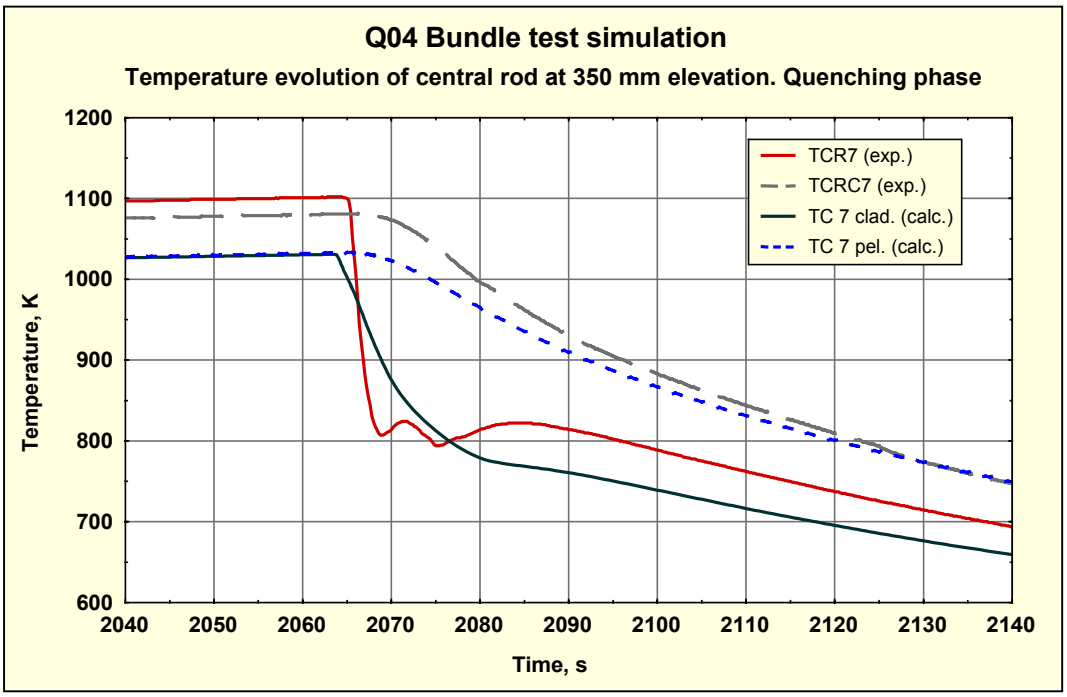

Fig. II-48. Central rod temperature evolution at 350 mm elevation. Quenching phase.

7 Analysis of Q-04 bundle test simulation results

7.1 Experimental observations

The experimental data of Q-04 test used in this work are presented by photos of unpolished cross-sections of the bundle and single fuel rod simulator, and measured oxide scale thickness at the different bundle elevations.

An investigation of the Q-04 test results allowed to expose the following main features of the bundle behaviour under the given test conditions:

- pronounced profile of the oxide scale thickness along axial direction for each fuel rod simulator;
- considerable gradient of the oxide scale thickness for the bundle in azimuth direction;
- the bundle remained as an assembly of individual rods, no blockage observed;
- in the axial direction the bundle was found after the test to be positioned approximately 70 mm lower than the shroud;
- the shroud deformed and the shape of the cross-section differed from the circle, the more significant deformation of the shroud occurred between 800 and 1100 mm bundle elevation, at the bundle elevation 1050 mm the shroud melting occurred, Fig. II-49a, b;
- the surfaces of sparse through-wall cracks were free from oxidation, Fig. II-50;
- in several cases the partial relocation of the molten cladding and pellet interaction of the remaining cladding were observed, Fig. II-51;
- in some cases due to steam penetration into the cladding-pellet gap, the inner oxidation of molten cladding occurred, Fig. II-52;
- no oxide scale breaching by molten cladding was observed.

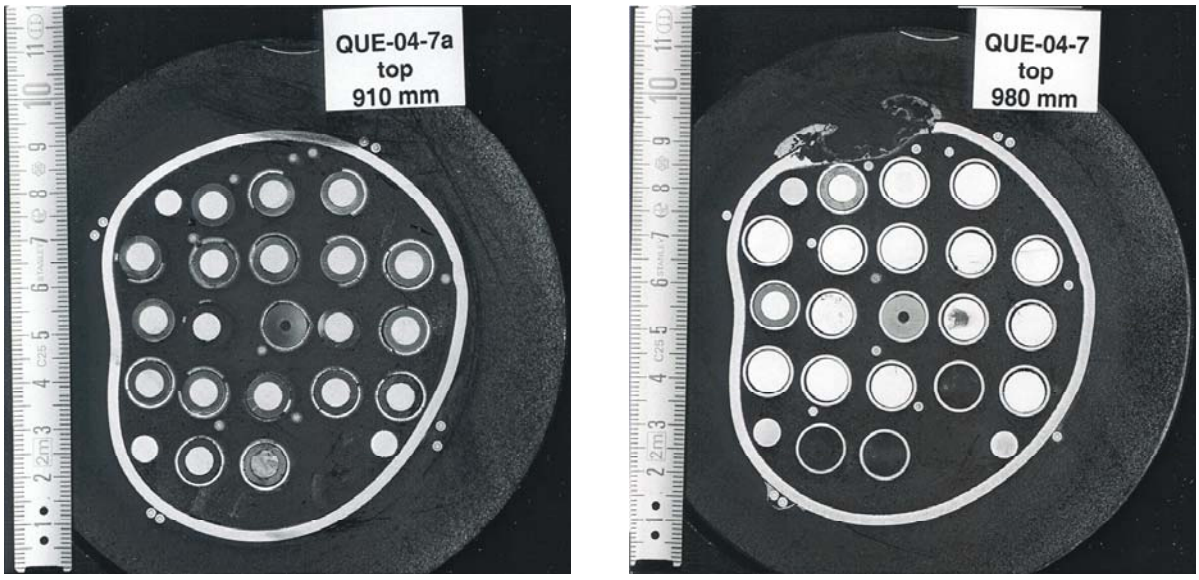

a. 980 mm bundle elevation (910 mm shroud elevation)

b. 1050 mm bundle elevation (980 mm shroud elevation)

Fig. II-49 View of the bundle cross-section at the different elevation (unpolished).

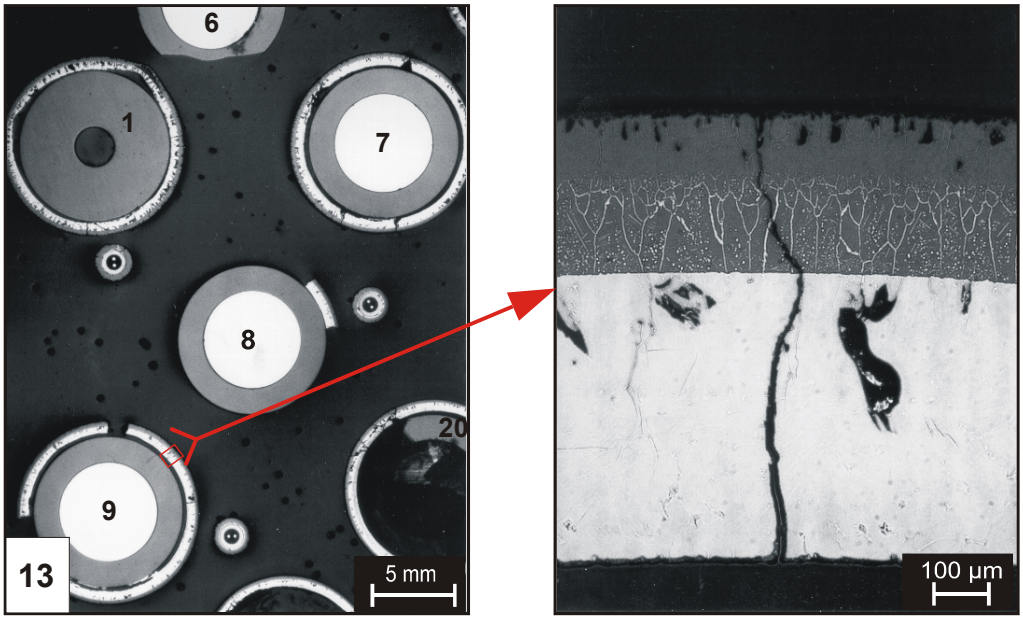

Fig. II-50 Cross-section at the bundle elevation 960 mm, rod # 9, cladding through-wall cracks non-oxidized.

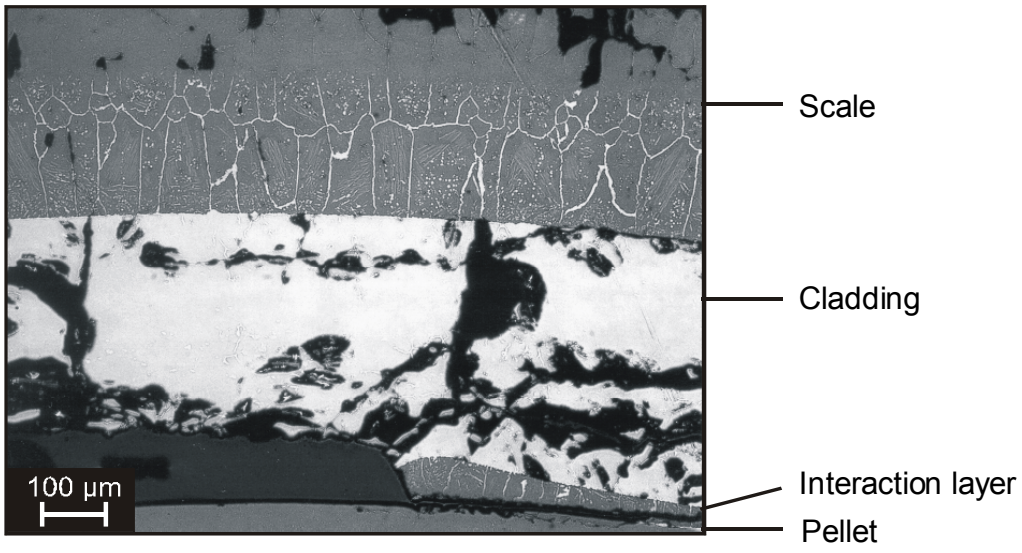

Fig. II-51 Cross-section at the bundle elevation 960 mm, rod # 4, partial relocation of the molten cladding and pellet interaction of the remaining cladding.

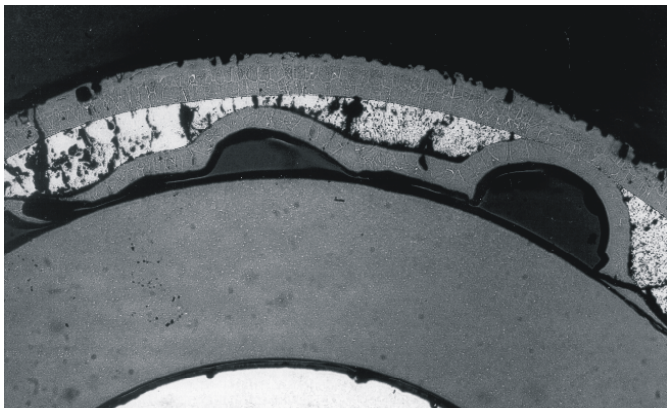

Fig. II-52 Cross-section at the bundle elevation 960 mm, rod # 3, internal steam oxidation of the cladding after partial relocation.

7.2 Calculation results

7.2.1 Oxide layer axial profile of the central rod after reflooding

Calculated temperature evolution of the central rod at different elevations in Q-04 test was considered in details in Section 7. In this part the other results of the central rod behaviour simulation are presented.

At about 2012 s from the start of data acquisition one of the solid Zircaloy rods was pulled from the bundle to check the extent of the attained oxidation. Unfortunately the oxide scale profile data for this removed solid rod were unavailable at the time of the current report preparation. Therefore, to verify the oxidation kinetics, the final oxide scale profile in axial direction was calculated and compared with measurements. Results are presented in Fig. II-53.

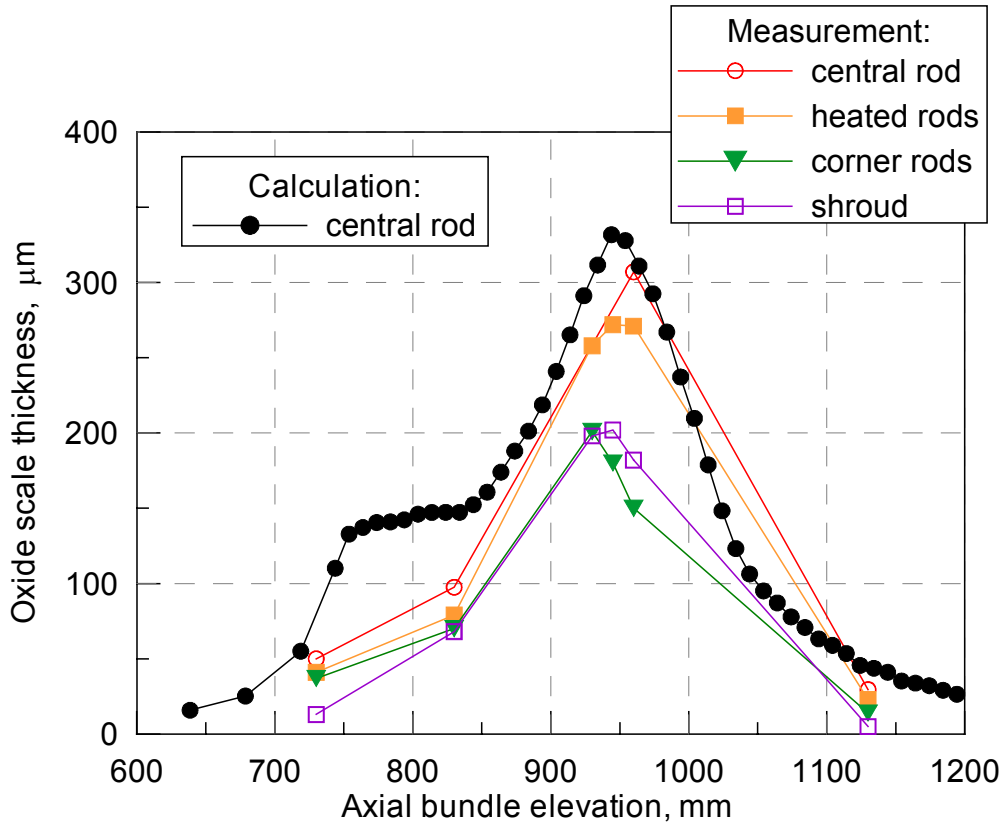

Fig. II-53 Calculated and measured outer oxide scale thickness profile along the axial direction after quenching.

One can see from Fig. II-53 that the calculated and measured oxide scale profiles of the unheated central rod are in a good agreement. Certain overestimation of the calculated oxide scale thickness occurred at the bundle elevation 750-850 mm.

The reason of this overestimation is not clear at the moment, as for the given experimental temperature evolution at this elevation (see Section 6) the well-verified S/Q oxidation model gives the oxide thickness much greater than the measured ones. The fact is that all three TCs located at 750 mm show temperature excursion up to 2100 K (see Fig. II-35), whereas the oxide scale thickness measured at this elevation on a number of rods does not exceed 50-55 μm (see Fig. I-84, Part I). There is also no evidence of a temporal steam starvation at this particular elevation which could resolve the contradiction between high temperatures and low oxide thickness. We also note that overestimation of the oxide thickness at 750-850 mm elevation will naturally lead to the overestimation of the total hydrogen production amount (see below, subsec. 8.2.3).

However, the above discussed oxide thickness overestimation takes place only on a small section of the bundle. In general, the calculated oxide scale profile of the central rod generally agrees with the measured one. This fact allows to assume that other features of the central rod behaviour are also correctly predicted by simulation.

7.2.2 The calculated state of the central rod after steam quenching

The final calculated state of the central rod after the preheating, pre-oxidation and steam quenching phases are presented in Table II-6.

In the first column of this Table II-the axial elevations of the central rod are presented. The second column presents the oxide layer thickness formed under external oxidation and the third one shows the state of the cladding wall.

One can see that the calculations predict that the central rod is still intact after the quenching phase, i.e. the cladding wall is not breached due to ballooning, flowering or tetragonal to monoclinic phase transition in the oxide scale. These predicted features agree with the post-test observations.

Absence of oxidised through-wall cracks under Q-04 test conditions corresponds to the conclusions derived from the results of the small-scale quench tests performed in FZK during the last several years [1]. Through-wall cracks formed in the case of highly pre-oxidised cladding (oxide scale was about 300 μm) and the initial temperature did not exceed 1673 K (1400 °C). If the initial quench temperature exceeded 1873 K (1600 °C), no or a few non-oxidised through-wall cracks were observed.

Since rod temperatures in the bundle quench test rig had the pronounced axial profile with the local maximum at the 940-960 mm, the oxide scale thickness has maximum at these locations. In contrast to QUENCH-01 the pre-oxidation stage of the QUENCH-04 test was shorter and the maximum oxide scale thickness was 300-350 μm at that elevations. The maximum initial temperature before quenching at the hottest elevations was about 2100-2200 K and at the elevation with the initial temperature near 1600-1700 K the oxide scale thickness was much less than the critical value.

The surfaces of the observed through-wall cracks are free from oxide. It is assumed that these cracks formed at temperature lower than the threshold temperature of marked oxidation (~ 1200 K). The possible reason may be the handling of the embrittled bundle after the test conduction.

Absence of the oxide scale breaching by molten Zircaloy also agrees with the small-scale tests results on clad failure performed in FZK in 1998-1999 [8]. The results of these tests allowed to reveal two possible mechanisms of breach formation [9]. At high heating rates the reason of breach formation was the intensive convective stirring of the melt and dissolution (erosion) of the outer oxide scale. At low heating rates the outer oxide scale formed at the pre-oxidation stage, continued to grow and the inner oxide layer appeared on the pellet surface. Owing to the volumetric expansion of oxide, the pellet-cladding gap volume disappeared leading to the oxide scale failure induced by the incompressible molten Zircaloy pressure.

Both these mechanisms need enough time and high temperatures, but during test QUENCH-04 the highest temperatures were reached and supported during tens seconds, then in the

quench phase temperature decreased very rapidly, in spite of the short-term temperature escalation at some locations.

Table II-6. Calculated state of central rod after quenching at different axial elevation.

Elevation [mm]	Outer oxide [μm]	Cladding state
1400	3	intact
1300	7	intact
1200	26	intact
1100	61	intact
1060	91	intact
1040	115	intact
1020	164	intact
1000	223	intact
980	280	intact
960	319	intact
940	322	intact
920	278	intact
900	230	intact
880	194	intact
860	167	intact
840	150	intact
820	147	intact
800	144	intact
780	141	intact
760	135	intact
700	40	intact
600	10	intact
500	0	intact
400	0	intact
300	0	intact
200	0	intact
100	0	intact
0	0	intact

7.2.3 Hydrogen absorption and generation for the central rod

The calculated results of the total hydrogen generation and hydrogen absorption for the central rod are shown in Fig. II-54. One can see that the total hydrogen generation increases during transient phase due to intensive oxidation caused by high temperatures. The total hydrogen production is near 586 mg, hydrogen production during quenching is 36 mg. Thus, as for the case of Q-01 test, the total hydrogen production for the central rod in the stages before quenching is much more than hydrogen generation during quenching.

Total mass of the dissolved hydrogen is 117 mg, all amount of the dissolved hydrogen is absorbed before quenching. The calculations predict that almost 50 % of absorbed hydrogen was dissolved between elevations 1300 –1400 mm at the pre-oxidation phase before the oxide scale formation at these elevations.

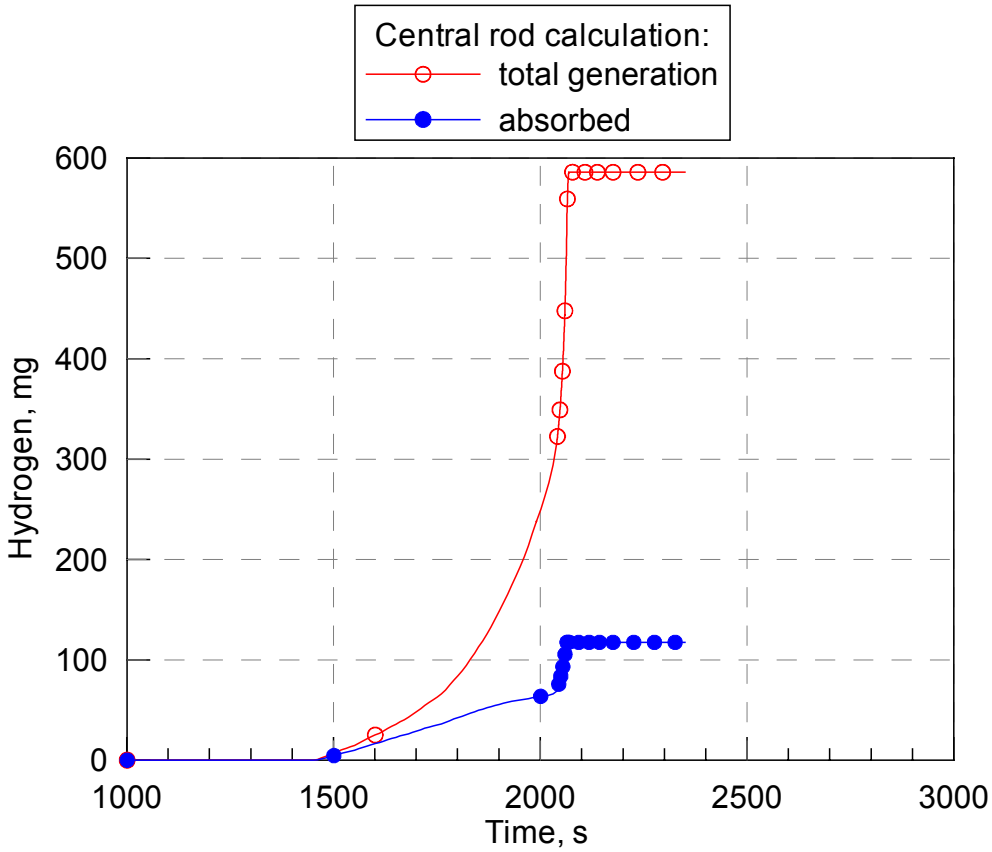

Fig. II-54 Calculation results for hydrogen absorption and generation in the central rod

The obtained data for the central rod were extrapolated to the whole bundle using the same procedure as in the case of Q-01 test (see Section 5). The results of this extrapolation are presented in Fig. II-55. As one can see, the calculated total amount of generated hydrogen exceeds the measured one. One of the possible reasons of this discrepancy may be discussed above overestimation of oxide scale thickness at 750-850 mm elevation (see subsection 8.2.1).

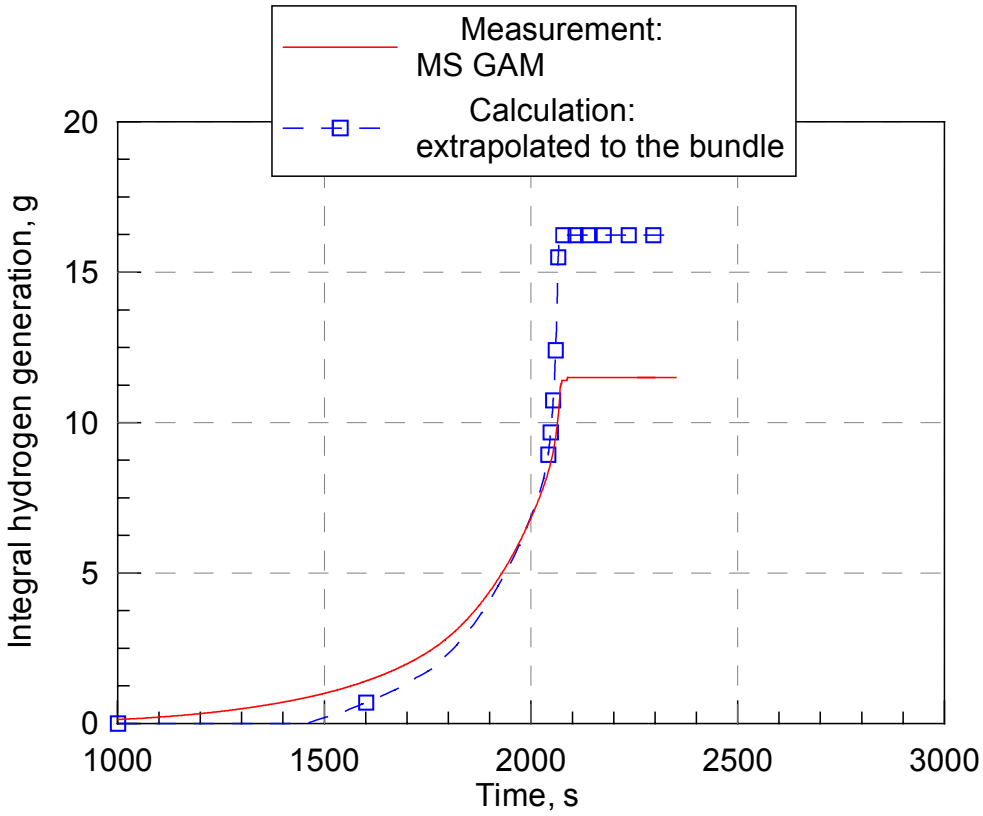

Fig II-55. Calculation result for hydrogen generation in the central rod extrapolated to the bundle. QUENCH-04.

8 Summary and conclusions

- The ‘effective channel’ approach to the QUENCH bundle tests simulation by the S/Q code was developed. This approach assumes the usage of the experimentally measured temperatures of heated rods and shroud for the formulation of the central rod boundary conditions.
- On the basis of such conditions the S/Q code allows the correct solution of the temperature problem inside the rod and so, allows detailed description of the cladding mechanical deformation, oxidation and hydrogen absorption processes during reflooding.
- The numerical procedure of experimental data recalculation including smoothing, interpolation and averaging operations was developed and performed for the Q-01 data. The set of smoothed bundle temperature evolution curves was obtained.
- The analysis of the smoothed bundle temperature evolution curves leads to the conclusion that at the end of reflooding only lower half of the bundle was filled by coolant due to intensive evaporation. That was qualitatively confirmed by the S/Q calculation, which gives the estimation of the evaporation rate.

- The simulation of the Q-01 bundle test on the basis of obtained smoothed TCs data set was performed. At the upper part of the bundle good agreement between measured and calculated temperature evolution of the central rod was obtained at all test phases. At the lower part of the bundle at the flooding phase of the test the calculated central rod temperature evolution curves are in a qualitative agreement with the bundle temperature evolution ones.

- Q-04 test experimental data were analysed and a number of the S/Q code auxiliary calculations for the data evaluation was performed. On the basis of this evaluation the set of bundle temperature evolution curves was obtained.

- The simulation of the Q-04 bundle test on the basis of obtained smoothed TCs data set was performed. Calculation results are in reasonable agreement with the experimental data.

- With respect to oxidation and mechanical deformation behaviour the performed calculations allowed to describe the following phenomena:

    - the axial profile of the oxide scale thickness;

    - failure mode and state of the central rod cladding after quenching;

    - oxidation of surfaces of through-wall cracks formed during flooding and of the inner cladding surface.

- Under the given test conditions heat release during quenching, even with account for oxidation of the through-wall crack surfaces and the inner cladding surface, does not lead to temperature escalation owing to high heat losses;

- Hydrogen production in the quench phase, with account for an amount of hydrogen release due to the through-wall crack surfaces and the inner cladding surface oxidation, is negligible in comparison with hydrogen generated during oxide scale formation.

References

[1] P. Hofmann, V. Noack, M.S. Veshchunov, A.V. Berdyshev, A.V. Boldyrev, L.V. Matweev, A.V. Palagin, V.E. Shestak, “Physico-Chemical Behavior of Zircaloy Fuel Rod Cladding Tubes During LWR Severe Accident Reflood,” FZKA 5846, Forschungszentrum Karlsruhe 1997;

[2] P. Hofmann, A. Miassoedov, L. Steinbock, M. Steinbrück, M. Veshchunov et al.: “Quench Behavior of Zircaloy Fuel Rod Cladding Tubes. Small-Scale Experiments and Modeling of the Quench Phenomena,” FZKA 6208, Forschungszentrum Karlsruhe, 1999

[3] M.S. Veshchunov, A.V. Berdyshev, A.V. Boldyrev, A.V. Palagin, V.E. Shestak, “Modelling of LWR Core Quench Phenomena. Part III,” Report IBRAE, December 1998;

[4] A.V. Berdyshev, A.V. Boldyrev, A.V. Palagin, V.E. Shestak, M.S. Veshchunov, “SVECHA/QUENCH Code for The Modeling of Reflooding Phenomena in Severe Accidents Conditions.” Proceedings of the Ninth International Topical Meeting on Nuclear Reactor Thermal Hydraulics (NURETH-9), paper Log_19 (CD-ROM edition), San Francisco, California, USA, October 1999;

[5] M.S. Veshchunov, A.V. Berdyshev, A.V. Boldyrev, A.V. Palagin, V.E. Shestak. “Modelling of LWR Core Quench Phenomena. Part IV,” Final Report IBRAE, December 1999;

[6] P. Hofmann, W. Hering, C. Homann, W. Leiling, A. Miassoedov, D. Piel, L. Schmidt, L. Sepold, M. Steinbrück, “QUENCH-01, Experimental and Calculational Results,” FZKA 6100, Forschungszentrum Karlsruhe, 1998.

[7] L. Sepold, P. Hofmann, W. Krauss, W. Leiling, A. Miassoedov, D. Piel, L. Schmidt, M. Steinbrueck, C. Homann, S. Horn, Internal Report, 1999.

[8] P. Hofmann, A. Miassoedov, “Experiments on the ZrO_2 Shell Failure Criteria,“ presented to CIT Meeting, Prague, June 7-8, 1999.

[9] P. Hofmann, J. Stuckert, A. Miassoedov, M.S. Veshchunov, A.V. Berdyshev, A.V. Boldyrev, “ZrO_2 dissolution by Molten Zircaloy and Cladding Oxide Shell Failure. New Experimental Results and Modelling,“ Wissenschaftliche Berichte, FZKA 6383, INV-CIT(98)-P026. Dezember 1999.

Appendix

Example of the **tc-coord.dat** input file

```
$-----------------------------------------------------------------
$ NUSETC     - number of TC used for the central rod behaviour
$            simulation
$-----------------------------------------------------------------
   17
$-----------------------------------------------------------------
$ HORIG, [m] - distance from the upper end of the rod to the zero
$            level (from which the axial coordinate (Z-coord) of
$            TC was measured).
$-----------------------------------------------------------------
   1.975
$-----------------------------------------------------------------
$            Zero level corresponds to the -475mm bundle level.
$-----------------------------------------------------------------
$ TC Number  - number of TC data column MINUS UNIT
$            in the file TC-TEMP.DAT
$
$            R-coord,Fi – polar TC coordinates
$            Z-coord    - axial TC coordinates (from zero level)
$
$ TC Number  R-coord,[m]  Fi,[dgr]  Z-coord,[m]
$-----------------------------------------------------------------
    1         0.        0.       1.825
    2         0.        0.       1.725
    3         0.        0.       1.625
    4         0.        0.       1.525
    5         0.        0.       1.425
    6         0.        0.       1.325
    7         0.        0.       1.225
    8         0.        0.       1.145
    9         0.        0.       1.045
   10         0.        0.       0.945
   11         0.        0.       0.825
   12         0.        0.       0.725
   13         0.        0.       0.625
   14         0.        0.       0.525
   15         0.        0.       0.425
   16         0.        0.       0.325
   17         0.        0.       0.225
```

Example of the **tc-temp.dat** input file

```
$---------------------------------------

$ TRZERO   0.   - if TC indications in [K],
$          273. - if TC indications in [C].
$---------------------------------------
           0
$---------------------------------------
$ Time[s] Temp. TC
                     1          2          3          4          5          6          7
$-------------------------------------------------------------
       0.00     786.00     744.00     826.00     784.00     806.00     871.00     876.00
       4.00     788.00     744.00     826.00     781.00     806.00     871.00     876.00
       8.00     788.00     744.00     826.00     784.00     806.00     871.00     876.00
      12.00     789.00     744.00     826.00     784.00     809.00     873.00     877.00
      16.00     789.00     744.00     829.00     786.00     809.00     874.00     877.00
      20.00     791.00     746.00     829.00     786.00     809.00     874.00     878.00
      24.00     791.00     746.00     829.00     786.00     811.00     876.00     879.00
      28.00     792.00     749.00     829.00     789.00     811.00     876.00     879.00
      32.00     792.00     749.00     831.00     789.00     811.00     876.00     880.00
      36.00     794.00     749.00     831.00     789.00     811.00     877.00     880.00
      40.00     794.00     749.00     831.00     789.00     811.00     877.00     880.00
      44.00     794.00     751.00     831.00     791.00     811.00     877.00     880.00
      48.00     795.00     751.00     833.00     791.00     811.00     877.00     880.00
      52.00     795.00     751.00     833.00     791.00     814.00     879.00     882.00
      56.00     797.00     751.00     833.00     791.00     814.00     879.00     882.00
      60.00     797.00     754.00     833.00     791.00     814.00     880.00     882.00
      64.00     797.00     754.00     833.00     794.00     814.00     880.00     882.00
      68.00     798.00     754.00     836.00     794.00     814.00     880.00     882.00
      72.00     798.00     756.00     836.00     794.00     816.00     880.00     883.00
```